Three-Dimensional Unsteady Hydrodynamics of Tidal Turbines

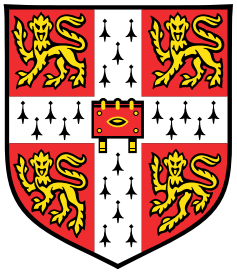

Amanda Sofie Magdalena Smyth

Supervisor: **Dr. A.M. Young**

Advisor: Prof. R.J. Miller

Whittle Laboratory, Department of Engineering
University of Cambridge

This thesis is submitted for the degree of
Doctor of Philosophy

Murray Edwards College July 2019

Declaration

The research presented in this thesis was conducted at the Whittle Laboratory, in the Cambridge University Engineering Department, between October 2015 and July 2019.

This thesis is the result of my own work and includes nothing which is the outcome of work done in collaboration except as declared in the Preface and specified in the text. It is not substantially the same as any that I have submitted, or, is being concurrently submitted for a degree or diploma or other qualification at the University of Cambridge or any other University or similar institution except as declared in the Preface and specified in the text. I further state that no substantial part of my thesis has already been submitted, or, is being concurrently submitted for any such degree, diploma or other qualification at the University of Cambridge or any other University or similar institution except as declared in the Preface and specified in the text. It does not exceed the prescribed word limit for the relevant Degree Committee.

Amanda Sofie Magdalena Smyth
July 2019

Publications

Smyth, A. S. M., Young, A. M., Di Mare, L., 2019. 'The Effect of 3D Geometry on Unsteady Gust Response, Using a Vortex Lattice Model'. Paper presented at AIAA SciTech, San Diego, US.

Smyth, A. S. M., Young, A. M., 2019. 'Three-Dimensional Unsteady Hydrodynamic Modelling of Tidal Turbines'. Paper presented at the 13th European Wave and Tidal Energy Conference (EWTEC), Naples, Italy.

Abstract

Three-Dimensional Unsteady Hydrodynamics of Tidal Turbines

Amanda Sofie Magdalena Smyth

Tidal power is an emerging industry in the renewable energy sector; a development which is uniquely beneficial to the United Kingdom, which has a significant tidal resource and a mature knowledge base for turbine technology. One of the challenges facing the tidal industry is the harsh nature of the operating environment, due to the presence of waves and ocean turbulence. The turbines sustain damage due to the fluctuating loads that result from the unsteady flow, either from high-cycle fatigue or from extreme loading events exceeding the ultimate tensile strength of components.

In this thesis, the problem of unsteady loading is addressed by identifying the shortcomings of the models currently used to estimate unsteady forces on turbines due to gusts, and by providing new low-order modelling tools for more accurate calculations of these forces. The focus of this thesis is on the assumption of locally two-dimensional (2D) flow used in the majority of turbine loading models. Tidal turbines are strongly three-dimensional (3D) in shape, with low aspect ratio and strongly tapered blades. As such, the assumption of locally 2D flow is unlikely to apply. In this thesis the consequences of this assumption are explored, dividing 3D effects into two categories: 3D geometry effects, and the effects of 3D features in the incoming unsteady flow. The effect of these 3D features is shown by studying generic aerofoil geometries and a model tidal turbine, using a combination of first-order inviscid modelling with a vortex lattice model (VLM) and higher-order viscous modelling with URANS CFD.

The VLM is used in the frequency-domain to perform a parametric study of a range of aerofoil geometries. The unsteady response of aerofoils with finite span, rotation or varying planform is shown to deviate strongly from 2D predictions by linear analytic theory (such as the Theodorsen or Sears functions). At low reduced frequencies and low aspect ratios, 3D effects are strongly visible. In the vicinity of the aerofoil tips, 3D effects are significant at any

reduced frequency. An exception is found in swept wings, where the unsteady response does not approach the 2D response in any conditions. The primary driver of the 3D load response is found to be the unsteady wake downwash, which is divided into contributions from the spanwise and streamwise components of wake vorticity. The former is modelled as extending infinitely in 2D models, while the latter is neglected altogether. URANS modelling and a time-domain vortex lattice model is used to estimate second order effects on the unsteady load response, due to viscous separation events and wake deformation, respectively. These second order effects on the unsteady loads are shown to be minor, and the URANS simulations also successfully validate the inviscid vortex lattice model.

For the analysis of 3D features in the incoming flow, this thesis uses eigenmode decomposition of the vortex lattice model, which finds the spatial shapes of the gusts that will cause the largest forces on a given aerofoil geometry. This is shown through the concept of "mode resonance": if a gust is similar in shape to a particular aerofoil eigenmode, that mode will contribute more to the total load response of the aerofoil. This analysis allows the definition of a "cut-off" spatial length scale for turbine load response; if the oncoming unsteady gust has a spanwise wavelength shorter than the cut-off value, the load response of the aerofoil to that gust will be negligible. This finding is used at the end of this thesis to show the impact of 3D flow features when evaluating the load response of a turbine in a realistic flow environment.

This thesis concludes that accounting for the effects of both 3D geometry and 3D flow is vital for accurate prediction of turbine load response to unsteady gusts.

Acknowledgements

I would like to sincerely thank my supervisor, Dr Anna Young, for her patient and tireless support during this project. As her "prototype" PhD student, I was given time, advice and mentoring in abundance. Over the past few years she has been a source of vital help, her support ranging from in-depth discussion about tidal turbine hydrodynamics, to correcting my hopeless "Swenglish" in various paper drafts, to driving me around the west coast of California. I am immensely grateful for the opportunity she offered when taking me on for this project, and attribute its successful completion in no small part to her efforts. I also want to gratefully acknowledge the support of my advisor, Professor Rob Miller. His ability to find sense and purpose in a collection of early, undeveloped ideas has been a tremendous help at a number of stages in the development of this project.

Without the support of my former Masters thesis supervisor, Professor Luca Di Mare, I would not have come to this point. He also helped develop the vortex lattice model used in this project, and introduced me to the concept of eigenmode decomposition. Numerous discussions with him about unsteady fluid dynamics is what formed some of the core ideas in this project. I am indebted to his early belief in my ability to do research, and to his patient help throughout my research career.

The Whittle Lab community has been a continuous source of support throughout this project. I would like to especially thank Dr Tom Hynes, who helped me to make sense of my own ideas, and to present them in an accessible format. I would also like to thank Dr Tim Williams for MATLAB support, and for good office company in the past few years. I am grateful to Dr Judith Farman for numerous technical discussions about tidal turbines, and for being the first to welcome me into the community. This is also true of Dr Carl Sequeira. Finally, I am grateful to the EPSRC, whose funding made this project possible.

Table of contents

Nomenclature

Roman Letters

A	Wetted area
c	Blade chord
$C(k)$	Theodorsen function
$C'(k)$	Loewy function
C_d	Drag coefficient
C_l	Local lift coefficient
Cl_N	Local normalised lift coefficient
Cl_{REL}	Local relative lift coefficient
C_p	Power coefficient
C_p/η	Unsteady power coefficient
C_t	Thrust coefficient
C_t/η	Unsteady thrust coefficient
$D_{turbine}$	Turbine diameter
I	Identity matrix
k	Reduced frequency
L_{eddy}	Turbulent eddy length scale
L_t	Transverse turbulence length scale
m	Number of spanwise lattice panels
n	Number of chordwise lattice panels
N	Total number of lattice panels
$\hat{n}$	Surface normal
N_b	Blade number
Q	Torque
T	Thrust
r	Radius
R	Hub radius
Re	Reynolds number
S	Surface area
$S(k)$	Sears function
$S'(k)$	Phase-shifted Sears function
t	Time
T	Wave period
U_∞	Mean axial freestream velocity
u_{gust}	Gust-induced velocity
u_{rot}	Rotational velocity
u_{wake}	Wake-induced velocity
V_L	Left eigenvector
V_R	Right eigenvector

Greek Letters

α	Angle of attack
β	Wave approach angle
η	Gust amplitude
γ	Streamwise wake circulation
Γ	Vortex lattice panel circulation
λ_{wave}	Wavelength of surface wave
λ_{gust}	Wavelength of unsteady gust
λ_{span}	Unsteady gust wavelength, as proportion of turbine diameter
Λ	Diagonal matrix of eigenvalues
ω	Time-harmonic frequency
Ω	Turbine rotational frequency
ρ	Density
θ	Tangential coordinate

Subscripts and superscripts

$\bar{[\ ]}$	Mean
$[\ ]'$	Fluctuation
$\hat{[\ ]}$	Amplitude
$\angle[\ ]$	Phase
$\dot{[\ ]}$	First time derivative
$\ddot{[\ ]}$	Second time derivative
$[\ ]_x$	Axial component
$[\ ]_{local}$	Local component
$[\ ]_{rms}$	Root Mean Square Value
$\Delta[\ ]$	Peak-to-peak amplitude
$[\ ]^H$	Hermitian; complex conjugate transpose

Acronyms

ADCP	Acoustic Doppler Current Profiler
ADV	Acoustic Doppler Velocimeters
AR	Aspect Ratio
BEMT	Blade Element Momentum Theory
CFD	Computational Fluid Dynamics
HATT	Horizontal-Axis Tidal Turbine
RANS	Reynolds-Averaged Navier-Stokes
TR	Taper Ratio
TSR	Tip Speed Ratio
URANS	Unsteady Reynolds-Averaged Navier-Stokes
VATT	Vertical-Axis Tidal Turbine
VLM	Vortex Lattice Model

Chapter 1

Introduction

1.1 Tidal power

The extraction of power from the ocean tides is an emerging technology in the renewable energy sector, a development which is uniquely beneficial to the United Kingdom. Conservative estimates suggest that tidal stream energy could provide over 10% of the UK's peak electricity demand [11]. Over the past two decades, a number of projects have emerged pushing for the development of commercial-scale tidal power arrays. Several different prototype designs have been proposed and tested, and their development has been greatly enhanced by the test sites at the European Marine Energy Centre (EMEC) in Orkney, which allow for a "plug-and-play" approach to device development[1]. As a result of the extensive preparation work done at EMEC and other sites around the world, tidal power is now approaching commercial readiness. In Scotland alone, 17 leases for tidal site development have been issued [98], and some of the world's first pre-commercial tidal arrays are currently being installed. Phase 1 of the MeyGen project has installed an array of four 1.5 MW turbines off the North coast of Scotland next to the island of Stroma, which will act as a precursor to a further expansion to a 86 MW farm (the site is leased for a total of 398MW)[2]. As of July 2019, a total of 17.5 GWh had been exported from the MeyGen site to the commercial grid[3].

Using smaller scale turbines, Nova Innovation installed the world's first grid-connected offshore tidal array in Bluemull Sound at Shetland in 2016[4]. In 2018 a Tesla Powerpack

[1] http://www.emec.org.uk/about-us/

[2] https://simecatlantis.com/projects/meygen/

[3] https://simecatlantis.com/2019/07/10/meygen-operational-update-3/

[4] https://www.novainnovation.com/bluemull-sound

battery storage system was integrated with the tidal array[5]. Hailed as the "holy grail" of tidal power, energy storage systems such as this allow a tidal array to provide continuous power to the grid even at slack water, so that tidal energy can contribute to baseload electricity, or respond to peaks in demand.

The transformation of the energy mix in the UK towards renewables is a crucial part of reaching the CO_2 emission targets set by the UK through international agreements. A frequently cited challenge in some of the most developed renewables industries, which are based on wind and solar power, is that renewable energy sources tend to be variable and unpredictable. In order to guarantee energy supply at all times, and to provide for peak requirements in unfavourable resource conditions, redundancy must be built into the supply. To replace an equivalent gas power plant with wind energy, the rated power of the wind resource must be in the order of 30% higher than that of the gas power plant [121]. Because of this, the predictability of tidal power is an attractive asset, and may provide the reliable renewable baseload energy which in other countries might be supplied by hydro power or geothermal sources.

One of the challenges facing the emerging tidal industry is the harsh nature of the operating environment. The nature of tidal flow presents unique challenges to device designers, due to the presence of significant waves and ocean turbulence. Conditions at typical tidal sites are characterised by unpredictable turbulence conditions, with length scales ranging from a few millimetres in the turbulent boundary layer on the blades, to eddies with horizontal length scales of hundreds of meters. All scales between these extremes exist to varying degrees, and can be generated by seabed bathymetry, wind, headlands, and interaction with surface waves. Devices are generally designed for steady uniform flow, and the variability in power extraction due to high turbulence is difficult to predict. The turbines also sustain damage due to the fluctuating loads that result from the unsteady flow – either from high-cycle fatigue or from extreme loading events exceeding the ultimate tensile strength of components. At a time when many companies were at a stage of turbine prototype deployment, a number of premature failures served to highlight the issue of extreme loading: high-profile turbine projects such as OpenHydro[6] and the Atlantis AK1000[7] were forced to interrupt their site testing due to damage to their turbines. As a consequence of these early failures, designers tend to over-engineer turbine blades and set cautious maintenance schedules as a way of

[5]https://www.novainnovation.com/post/a-world-first-for-nova-innovation-the-holy-grail-of-baseload-tidal-power

[6]https://www.greentechmedia.com/articles/read/a-big-setback-for-tidal-power#gs.okn0wa

[7]https://www.bbc.co.uk/news/uk-scotland-highlands-islands-11492829

preventing damage to the turbines, which leads to increased device costs.

The oscillating forces on turbines cause issues with reliability and operational life which must be resolved in order for the tidal industry to be truly competitive. A 2011 study estimated that turbine reliability at the time would result in one failure every two years per turbine [28], which is far from adequate considering the high cost of maintenance at sea. The problem is aptly summarised by Clark in his report from the Turbulence in Marine Environments (TiME) project [24], stating that there is a "'chasm' between environmental measurement practice and robust engineering prediction/simulation of turbulent effects". In essence – as shown by the premature failures of turbines and the overly-cautious engineering practices that followed – the models used to estimate unsteady forces on tidal turbines are not capable of doing so with the required accuracy.

This thesis aims to address this problem by identifying some of the major shortcomings of the models currently used to estimate unsteady turbine load, and by providing new low-order modelling tools for more accurate calculations. The focus will be on one of the most significant assumptions involved in current modelling theories: the assumption of locally two-dimensional (2D) flow.

Much of tidal turbine preliminary design is based on strip-theory methods, which divides the turbine blade into 2D blade sections along the span, the properties of which are interpolated to find the torque and thrust of the turbine. Three-dimensional (3D) effects, such as load reduction due to proximity to the blade tip, are considered through the use of correction factors [15]. Unsteady effects are included at the 2D blade section level. There is however no method for correcting the unsteady loading for 3D effects. In addition to this, the effect of 3D geometry on the unsteady load performance of an aerofoil is virtually unknown.

The 3D effects relevant to tidal turbines can be divided into two categories: 3D geometry effects, and the effects of 3D features in the incoming flow turbulence. Neither of these are fully understood for the purpose of tidal turbine modelling, and the limits of applicability of the assumption of locally 2D flow have not been established. This thesis will address both 3D geometry effects and 3D unsteady flow effects, and establish their impact on unsteady loads experienced by tidal turbines.

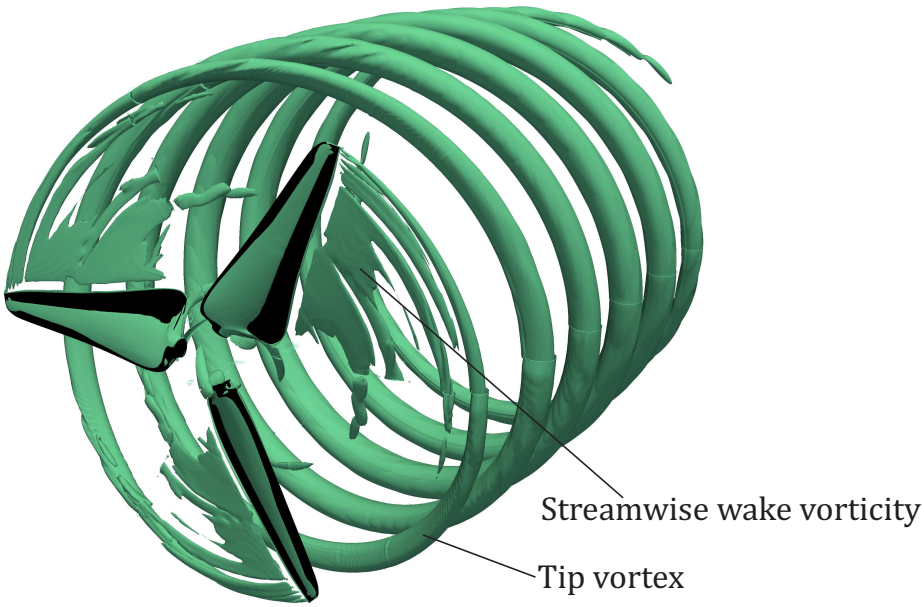

Fig. 1.1 Illustration of the wake vorticity shed from tidal turbine blades. Iso-contours of q-criterion, obtained from RANS CFD simulation of a third of a turbine annulus, extrapolated to full-annulus.

1.2 The effects of 3D aerofoil geometry

Many of the modelling practices used for tidal turbines were developed first for the wind industry. Wind turbine blades are generally long and slender with high aspect ratios, and so the assumption of locally 2D flow is likely to apply, especially at the outboard blade sections where the majority of power is generated. For a given rated power, a tidal turbine will have a diameter approximately a third of that of the equivalent wind turbine, due to the difference in density between air and water [139]. The smaller diameter means that tidal turbines have much lower aspect ratio blades than wind turbines, making 3D flow more prevalent, and as such the assumption of 2D flow will lead to larger errors when modelling a tidal turbine blade.

While the smaller size of the device may be a benefit from a cost perspective, the thrust loading on a tidal turbine is much higher than on a wind turbine with the same rated power [139]. Furthermore, the lower rotor inertia coupled with the higher density of water compared to air mean that the tidal turbine will be more susceptible to unsteady loading. This means that accurate unsteady load calculations which take the real 3D geometry into consideration are more important for tidal turbines than for wind turbines. By copying design tools from the wind industry, designers are therefore using a less accurate model despite the

calculation being more critical in water than in air.

Inherent to any finite-span aerofoil geometry, or to aerofoils with spanwise variation in planform, is the presence of a streamwise component of vorticity in the aerofoil wake. This vorticity is most clearly visible as the tip vortices shed by aeroplane wings. The rotation of a tidal turbine means that the tip vortices form a helical shape moving downstream (see Figure 1.1). The streamwise wake vorticity induces a velocity component on the aerofoil, called downwash, which works to reduce the effective angle of attack at each blade section and therefore reduces the lift generated by the aerofoil. For steady-flow calculations on 3D geometries, the effect of the streamwise vorticity can be included as correction factors to the blade loading calculated at each 2D section.

When a 2D aerofoil is subjected to unsteady inflow velocity, the angle of attack changes as a function of time. As it does, the aerofoil sheds vorticity with strength equal and opposite to the change in aerofoil circulation, in order to preserve Kelvin's theorem (excluding viscous dissipation, the circulation in a domain must be constant in time). This generates an unsteady wake made up of spanwise vortex lines which extend to infinity in the spanwise direction.

In classical 2D aerofoil theory, the unsteady loading on an aerofoil is a function of the interaction of the aerofoil with its own unsteady spanwise wake vorticity. The presence of the wake imparts aerodynamic damping on the aerofoil, reducing the amplitude of the effective angle of attack oscillations. In addition to this, acceleration forces are generated due to the unsteady flow (referred to as added mass forces), and these cause the aerofoil lift to deviate from the quasi-steady equivalent.

The problem with the 2D models generally used to estimate unsteady loading on tidal turbines is that they model the spanwise wake vorticity as infinite, and they do not include the presence of the streamwise wake vorticity. In some cases, the streamwise wake vorticity is assumed to be quasi-steady, but this is a potentially hazardous assumption which may result in the aerodynamic damping effect of the unsteady wake being severely over-predicted.

In this thesis, the behaviour of the streamwise wake vorticity in unsteady flow conditions is shown to be a primary driver of unsteady flow response. In order to show its effects on a variety of geometries, a parametric study is carried out for a range of aerofoil geometries, using a low-order 3D model capable of first-order predictions of unsteady aerofoil loading.

1.3 The effects of 3D unsteady gusts

The unsteady flow in the marine environment is strongly three-dimensional. Turbulent length scales range from a fraction of the turbine chord to several times the turbine diameter. It has been suggested that turbulent eddies of similar scales to the turbine diameter or smaller result in significant interaction with the turbine hydrodynamics, but no conclusive evidence has been given for this assertion. In experimental testing, uniform planar motion of the turbine is often used as a substitute for realistic turbulence (e.g. [91][137][88]), as this is easier to reproduce in a controlled manner. However, this simple flow situation provides limited insight into turbine response to realistic three-dimensional turbulence.

In academic research, modelling of turbine-turbulence interaction usually takes one of two approaches. The first is to model the turbine in a simplified way – using actuator disks [41], actuator lines [4], or blade-element momentum theory (BEMT) [100] – in a large resolved modelling domain. The second approach is to resolve the turbine geometry fully in a smaller computational domain. The former allows for the modelling of the ocean turbulence, accounting for the very large eddy length scales, and enabling the modelling of several turbines at once on an array-scale. The turbines themselves, however, are not sufficiently resolved to make good predictions about their loads or performance. The latter method allows for detailed modelling of the turbine and its interaction with the turbulent eddies, but the size of the domain is limited by the associated computational cost. This restriction in domain size makes the generation of realistic turbulence a challenge. Thus, resolving both realistic turbulence and a realistic turbine in a fully 3D viscous calculation is beyond the scope of current computational resource.

The aim of most studies on turbine-turbulence interaction is to link measurable properties of the turbulence to turbine response. Experimental studies have attempted to connect turbine performance to commonly measured statistical properties of turbulence, mainly correlating turbine power and loads to turbulence intensity and length scales [12]. While the streamwise turbulence intensity is generally found to correlate with increased unsteady loading, it has proved difficult to find a consistent trend in the contribution of turbulent length scales to turbine performance. In general, there is a lack of physical understanding in terms of the mechanisms of turbine-turbulence interaction, which hampers the study of turbines in turbulent conditions.

From a practical perspective, we are left with a few questions: What properties of the turbulence correlate with turbine performance? What level of measurement fidelity is necessary

to capture all the turbulent eddies in the flow that have the potential to cause damage? What types of turbulent eddies should we be looking out for at potential tidal sites? In short, what kind of turbulence do we need to worry about?

To answer these questions, and to gain further understanding into the impact of spatial three-dimensionality of turbulent gusts, the low-order model used in this thesis will be used to perform eigenmode decomposition on the unsteady response of 2D and 3D aerofoil geometries. Eigenmode decomposition allows for a generalised view of aerofoil-gust interaction: instead of simply measuring the aerofoil response to a wide range of gusts, and infer from that the effect of 3D gusts on the aerofoil response, eigenmode analysis tells us the *type of gusts to which a certain geometry is sensitive*. This means that a single calculation can be used to see how an aerofoil would respond to a wide range of different gusts. The concept of "mode resonance" will be introduced, which states that if a gust in the flow is similar to an eigenmode of the aerofoil, that gust will generate a larger load response compared to that of a gust that does not match an aerofoil eigenmode. This principle can then be used to determine what types of gusts in the flow are potentially hazardous, and also what the general effect of gust three-dimensionality is on the resulting aerofoil load response.

1.4 Research questions and thesis outline

In response to the issues outlined above, this thesis will answer the following research questions:

1. What is the effect of 3D aerofoil geometry on the unsteady load response?
2. What are the limits of applicability of classical 2D unsteady aerofoil theories to 3D geometries?
3. How does spatial three-dimensionality of the unsteady flow field affect the resulting unsteady load response of a tidal turbine?

Chapter 2 will provide an overview of the current state of research into tidal turbine technology, unsteady aerodynamics and 3D effects. Chapter 3 of this thesis contains the technical details of the methods used. Firstly, of the inviscid vortex lattice model built for this project, and secondly of the steady and unsteady RANS CFD simulations.

Chapters 4 and 5 will deal with the effects of 3D geometry on unsteady load response, and will answer research questions 1 and 2. Chapter 4 uses an inviscid vortex lattice model

to perform a parametric study of the unsteady load response of a range of 3D geometries. Chapter 5 looks at second-order effects such as wake distortion and viscous stall through URANS CFD simulations, and also validates the results of the inviscid vortex lattice model.

Chapters 6 and 7 will examine the effects of 3D gusts, and answer research question 3. In Chapter 6 the vortex lattice model will be used to perform eigenmode decomposition of 2D and 3D aerofoil geometries. The 2D cases will be used to demonstrate the properties of the eigenmodes, while the 3D cases will be used to find the effect of spatially-varying gusts on aerofoil response. In Chapter 7 the practical implications of the findings in Chapter 6 will be illustrated, by using examples of representative site data and evaluate how the 3D nature of the flow is likely to impact turbine fatigue life. Finally, Chapter 8 will summarise the conclusions and give suggestions for future work.

Chapter 2

Context and Background

2.1 Introduction

The topic of this thesis is the unsteady hydrodynamic load response of horizontal-axis tidal turbines, and to what extent three-dimensional effects influence the load prediction. This chapter explores the academic and industrial context to the work.

2.2 Tidal power

The concept of harnessing the kinetic energy of tidal currents has been used in various forms for centuries [10], and received renewed attention as a consequence of the 1970s oil price crisis. The high power density of water coupled with the predictability of the tidal resource means that the technology is frequently cited as a competitive option for renewable energy development. The last two decades have seen significant growth in investment and commercial development of tidal devices, with a variety of design concepts being proposed. The two most common tidal turbine designs are horizontal-axis tidal turbines (HATTs) and vertical-axis tidal turbines (VATTs), both of which have near-equivalents in the wind industry. A number of less common designs have been proposed and developed, such as the "flapping-foil" tidal device by EEL Energy[1], and the "Archimedes screw" design developed by Jupiter Hydro[2]. Out of the available designs, HATTs are generally favoured, and are the most common for use in large-scale pre-commercial projects. Their design is based on the mature technology behind horizontal-axis wind turbines, and many of the design practices used for wind turbine development have been used to develop commercial-scale HATTs. This thesis will deal

[1] https://www.eel-energy.fr/
[2] https://jupiterhydro.com/

exclusively with HATTs, which will be referred to simply as "tidal turbines" from now on.

The UK is uniquely placed to benefit from the development of tidal power, as it has one of the largest estimated tidal resources in the world. Conservative estimates state that 10% of the UK's peak electricity demand could be supplied from tidal energy [11]. As outlined in Chapter 1, a number of ambitious projects have recently proved the capability of tidal power as a valued addition to the renewable energy mix. While the tidal industry in the UK has suffered setbacks in recent years, with the withdrawal of companies and reduction in government funding, there is a mature knowledge base still available in the UK, both in industry and academia. Several commercial developments and an increasing number of grid-connected turbine arrays prove that tidal power is a growing industry with huge potential as a reliable renewable energy resource.

2.3 Environmental conditions

The effect of the operating environment on the turbines' performance and lifetime is one of the primary challenges facing the tidal industry. While the turbulence intensity has generally been measured to be lower on tidal turbine sites compared to typical wind turbine conditions, tidal turbines experience larger loads even from small velocity changes compared to wind turbines. This is due to the relationships: Power = Thrust$\times$Velocity, and Power = Torque$\times$Angular velocity [139]. Because the flow velocity and turbine rotational speeds are lower for tidal turbines than for wind turbines, the steady-state torque and thrust are much higher for a given power output. This means that the unsteady forces generated by the same percentage change in velocity are much larger for a tidal turbine than for a wind turbine. Furthermore, the increased density of water over air means that the turbine rotor itself also has significantly lower inertia compared to the fluid around it, compared to a wind turbine in air, meaning that it reacts much faster to velocity fluctuations. These two factors (high steady-state loads and low rotor inertia) mean that unsteady loading is a significant problem.

The single-point longitudinal turbulence intensity is one of the most common predictors of the blade loads for wind and tidal turbines. The turbulence intensity is given by the standard deviation of the turbulent fluctuations divided by the mean velocity [94]:

$$\frac{u'_{rms}}{U_\infty} \tag{2.1}$$

The averaging period for the turbulent fluctuations is typically 10 minutes, during which the mean velocity is considered to be constant. Measured turbulence intensities at tidal sites tend to fall in the range 10-20% [91]. The two length scale parameters commonly used to characterise the turbulence at potential sites are the mixing length scale and the integral length scale. The mixing length scale is determined by the mean shear gradient in the flow, while the integral length scale is defined as the spatial integral of the autocorrelation function of velocity [125].

A report from the 'Turbulence in Marine Environments' (TiME) project illustrates the challenge of unsteady flow to the tidal industry [24]. The report suggests that there is currently a "chasm" between measurements of turbulent marine conditions and robust engineering predictions of device performance. The intention of the report is to provide a framework for the classification of marine turbulence, as a first step in evaluating the impact of turbulence on tidal turbines. The paper outlines the following main sources of marine turbulence:

- Inflow turbulence – the turbulent boundary layer generated by the proximity to the sea bed, characterised as high Reynolds number boundary layer flow.
- Bed roughness – Bathymetry features generating coherent turbulent eddies with length scales linked to the upstream seabed profile.
- Channel shape – related to bed roughness, the shape of the tidal channel may generate coherent structures. This category includes features like bays and headlands.
- Stratification – Vertical temperature or density gradients introduce buoyancy effects that may affect stability.
- Wind shear – surface effects can generate velocity shear profiles and consequently generate turbulence.

To these categories, the effects of surface waves can be added. The report also categorised turbulent eddies by length scale; small (less than the turbine blade chord), mid-scale (up to the turbine diameter), and large (larger than the turbine). Large eddies generally exert uniform effects on the whole turbine, but may cause intermittency and fluctuation on an array or wake scale. The final characterisation is that of the time-dependent nature of the turbulence; periodic, aperiodic or steady-state. The project showed that blade loading is affected by all combinations of turbulent length- and time-scales from all sources listed above.

The TiME report illustrates that tidal turbines are affected by turbulence of a wide range of length scales, ranging from a fraction of the blade chord to several times the turbine

diameter. It is therefore vital that the industry has the capability to model the interaction of a turbine with turbulence over these scales.

2.3.1 Turbine-turbulence interaction

Despite its importance, the interaction of a turbine with the whole range of turbulent length scales found in the approach flow is relatively unexplored area of research [18] [21]. An analytical study by Durbin and Hunt [33] suggests that the interaction of turbulent eddies with a bluff body object varies significantly depending on the length scale ratio between the turbulent eddy and the object. If the eddies are of the same order of magnitude or smaller than the bluff body, quasi-steady predictions are unrealistic. However, recent studies on the effects of turbulent length scales on steady and unsteady turbine performance have shown inconclusive or conflicting results about the role of length scales ([2] [17] [19] [12]). Blackmore et al [12] used grid-generated turbulence to study the effect of different intensities and length scales, and found that increasing the turbulent length scale increased both the mean power and thrust coefficients of their model turbine. Their results seemed to indicate that the turbulent length scales had a much higher impact on the mean turbine performance than the turbulence intensity, which is in opposition to previous findings. Blackmore et al also found that increasing the integral length scale of the turbulence led to a substantial increase in fluctuating loads. They concluded that the ratio between the turbulent length scales and the turbine diameter may be an important parameter for turbine performance.

Complex flow interaction from upstream topology is also an important topic for wind turbines, where it has been shown to have significant effects on the power output. Howard et al [62] performed experiments on model wind turbines in complex flows. Upstream interference was generated by placing the model turbine first in the wake from a sinusoidal hill, then in the wake of another turbine. The hill had a stronger impact on the spectral response than the turbine wake did: the incoming wake, while reducing the mean voltage, also reduced the impact of large-scale turbulent structures on the downstream turbine. It was suggested that the upstream turbine was breaking apart eddies larger than the turbine diameter, thus reducing large-scale turbulence. The hill, on the other hand, generated more large scale turbulence interaction. In both cases the dominant effect on rotor kinematics was found to be from large scale flow structures in the incoming turbulent boundary layer.

The findings of Howard et al are similar to those of Chamorro et al [19], who performed tank tests to investigate the response of a tidal turbine to large scale coherent turbulence. The power spectrum was found to be strongly correlated to the coherent turbulence. The vorticity

shed by a cylinder upstream was found to interact with and break up the tip vortices in the near-field, accelerating the mixing out of the turbine wake. Spectral characteristics of the downstream flow showed that large scale turbulence had a damping effect on the turbine wake and tip vortices. This effect was most pronounced with relatively small cylinders, generating vortices smaller than the turbine diameter. When using larger cylinders, producing vortices larger than the turbine diameter, Chamorro et al observed that the reduction of the tip vorticity was diminished. Interestingly, they further found that turbulence intensity was not a good measure of interaction between freestream vorticity and the turbine wake; cylinders placed further upstream generated lower turbulence intensity but completely damped out the tip vortices, while a closer cylinder generated a higher turbulence intensity but did not fully damp out the tip vortices. This finding, and the studies cited above, suggests that the length scale of the turbulence may have a key role in determining steady and unsteady turbine performance.

The studies cited above show the complex nature of turbulent flow and its interaction with turbines and their wakes. From an engineering perspective, it is desirable to identify measurable parameters that determine the effect of turbulence on the turbine. However, as the previous work shows, neither turbulence intensity nor turbulent length scales can be used at the moment to determine turbulent interaction effects with certainty. Further understanding of the flow-physical mechanisms underlying turbine-turbulence interaction is needed in order to quantify turbulent effects on tidal turbine performance.

2.3.2 Site conditions

While site data is often sparse, some general comments can be made about the turbulent flow at a typical tidal site. It is usual to observe turbulent flow features on a scale comparable with the turbine diameter, and studies of flows around islands with significant recirculation zones have shown features that are likely to cause high turbulence intensities over a wide range of turbulent length scales [39]. Tidal power sites tend to be close to islands and headlands, where such recirculation will be prevalent (as opposed to estuaries, where the flow is close to parallel and has very low turbulence intensity).

Secondary flows – generally occurring in tidal channels as a pair of counter-rotating streamwise vortices – are also a key source of large-scale unsteady flow structures. Site data analysis has shown that the width of secondary flow cells is of the order of magnitude of the channel depth [69]. Secondary circulation of tidal flows around headlands has been shown to be stronger than that predicted by the standard logarithmic streamwise velocity profiles, and

the strength of the secondary flow can vary from 5 to 15% of the streamwise flow ([91], [106]).

When analysed statistically, typical turbulence intensities for tidal turbine sites have been shown to be of the order of 10-20%, with dominant time scales of 6-10 seconds [91]. In tidal flow measurements it is also found that the length and time scales prevalent indicate the dominance of large anisotropic eddies in the turbulent kinetic energy spectra, which may in some cases be caused by proximity to headlands [128]. These large eddies are predominantly horizontal motions at scales greater than the water depth, and they dominate the turbulent spectra.

The wave environment at prospective tidal sites is highly variable, but measured conditions at the site of the European Marine Energy Centre (EMEC) can be regarded as a sample of expected conditions. A limited study of the wave conditions was performed by McCann et al [85] and significant wave heights in the range of 0.25 - 3.25 m were found, with the majority of the waves occurring in the 0.25 - 1.25 m range. Extreme wave conditions at the site, expected on a 10-year basis, were cited as 9.9 m waves. In this case, and generally for offshore wave conditions, the data is reported in terms of significant wave heights, which is defined as the mean amplitude (trough-to-crest) of the highest third of the recorded waves. Measurements suggest that regular waves at typical tidal sites can permeate to approximately 15 m below the surface [99].

The estimation of realistic tidal site wave effects is however limited by the complexity of wave-current interaction, which among other effects can cause very steep waves to occur if the waves move in the opposite direction to the tide [72]. The effects of waves on tidal turbines is generally calculated using linear wave theory in design software (for example, in Tidal Bladed [13]), which uses measured significant wave heights and wave periodicity to estimate the induced velocity at various depths. In the presence of steep waves and extreme conditions, linear theory has been shown to underestimate the dynamic behaviour of the blade root bending moments [6]. In addition to this, waves are frequently assumed to travel in-line with the tidal current for the purpose of modelling (for example, by McCann et al [85]). However, measurements of prospective sites indicate that significant misalignment occurs [79], and this will influence the wave interaction with the current and the tidal turbines.

The flow regimes at potential tidal turbine sites are not only highly variable, but the origin of the variability is also difficult to ascertain in many cases [52]. This makes it difficult to make accurate predictions about the conditions at a given tidal turbine site. The consensus is, however, that ocean turbulence and the wave environment has a significant effect on the

performance and lifetime of turbines. It is therefore vital to build new understanding about which flow features will be most damaging to turbines, and therefore should be measured at a site. For this purpose a low-order method is developed and used in Chapter 6 of this thesis, to improve the understanding of how turbulent length scales affect the loads experienced by tidal turbines.

2.4 Turbine modelling: Blade Element Momentum Theory (BEMT)

The design and analysis of tidal turbines is based on methods used by the wind industry. This is an intuitive and mostly appropriate choice, given the similarities in function and shape of the devices. Models based on Blade Element Momentum Theory (BEMT) are the most commonly used tools to evaluate the performance of both wind and tidal turbines [59]. One of the most widely used commercial BEMT codes for tidal turbine design is Tidal Bladed [13], derived from the software Bladed which was developed for wind turbines.

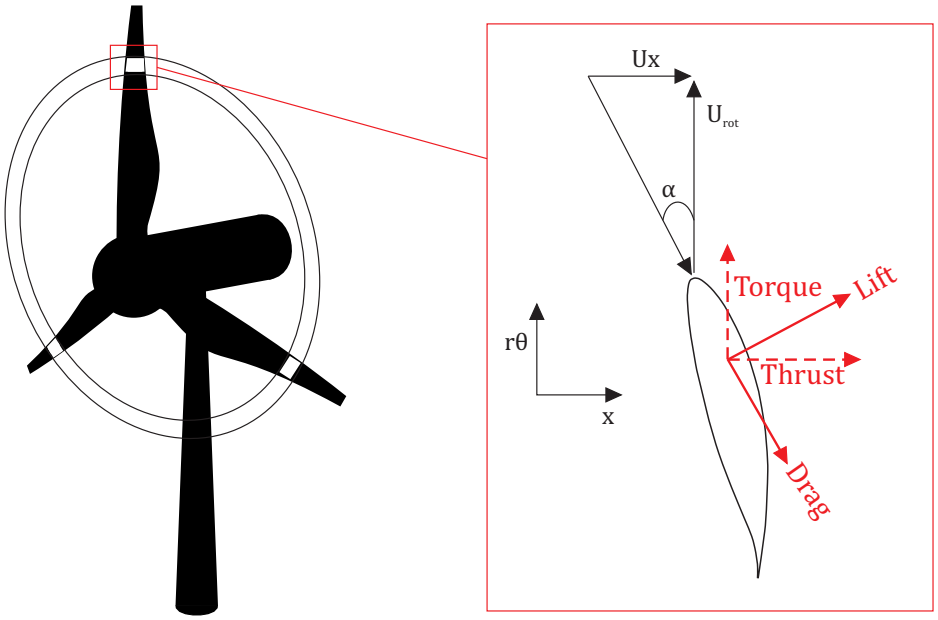

Fig. 2.1 Illustration of the blade discretisation process of Blade Element Momentum Theory (BEMT).

In BEMT, the aerodynamic performance of a turbine blade is found by discretising the blade into annular 2D sections (see Figure 2.1). The lift and drag properties of each section are taken from tabulated 2D aerofoil data. The performance of the turbine is then found by

integrating the resulting aerodynamic loads along the blade span, and an iterative process is used to find the optimum distribution of twist and chord along the blade span. 3D effects are accounted for through the use of various correction factors, such as Prandtl's tip-loss correction [45]. The details of BEMT modelling can be found in textbooks, such as [15].

In BEMT, each annular 2D element is assumed to be impenetrable. Within each independent annulus section, a streamwise momentum balance is applied taking three quantities into account; firstly the mass and momentum of the incoming flow approaching the blade element. Secondly, the mass and momentum of the wake flow created at the trailing edge of the aerofoil. Thirdly, the aerodynamic force on the blade element. The influences of all three are jointly computed to include interaction effects. For the case of high loading, where there will be an increased amount of radial flow (violating the impenetrability assumption), empirically derived correction factors are applied. The assumptions of this method are not valid at high thrust, since large thrust forces will create both separation and large recirculating vortices [59], neither of which are accounted for in BEMT. Notably, the thrust experienced by a wind turbine – for which BEM is widely used and validated – is less than a quarter of that experienced by a tidal turbine for the same power output [139].

2.4.1 Limitations of BEMT modelling for tidal turbines

BEMT is only strictly applicable if the turbine blades have uniform circulation, since non-uniform circulation implies radial flow, leading to exchange of momentum between adjacent annular sections. The error induced by relaxing this constraint is, however, small for most realistic turbine designs [15]. Prandtl's tip-loss correction, which is commonly used to account for the effects of having a finite blade, is also limited by the assumption of constant spanwise circulation [124]: the physical basis of the correction is obtained by describing the rotor as a vortex line with constant circulation along the blade, which then detaches at the blade tip and moves downstream, forming the tip vortex. The influence of the tip vortex is introduced in the effective velocity of an annular blade element as an "interference factor" [45]. While these limitations of BEMT are known, the method is considered accurate enough for preliminary design calculations.

There are, however, a number of studies that suggest BEMT modelling is less than reliable even for steady performance predictions. Tangler [124] writes that several studies have shown that BEMT regularly over-predicts peak turbine power compared to experimental tests, and in other ways often give unreliable predictions. Tangler states that a major source of error is the assumption of no interaction between 2D annulus segments, when in reality

the geometry and therefore the resulting flow field are both highly 3D. Furthermore, the incoming flow to a tidal turbine is non-uniform due to the presence of the shear layer, and this further invalidates the assumption of 2D annular flow. The presence of a shear layer is of greater consequence for tidal turbines than for wind turbines, as tidal turbines are smaller relative to the thickness of the ocean floor shear layer, and often operate fully immersed in the boundary layer.

Tangler [124] compared a wind turbine performance prediction from a 2D BEMT solver to that made by a 3D lifting surface method, and the latter was found to perform better compared to experiments at higher wind speeds. The performance of the outboard region of the turbine was, however, predicted accurately by the BEMT method. This is often cited as a reason for the suitability of BEMT modelling: the majority of the power produced by a turbine is generated in the outboard blade region. However, care is needed when assuming this to be directly applicable to tidal turbines. A tidal turbine will have a diameter of less than a third of a wind turbine with the same rated power [139]. As such, tidal turbines tend to have lower aspect ratios and to be more strongly tapered than wind turbines. This makes the assumption of locally 2D flow less likely to apply, even on the outboard blade sections.

An additional consequence of the 2D impenetrable elements used by BEMT is that corrections are needed to account for rotational flow effects. It has been established in wind turbine applications that the inboard blade pressure distributions differ considerably from the 2D predictions, leading to very high maximum loads on these sections [134]. Rotational effects seem to be the primary contributor to this situation: in the rotating flow environment, Coriolis forces will act on the boundary layer to delay stall by alleviating adverse pressure gradients.

Models proposed to deal with three-dimensional rotational effects have been applied with varying degrees of success, notably the studies of steady three-dimensional flow by Du and Selig [31] [32]. They based their analysis on laminar boundary layers developing while influenced by rotational effects. They found that flow separation is suppressed to a small extent by rotational effects. A study by Wang and Coton [134] used a lifting line model in order to evaluate three dimensional rotational effects, which were included through a series of correction factors. Their results indicated that the 3D corrections did improve the prediction of wind turbine blade load, but the improvements were mainly confined to the inboard blade sections. At 30% span, the level of improvement was in the order of 50%, with the loading pattern well represented. This rapidly changed when moving radially

outwards; at 47% span the improvement was around 25%. Further out little change was noted.

Despite the misgivings described above, BEMT remains a trusted tool for industrial applications, and forms the basis for tidal turbine design practices. Typically, a BEMT solver will be the only tool used in industry to predict both steady performance and unsteady loading on a new turbine design. Coupled RANS or LES and lower-order models (such as BEMT, actuator discs or actuator lines) have also been used for research purposes (e.g. [34] [29] [101]), for the purpose of creating a fully resolved realistic turbulence field interacting with low-order models of the turbine. In the end, all these low-order models rely on the assumption of locally 2D flow in order to evaluate the hydrodynamic blade loading, in both steady and unsteady flow conditions. In this thesis, a low-order, 3D inviscid solver will be used to understand the effects of both 3D geometry and flow features on the unsteady loading of a tidal turbine.

2.5 Unsteady fluid dynamics

As stated above, tidal turbines operate in turbulent flow environments, with strongly varying inlet flow conditions. A number of studies have highlighted the need to account for turbulent flow interaction when evaluating the lifetime performance of tidal turbines. Following below is an overview of the models used to estimate turbine response to unsteady flow.

2.5.1 Pre-stall conditions

Quasi-steady methods of load and performance evaluation are often used to model turbine interaction with turbulent gusts, but this is usually insufficient to predict the turbine behaviour accurately [36]. As an example, Figure 2.2 illustrates the unsteady aerodynamic effects of sinusoidal gust forcing on 2D aerofoil load response in pre-stall conditions, as represented by a $C_l - \alpha$ characteristic. The quasi-steady response is shown in black – under these conditions the aerofoil lift will simply move up and down the steady-state $C_l - \alpha$ characteristic. If the aerofoil responds unsteadily to an incoming gust, however, the lift response will follow the red line instead – with a different amplitude from the quasi-steady result and a phase lag (which causes the hysteresis loop shown on the right-hand plot).

In order to capture this unsteady response, two effects must be accounted for: the added mass and the unsteady wake [75]. The added mass is defined in this thesis as the acceleration of the potential field around the aerofoil, due to the transient flow movement, which imparts a resultant force on the aerofoil proportional to the time rate-of-change of the aerofoil circu-

lation. If the unsteady flow occurs with high frequency, this added mass force may become very large. The second effect, the unsteady wake, is generated to satisfy Kelvin's theorem of constant circulation in the flow. The unsteady gust causes a time-varying flow incidence angle on the aerofoil, meaning that the aerofoil circulation changes as a response to the gust. According to Kelvin's theorem, this means vorticity of equal and opposite strength to the changing aerofoil circulation must be shed from the trailing edge. This vortical wake induces a downwash velocity on the aerofoil, imparting unsteady aerodynamic damping on the aerofoil lift.

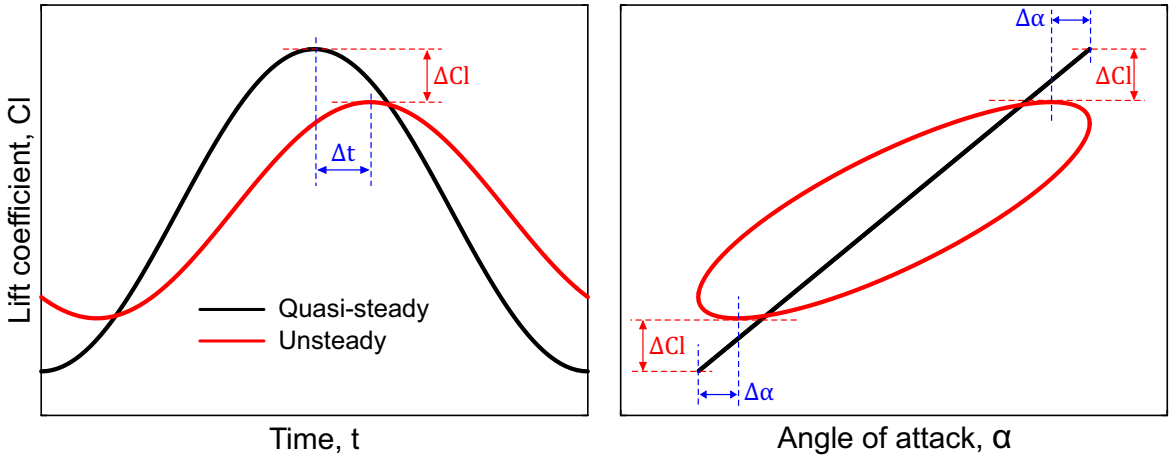

Fig. 2.2 Unsteady load response of a 2D aerofoil. The amplitude reduction and the phase lag in the time-varying lift gives rise to the hysteresis effect on the Cl-alpha curve.

The aerodynamic damping induced by the wake downwash causes a reduction in load amplitude, and also a phase shift in the location of the peak aerofoil load response. This causes a hysteresis curve to form in the $C_l - \alpha$ characteristic. The added mass force also induces hysteresis to the lift curve, as it is proportional to the rate of change of circulation, and as such has its peak magnitude 90^o out of phase with the gust. The wake downwash and the added mass therefore work in opposition to each other, in terms of both force and phase: if the direction of the hysteresis curve is anticlockwise, the wake downwash is dominating over the added mass effect. If on the other hand the hysteresis curve is in the clockwise direction, the load response of the aerofoil leads the forcing gust, which is generally indicative of dominant added mass response.

Two different methods are commonly used in conjunction with BEMT to evaluate the transient flow response of a tidal turbine: dynamic inflow models, and classical unsteady aerofoil theory. Both of these methods are 2D, and dynamic inflow is the more commonly

used. Dynamic inflow accounts for time-varying boundary conditions in the momentum balance equation normally used to determine steady performance. In its most basic form, dynamic inflow is usually limited to determining the added mass forces, while neglecting circulatory and wake effects [74]. The added mass force is accounted for by estimating the time-varying pressure gradient, based on the calculated steady pressure field. This method is axisymmetric, and effectively uses an actuator disc model of the turbine. More advanced dynamic inflow models that include circulatory forces and wake effects have been developed for helicopter rotor applications [103], and have been adapted for use in wind turbines [123]. However, even the more advanced dynamic inflow models neglects 3D wake effects that involve interaction between the 2D annular elements.

Dynamic inflow methods often improve predictions of net power, but do not contribute much to the prediction of unsteady blade loads [74]. Studies by Whelan [137] and McNae [88] both show dynamic inflow modelling to predict the right trends, but the wrong magnitudes for the unsteady load response. When analysed at a 2D blade sectional level, dynamic inflow modelling has been shown to be equivalent to classical unsteady aerofoil theory [40] [103] [104], which will now be discussed.

Classical unsteady aerofoil theory assumes that the flow can be approximated as inviscid flow over a 2D flat plate at zero mean angle of attack. The wake is assumed to leave the trailing edge along the horizontal axis, with the steady freestream velocity, and gust amplitudes are assumed to be small. These simplifications allow for the analytical derivation of unsteady transfer functions. These unsteady transfer functions give the load response to a given incident flow variation as a function of the quasi-steady 2D lift coefficient. As such, they are readily applicable to BEMT methods, and to other 2D strip-theory approaches.

Any given unsteady transfer function will only be applicable to the specific gust event for which it was derived. The appropriate choice of transfer function for a given application is an important one for designers: the difference in loading given by two different transfer functions can generate an order of magnitude difference in the estimation of tidal turbine fatigue life [115]. The problem of finding the aerodynamic loads on an oscillating aerofoil was first addressed by Glauert [44] in 1929, but was later solved by Theodorsen [126] in 1935, whose solution (the Theodorsen function) formed the basis of much of the unsteady aerodynamic theory developed later. A selection of unsteady transfer functions is shown in Table 2.1, with descriptions of the types of gusts to which they can be applied.

Table 2.1 A selection of common unsteady transfer functions, with descriptions of the gusts to which they are applicable.

Unsteady transfer function	Applicable unsteady forcing
Theodorsen, $C(k)$ [126]	Harmonic transverse gusts acting uniformly along the aerofoil chord, as well as harmonic pitching and heaving.
Loewy, $C'(k)$ [81]	Equivalent to the Theodorsen function, with correction to account for "returning wake" effects.
Sears, $S(k)$ [131]	Harmonic transverse gusts varying sinusoidally across the aerofoil chord.
Wagner, $\Psi(s)$ [133]	Step-change in aerofoil pitch.
Kussner, $\Phi(s)$ [70]	Sharp-edged gust.

Another method that has been used to evaluate unsteady turbine loads is the Morison equation (in [36] and [136]), which is commonly used to calculate the oscillatory loads on oil platforms and other offshore structures. The effect of the turbine is approximated as that of a porous disc, and the associated thrust coefficient is used in the Morison equation to find the oscillating thrust on the structure, along with an inertial (added mass) force. The thrust and inertial coefficients are found through experimental testing. Whelan et al [136] found that the Morison equation predicted the unsteady thrust of a model turbine geometry only if a corrected version derived by Verley and Moe [130] was used, where the mean and oscillatory thrust coefficients were obtained and used separately. This third method is not in common usage in industry or academia for tidal turbine load estimates.

In this thesis, the unsteady load response as given by 2D classical aerofoil theory is used as representative for industry-standard load calculations using strip-theory methods. Unsteady transfer functions will be used as the 2D comparison to the 3D modelling that will be carried out in later chapters. The unsteady gusts investigated will be harmonic throughout, since harmonic gust forcing is often assumed when investigating turbine loads induced by waves or turbulence [115]. The relevant unsteady transfer functions for harmonic gusts will be outlined in the following section.

2.5.2 Unsteady transfer functions

For harmonic gusts, the degree to which an aerofoil exhibits unsteady load response is determined by the reduced frequency. This is given by:

$$k = \frac{\omega c}{U} \tag{2.2}$$

Here ω is either the angular oscillation frequency of the aerofoil, or the angular frequency of the forcing gust. U is the mean incident flow velocity, and c is the aerofoil chord. Historically the reduced frequency has been defined using the aerofoil semi-chord, $b = c/2$. However, recently the use of the full chord length for reference has become more common [115], and this convention will be used throughout this thesis. The reduced frequency is a measure of the gust wavelength relative to the aerofoil chord, and has repeatedly been found to be the dominant parameter determining the properties of unsteady flow in 2D [74].

The Theodorsen function is arguably the most commonly used unsteady transfer function. The expression for the unsteady lift obtained from the Theodorsen function, for an aerofoil of chord $c = 2b$ undergoing a combination of pitching and heaving motion, is given by [75]:

$$Cl = \pi b \left[\frac{\ddot{h}}{V^2} + \frac{\dot{\alpha}}{V} - \frac{ba\ddot{\alpha}}{V^2} \right] + 2\pi \left[\frac{\dot{h}}{V} + \alpha + \frac{b\dot{\alpha}}{V} \left(\frac{1}{2} - a \right) \right] C(k/2) \tag{2.3}$$

The parameter a represents the pitch axis location relative to the mid-chord of the aerofoil, and is measured in terms of semi-chords. The pitch angle is given by α and the heave height by h, with dots over the parameters representing the first and second time derivatives. The function $C(k/2)$ is the Theodorsen function, which takes the reduced frequency as an input parameter. The Theodorsen function is expressed in terms of Hankel functions (H):

$$C(k) = \frac{H_1^{(2)}(k)}{H_1^{(2)}(k) + iH_0^{(2)}(k)} \tag{2.4}$$

The Hankel functions are, in turn, defined as:

$$H_v^{(2)}(k) = J_v(k) + iY_v(k) \tag{2.5}$$

Here $J_v(k)$ and $Y_v(k)$ are Bessel functions of the first and second kind, respectively, and the subscript v is an index indicating the order of the Bessel function.

The first term in Equation 2.3 arises from the added mass forces. The second term represents the so-called "circulatory" component of the unsteady load response, as it arises from the creation of circulation around the aerofoil. If, instead of aerofoil movement, the unsteady forcing arises from a harmonic unsteady gust acting uniformly across the aerofoil chord (see Figure 2.3a), Equation 2.3 simplifies to:

$$Cl = [2\pi C(k/2) + i\pi k/2]tan^{-1}(\hat{\alpha})e^{i\omega t} \tag{2.6}$$

The harmonic gust forcing is given by the amplitude of the oscillating incidence angle $\hat{\alpha}$ times the harmonic function $e^{i\omega t}$. The Theodorsen function $C(k)$ is equal to one at $k = 0$, giving the classical response for the lift of a flat plate at quasi-steady conditions ($Cl = 2\pi\alpha$). As such, the expression in brackets in Equation 2.6 can be seen as a transfer function between the steady and unsteady response.

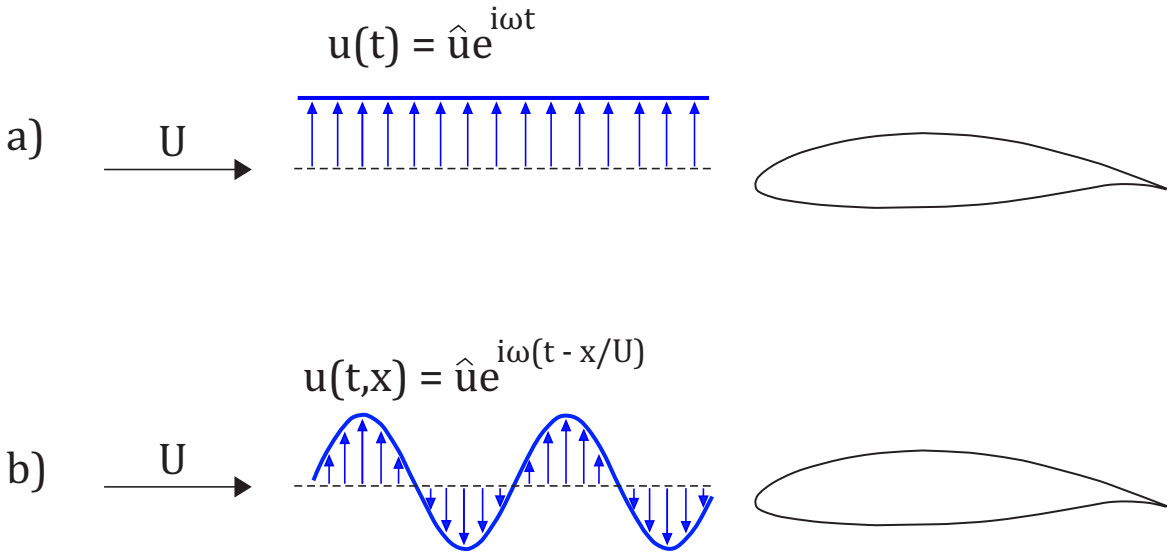

Fig. 2.3 (a) Uniform and (b) sinusoidal gusts arriving at 2D aerofoils.

In the case of a harmonic sinusoidal gust interaction with a 2D aerofoil (see Figure 2.3b) the Sears function developed by von Karman and Sears [131] must be used to evaluate the lift. The lift coefficient is given as [75]:

$$Cl = 2\pi S(k/2)tan^{-1}(\hat{\alpha})e^{i\omega t} \tag{2.7}$$

The transfer function $S(k/2)$ between the steady and unsteady response is the Sears function, which is expressed in terms of Bessel functions as:

$$S(k) = [J_0(k) - iJ_1(k)]C(k) + iJ_1(k) \tag{2.8}$$

Here $C(k)$ is the Theodorsen function as given by Equation 2.4. The Sears function was originally derived with the gust referenced to the mid-span of the aerofoil. In order to obtain the correct lift response for a gust referenced to the leading edge of the aerofoil, as is now common, a transform must be applied to the original Sears function. This transform gives the new function $S'(k)$, in terms of its real and imaginary components, as:

$$Re[S'] = Re[Scos(k)] + Im[Ssin(k)] \tag{2.9a}$$

$$Im[S'] = -Re[Ssin(k)] + Im[Scos(k)] \tag{2.9b}$$

Both the Sears and Theodorsen functions are designed to model an aerofoil which is moving linearly through a flow. When calculating the unsteady aerodynamic loads on rotors, an additional factor must be accounted for: the "returning wake". A returning wake is illustrated in Figure 2.4, for a single flat plate rotating at a tip-speed ratio (TSR) of 10. As the blade rotates, it passes close to the unsteady wake shed previously, and this alters the unsteady load response. Loewy [81] therefore developed a correction to the Theodorsen function to account for the returning wake effects. The resulting Loewy function is expressed as [75]:

$$C'(k) = \frac{H_1^{(2)}(k) + 2J_1(k)W}{H_1^{(2)}(k) + iH_0^{(2)}(k) + 2(J_1(k) + iJ_0(k))W} \tag{2.10}$$

where W is a function of various parameters concerning the returning wake, and is given by:

$$W\left(\frac{kh}{b}, \frac{\omega}{\Omega}\right) = \left(e^{\frac{kh}{b}} e^{i2\pi(\frac{\omega}{\Omega})} - 1\right)^{-1} \tag{2.11}$$

The parameter h denotes the spatial separation distance between the returning wake sheets, while Ω denotes the rotational speed of the rotor blade. If the ratio ω/Ω is an integer, the effect of each returning wake sheet act "in-phase" with each other. Note also that as h goes to infinity, W goes to zero, reducing Equation 2.10 to the standard Theodorsen function. There is no equivalent transform for correcting the Sears function for sinusoidal gusts interacting with rotor blades. In the case of a tidal turbine, the rotational speed is high relative to the

flow speed, and so the wake will convect away from the rotor relatively slowly. This means that returning wake effects are likely to be significant [115].

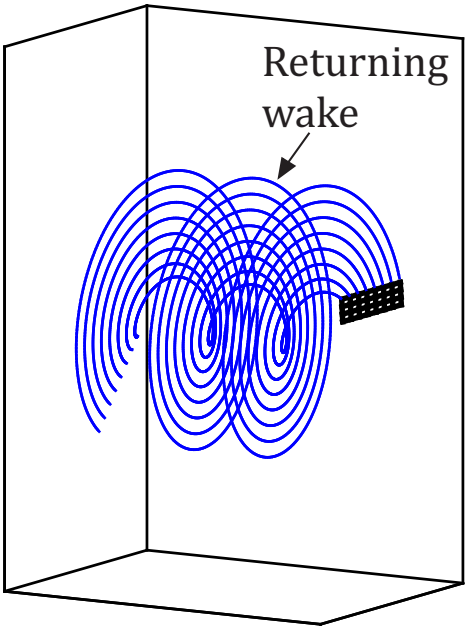

Fig. 2.4 Illustration of the returning wake from a rotating flat plate.

2.5.3 Validation of classical unsteady aerofoil theory

Historically there has been inherent difficulty in doing experimental work on oscillatory wings, and so there has been little data available to verify the results found by the unsteady transfer functions described above. Accounting for wind tunnel interference is difficult, and errors of 10% can be considered small in this context [1]. Leishman [75] includes a series of experimental validation cases of the Theodorsen function from a number of different studies in his overview of 2D unsteady transfer functions as used in helicopter aerodynamics. A series of experimental tests exploring the limits of applicability of the Kussner function for sharp-edged gusts (see Table 2.1) has recently been performed by Corkery et al [26], and the 2D transfer function predicts the transient inertial load response remarkably well. Further experimental work on verifying the applicability of classical aerofoil theory to engineering flow situations has been carried out by [120], [25] and [135], among others.

For the purpose of establishing the applicability of classical aerodynamic theory to tidal turbines, Sequeira and Miller [115] performed a parametric study of a representative 2D aerofoil section undergoing unsteady gust forcing, using unsteady Reynolds-Averaged

Navier-Stokes (URANS) simulations. The returning wake effects were found to be of vital importance for accurate load predictions. The turbulence in the ocean environment was also deemed to be represented best by sinusoidal gust interaction; as the turbine blade rotates through spatially varying turbulence, the blade will see an incidence change that can be approximated as sinusoidal, with different harmonics. This means that the Sears function is the appropriate choice of unsteady transfer function to determine the effects of turbulence. However, Sequeira and Miller found that the Sears function overestimated the lift response of the 2D blade section. It was speculated that this was due to distortion of the gust by the presence of the aerofoil, but the lack of correction in the Sears function for returning wake effects is the more likely culprit, as will be seen in Chapter 4 of this thesis (see Section 4.2.3).

When considering experiment design, it is of interest to know whether the effect of gust interaction can be replicated by heaving or pitching motion of the aerofoil. This because it is easier experimentally to produce precise aerofoil movement than it is to produce an unsteady gust. Leung et al [77] carried out a series of tests on 2D aerofoil sections to find out whether gust interactions could be modelled using a combination of pitching and plunging motions. This aerofoil motion was found to be able to predict gust response to within 10% accuracy if the reduced frequency was less than 0.5. At higher frequencies the deviations were generally over 10%. The two primary causes of this discrepancy were found to be the nonlinear chordwise distribution of gust-induced flow, and also the wake deformation which occurs in the case of a moving aerofoil.

Another important consideration for the purpose of load prediction and experimental testing is the linearity of unsteady flow effects, since the unsteady transfer functions of classical aerofoil theory are based on the assumption of linearity. An experimental study by Milne et al [90] explored multi-frequency oscillatory forcing of a model tidal turbine, by axially oscillating the turbine at single and dual frequencies. Comparing the dual frequency loading with the superposition of two single-frequency cases, they found that the response was approximately linear. They further found that the presence of small separations on the blades increased nonlinearity, but in these cases linear theory provided conservative estimates. However, Milne et al tested oscillatory forcing only in a low frequency range (k =0.04-0.1, based on Equation 2.2), meaning that the lowest forcing frequency used was close to quasi-steady – conclusions of linearity for unsteady loading cannot be made in such a case. The relatively stringent high-frequency filtering used in post-processing may also have removed high-frequency second-order effects. Looking instead at the lift response of wings in grid-generated turbulence, spectral decomposition of the velocity is often used in combination

with the Sears function to calculate the unsteady loads, assuming linearity [82][107]. This method is used when calculating the gust-induced loading on slender bridges [84]. Looking at the applicability of the Sears function to thick aerofoils in turbulent flow, Lysak et al [82] found good agreement with water tunnel experiments if the function was modified to account for thickness, maintaining linearity. Sankaran and Jancauskas [107] examined the use of the Sears function in a similar manner when calculating the turbulence-induced loading on rectangular sections of varying thickness (representing bridge sections), in a reduced frequency range of $k = 0.04 - 0.6$ (based on Equation 2.2). The study found excellent agreement with the Sears function at reduced frequencies higher than 0.2. At lower frequencies the section thickness caused significant deviations, due to separation effects, while thin sections showed good agreement. The studies cited above offer tentative confirmation that unsteady flow effects generally exhibit linearity, making classical aerofoil theory applicable to multi-frequency forcing.

A frequently cited limitation of classical aerofoil theories is the approximation of a zero thickness aerofoil at zero mean incidence, for which the transfer functions were derived. The consequence of this limitation is that upstream deformation of the gust by the presence of the aerofoil is neglected, as the two are assumed to be uncoupled. Goldstein and Atassi [46] [5] developed the unsteady aerofoil theory further, extending it to a second-order model that accounted for the coupled nature of the aerofoil and the gust. This allows for the inclusion of camber and nonzero mean angle of attack on an aerofoil interacting with a sinusoidal gust. The ability of the Atassi function and the Sears function to predict the response of an aerofoil undergoing sinusoidal gust forcing was recently investigated by two separate experimental studies [25] [135]. The Atassi function was initially found to be substantially more accurate [25], however this was found to be partially due to the type of gust used to perform the experiment [135]. In fact, the Atassi function and the Sears function give identical results for any combination of camber and angle of attack, if the sinusoidal gust varies spatially only in the streamwise direction. The coupling between the loaded aerofoil and the gust only occurs if there is also a vertical variation in the gust properties [5].

While the application of classical unsteady aerofoil theory is limited to pre-stall conditions, it is generally considered to be reliable for 2D aerofoils as long as no large-scale stall events occur. This is, however, dependent on the appropriate choice of unsteady transfer function given the gust conditions and aerofoil geometry, which remains a challenge for engineering design. One of the aims of this thesis is, therefore, to create a more generalised approach to modelling unsteady aerofoil response, by using eigenmode decomposition (see

Chapter 6). A further challenge is understanding the implications of 3D geometry and flow features on the validity of 2D unsteady flow modelling. This will also be discussed in this thesis.

2.5.4 Viscous effects: dynamic stall

Much recent attention to the unsteady loads affecting tidal turbines has been directed towards the phenomenon of dynamic stall (see for example [108] [74]). Dynamic stall is characterised primarily by the creation of a strong leading edge separation vortex that convects along the aerofoil suction surface. This increases the resulting lift to a point far beyond the stall limit of the aerofoil under steady conditions. See Figure 2.5 for an illustration.

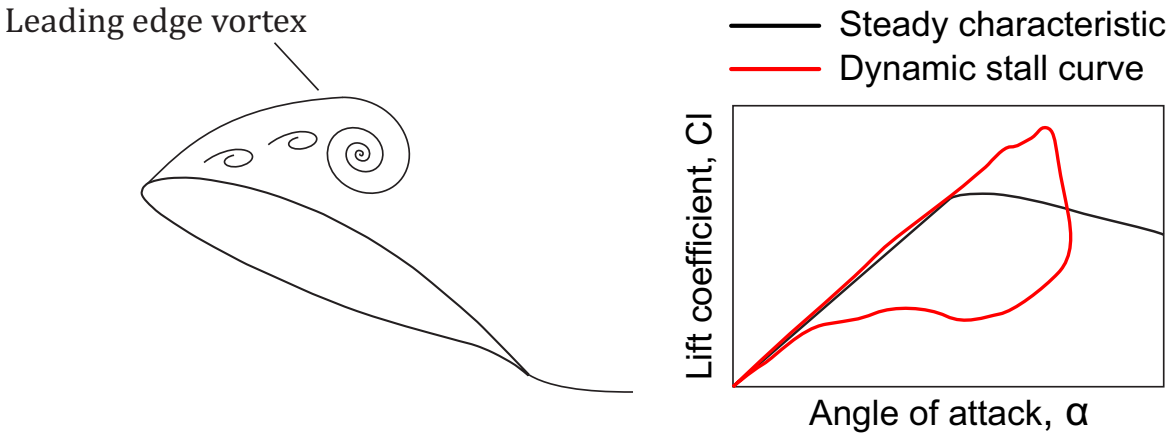

Fig. 2.5 Illustration of dynamic stall, and the effect on the aerofoil lift characteristic (adapted from [75]).

The parameters that influence the formation of dynamic stall are plentiful and complex, and many of them virtually unexplored. A summary is provided by McCroskey [87] of the features affecting dynamic stall, and the degree to which they matter. Parameters such as reduced frequency of oscillation, the mean flow angle and oscillation amplitude are major factors affecting the behaviour of dynamic stall. Aerofoil shape can be a significant parameter in some cases, and the effects of Mach number and Reynolds number are largely unknown. The effect of the type of motion experienced by the aerofoil is relatively unexplored, as are 3D effects.

Dynamic stall is an inherently viscous phenomenon and is dominated by dynamic boundary layer separation [49]. Analytical models are very hard to develop for such conditions, and so the range of dynamic stall models available all rely to a greater or lesser extent on

empirically tuned coefficients. The simplest dynamic stall models compute the resulting lift as a function of both the inviscid lift and the fully separated lift, with a parameter describing the degree of separation [59]. One of the most widely used models is the Leishman-Beddoes dynamic stall model [76], which benefits from a greater degree of generality compared to many other models. It does not require many empirically tuned coefficients but is only valid for supersonic flow. A study by Gupta and Leishman [55] modified the Leishman-Beddoes semi-empirically to model subsonic flow. The onset of leading edge separation is one of the most important aspects of dynamic stall modelling, and different models have different criteria. The Leishman-Beddoes model uses two criteria – a critical leading edge pressure and associated pressure gradient – to determine the onset of the leading edge vortex.

Testing of dynamic stall models is generally done against pitching aerofoil experiments – see for example [73] – and it is during aerofoil pitching that dynamic stall occurs most readily [50]. An interesting take on the dynamic stall phenomenon is given by McCroskey [86], who presents a method for modelling dynamic stall through discrete vortex methods. The precursor to this work is the discrete vortex modelling developed to model bluff-body separation. While the essential features of the separation are reproduced, the locations and frequency of the vortices have to be specified empirically.

An experimental study by Lee and Gerontakos [73] found that the leading edge vortex created in a dynamic stall event convected down the suction surface at a speed that was not affected by the reduced frequency of the oscillating flow. This seems to suggest that dynamic stall can be initiated by oscillating flow conditions, but the resulting physics are more significantly determined by mean freestream conditions and aerofoil shape.

The properties of dynamic stall behaviour have been found to be different for aerofoils which exhibit leading edge as opposed to trailing edge separation [74]. The most advanced low-order models developed to date that include dynamic stall are developed for aerofoils with leading-edge separation. In the case of thick aerofoils common to wind and tidal turbines, trailing edge separation will take place long before leading edge separation [102]. This leads to difficulties in predicting the properties of the leading edge separation vortex for a dynamic stall model. The development of dynamic stall is also known to be suppressed by trailing edge stall, and this may reduce its impact on tidal turbine blades.

While this thesis deals primarily with pre-stall conditions, a description of the current state of research for dynamic stall has been included due to its potential importance for

unsteady turbine loading. It is not yet firmly established how common dynamic stall events are in tidal turbine applications, nor how significant their effects are on the turbine loading. When it does occur, dynamic stall is generally near the hub of the turbine, in which case the effects on the blade bending moment will be relatively small [109].

2.6 Unsteady loads on wind and tidal turbines

Unsteady blade loading is now recognised as one of the primary challenges in tidal turbine development, and is also of significant interest for wind turbines. A range of studies on the topic illustrate that this is a complex problem and that the low-order models used presently to estimate turbine load response are inadequate. Studies have shown industry-standard BEMT models to give errors in the order of 20% or more in the prediction of unsteady loads [110] [117]. There is therefore a need for improved understanding of the flow physics behind unsteady loading. Increasing the fidelity of the computational solver, however, does not always lead to more accurate answers. In some cases, BEMT has also been shown to give better unsteady loading predictions than fully-resolved computational fluid dynamics (CFD) simulations [61], in cases when tabulated aerofoil data is more accurate than the simulated aerofoil performance.

Recently a number of experimental studies have been performed to explore unsteady turbine loading, and to understand the relative significance of added mass and unsteady wake effects. In studies by Whelan [136] and Milne [91] the unsteady response of a model tidal turbine was found for oscillatory or ramp-movement of the turbine in steady flow conditions. In both of these cases a phase lead was observed relative to the forcing function, which was attributed to the dynamic inflow induced by the unsteady wake as opposed to the added mass. This type of phase lead is not predicted by 2D unsteady transfer functions used in BEMT models. McNae [88] – performing oscillatory testing of a model-scale turbine at a higher frequency – found that as the frequency of oscillation increased, the phase of the load response began to lag behind the forcing function, having initially had a phase lead. In all the above studies, there was qualitative agreement between experiments and BEMT models but the magnitude of the unsteady loading was not reproduced accurately by BEMT.

Oscillatory turbine movement in the axial direction is sometimes used as a way to represent the effect of turbulence on the turbine, as it is easier to achieve experimentally than realistic large-scale turbulence (for example, this is done in [91]). The two experiments are, however, not necessarily interchangeable. McNae [88] undertook experimental testing to

show the difference between the load response generated by a step-change in flow velocity, and that caused by blade pitching. For the blade pitching case, an instantaneous large load spike occurred, then a smaller spike before the load response settled to the new level. In the case of the flow change, the initial large spike in load did not occur, and the transient load overshoot had smaller amplitude and decayed faster.

An experimental tank study by Chamorro et al [18] suggests a significant dependence of tidal turbine performance on the flow turbulence. Comparing the upstream turbulent spectrum to the resulting power spectrum of a model turbine, a strong coupling was found between the turbine power and the turbulent energy cascade in the low frequency range. In the high frequency region the turbine did not respond to the flow turbulence. Chamorro et al went on to identify a critical frequency below which turbulent structures are coupled to turbine performance. The critical frequency was found to increase linearly with the angular frequency of the rotor.

When investigating the applicability of unsteady transfer functions (introduced in Section 2.5.2) to tidal turbines, Sequeira and Miller [115] used the characteristic integral and mixing length scales of measured channel turbulence to estimate the range of reduced frequencies experienced by 2D tidal blade sections as a result of turbulence. For their 18 m diameter example turbine, the range of reduced frequencies at mid-span was estimated to be 0.02-0.65. As the blade rotational speed is lower near the hub, the reduced frequency in this region will increase, while it will decrease near the tip where the rotational speed is higher (see Equation 2.2). They further found that surface waves would cause mid-span reduced frequencies in the range 0.05-0.21, and that rotation through nominally steady features (such as the shear layer, or the potential field of the support structure) could generate reduced frequencies in the range 0.21-0.63. The analysis by Sequeira and Miller will be introduced in more detail in Chapter 7.

Note that the reduced frequencies cited above are for single-harmonic gusts. Many unsteady inflow conditions are not harmonic, but can be modelled through a superposition of several single-harmonic gusts. Because of this, reduced frequencies larger than those found by Sequeira and Miller are likely to be important in analysis of unsteady flow response. Based on this observation, and the frequency ranges cited above, the reduced frequencies investigated in this thesis will generally be confined to the range 0.0-2.0.

Surface waves have been recognised in a number of studies as a significant cause of unsteady turbine loading [109] [92]. Using measured site data from various sources, combined

with linear wave theory, Sequeira and Miller [115] mapped out the gust amplitudes likely to affect a tidal turbine due to surface waves. At mid-span they found that the gust amplitudes experienced could range from 2 to 170% of the mean axial flow. The limit for static stall for the aerofoil was at a gust amplitude of 130% of the mean axial flow.

Gaurier et al [42] performed tests in a flume tank on a model-scale turbine, investigating the effect of turbulence and waves on the mean and unsteady performance. The standard deviation of the unsteady blade loading was found to increase with turbine rotational speed. Scarlett et al [109] developed a BEMT model with rotational augmentation and a modified version of the Beddoes-Leishman dynamic stall model (this model gives the same unsteady load response as the Theodorsen function in pre-stall conditions), in order to study the interaction of a turbine with unsteady flow. Unlike Gaurier et al [42], they found that the primary factor governing blade load response to waves was the wave frequency, rather than the rotational frequency of the turbine.

The studies cited above confirm the observation from the Turbulence in Marine Environments project report [24], that there is currently no robust engineering model for assessing the unsteady loads affecting tidal turbines. This is the case even in the simple case of planar oscillatory flow. Considering the importance of accurate fatigue life calculations, it is vital for further growth of the tidal turbine industry to have access to tools capable of capturing turbine load response to waves and turbulence.

2.7 Three-dimensional effects

The topic of this thesis is the response of an aerofoil to unsteady gusts in realistic, 3D situations – a topic which is largely unexplored in relation to wind and tidal turbines. As discussed in Sections 2.4 and 2.5.1, the state of the art design codes assume that the unsteady response of a tidal turbine blade can be considered as the sum of a series of 2D aerofoil sections which do not interact with one another. Three-dimensional and rotational effects have mainly been considered in terms of their effect on the blade boundary layers, and the resulting stall-delaying effect [74].

Unsteady gust interaction with aerofoils in 3D can be divided into two broad categories: 3D geometry effects, and 3D gust effects. The former deals with unsteady flow acting uniformly and in-phase along the span of a 3D aerofoil, such that the gust itself could be considered 2D. The latter deals with unsteady gusts that vary in magnitude and phase along

the span of the aerofoil. An overview of previous work in both these categories is given below.

2.7.1 3D geometry effects

There has recently been growing interest in the effect of 3D aerofoil geometry on unsteady aerodynamic response. Keddington [67] used CFD simulations to show that an oscillating finite wing gives different load response from that predicted by 2D or quasi-steady 3D models, and a number of recent studies have studied the effect of a finite span and sweep on unsteady aerofoil response, pre-and post-stall [89] [113] [8]. In the past, some attempts have been made to extend the Theodorsen function to account for a finite wing, or for varying planform of the aerofoil (see, for example [7] [140] [60] [116]). Each of these studies were however limited in scope, and the effect of 3D geometry on the unsteady aerofoil aerodynamics remains poorly understood.

As explained in Chapter 1, one of the primary changes to the aerodynamic system as a result of 3D geometry is the presence of streamwise wake vorticity. This component of the wake is not included in the 2D analysis of classical unsteady aerofoil theory. In addition to this, the spanwise component of the wake vorticity varies in strength along the span, and is finite for a finite-span geometry. This is also not accounted for in classical 2D theory.

Yates [140] published a theory for flutter prediction using a strip-theory method with Theodorsen's function to calculate unsteady effects, and applied corrections for finite span and sweep. The impact of the finite wing geometry was taken to be indicated by the lift and pitching moment produced at each wing section in the steady state. Barmby et al [7] extended Theodorsen's 2D oscillating aerofoil theory to swept wings, with the method coinciding with Theodorsen at zero sweep. The method simply used the local quasi-steady lift for a swept wing in the unsteady transfer function, instead of the purely two-dimensional lift. Neither of these methods account for the difference in flow physics inherent to 3D aerofoils, they simply attempt to add corrections to the 2D response.

Hobbs [60] included the effect of finite wing span on the transient load response of an aircraft tail encountering a sudden gust field. He considered two consequences of the finite span on the transient load: the addition of streamwise trailing vortices to the starting vortex system, and the fact that the starting vortex is finite in the spanwise direction. The former was not considered important for moderate aspect ratios, since the short transient load times were assumed not to allow the trailing vortices to develop enough to be important. Hobbs

accounted for the latter by subtracting the influence of the tip-to-infinity starting vortex, which would otherwise be included in the 2D analysis. He found that this correction made a difference primarily at steady-state, and was relatively unimportant to the transient response. More recently, Snel [116] has also attempted to account for 3D effects by noting that the 2D wake vorticity is finite in the spanwise direction. However, this study also neglected the unsteady effect of the streamwise trailing vortices. The effects of both the spanwise and streamwise wake vortices on unsteady load response will be considered in Chapter 4 of this thesis.

Boutet and Dimitriadis [14] developed an unsteady lifting line model in conjunction with the 2D Wagner function (see Table 2.1), for the purpose of modelling 3D wing response to a sudden change of pitch angle. However, the 3D wake downwash was considered to be quasi-steady in their study. The impact of this simplification will be examined in Chapter 5.

Some of the most extensive work on evaluating the effect of 3D geometry on unsteady aerofoil dynamics has been done for modelling of vibration and flutter in turbomachinery cascades (see for example [57] [129]). Golubev et al [47] studied the effects of three-dimensional swirling flow in cascades, and compared their experimental results to classical strip theory estimates. Unsteady response in 3D showed significant deviation from that predicted by strip theory (where the aerofoil only sees wake downwash patterns from its own 2D plane). Hall and Lorence [57] calculated the unsteady flow dynamics of a turbomachinery cascade, using the linearised harmonic Euler equations in 3D. The flow field was assumed to be composed of the nonlinear mean flow plus an unsteady harmonic perturbation. Their results showed that 3D effects were significant, and that strip-theory results risk significant over-prediction of the aerodynamic damping of vibrating blades. In general, strip theory was shown to be a poor predictor of the unsteady flow near the blade tips.

The most extensive analytical and semi-analytical studies of the effect of 3D geometry on unsteady turbomachinery aerodynamics were carried out by Namba [96] [95] and Schulten [111]. Namba and Toshimitsu [96] performed a semi-analytical analysis of the 3D unsteady flow field in ducted fans, including the effect of finite aerofoil loading. In particular, they investigated the effects of spanwise non-uniform amplitude of cascade blade vibrations, and spanwise non-uniform steady loading due to varying steady angle of attack along the blade span. Their results were compared to a conventional strip-theory approach.

Even with the limitation of low mean loading and low-amplitude oscillations, Namba and Toshimitsu's analysis showed that the inclusion of 3D effects can significantly alter the unsteady flow field. They showed that strip theory overestimates the spanwise non-uniformity, with the 3D flow working to suppress the spanwise variation in the aerodynamic force. Strip theory also tended to give higher absolute values of aerodynamic work per unsteady cycle than the 3D predictions. For some blade vibrational modes, the unsteady response near the blade tip was suppressed enough by the 3D effects that the centre of the blade span produced more unsteady aerodynamic work than the tip, in direct opposition to the result predicted by strip theory. 3D effects were observed to increase with decreasing reduced frequency, and with decreasing aspect ratio. The local unsteady moment coefficient was shown to be vastly over-predicted using strip theory, compared to using full 3D theory. Schulten [111] extended Namba's theory to account for blade lean, finding that this increased the unsteady effects significantly.

Namba writes further in the AGARD Manual on Aeroelasticity in Axial-Flow Turbomachines [95] about the then-current state of 3D corrections to 2D strip theory in turbomachinery. In supersonic flow the strip theory approach works remarkably well, but for subsonic and transonic flows there are significant differences. The origin of the discrepancy is attributed to the effect of the downwash velocity induced by the streamwise components of wake vorticity. The effect was shown to decrease with increasing reduced frequency (Equation 2.2), by considering a single lifting line with harmonically varying strength extending downstream, and examining how the velocity induced by the vortex line on an upstream location changes with oscillation frequency (see Figure 2.6 for an illustration). The unsteady downwash is shown to reduce in strength exponentially as the oscillation frequency increases: the downwash velocity v induced by the trailing vortex line in Figure 2.6 is given by [95]:

$$v = -\frac{d\Gamma}{d\mu} e^{i\omega t}(y-\mu)\frac{1}{4\pi}\int \frac{e^{-\frac{i\omega\eta}{U}}}{(x^2-\eta^2)^{3/2}} d\eta \tag{2.12}$$

The expression in Equation 2.12 can be shown to decrease exponentially as ω/U goes to infinity. As ω/U goes to zero, the expression reduces to the quasi-steady downwash.

The same frequency effect is noted by Cheng [20], who identifies several categories of gust wavelength relative to the chord and span of an aerofoil, and states that the response to the highest-frequency gusts is locally 2D due to self-averaging of the high-frequency periodic wake.

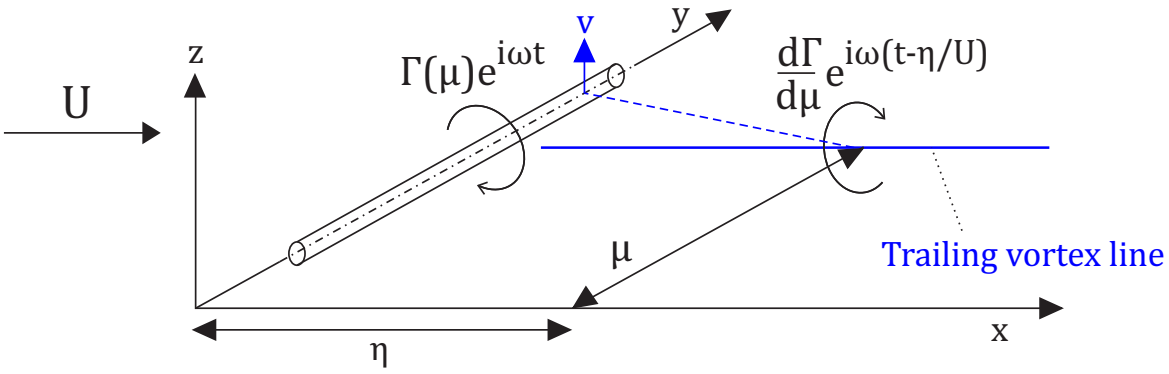

Fig. 2.6 Illustration of a simple model demonstrating the effect of streamwise vorticity downwash as the reduced frequency increases. An unsteady lifting line along the y-axis gives rise to a trailing vortex line with time-varying circulation. The trailing vortex line gives rise to induced downwash velocity on the lifting line. Adapted from [95].

The semi-analytical results of Namba and Schulten have been used in validation of 3D unsteady linearized Euler codes for use in turbomachinery cascades [43] [105] [57]. The results have been used to show that standard strip theory without corrections is not appropriate for use in unsteady turbomachinery cascades. Prasad [105] found in one such study that strip theory assumptions were invalid also in the case of spanwise uniform gust excitation.

Another notable set of analytical studies of 3D unsteady aerodynamics was carried out by Chopra and Kambe [22] [23]. Through the use of unsteady lifting line theory, they calculated the spanwise distribution of unsteady thrust induced by oscillating aerofoils, with the aim of representing the undulating propulsion of aquatic animals. They found that the inclusion of the streamwise wake vorticity inherent to 3D geometries significantly reduced the efficiency of the propulsive motion.

Many unsteady aerodynamic models based on lifting-line theory have been developed over the past half-century. One of the main characteristics of these methods is that the flow is assumed locally 2D, but the local angle of attack is recognised as being affected by the 3D wake. The basic version of this model utilises a superposition of horseshoe vortices which have constant strength in time, meaning that the streamwise wake vorticity is quasi-steady. Various extensions have sought to extend the analysis to unsteady frequency ranges, for example [3] and [20]. The majority of these studies are limited in scope, either by the aerofoil shape and planform or the frequency range in which the solutions are applicable; many studies perform the analysis by asymptotically relating the wavelength of the unsteady gust to either the aerofoil span or chord, which prevents their uniform validity for wavelengths

greater than the chord length [112].

Sclavounos [112] introduced a method of analysis to bridge this gap, by developing an unsteady lifting-line theory which reduced to Prandtl's lifting-line equation in the limit of zero frequency, and approached strip theory results as given by the Theodorsen function at high frequencies. The added mass was found using a strip-theory approach. Unified theories for a wider range of frequencies and geometric constraints have also been presented [54] [122]. In general, lifting line models are valid on the assumption that the aerofoil aspect ratio is high. The validation of unsteady lifting line models has been a challenge historically, but Bird and Ramesh [9] recently carried out a study evaluating the applicability of Sclavounos' theory by comparing it to CFD simulations. The model performed well within the limits of the assumptions used to derive the theory, but deviated significantly in the limit of low aspect ratios or high frequencies.

The importance of 3D aerofoil geometry in determining unsteady aerofoil loading is illustrated by the examples given above. Several studies confirm that strip theory is insufficient in predicting aerodynamic loads of finite-span aerofoil geometries. As such, it is likely that one of the primary limitations of current models for unsteady tidal turbine loading is the assumption of locally two-dimensional flow. The influence of 3D geometry on load response will be discussed in Chapters 4 and 5 of this thesis, where a 3D vortex lattice model will be shown to give improved load estimates over the range of gust frequencies experienced by a tidal turbine.

2.7.2 3D gust effects

As well as considering the impact of 3D geometry on gust response, it is important to understand the effect of unsteady flow features which are not idealised, 2D gusts. A number of studies have explored the response of infinite-span aerofoils with uniform planform to 3D gusts varying in the spanwise direction. In the study of turbulent flow interaction with bridges (which can be modelled as infinite-span aerofoils), the effect of spanwise gust three-dimensionality has been found to be related to the ratio of the turbulent length scales of the unsteady flow to the section chord length [84].

A study by Filotas [37] used a method based on linear incompressible lifting surface theory to analyse the case of an aerofoil passing through an inclined sinusoidal gust. The results were compared to predictions by the Sears function for 2D aerofoil interaction with sinusoidal gusts (see Table 2.1). The study showed that the presence of just a small deviation

from perpendicular gust oscillation leads to a response that deviates from the Sears function. Graham [51] carried out a study of the loading generated on an infinite-span wing by an unsteady flow of the form $e^{i(dx+\eta y-\omega t)}$ (meaning that the gust front is not parallel to the wing leading edge) and showed that this spanwise misalignment caused both a smaller unsteady load amplitude and different phase from that predicted by the 2D Sears function. Jackson et al [63] then used superposition of Graham's function for various sinusoidal gust frequencies to compute the aerofoil load spectrum in response to grid turbulence in a wind tunnel test. Studies such as these indicate that spanwise gust variation is an important 3D flow property, and that using simply the incident flow velocity at a given 2D blade section is an oversimplification.

Recent studies of unsteady flow interaction with aerofoils have primarily focused on high-fidelity viscous simulations, utilising the growing capacity of computers to perform Large Eddy Simulation (LES). Despite increased computational capacity, studies are still generally limited to 2D aerofoils, or small 3D aerofoils with no significant 3D geometry features, often modelled with periodic boundaries as infinite wings (see for example [8] [48]). A series of studies by Golubev et al [49] [48] analysed the unsteady forces affecting small urban air vehicles. The studies focused on low Reynolds number flows simulated using LES. As such, viscous forces and large-scale separation often dominate the aerofoil response. A recent paper [66] initiated a parametric study focusing on 3D gust effects, investigating the impact of gusts with streamwise, spanwise and transverse flow components on an infinite, uniform wing. They found that Atassi's 2D model [5], accounting for blade camber and upstream gust influence, compared quite well with 3D high-fidelity simulation at low angle of attack, but slightly underestimated the load amplitude.

Very few studies have been undertaken into the three dimensional nature of the unsteady flow over tidal turbine blades. The experimental work by Blackmore et al [12] using grid-generated turbulence is one of the few recent studies on the topic of 3D unsteady flow interacting with a tidal turbine. A numerical study into the transient fluid-structure interaction of tidal turbines was carried out by Young et al [142], using a coupled boundary element and finite element method to evaluate the structural response to spatially varying inflow. Their results show that there is a risk of cavitation at the blade tips under unsteady flow if the tip region is near the free surface and highly loaded. Young et al also found that added mass effects coupled with the high density of water reduced the natural frequency of the blades, compared to what it would be when operating in air. However, no general conclusions

were drawn on the applicability of 2D approximations in tidal turbine performance evaluation.

While models do exist for the interaction of 3D gusts with infinite-span aerofoils, the understanding of 3D unsteady flow interaction with a finite-span geometry – let alone a rotor geometry – remains vague at best. Considering the highly three-dimensional nature of turbulent ocean flows, this is undoubtedly an uncertainty of significant consequence for the tidal turbine industry.

2.8 Summary

In this chapter, the background to the current study has been presented. The highly unsteady 3D flow environment in which tidal turbines operate has been described, and the most common engineering modelling methods used for tidal turbine design and performance prediction have been discussed, along with their associated limitations.

One of the primary limitations in the state-of-the-art models is the assumption of locally two-dimensional flow, with each blade section assumed to be independent of the others along the blade span. A number of correction factors exist to adjust the steady flow performance to account for 3D and rotational effects. However, no such corrections exist for the dynamic inflow models or functions from classical aerofoil theory that are commonly used to estimate unsteady flow effects. This assumption of 2D geometry has been shown to be inaccurate in a range of engineering applications. The impact of 3D geometry on unsteady loading will be investigated in detail in Chapters 4 and 5 of this thesis.

Spanwise variation in gust properties has also been shown to radically alter the unsteady loads experienced by aerofoils. However, these studies have generally been limited to infinite-span cases, with no 3D properties of the aerofoil geometry. Tidal turbines operate in a flowfield with 3D, anisotropic unsteady flow features, and as such there is a need for understanding of the interaction of realistic, 3D turbine geometries with realistic, 3D gusts. This will be discussed in Chapters 6 and 7 of this thesis.

The continued development of tidal turbines creates an urgent need for a reliable model for unsteady gust interaction which can accurately predict unsteady turbine loads. The models currently in use are unable to predict turbine load response, even to gusts acting uniformly over the turbine blades. As a step towards the goal of bridging the "chasm" between ocean turbulence and turbine fatigue loading, this thesis will focus on quantifying the effect of 3D

geometry and 3D gust shapes on unsteady turbine loads, and to determine the flow physics governing the 3D gust interaction.

Chapter 3

Numerical Methods

3.1 Introduction

The work presented in this thesis is based on numerical modelling of fluid dynamic systems. Two different modelling approaches are used: inviscid modelling with a vortex lattice model (VLM), and viscous modelling with a Reynolds-Averaged Navier-Stokes (RANS) solver. The VLM has the advantage of speed. A viscous simulation might take hours or days for a case where the VLM would take seconds or minutes. It is capable of modelling complex 3D geometries undergoing unsteady flow forcing, and is accurate for first-order predictions. Therefore, it is unrivalled as a modelling method if the objective is rapid evaluation of a wide range of geometries and unsteady flow states.

The key limitation of the VLM is that it models the flow as inviscid, with no flow separation. In order to both validate the VLM and to show the impact of viscosity on the unsteady turbine performance, the VLM results will be compared to steady and unsteady RANS simulations. The RANS simulations are carried out using the open-source CFD software OpenFOAM. It is the most widely used open-source CFD code, with an active online community, and has been used in a range of projects related to tidal power research (see for example: [80] [138]).

This chapter describes the structure of the time-and frequency-domain VLMs, including steady 3D and unsteady 2D validation. The setup of the RANS simulations is then described, including the development of the mesh. The numerical modelling described in this chapter forms the basis of the analysis performed in the remainder of this thesis.

3.2 Inviscid modelling: the vortex lattice model (VLM)

A significant body of past work using VLMs for a wide variety of complex problems shows that in the absence of separation and for incompressible flow, a VLM can accurately capture the load response of complex geometries to unsteady, three-dimensional flow. There are a number of studies showing the applicability of vortex panel methods for preliminary aerodynamic design and performance analysis, in a variety of fields from wind turbines to fighter jets (see for example: [68] [83] [64]). The model described in this section is based on that outlined by Katz and Plotkin [64], with modifications to allow for frequency-domain calculations.

The VLM used in this thesis was developed in two versions: a frequency-domain solver and a time-domain solver. The frequency-domain VLM solver evaluates the time-history of the flow by solving a single matrix equation, allowing rapid computation even at high lattice resolution. The time-domain VLM solver evaluates the flow field at each discrete time-step, which allows for non-harmonic inflow conditions but is significantly more time consuming. To reduce the calculation time, the time-domain VLM is generally run with a coarser lattice, since the computational time increases exponentially with the number of lattice points. This may impact the accuracy of the time-domain model. In Chapter 4 the capability of the frequency-domain VLM to evaluate the unsteady performance of a range of geometries is used to show the effect of 3D aerofoil geometry on unsteady flow response.

The limitation of the frequency-domain VLM is that it requires pre-existing knowledge of the shape of the wake. It is normally assumed that the wake moves with the steady freestream velocity, and thus the wake shape can be calculated in advance. This is called using a "prescribed wake" in the frequency-domain VLM. In the time-domain VLM the wake vortices convect with the local flow velocity at each time step, and thus the wake shape is calculated, not prescribed. A point of repeated emphasis in the literature is the importance of the near-wake resolution and shape in determining the blade loads. For this reason, the errors associated with the prescribed-wake model will be assessed in Chapter 5, where both the frequency-and time-domain VLMs are used to evaluate the unsteady performance of a model tidal turbine.

3.2.1 VLM theory

Vortex lattice models are based on potential flow theory, which assumes incompressible and inviscid flow. The velocity field can then be expressed in terms of a potential:

$$\mathbf{U} = \nabla\Phi \tag{3.1}$$

This in turn means that the field properties can be obtained from solutions of Laplace's equation, which we obtain from the continuity equation:

$$\nabla^2\Phi = 0 \tag{3.2}$$

The Laplace equation is linear, allowing for the superposition of individual solutions. Due to this inherent linearity of the potential flow problem, complete solutions to the Laplace equation can be given by a distribution of "elementary" solutions along the problem boundaries. These must satisfy the boundary conditions for a submerged body in a fluid: on solid surfaces the surface-normal component of velocity must be zero, and far away from surfaces the disturbance induced by the solid body must decay.

The most commonly used elementary solutions are point sources, point doublets, linear polynomials of position, or point vortices. These all fulfil the boundary conditions stated above. Source elements are mainly used to simulate the effect of thickness, while vortices and doublets are used for lifting problems, where asymmetry is required. The effect of blade thickness is outside the scope of the present study, so only vortex elements are used in the VLM presented in this chapter.

3.2.2 Numerical method

In the 2D configuration, the vortex lattice is built of lumped-vortex elements. The aerofoil is divided into flat plate panels, each with an associated point vortex and collocation point (see Figure 3.1). The point vortex is placed at the quarter-chord of each panel, and the associated circulation, Γ, of each vortex gives the aerofoil its lifting properties. The collocation point is placed at three-quarter chord of each panel; this ensures implicitly that the Kutta condition is met. The boundary conditions and blade forces are evaluated at the collocation points.

In an unsteady flow, the aerofoil circulation will change with time, and so vorticity must be shed to satisfy Kelvin's theorem:

$$\frac{d\Gamma}{dt} = 0 \tag{3.3}$$

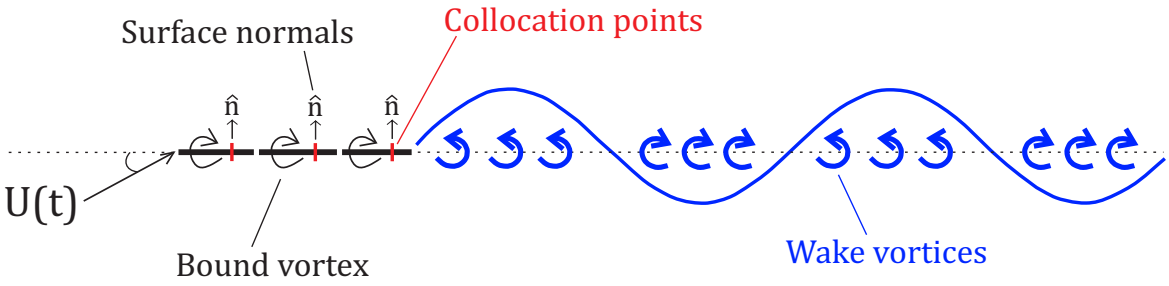

Fig. 3.1 2D configuration of the vortex lattice model.

The unsteady vortical wake is modelled by allowing point vortices to shed from the trailing edge of the aerofoil into the freestream. At each time step a single point vortex is shed, with strength equal and opposite to the change in aerofoil circulation.

The model is similar in 3D, but the vortical elements are vortex rings instead of point vortices (see Figure 3.2). In this model Kelvin's condition is inherently satisfied, as each vortex ring is contained in the domain and does not start or finish outside the domain boundaries. As such, the wake is generated by allowing the trailing edge vortex rings to shed into the freestream at each time step.

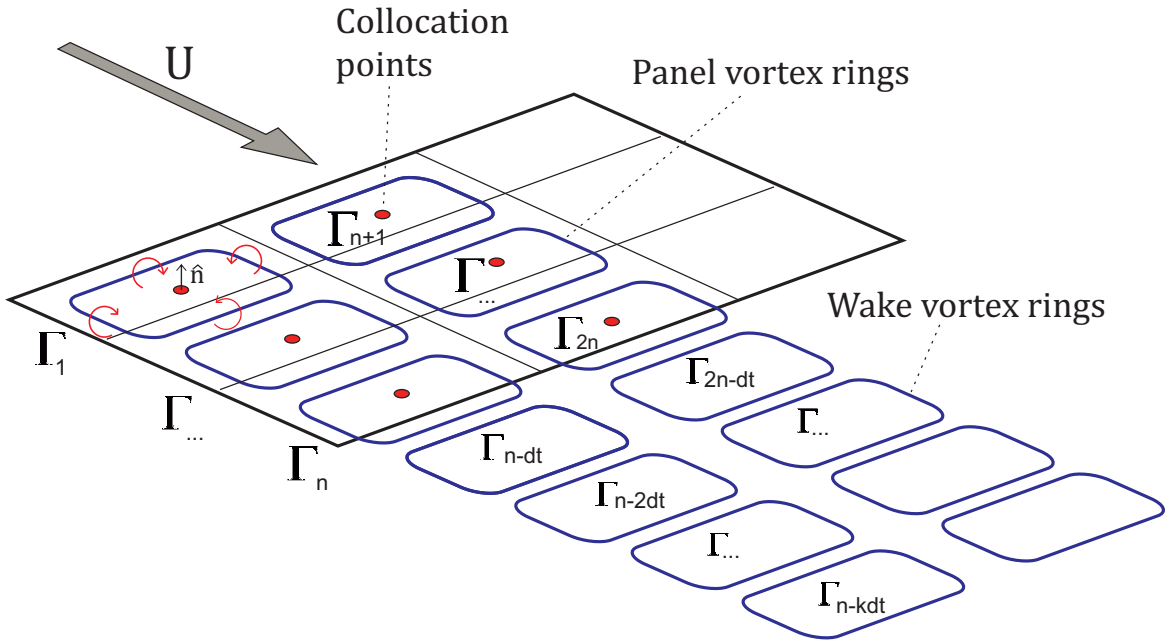

Fig. 3.2 3D configuration of the vortex lattice model.

In order to find the load distribution on the aerofoil, the unknown array of bound vortex circulation, Γ, must be found. This is done by applying Neumann's boundary condition

of zero flow normal to the surface at each collocation point. The flow velocities acting at each collocation point originate from the steady freestream velocity, the blade rotation, the unsteady gust velocity, and the downwash velocity induced by the wake. The matrix equation resulting from applying the boundary condition has the following form:

$$(\mathbf{A\Gamma} + \mathbf{U}).\hat{\mathbf{n}} = 0 \tag{3.4}$$

In this notation, $\mathbf{U}$ represents the combined effect of the velocities listed above acting on the aerofoil collocation points. $\hat{\mathbf{n}}$ is the surface normal vector on each panel. The matrix $\mathbf{A}$ is the influence matrix. It contains the information about the aerofoil geometry, and calculates the velocity induced by each aerofoil vortex on each collocation point, given the vector of vortex circulations $\mathbf{\Gamma}$. The format of this matrix differs depending on whether the model is 2D or 3D, and on whether the model is in the time- or frequency-domain. The differences will be illustrated in the following two sections.

In the VLM solver, Equation 3.4 is inverted to obtain the aerofoil circulation vector, $\mathbf{\Gamma}$. Having obtained the circulation, the lift properties of the aerofoil are found using the Kutta-Joukowski theorem. The lift force caused by the circulation of a single panel is obtained through the vector form of the Kutta-Joukowski theorem as follows:

$$\mathbf{F} = \rho(\mathbf{U} \times \mathbf{\Gamma}) + \mathbf{F}_{am} = \rho[(\mathbf{U}_{rel} + \mathbf{u}_{gust} + \mathbf{u}_{wake}) \times \mathbf{\Gamma}] + \mathbf{F}_{am} \tag{3.5}$$

The expression $\mathbf{F}_{am}$ is the added mass force. The velocity vector $\mathbf{U}_{rel}$ represents the relative velocity of a panel. For rotational cases this includes the blade rotational velocity $\mathbf{u}_{rot}$, giving:

$$\mathbf{U}_{rel} = \mathbf{U}_\infty + \mathbf{u}_{rot} = \mathbf{U}_\infty + TSR|\mathbf{U}_\infty|\mathbf{e}_\theta \tag{3.6}$$

Here TSR denotes the tip-speed ratio – the ratio between the blade rotational speed at the blade tip and the mean freestream axial velocity. $\mathbf{e}_\theta$ is the tangential unit vector in polar coordinates, centred on the turbine rotational axis. The added mass force $\mathbf{F}_{am}$ is found from the time derivative of the potential field as follows:

$$\mathbf{F}_{am} = \rho \int_0^c \frac{\delta}{\delta t} \Delta\Phi \tag{3.7}$$

The expression $\Delta\Phi$ is the potential field difference across the upper and lower surfaces of the aerofoil, which for a vortex panel method is equal to the vortex strength at each panel, Γ.

The majority of the influence matrix, **A**, is found by applying the Biot-Savart Law to the aerofoil and wake vortices. The Biot-Savart law for the velocity induced by a vortex line with strength Γ is given by:

$$\mathbf{v} = \frac{\Gamma}{4\pi} \frac{\mathbf{r}_1 \times \mathbf{r}_2}{|\mathbf{r}_1 \times \mathbf{r}_2|^2} \left[\mathbf{r}_0 \cdot \left(\frac{\mathbf{r}_1}{|\mathbf{r}_1|} - \frac{\mathbf{r}_2}{\mathbf{r}_2} \right) \right] = \Gamma \mathbf{a} \tag{3.8}$$

In this notation, for the velocity induced at point $\mathbf{p}$ by a vortex line between the points $\mathbf{p}_1$ and $\mathbf{p}_2$, the vectors $\mathbf{r}_1$ and $\mathbf{r}_2$ are given by $\mathbf{p}_1 - \mathbf{p}$ and $\mathbf{p}_2 - \mathbf{p}$, respectively. The vector $\mathbf{r}_0$ is given by $\mathbf{p}_1 - \mathbf{p}_2$. The notation is illustrated in Figure 3.3. The dot product of the vector $\mathbf{a}$ in Equation 3.8 and the panel surface normal $\hat{\mathbf{n}}$ makes up most of the influence matrix **A**, as will be shown in the next section.

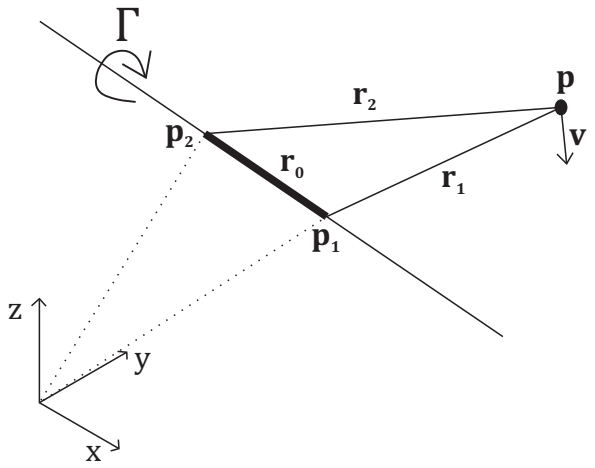

Fig. 3.3 Illustration of vortex segment inducing velocity at a point $\mathbf{p}$, showing the notation used when applying the Biot-Savart law in this chapter.

3.2.3 Time-domain VLM

As stated above, two versions of the VLM were used in this thesis: one using time-domain modelling and the other using frequency-domain modelling. The speed of the frequency-domain solver derives from the fact that Equation 3.4 only needs to be solved once for the full time-history of the flow. Using a time-domain solver, by contrast, requires Equation 3.4 to be solved every time step. The disadvantage of the frequency-domain solver is that the shape of the wake must be known or estimated using simplified assumptions of the flow.

The simplest way to define the wake shape is to assume that the wake vortices leave the trailing edge with the steady freestream flow speed, which is often done in frequency-domain VLM. Any modelling method in which the shape of the wake is assumed prior to solving is called "prescribed-wake" modelling. In reality, the wake vortices interact with each other and the unsteady flow, leading to additional distortion of the wake. Vortex models which allow the wake to interact with other flow features in a time-stepping solver are called "free wake" models.

In the case of turbines, which extract kinetic energy from the flow, the two main wake distortion effects that may have to be accounted for are wake rollup near the tip and hub, and an overall flow deceleration in the wake. In addition to this, the wake can be further distorted by unsteady gusts. The purpose of using both time-domain and frequency-domain calculations in this thesis is to estimate the effects of each of these wake distortion effects on the unsteady flow response. By solving for the entire flow field at every time step, the time-domain solver is able to capture the effects of wake distortion.

In the time-domain, Equation 3.4 is solved at each discrete time step, which simplifies the calculations but is substantially more time-consuming. The wake-induced velocity at a given time step is calculated using the Biot-Savart law (Equation 3.8) with the wake vortex circulations found in the previous time step. The resulting influence matrix $\mathbf{A}$ has the following form:

$$\mathbf{A\Gamma} = \begin{bmatrix} a_{1,1} & a_{1,2} & \dots & a_{1,n} & a_{1,n+1} & a_{1,n+2} & \dots & a_{1,N} \\ a_{2,1} & a_{2,2} & \dots & a_{1,n} & a_{2,n+1} & a_{2,n+2} & \dots & a_{1,N} \\ \vdots & \vdots & \ddots & \vdots & \vdots & \vdots & \ddots & \vdots \\ a_{N,1} & a_{N,2} & \dots & a_{N,n} & a_{N,n+1} & a_{N,n+2} & \dots & a_{N,N} \end{bmatrix} \begin{bmatrix} \Gamma_1 \\ \Gamma_2 \\ \vdots \\ \Gamma_N \end{bmatrix} = - \begin{bmatrix} U_1 \\ U_2 \\ \vdots \\ U_N \end{bmatrix} \tag{3.9}$$

Each row represents the influence of each panel vortex on the panel collocation point associated with that row. For simplicity of notation, the vector $\mathbf{a}$ from Equation 3.8 is written as a scalar in Equations 3.9, as the dot products with the panel normal vectors, $\hat{\mathbf{n}}$, have been applied. The matrix size is $[N] \times [N]$, where N is the total number of panels (given by multiplying the number of panels across the chord, n, by the number of panels across the span, m). The aerofoil circulation vector $\mathbf{\Gamma}$ is obtained by inverting Equation 3.4 at each time step. The time-history of unsteady loading is then calculated using Equation 3.5. At each time step the circulations of the new shed wake vortices are found and stored for use in the next time step.

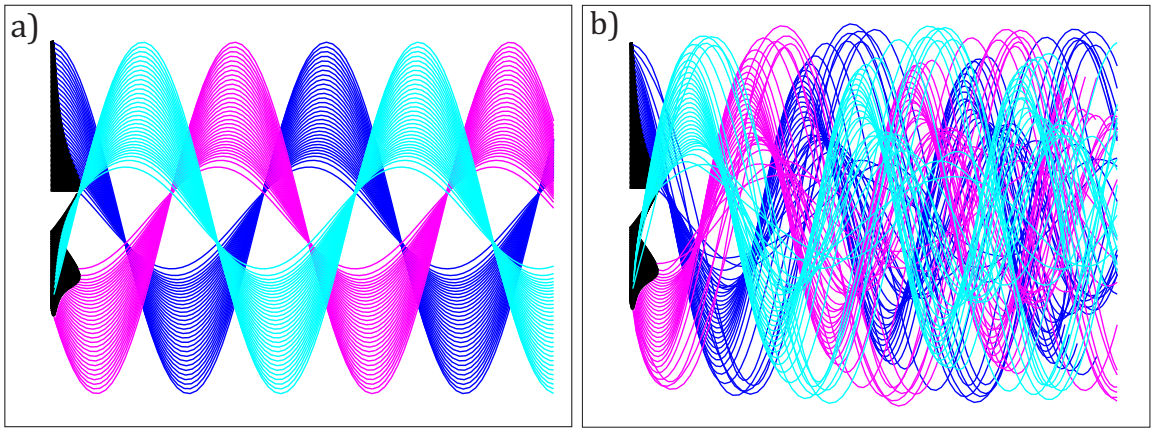

Fig. 3.4 Examples of wake shapes produced by the time-domain VLM. (a) Prescribed-wake using Equation 3.11a, (b) wake rollup using Equation 3.11b.

Using the time stepping VLM, it is possible to calculate the positions of each wake vortex as a summation of influence by the steady freestream velocity $\mathbf{U}_\infty + \mathbf{U}_{rot}$, the unsteady gust velocity $\mathbf{u}_{gust}$, and the velocity induced by all the other wake vortices in the flow $\mathbf{u}_{wake}$. The movement of each wake vortex at each time step is obtained by:

$$d\mathbf{l} = dt.\mathbf{U} \tag{3.10}$$

The velocity vector $\mathbf{U}$ can be obtained in four different ways: (1) using only the freestream velocity, (2) including the effects of the surrounding vortices, (3) including the effect of the gust distorting the wake, or (4) including both the surrounding vortices and the gust distortion. Each of these cases are represented by the following equations for $\mathbf{U}$:

$$\mathbf{U} = \mathbf{U}_\infty + \mathbf{u}_{rot} \tag{3.11a}$$

$$\mathbf{U} = \mathbf{U}_\infty + \mathbf{u}_{rot} + \mathbf{u}_{wake} \tag{3.11b}$$

$$\mathbf{U} = \mathbf{U}_\infty + \mathbf{u}_{rot} + \mathbf{u}_{gust} \tag{3.11c}$$

$$\mathbf{U} = \mathbf{U}_\infty + \mathbf{u}_{rot} + \mathbf{u}_{wake} + \mathbf{u}_{gust} \tag{3.11d}$$

The velocity vector as given by Equation 3.11a assumes the wake to move with the steady freestream velocity, which effectively results in a prescribed wake like the one used in the frequency-domain VLM outlined in the next section. If this equation is used to obtain the wake shape, the time-stepping VLM gives identical results to the frequency-domain VLM. An example of this wake is shown in Figure 3.4a, for a tidal turbine geometry rotating at TSR 4. The velocity vector given by Equation 3.11b includes the effects of the surrounding

wake vortices, which will be referred to as "wake rollup". An example of the wake shape that results from this inclusion is shown in Figure 3.4b, for steady-flow operation. As mentioned before, one of the primary effects resulting from the influence of the other vortices is that the wake propagation speed in the shadow of the turbine is significantly reduced (in the case of a propeller, which adds kinetic energy to the flow, the effect would be reversed and the wake propagation speed would increase).

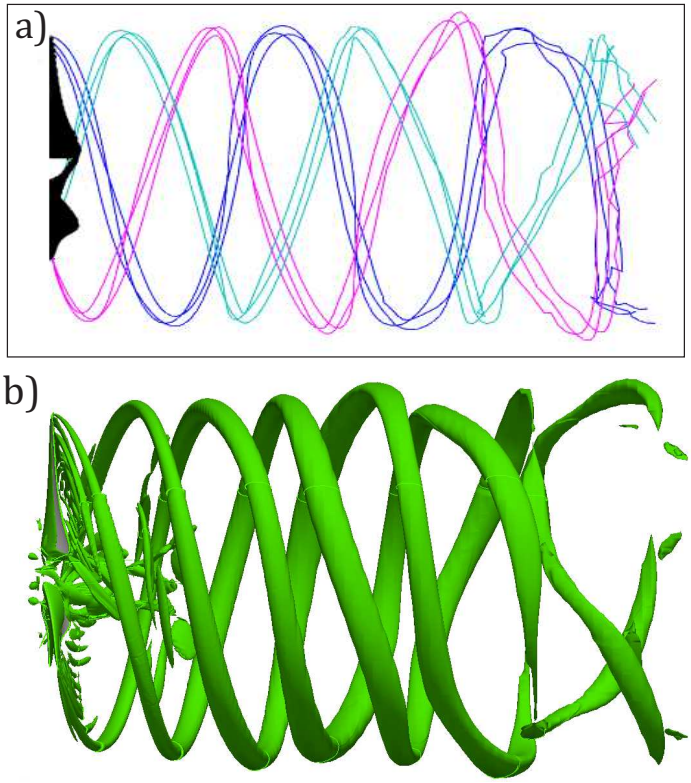

Fig. 3.5 Wake development in (a) the VLM code, including the effect of wake rollup and distortion by the unsteady gust (using Equation 3.11d), and (b) in URANS simulation of the same gust, showing vorticity contours obtained using the q-criterion.

The velocity vector given by using Equation 3.11c includes the distorting effect of the unsteady gust. Finally, the velocity vector given by Equation 3.11d includes the combination of both wake rollup and gust distortion. An example of a VLM-generated wake using Equation 3.11d is shown in Figure 3.5a, for a gust acting uniformly across the turbine and oscillating harmonically in the axial direction. It is compared qualitatively with the results of an URANS simulation (Figure 3.5b), the setup of which will be presented later in this chapter. It can be seen that the qualitative agreement between the two simulations is good, in terms of the development of the downstream wake. Note that the URANS results are performed on a

third of the annulus with periodic boundaries, and the results in Figure 3.5b are extrapolated to show the full annulus.

3.2.4 Frequency-domain VLM

The main version of the VLM used in this thesis is the frequency-domain model with a prescribed wake, assuming the wake to propagate with the steady freestream velocity (as in Equation 3.11a). In the frequency domain, all time-dependent variables are assumed to vary harmonically with the form:

$$\Gamma = \hat{\Gamma} e^{i\omega t} \tag{3.12}$$

The frequency, ω, is the time-harmonic frequency of the forcing gust. Using this simplification, Equation 3.4 can be solved for the circulation amplitude $\hat{\Gamma}$, which when multiplied by $e^{i\omega t}$ gives the unsteady load response at any time.

Solving Equation 3.4 in the frequency-domain requires special treatment of the wake-induced velocity, $\mathbf{u}_{wake}$. Since the strength of the wake circulation is unknown, a function is needed to relate the wake circulation to the bound aerofoil circulation. This is done slightly differently in 2D and 3D calculations. In both cases, the wake circulation is assumed to vary harmonically as Equation 3.12. This means that the influence of the whole wake can be expressed as a harmonic sum, which in 2D gives the wake-induced velocity as:

$$\mathbf{u}_{wake} = \hat{\Gamma}_{wake} \sum^{k} \mathbf{a}_{ik} e^{-k\omega dt} = \hat{\Gamma}_{wake} \mathbf{b}_i \tag{3.13}$$

The vector **a** is the same as in Equation 3.8, and, along with vector **b**, makes up the influence matrix **A** in Equation 3.4. Equation 3.13 adds an additional unknown to the system through the wake circulation $\hat{\Gamma}_{wake}$. To close the set of equations, Kelvin's theorem (Equation 3.3) is required as a connection between the wake circulation and the bound aerofoil circulation. The resulting frequency-domain influence matrix in 2D is given by:

$$\mathbf{A}\hat{\boldsymbol{\Gamma}} = \begin{bmatrix} a_{1,1} & a_{1,2} & \dots & a_{1,n} & b_1 \\ a_{2,1} & a_{2,2} & \dots & a_{2,n} & b_2 \\ \vdots & \vdots & \ddots & \vdots & \vdots \\ a_{n,1} & a_{n,2} & \dots & a_{n,n} & b_n \\ i\omega & i\omega & \dots & i\omega & 1/dt \end{bmatrix} \begin{bmatrix} \hat{\Gamma}_1 \\ \hat{\Gamma}_2 \\ \vdots \\ \hat{\Gamma}_n \\ \hat{\Gamma}_{wake} \end{bmatrix} = - \begin{bmatrix} (\hat{u}_{gust})_1 \\ (\hat{u}_{gust})_2 \\ \vdots \\ (\hat{u}_{gust})_n \\ 0 \end{bmatrix} \tag{3.14}$$

The final column of the influence matrix **A** in Equation 3.14 represents the summed influence of the wake vortices, given by Equation 3.13. Kelvin's theorem (Equation 3.3) is represented

by the final row of Equation 3.14. Since the circulation is assumed to vary harmonically according to Equation 3.12, the time rate-of-change of circulation is given by $d\Gamma/dt = i\omega\Gamma$. The size of the influence matrix is $[n+1] \times [n+1]$, where n is the number of panels along the chord of the aerofoil. The 2D form of the VLM as given in Equation 3.14 will be used in Chapter 6, and also later in this chapter to validate the unsteady load predictions from the VLM against 2D classical aerofoil theory.

As mentioned above in Section 3.2.2, Kelvin's theorem is inherently satisfied in the 3D VLM. Because of this, the wake-induced velocity can be obtained by noting that the wake is formed by the trailing edge vortex rings being shed into the flow (see Figure 3.2). As such, the circulation strength of a given wake vortex is the same as that of the trailing edge panel vortex at the time the vortex was shed. This allows the wake-induced velocity to be calculated, retaining the notation in the Biot-Savart law (Equation 3.8) and the wake numbering in Figure 3.2:

$$\mathbf{u}_{wake} = \hat{\Gamma}_{TE} \sum^{k} \mathbf{a}_{ik} e^{-k\omega dt} = \hat{\Gamma}_{TE} \mathbf{b}_i \tag{3.15}$$

Note that Equation 3.15 is identical to Equation 3.13, except for its dependence on Γ_{TE} rather than Γ_{wake}. The time step dt used to calculate the wake-induced velocity in Equations 3.13 and 3.15 is not used for explicit time-stepping in the frequency domain, but is chosen as an input parameter that determines the resolution of the wake. Sufficient wake resolution is vital for accurate unsteady calculations. The accuracy condition found in this project was that the length of the wake vortex line in the streamwise direction had to be shorter than the chordwise length of the aerofoil panels. Throughout this work the time step dt was chosen so that the aerofoil panels were at least twice as long as the discretised wake vortex lines.

In the 3D frequency-domain VLM, which is used for the main body of work in this thesis, the influence matrix is given by:

$$A\hat{\boldsymbol{\Gamma}} = \begin{bmatrix} a_{1,1} & a_{1,2} & \dots & a_{1,n}+b_1 & a_{1,n+1} & a_{1,n+2} & \dots & a_{1,N}+b_1 \\ a_{2,1} & a_{2,2} & \dots & a_{1,n}+b_2 & a_{2,n+1} & a_{2,n+2} & \dots & a_{2,N}+b_2 \\ \vdots & \vdots & \ddots & \vdots & \vdots & \vdots & \ddots & \vdots \\ a_{N,1} & a_{N,2} & \dots & a_{N,n}+b_N & a_{N,n+1} & a_{N,n+2} & \dots & a_{N,N}+b_N \end{bmatrix} \begin{bmatrix} \hat{\Gamma}_1 \\ \hat{\Gamma}_2 \\ \vdots \\ \hat{\Gamma}_N \end{bmatrix}$$

$$= - \begin{bmatrix} (\hat{u}_{gust})_1 \\ (\hat{u}_{gust})_2 \\ \vdots \\ (\hat{u}_{gust})_N \end{bmatrix} \tag{3.16}$$

The wake influence is included in the final column, but now as a function of the trailing edge circulation, rather than of the wake circulation itself (as was the case in Equation 3.14). The matrix size is $[N] \times [N]$, where N is the total number of panels (given by multiplying the number of panels across the chord, n, by the number of panels across the span, m). Lattice resolution studies were undertaken at all stages of this work, to ensure convergence of the VLM results. Generally, chordwise lattice resolution was found to be of higher importance for convergence than the spanwise lattice resolution. For the frequency-domain VLM, the lowest lattice resolution $[m \times n]$ used for the results in this thesis is $[20 \times 20]$ for each blade, and the highest resolution used is $[100 \times 80]$. In Equation 3.16 the vectors **a** and **b** are again written as scalars, having applied the dot products with the panel normal vectors.

Having found the influence matrix **A**, the unknown vector of circulation amplitudes $\hat{\boldsymbol{\Gamma}}$ can be obtained by inverting Equation 3.4. The Kutta-Joukowski theorem (Equation 3.5) is then used to obtain the unsteady lift amplitude of the aerofoil. Multiplying this by $e^{i\omega t}$ gives the time-history of aerofoil loading as a response to harmonic gust forcing.

3.2.5 Correcting the frequency-domain wake for steady distortion

While the time-domain VLM has the ability to quantify the effects of wake shape and distortion on the aerofoil response to individual gust events, it has limitations. Because of the computational time requirement for sufficiently high-resolution cases, the time-stepping VLM is an impractical tool for carrying out a parameter sweep of unsteady response to a variety of gusts. For a thorough parameter sweep, it is necessary to use the frequency-domain model with a prescribed wake.

However, a small modification to the frequency-domain model allows for the inclusion of steady-state wake distortion when calculating the unsteady response. Unsteady wake

deformation cannot be included in the same way, as the wake shape would change at every time step. So, while the full distorting effects of the unsteady flow cannot be included in the frequency-domain VLM, an improvement can be made to the predictions by including the steady-state wake rollup.

To implement this change, the time-stepping code described in Section 3.2.3 is used to find the wake shape under steady flow conditions, using Equation 3.11b to generate the wake. The path of the resulting steady wake is then used as the prescribed wake shape for the unsteady frequency-domain model described in Section 3.2.4. Steady-state calculations have less stringent requirements on the wake resolution than unsteady calculations, and so the time-stepping case can be run with a coarser wake discretisation than the unsteady case, which saves time. The wake then needs to be "transferred" from the low-resolution, steady case to the high-resolution, unsteady case. This is done by considering the ratio of the time-domain time step to the implicit frequency-domain time step used in Equation 3.15. For example, if the time-domain value of the time step dt is twice as long as that of the implicit frequency-domain dt, each steady wake vortex is divided into two equal parts before being used in the unsteady model. This process is illustrated in Figure 3.6. Note that it is not necessary to have an integer ratio between the two time steps.

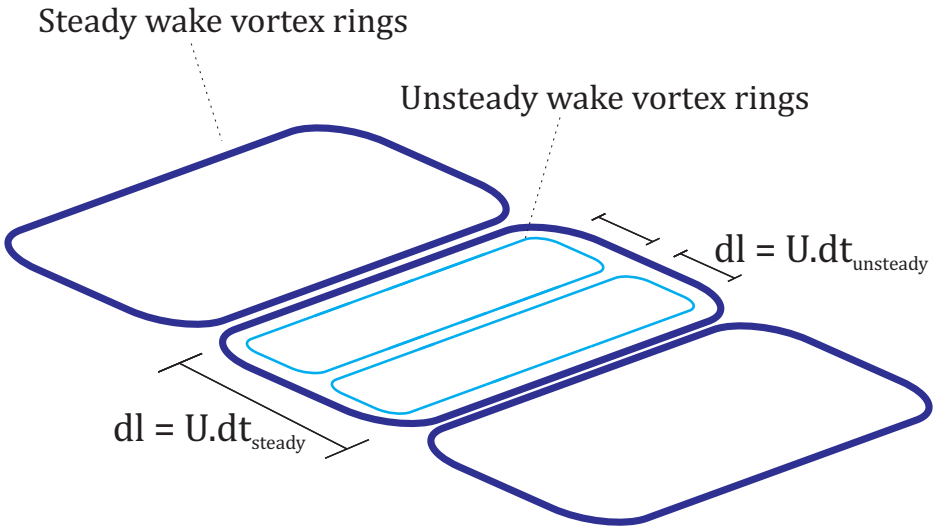

Fig. 3.6 Detail of the "transfer" process of the coarse time-stepping wake to the high-resolution frequency-domain wake. In this case $dt_{steady} = 2dt_{unsteady}$.

The increase in computational time required to implement the wake correction is minimal, as the wake only needs to be generated once for a given steady-state operating condition. The resulting wake shape can then be used for any type of gust by the frequency-domain solver.

3.2.6 Steady-state validation

In this section, the 3D VLM outlined above is validated against steady, 3D cases included by Katz and Plotkin in their book [64]. The validation cases include tapered, swept and rotating blades. These cases were themselves verified against experimental data by Katz and Plotkin. A summary of the results from the steady performance validation of the 3D VLM can be seen in Figure 3.7. In each case, data from the VLM is shown as dots, while the validation cases from Katz and Plotkin are given as lines.

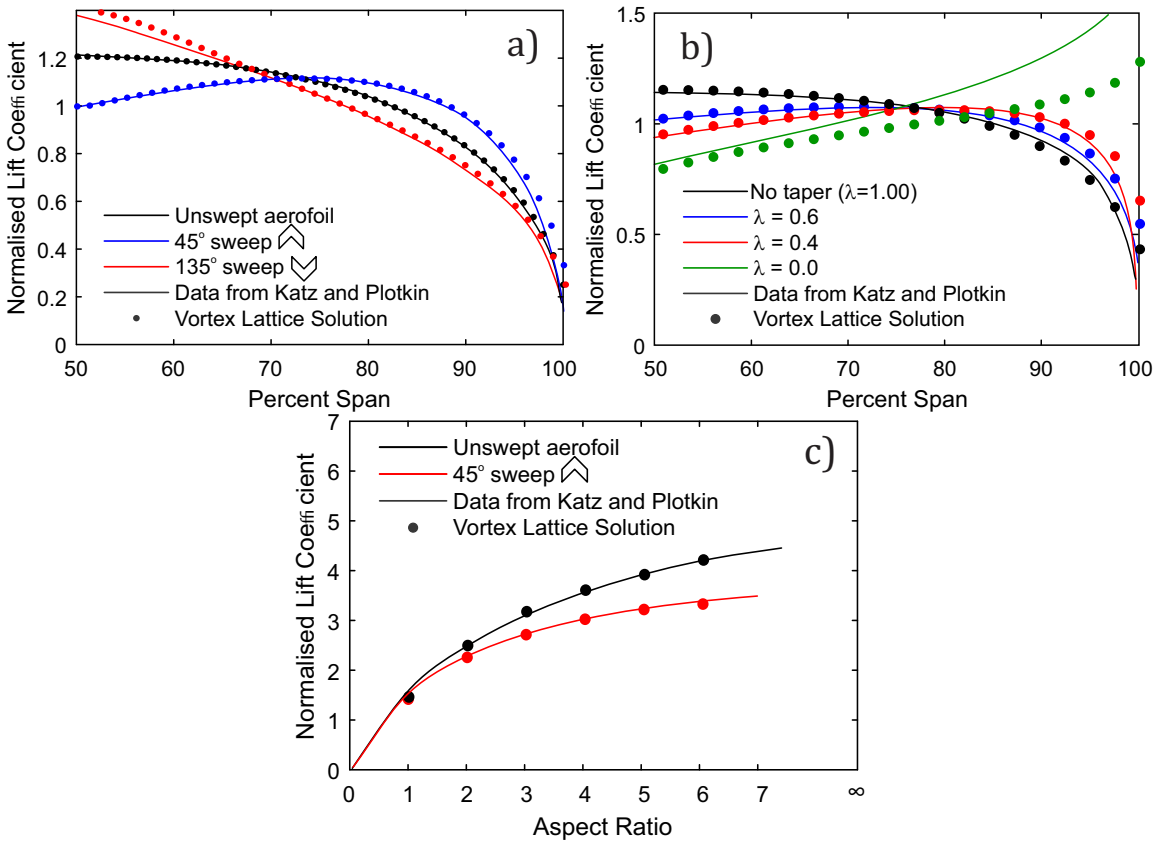

Fig. 3.7 Steady-state validation cases for the VLM code. Validation of (a) swept geometry, (b) tapered geometry, and (c) different aspect ratios. The validation data is obtained from Katz and Plotkin [64].

Figure 3.7a shows the spanwise lift variation of a wing with aspect ratio 4, at zero sweep, 45^o sweep, and 135^o sweep. Figure 3.7b shows the spanwise lift variation for a wing with aspect ratio 7.28 and with different taper ratios. Figure 3.7c shows the total lift coefficient of aerofoils with varying aspect ratio, at zero and 45^o sweep. In Figure 3.7a and b the lift coefficient is normalised by the spanwise average, while in Figure 3.7c the total lift

coefficient for each case is normalised by the angle of attack in radians (effectively giving the lift slope of each wing). The vortex lattice model generally agrees well with the test cases, in terms of both the total lift and the spanwise loading distribution. The only exception to this is at the limit of zero taper ratio ($\lambda = 0.0$, green line in Figure 3.7b). The panel method struggles to fully capture the solution as the chord length goes to zero. This is however a relatively extreme geometry for both turbine blades and aircraft wing geometries, and will not be considered in the present study. Because of this the tapered wing results in Figure 3.7b are satisfactory.

Katz and Plotkin [64] use an experimental test by Caradonna and Tung [16] to validate their time-stepping panel method on a rotor geometry. This has been replicated here using the frequency-domain VLM described in Section 3.2.4 and the time-domain VLM described in Section 3.2.3. The former is effectively a prescribed-wake VLM, assuming the wake to leave the trailing edge with the freestream velocity, whilte the latter is a free-wake VLM, using Equation 3.11b to generate the wake. The experiment was performed on a two-bladed rotor with a NACA 0012 aerofoil, which in the present study is modelled as a flat plate. The results of Katz and Plotkin are shown in Figure 3.8, along with results obtained from the prescribed-wake VLM and the free-wake VLM. The results are shown in two different operating conditions, and the lift coefficient is defined with respect to relative flow conditions at the blade tip.

Figure 3.8a shows the spanwise lift distribution of the rotor after it has started from a stationary position, and then rotated a quarter of a full rotation. As such, the wake has not had the time to develop, and its influence on the blade loading is reduced. In this case, the agreement between the validation data (solid line) and the prescribed-wake VLM (black dots) is good.

In Figure 3.8b, the spanwise lift distribution is shown when the rotor is in "steady hover" after several rotations, meaning that the wake is fully developed. The differences between the prescribed-wake (black dots) and free-wake (dashed line) solvers can be seen: the prescribed wake model predicts an approximately linear variation in lift along the span in the steady-hover condition. The free-wake VLM predicts a nonlinear increase, and is in much closer agreement with Katz and Plotkin (solid line). Note that the free-wake VLM results are only shown from 40% span because of numerical errors on the inboard sections; because the rotor wake is sucked towards the blades, the wake vortex segments come in close proximity with the blade lattice, causing unphysical spikes in loading to be predicted by the free-wake VLM.

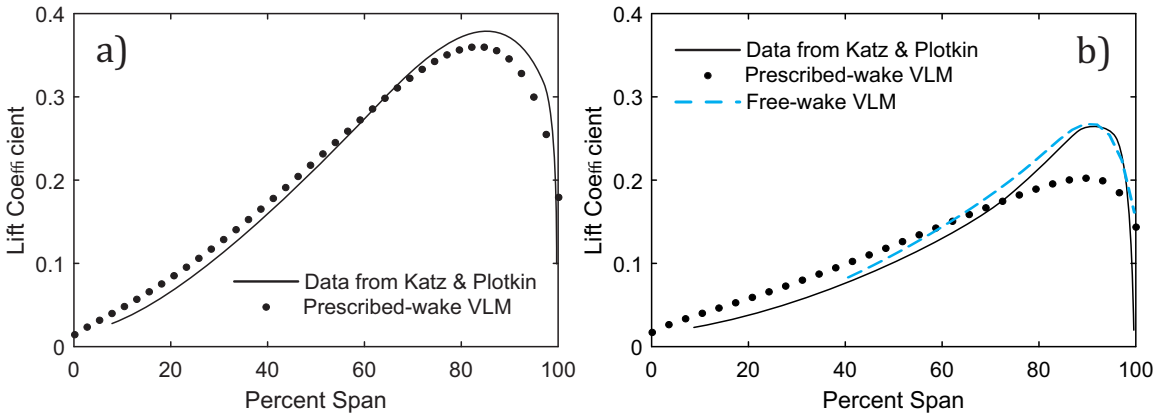

Fig. 3.8 Validation cases of a two-bladed rotor geometry. An impulsively started rotor that has (a) rotated a quarter of a full rotation, and (b) has reached fully-developed steady hover conditions.

This does not occur when the VLM is used for turbine modelling, as the mean freestream velocity ensures that the wake moves away from the turbine blades.

The discrepancy in the prescribed wake model in Figure 3.8b may be explained by the effect of vortex rollup, which is present in the experiments and is modelled by the free-vortex solver. In the case of a helicopter rotor configuration, wake rollup causes the wake to move inwards towards the axis of rotation, and therefore results in increased wake downwash in the mid-span region, reducing the loading in this region compared to near the blade tip. In the prescribed-wake vortex lattice method wake rollup is not modelled, and so a more linear variation in lift coefficient along the span is predicted. By including wake rollup, the time-stepping VLM code outlined in Section 3.2.3 is capable of capturing the nonlinear spanwise load increase.

3.2.7 Unsteady validation in 2D

There is no established analytic transfer function for predicting the unsteady load response of 3D geometries, as there is for 2D aerofoil sections. As such, the 2D frequency-domain VLM introduced in Section 3.2.4 is used to validate the unsteady response prediction of the VLM against classical 2D unsteady aerofoil theory. The unsteady load response predicted by the 3D VLM is validated against URANS simulation in Chapter 5 of this thesis.

Figure 3.9 shows the unsteady load response of a 2D flat plate undergoing sinusoidal gust forcing, as predicted by the VLM and the 2D Sears transfer function for sinusoidal gusts (introduced in Chapter 2 Section 2.5.2, given by Equation 2.7). Figure 3.9a shows the

normalised magnitude and Figure 3.9b the phase of the unsteady response. The magnitude has been normalised by the quasi-steady load response of a flat plate (given by $Cl = 2\pi\alpha$). Both magnitude and phase are shown against the reduced frequency (Equation 2.2, introduced in Chapter 2 Section 2.5.2). Figure 3.9 shows that the agreement between the 2D VLM and classical aerodynamic theory is good, confirming that the vortex lattice captures the relevant inviscid unsteady flow physics.

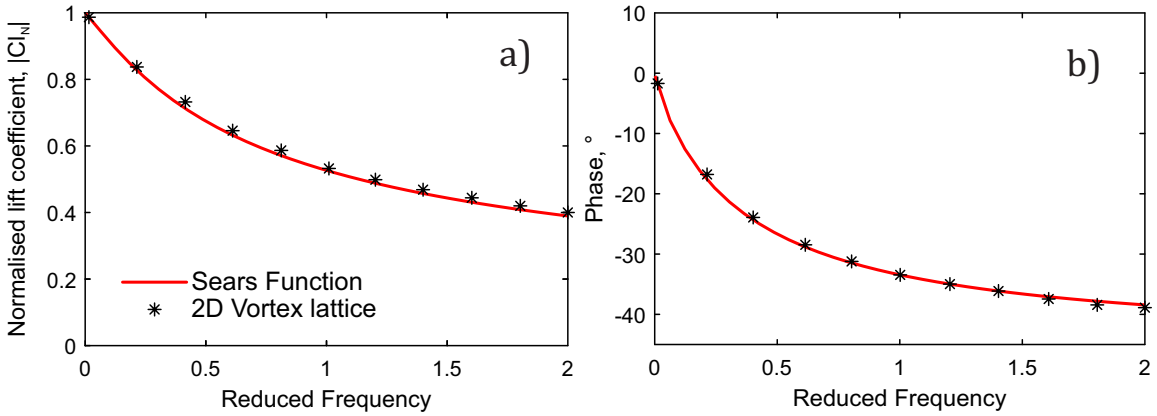

Fig. 3.9 Unsteady load response of a flat-plate aerofoil as predicted by the 2D VLM, validated against classical aerodynamic theory through the 2D Sears function. (a) Amplitude and (b) phase.

3.3 Viscous modelling: URANS

In order to validate the results obtained by the inviscid VLM, and to investigate the impact of viscous effects, nonlinear effects and stall, Unsteady Reynolds-Averaged Navier-Stokes (URANS) simulations were carried out using the open-source CFD software OpenFOAM. The simulations were performed on a single turbine geometry, based on a model turbine that has been used extensively for experimental work. The following sections outline the simulation software, the turbine geometry, the mesh, and the setup of the RANS simulations.

3.3.1 OpenFOAM

OpenFOAM (Open-source Field Operation And Manipulation) [53] is an open-source collection of precompiled $C++$ libraries for the numerical solution of partial differential equations, consisting of continuum solvers and data manipulation utilities. As such, it has a high degree of versatility, with a wide range of tools and user customisation available. It is also the most widely used open source CFD software, with dedicated conferences and an active

online community. It is used both in industry and academia, and is relatively common as a simulation tool in tidal power research. A wide range of solvers are available for a multitude of continuum problems, including multiphase, reacting flows, cavitation, compressibility, as well as more standard solvers for steady and unsteady flows. The choice of solver is governed by the flow properties of the case that is to be modelled. There is capability for RANS, URANS, LES and DNS, with a wide range of customisable settings and turbulence models available for each. With all this in mind, OpenFOAM was chosen to carry out the viscous modelling in this thesis, as it is a low-cost option with all the modelling capability of commercial software.

For the steady RANS simulations presented in this thesis, the solver "SRFSimpleFoam" was used, which uses the SIMPLE (Semi-Implicit Method for Pressure-Linked Equations) algorithm. SRF stands for "Single Rotating Frame", meaning that the solver operates in a single rotating frame of reference. The solver adds Coriolis and centripetal forces to the governing equations and computes all velocities in the relative frame.

The solver "pimpleDyMFoam" was used for the URANS simulations. The PIMPLE algorithm used in this solver is a combination of the PISO (Pressure Implicit with Splitting of Operator) and SIMPLE algorithms. For URANS simulations to run steadily, a limitation on the length of the time step is usually set by the Courant number, defined as:

$$C = \frac{u\Delta t}{\Delta x} \leq 1 \tag{3.17}$$

This condition states that the flow may not move further than the discretisation length of the computational domain in a single time step, to ensure stability. The PIMPLE algorithm, however, allows stable transient simulations at Courant numbers much larger than 1, by applying under-relaxation to each time-step until a certain convergence criterion is met, before allowing the time-step to complete with no applied relaxation factors. The letters "DyM" in the OpenFOAM solver stand for "Dynamic Mesh", meaning that the solver has moving mesh capability.

The turbulence model used throughout this study was $k\omega - SST$, which has been found in many previous studies to offer the closest agreement with experimental data for tidal turbine performance [114][127].

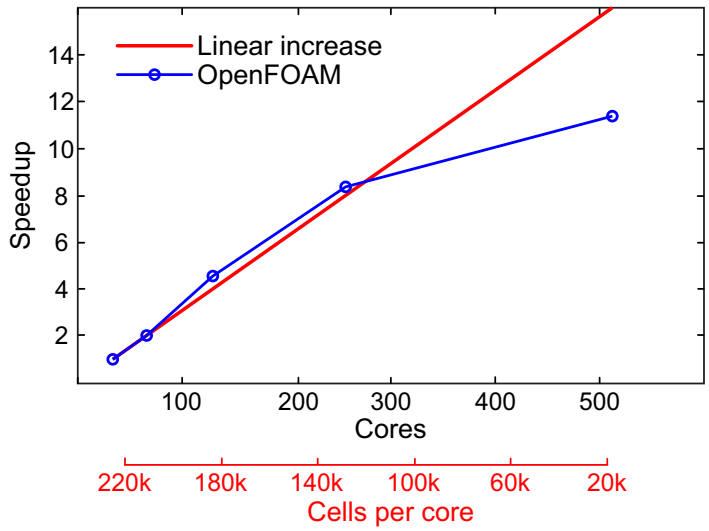

Fig. 3.10 Scalability check of OpenFOAM parallel simulation on multiple processor cores.

All simulations were performed on the Cambridge High Performance Computing cluster (Cambridge HPC), on the CSD3 cpu-cluster. A scalability check was performed to ensure that OpenFOAM had the ability to scale to multiple processors. Literature suggested that OpenFOAM had good scalability properties [27], and that speedup remained linear up to around 1,000 processors, beyond which performance would deteriorate[1]. This was verified by the scalability check, the results of which are presented in Figure 3.10. A preliminary mesh with around 7 million cells was tested for scalability, using the steady-state solver "SRFSimpleFoam". The results in Figure 3.10 verify the conclusions from literature that OpenFOAM does have good scalability properties, though in this case the limit is reached at between 300 and 500 cores. The scalability limit can also be expressed as the number of cells for each core (red axis) – approximately 100,000 cells per core in this case. Division of the computational space beyond this value did not result in any speedup benefit. As such, the number of computational cores used for the URANS simulations in Chapter 5 were chosen such that there was approximately 100,000 cells per core.

3.3.2 The turbine

Chapter 5 of this thesis consists of a study of the unsteady load response of a model tidal turbine geometry. The turbine on which the geometry is based has been used extensively in experimental studies of steady and unsteady turbine performance. It is a three-bladed horizontal axis turbine, 700 mm in diameter. The rated tip-speed ratio (TSR) – the ratio between the blade tip speed and the mean axial flow velocity – is 4. The mid-span Reynolds

[1] Cant, R. S., private communication.

Table 3.1 Summary of model turbine properties.

Parameter	Nomenclature	Value
Blade number	N_b	3
Diameter	D_t	700 mm
Hub radius	R_{hub}	55.5 mm
Tip-speed-ratio (rated)	TSR	4
Reynolds number, mid-span	$Re_{mid-span}$	130,000

number at rated TSR is in the order of 130,000. Further details of the design and performance of the turbine can be found in [141]. A summary of the geometry and operational features of the turbine can be found in Table 3.1. The blade section is representative of a typical tidal turbine design. The blade twist is such that the angle of attack distribution is in the order of 20^o at the hub and 9^o at the outboard blade section and near the tip.

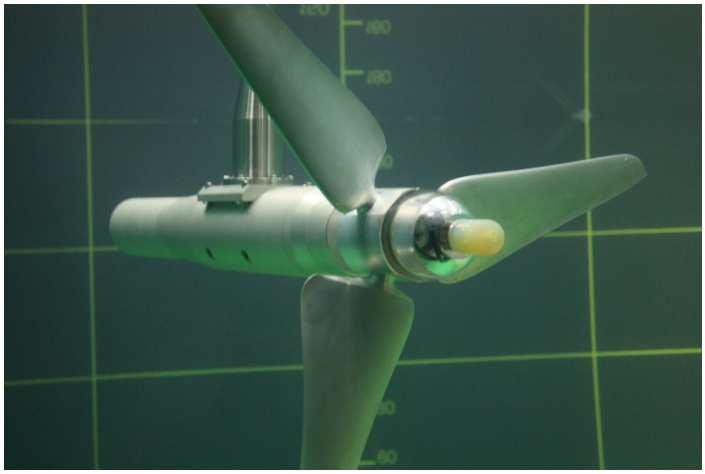

Fig. 3.11 The model tidal turbine (from [35])

The blades of the model turbine are attached to a nacelle and mounted on a support strut (see Figure 3.11). Neither the nacelle nor the support strut is included in the VLM or RANS modelling in this thesis, as the focus is on the interaction of unsteady flow with the blades. Therefore, the turbine thrust measured in experiments will not match that predicted by RANS or VLM, unless the thrust on the nacelle and support strut is estimated and added to the RANS and VLM predictions. This was done for the results shown in this section; the thrust on the nacelle was estimated by representing it as flow past a sphere of the same diameter, and the thrust on the support strut was estimated based on the drag of a cylinder. The thrust

was obtained from the following relation:

$$T = C_d 0.5 \rho V^2 A \tag{3.18}$$

Here the coefficient C_d represents the parasitic drag of the body, V the mean flow speed and A the wetted area of the body. The use of the mean flow speed is an approximation, since in reality the support strut will be partially immersed in the turbine wake, which reduces the incident flow velocity. Based on values of C_d obtained from [132], for the Reynolds number associated with the experimental tests, a correction thrust of 110 N was added to the RANS and VLM results. This improved the agreement of the steady-state RANS simulation with the experimental measurements, as will be shown in Section 3.4. Note that this additional thrust force, due to drag from the nacelle and support strut, supplies almost 50% of the total thrust coefficient at rated TSR.

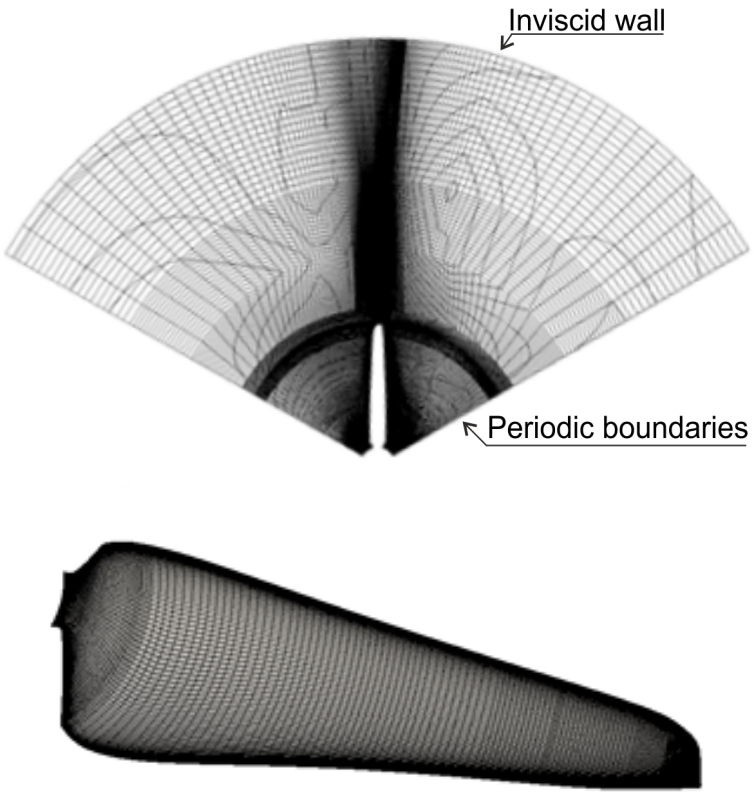

Fig. 3.12 Front-view slice of the 3D mesh, at the location of the turbine blade, and detail of the surface mesh of the blade.

3.3.3 The mesh

All meshes used for the simulations in this thesis were created using the meshing software Pointwise. OpenFOAM is a fully unstructured solver, but structured meshes were used throughout this work. This was due to initial tests suggesting that structured meshes gave more stable and accurate results than unstructured or hybrid meshes. Pointwise has the option of creating hybrid structured-unstructured meshes, with the necessary prism mesh around the aerofoil boundary layer merging into an unstructured mesh when sufficiently far away from the aerofoil. While efficient for meshing purposes, the interface between structured and unstructured meshes often resulted in highly skewed cells, causing solver instability. The total cell count was also repeatedly found to be lower for the structured mesh than that of unstructured or hybrid meshes with similar quality and mesh density criteria. This was a benefit of the structured mesh, as it had a lower computational cost as a result. For these reasons, a structured mesh was used for all the simulations shown here.

A single blade was modelled in a third of an annulus, using periodic boundary conditions on the circumferential boundaries in order to capture the returning wake effects from the remaining two blades. As explained above, the turbine hub and nacelle are not modelled, and the centre and far-field boundaries are modelled as inviscid walls (see Figure 3.12). The blade surface was modelled using the no-slip boundary condition. The mesh density is increased in the region of the tip vortex, and near the blade hub.

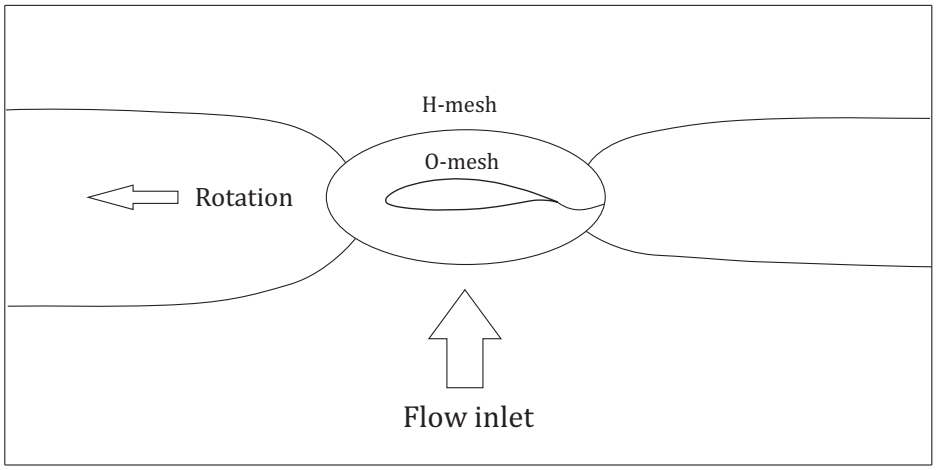

Fig. 3.13 Mesh structure of 2D annular blade section.

At the 2D annular level, the mesh structure is an H-mesh surrounding an O-mesh (see Figure 3.13). This configuration was chosen as it could deal with the significant change in

blade twist along the span, without creating highly skewed cells. OpenFOAM is notoriously sensitive to cell skewness, which causes the simulation to become unstable and crash without warning. Because of this sensitivity to cell skewness, the mesh was created using strict quality controls for this metric.

The required chordwise aerofoil resolution and $y+$ value were determined through 2D simulations of a representative blade section. The pressure coefficient and lift characteristic were compared to results from MSES [30]. MSES solves the Euler equation in 2D, modelling the flow as inviscid and incompressible but coupled to a boundary layer formulation through the displacement thickness, in order to simulate viscosity. It is also possible to apply a trip at a specified location on the aerofoil in order to create a turbulent boundary layer, which was done at the leading edge for the validation cases used in this section. MSES has itself been extensively validated against 2D NACA aerofoil data, and is widely used in the aerospace industry as a baseline tool for predicting steady aerofoil behaviour. This makes it a suitable validation tool.

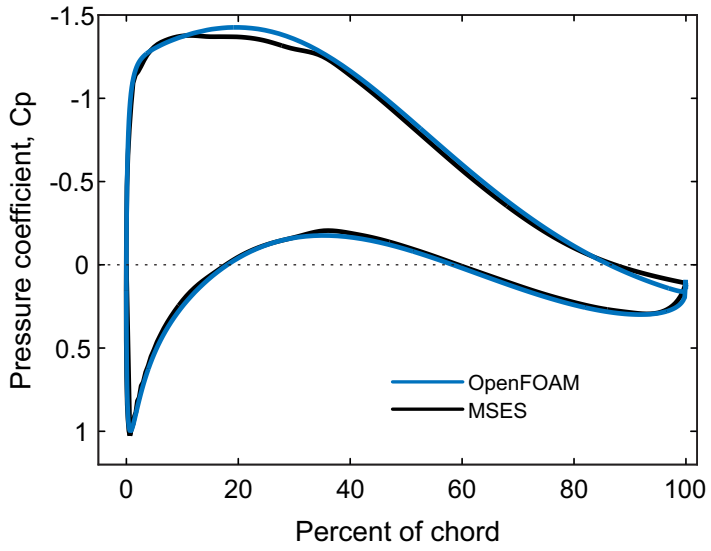

Fig. 3.14 Pressure coefficient distribution of the 2D aerofoil, as predicted by MSES and OpenFOAM, at 5^o angle of attack.

Using a $y+$ value of 60 in the 2D OpenFOAM simulation gave good agreement with the pressure coefficient predicted by MSES in pre-stall conditions, and was found to be a good compromise between accuracy and computational cost. $Y+$ values of 30 and 120 were also trialled, and did not significantly change the pressure coefficient in pre-stall conditions. Using a $y+$ value of 120 somewhat reduced the ability of the solver to predict stall initiation.

As such, a $y+$ value of 60 was chosen for the final 3D mesh, with wall functions to simulate boundary layer effects. Figure 3.14 shows the chordwise pressure coefficient distribution for the chosen $y+$ value of 60, at 5^o angle of attack, using wall functions to model the boundary layer. It can be seen that the agreement is good on both surfaces of the aerofoil (trial cases were also performed using a $y+$ value less than 1, with no wall functions, but were not considered for the final 3D mesh due to computational cost).

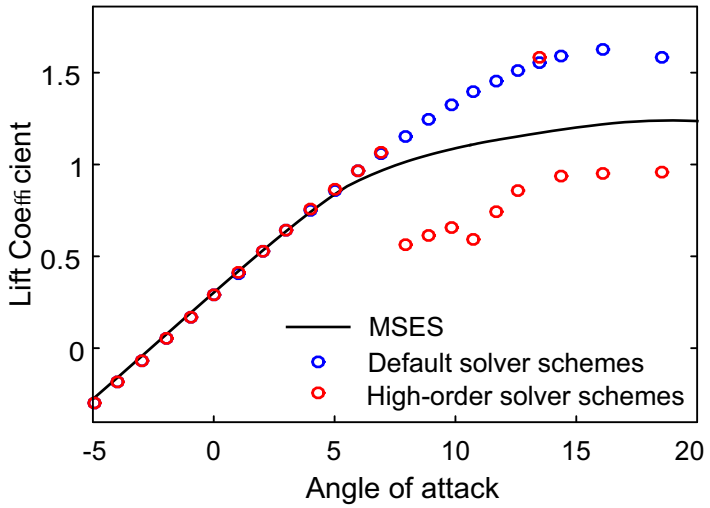

Fig. 3.15 Validation of the 2D lift curve, using OpenFOAM solver "SRFSimpleFoam" with different discretisation schemes.

The relatively large thickness of the aerofoil used means that it stalls via trailing edge separation, which creates a gradual loss of lift at high angles of attack. This gradual lift reduction can be seen in the steady lift characteristic predicted by MSES in Figure 3.15 (black line). This is chosen intentionally for tidal turbines, as this results in more favourable operation in stall conditions. However, this gradual trailing edge stall was not captured well by the standard solver discretisation schemes used in OpenFOAM. The blue circles on Figure 3.15 show the aerofoil performance with the default settings. It can be seen that the flow remains attached at higher incidence angles than predicted by MSES.

OpenFOAM allows for customisable functions for the time, gradient and divergence discretisation. In theory, higher-order discretisation schemes will give more accurate solutions. The results obtained using higher-order discretisation schemes are shown as red circles on Figure 3.15. It can be seen that these higher-order schemes capture the angle of attack at which stall begins, but not the lift curve beyond this point: the high-order solver schemes predict an abrupt loss of lift while MSES shows a gradual decline. For the simulations

presented in the rest of this thesis the default OpenFOAM solver schemes were used, as they were more stable (see Table 3.2 for the default schemes chosen). As such, it is important to know that the 3D RANS calculations are likely to predict the flow to remain attached at higher incidences than the experimental results.

Table 3.2 Summary of the default discretisation options chosen for the 3D OpenFOAM simulations.

Discretisation variable	Chosen option	Description
Time	Euler	1st order scheme, used for unsteady simulations.
Gradient of velocity, pressure and turbulence variables	Linear	Central differencing method, second order.
Divergence of velocity	Linear Upwind, bounded	Second order with an upwind bias.
Divergence of turbulence variables	Limited Linear, bounded	Second order, limiting towards upwind in regions of rapidly changing gradient.

Chordwise resolutions of 100 and 140 cells on both the pressure and suction surfaces were tested and were shown to give similar results in terms of both steady and unsteady lift response. In the final 3D mesh the pressure and suction surfaces each have 110 cells. The trailing edge is round and has 12 cells. A spanwise cell count of 79 was used, with cells clustered toward the hub and tip, in order to capture the more complex flows in these regions. Doubling the number of spanwise cells was shown to make no difference to the steady performance of the turbine.

A study was carried out to determine the appropriate inlet and exit lengths of the computational domain. Starting with inlet and exit sections with lengths equal to 1 turbine diameter each, the exit section was gradually extended until the change to the turbine performance was less than 1% compared to the previous simulation. The same procedure was repeated for the inlet section. This resulted in an inlet length of two turbine diameters and an exit length of 4 turbine diameters, relative to the blade-centred block (see Figure 3.16 for illustration of the computational domain). This was a compromise between performance and computational

cost. The radial domain distance is 2.8 turbine diameters, chosen based on the depth of the test tank at Ifremer in Bologne, France, where the experimental testing of the model turbine was performed. The total cell count of the final mesh used is approximately 17 million.

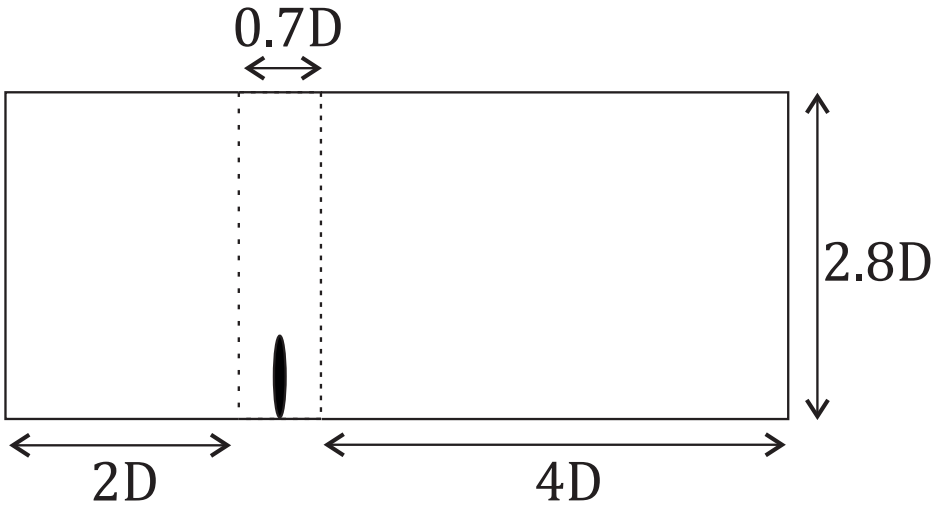

Fig. 3.16 Computational domain

A concern on generating the final 3D mesh was the effect of reflected pressure waves from the exit plane when running unsteady gust simulations. This can occur if there is insufficient distance between the rotor plane and the exit boundary. However, there was no sign of such interference during simulation, meaning that the exit boundary was placed at sufficient distance from the blade.

3.4 Steady performance validation – URANS and VLM

In this section the steady performance of the turbine as predicted by the RANS CFD and the VLM is validated against experimentally measured data. The performance is shown in terms of the turbine power and thrust coefficients. The power coefficient is defined as:

$$C_p = \frac{Q\Omega}{0.5\rho U_\infty^3 A} \tag{3.19}$$

Here Q is the turbine torque, Ω is the rotational speed in radians per second, U_∞ is the mean axial flow speed and A is the swept area of the turbine. The power coefficient is a measure of how well the turbine extracts energy from a given swept area in the tidal flow. The thrust

coefficient is given by:

$$C_t = \frac{T}{0.5\rho U_\infty^2 A} \tag{3.20}$$

where T is the thrust. Generally, turbine designers aim to minimise the thrust coefficient for a given power coefficient, as a large amount of thrust is detrimental to the longevity of the turbine support structure. Both torque and thrust are relevant for fatigue life calculations, and so both will be considered in this thesis.

Figure 3.17 shows the steady power and thrust coefficients for the turbine. The black line shows the experimentally measured performance. The agreement between the experimental data and the steady RANS simulation (green circles) is good at the rated TSR of 4. The results then deviate at higher and lower TSR. There are a several potential reasons for this discrepancy. As illustrated in Figure 3.15, the stall characteristics of the aerofoil are not captured accurately in the CFD simulation. The flow tends to remain attached at higher angles of attack, which leads to over-prediction of the torque at low TSR, as observed in Figure 3.17a. The reason for the discrepancy at high TSR is not as clear, but may be caused by the absence of a turbine nacelle in the RANS simulation, which would cause further turbine losses. However, the agreement around the rated TSR is deemed sufficient for the simulations done in this thesis: the largest amplitude gust considered in Chapter 5 is 15% of the axial freestream velocity. This results in the TSR varying between 3.48 and 4.7. Figure 3.17 shows that the agreement between RANS and experiments in this TSR range is acceptable.

The dark blue line in Figure 3.17a shows the performance predicted by the prescribed-wake VLM, assuming that the wake leaves the trailing edge with the freestream velocity (i.e. no wake distortion or rollup effects are included – Equation 3.11a). The predicted TSR of peak power is similar to the RANS and experimental results, but the magnitude is over-predicted. The light blue line shows the steady performance as predicted by the time-stepping VLM, using the free-wake model that allows for wake rollup and distortion (using Equation 3.11b). As mentioned above in Section 3.2.3, the mean flow slows down in the turbine shadow, leading to the wake remaining close to the turbine for longer. This causes the wake vorticity to exert more of an influence on the turbine loading (a phenomenon known as 'aerodynamic damping'), and thus reduces the power coefficient.

There is still remaining discrepancy between the VLM and the experimental and RANS results, even when using the VLM that includes wake rollup. This can be largely attributed

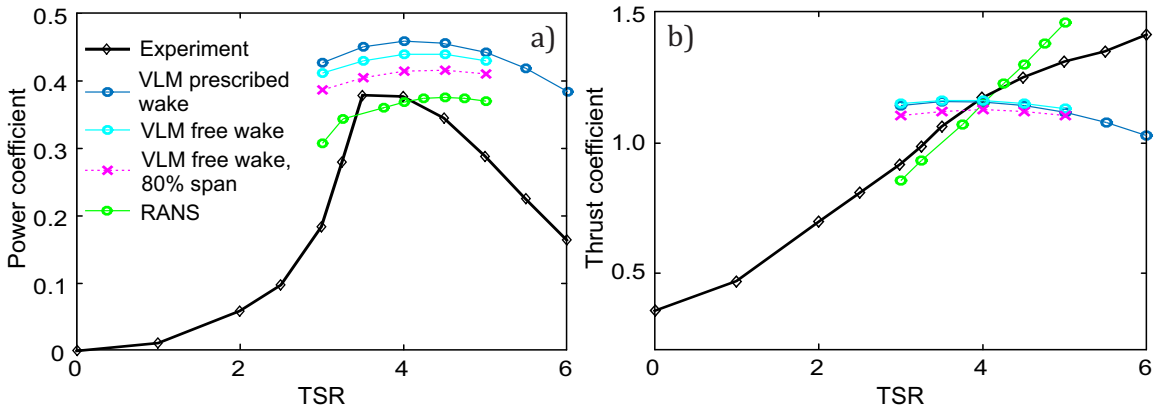

Fig. 3.17 Steady performance of the turbine, as predicted by prescribed-wake VLM, free-wake VLM, and RANS simulation. (a) Power coefficient, and (b) thrust coefficient. The results are compared to experimental measurement.

to the inability of the VLM to capture aerofoil stall. The angle of attack in the hub region of the turbine is very high, in the order of 20-30^o even at rated TSR. The inviscid model will predict very large power generation at such high incidence angles, which is not physical. The pink line in Figure 3.17a shows an estimate of the discrepancy caused by the lack of hub stall in the panel method. It includes only the power and thrust generated over the outermost 80% of the blade span. This characteristic does give a closer agreement with the RANS results. Doing the equivalent to the RANS results, neglecting the innermost 20% of the span, reduces the power coefficient by less than 1% (this is not shown in Figure 3.17, as it does not make a visible change to the power curve). This illustrates that a substantial proportion of the discrepancy between the vortex lattice method and CFD is attributable to the lack of stall in the inviscid code.

The low Reynolds number of the experiments and CFD simulations may also contribute to the discrepancy between these and the inviscid VLM results. The higher the Reynolds number in a real flow, the more accurate an inviscid estimate of aerofoil performance in the flow will be. Since the Reynolds number in the simulations and experiments is only in the order of 130,000, this may be the cause of the remaining discrepancy between these and the VLM results.

The steady thrust coefficient is shown in Figure 3.17b. The correction parameter described in Section 3.3.2 has been included in the RANS and VLM calculations, to account for the support strut and nacelle, which are not simulated. With this correction the agreement of the RANS simulation with the experiment is good. The inviscid VLM, while accurate at

rated TSR, shows a different trend from both the RANS simulation and the experiment. This is expected, as the viscous terms will significantly affect the steady thrust, especially at off-design conditions; at lower TSR values the angle of attack across the span will increase, meaning that the inviscid code (which cannot capture flow separation) will predict large thrust. As the TSR increases, the angle of attack along the span decreases, reducing the thrust. This is different from the experimental results and viscous simulations, since in these the flow will separate at low TSR, predicting a lower thrust that will then increase as the TSR is increased. This is the likely reason for the difference in the viscous and inviscid results in Figure 3.17b.

3.5 Summary

A summary of the computational models used in this thesis has been provided. First the inviscid vortex lattice models (VLMs) were described, and the differences between the frequency-domain and time-domain models were outlined. Validation of the 3D model was performed against steady baseline cases for swept and tapered wings at different aspect ratios, and for a rotor geometry. The 2D VLM was used to validate the unsteady response against predictions by classical aerofoil theory. The agreement was good throughout, and as such the various VLM codes will be used extensively in the coming chapters to provide insight into the 3D effects on unsteady hydrodynamic response.

The RANS simulations used in this study were also introduced, and the capabilities of the open-source CFD software OpenFOAM were described. The properties and geometry features of the model tidal turbine used in Chapter 5 were outlined, followed by the step-by-step development of the 3D turbine mesh. This included mesh sensitivity studies on 2D aerofoil section mesh resolution, spanwise mesh resolution, and inlet/outlet domain length. The final mesh models a third of an annulus of the turbine, with periodic boundaries to include the effects of the remaining two blades.

Finally, the steady performance of the model turbine as predicted by RANS simulation was validated against experimental data, and compared to the VLM results, and the sources of disagreement discussed. As the RANS simulation was capable of capturing the turbine blade performance at the design point, the resulting 3D mesh forms the basis of the viscous simulations in Chapter 5.

Chapter 4

The effect of 3D geometry on unsteady gust response

4.1 Introduction

When estimating the unsteady loads experienced by a tidal turbine during its lifetime, designers will generally rely on strip-theory methods combined with 2D models of unsteady aerofoil loads. The assumption of locally 2D flow has however not been verified for tidal turbines, and is unlikely to apply [139]. While the study of attached, 2D, unsteady flow is a mature field, the effect of significant 3D flow and geometry features on unsteady aerofoil loads is not well understood. This chapter explores the effects of 3D geometry on unsteady load response, and how it differs from predictions made by classical 2D aerofoil theory.

For attached flow, the physics underlying unsteady load response can be fully captured by inviscid modelling: the aerodynamic damping of the unsteady vortical wake and the added mass force are the primary sources of deviation from the quasi-steady lift [75], and both of these can be modelled inviscidly. The unsteady flow response is driven by the interaction of the aerofoil with its own wake; in 2D unsteady flow, the aerofoil sheds vorticity in response to the changing angle of attack, which in turn induces a downwash velocity at the aerofoil leading edge. In 2D, the wake vorticity vector is aligned with the spanwise co-ordinate of the aerofoil. One of the primary differences between 2D and 3D flow is that in 3D there is also a streamwise vorticity component in the vortical wake. In addition to this, the spanwise wake vorticity is finite in length, ending when the aerofoil span ends. It will be shown in this chapter that these two aspects of 3D aerofoil geometry result in significant deviation from

the load response predicted by 2D theory.

The modelling presented in this chapter is carried out using the frequency-domain vortex lattice model (VLM) with a prescribed wake, as described in Chapter 3, assuming the wake to leave the trailing edge with the steady freestream velocity. The results are then compared to predictions obtained using unsteady transfer functions obtained from classical 2D aerofoil theory (introduced in Chapter 2, Section 2.5).

The goals of this chapter are to illustrate the primary differences between the unsteady flow response of 2D and 3D aerofoils, and to identify the relevant geometry parameters governing the deviation from 2D response.

4.2 3D geometry considerations

In this section, the key departures from 2D behaviour introduced by 3D geometry will be discussed in turn. They are: the wake downwash, the spanwise variation in reduced frequency and the returning wake.

4.2.1 Unsteady wake downwash in 3D

When the angle of attack of a 2D aerofoil changes with time, a vortical wake is generated in response, consisting of vortices with circulation equal and opposite to the change in aerofoil circulation. This unsteady vortical wake induces a downwash on the aerofoil. This downwash acts to counteract the unsteady change in incidence, and thus provides damping to the unsteady load response. In the case of a step change in angle of attack, this results in a transient change in blade loading that stabilises to the new steady value over time. For harmonic angle of attack variation the wake damping works to reduce the amplitude of the oscillating load. In a 2D system the unsteady wake can be represented as a series of point vortices, which are equivalent to vortex lines running parallel to the trailing edge of the aerofoil: the direction of the vorticity vector is in the spanwise direction relative to the aerofoil (see Figure 4.1). In a 2D system this vector extends to infinity with constant circulation strength.

Inherent to a 3D aerofoil, with finite span and geometry variation in the spanwise direction, is the presence of streamwise wake vorticity, even in steady flow conditions. The pressure difference between the upper and lower aerofoil surface means that a finite aerofoil will always have flow moving in the spanwise direction: towards the tip on the pressure

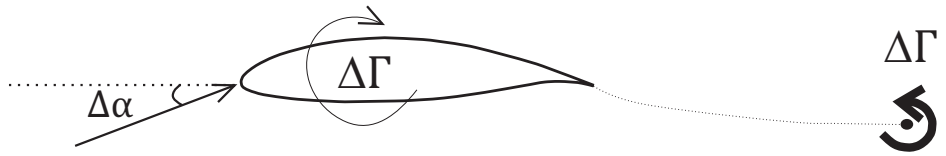

Fig. 4.1 Illustration of how a step change in angle of attack results in a vortex being shed from the aerofoil.

surface and away from the tip on the suction surface. This results in a flow circulation pattern, and in the generation of a vortical wake where the vortex vectors point in the streamwise direction relative to the aerofoil (see Figure 4.2 for an illustration).

For a finite, 3D aerofoil, the streamwise wake vorticity will contribute a further downwash component and thus reduce the loading, even in the steady state. A variety of corrections are available for use in 2D strip-theory methods to adjust the aerofoil lift as a result of this additional downwash. One of the most common of these for tidal turbine modelling is Prandtl's tip loss correction [45]. There is however no established theory that describes how this streamwise wake vorticity behaves in unsteady flow conditions. The purpose of this chapter is to investigate the role of the streamwise wake vorticity in unsteady hydrodynamic loading, and to find the flow and geometry parameters that determine the extent of its influence.

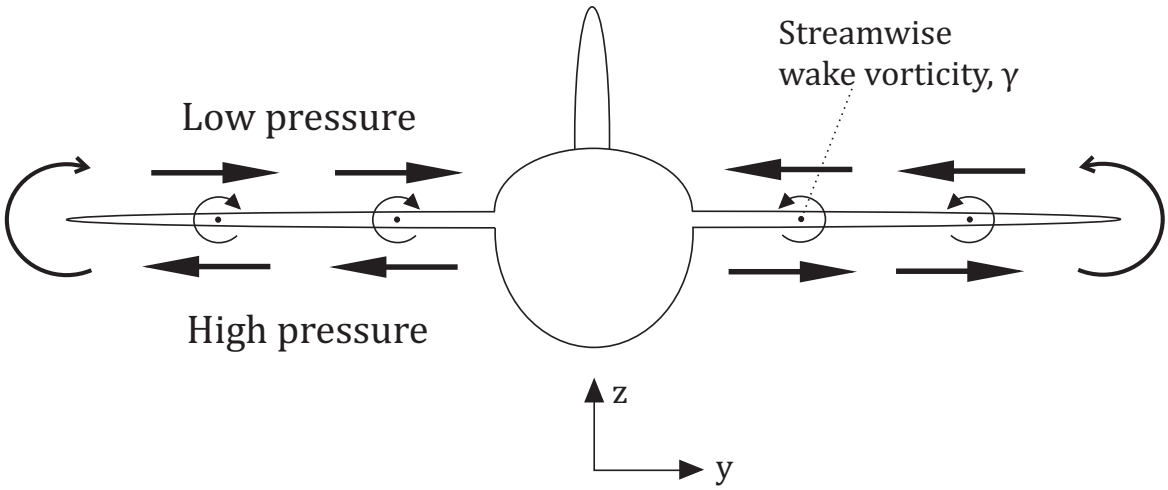

Fig. 4.2 Illustration of the generation of streamwise wake vorticity on a finite-wing geometry.

Figure 4.3 shows a simplified illustration of the 3D vortex lattice model introduced in Chapter 3, which is used to carry out the analysis in this chapter. The model consists of a lattice of vortex rings, which give the aerofoil its lifting properties and make up the building blocks of the vortical wake. Figure 4.3 shows how the streamwise and spanwise components

of the wake vorticity are defined throughout this chapter. The downwash induced by the unsteady wake is calculated using the Biot-Savart law (Equation 3.8 in Chapter 3) applied separately to the streamwise and spanwise components of the wake vorticity. In this way the distinct influence of each wake component can be quantified.

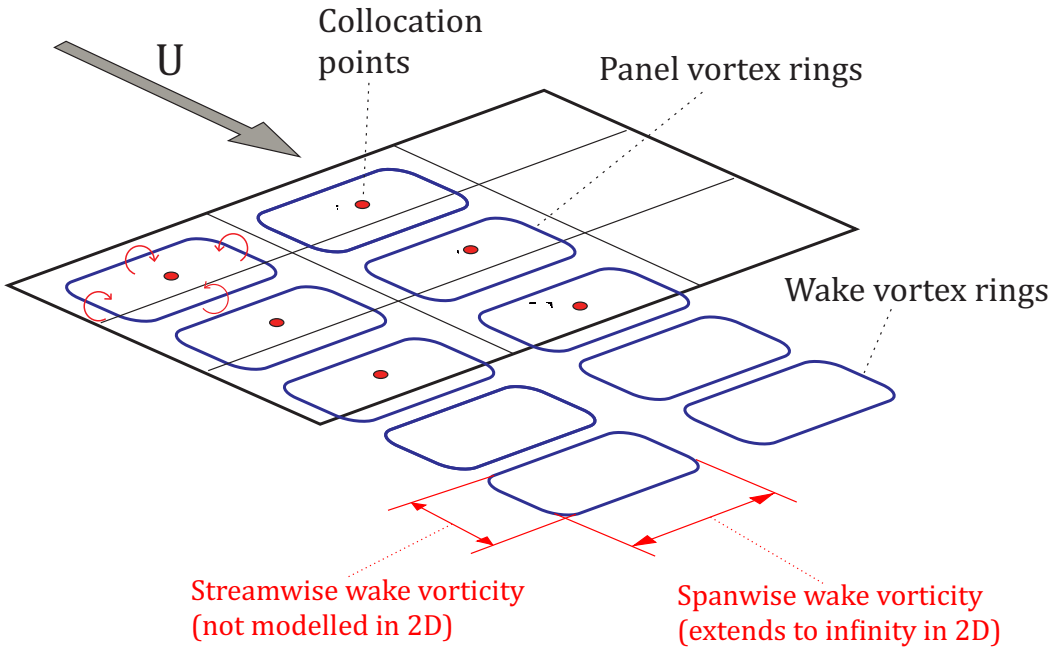

Fig. 4.3 Simplified view of the vortex lattice model, illustrating the difference between spanwise and streamwise wake vorticity.

Figure 4.3 also shows the other important change to the wake between 2D and 3D aerofoils: the spanwise component of the wake vorticity is finite. In 2D analysis this wake component is assumed to extend infinitely in each direction, at the same circulation strength. This is not the case in a 3D finite-aerofoil system, where the spanwise wake component of vorticity ends where the aerofoil ends. The finite nature of the spanwise wake vorticity will result in deviation of unsteady load response from the 2D prediction, since the wake downwash from a finite wake is different from that of an infinite wake. This will be shown in Section 4.4 of this chapter.

4.2.2 Spanwise variation in reduced frequency

For harmonically oscillating flow, the established non-dimensional parameter that governs the unsteady aerodynamic response is the reduced frequency, k, which is defined as:

$$k = \frac{\omega c}{U} \tag{4.1}$$

Here ω represents the gust time-harmonic frequency, c is the local aerofoil chord, and U is the local flow velocity in the aerofoil frame of reference. For rotating geometries, U is the relative velocity at a given blade section. The reduced frequency is effectively a measure of how many chord lengths a fluid particle travels during a gust wavelength, and has repeatedly been found to be the dominant parameter in determining the properties of unsteady flow in 2D [75]. However, it has not been firmly established whether this formulation of the reduced frequency is an appropriate choice for a 3D geometry.

As stated above, the reduced frequency is defined by local values of chord length and relative velocity. This means that for a rotating geometry, or an aerofoil with significant spanwise geometry changes, the reduced frequency will vary along the span. In this chapter the applicability of the local 2D reduced frequency to a 3D system is investigated.

4.2.3 Returning wake

The inclusion of returning wake effects for rotating systems is vital for the accuracy of unsteady models, as was shown by Sequeira and Miller [115] in their 2D study of the applicability of classical aerofoil theory to tidal turbines. This is also true in 3D systems.

In an application where a wing is rotating, such as a helicopter or a tidal turbine, the wake forms a helical shape downstream of the aerofoil and therefore comes back into close proximity with the aerofoil N_b times per revolution (where N_b is the number of blades on the rotor). When the flow interacting with a rotating system is unsteady, a "resonance" condition can appear in the wake, where the downwash from successive returning wake sheets either reinforce or counteract one another. The concept of a returning wake was introduced in Chapter 2 section 2.5.2.

As mentioned in Chapter 2 (Section 2.5), in classical aerofoil theory there are several unsteady transfer functions, each applicable to a specific type of gust. For example, the Theodorsen function is used for gusts acting uniformly across the aerofoil chord, while the

Sears function is developed for sinusoidal gusts. In 2D theory the returning wake can be accounted for by using the Loewy function (Equation 2.10) as a correction to the Theodorsen function (Equation 2.3). There is however no equivalent to the Loewy function correction for other unsteady transfer functions, which may significantly reduce their applicability to rotating systems.

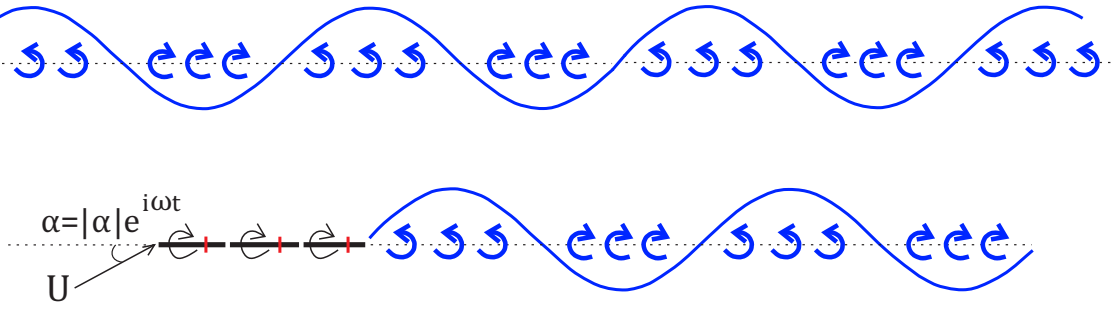

Fig. 4.4 Illustration of the returning wake in a 2D framework.

In their study of the applicability of classical unsteady aerofoil theory to tidal turbines in a 2D framework, Sequeira and Miller [115] noted a discrepancy between the unsteady response to a sinusoidal gust as predicted by the Sears function and their URANS simulations. While they proposed that this may be due to distortion of the gust by the aerofoil potential field, the absence of a returning wake in the Sears function was also a likely cause of this discrepancy.

The versatility of the VLM code used in this thesis allows it to calculate the load response of a 2D aerofoil undergoing sinusoidal gust forcing, including the effect of the returning wake. An illustration of the returning wake as modelled in the 2D VLM is shown in Figure 4.4. Using the 2D form of the VLM described in Chapter 3 (Section 3.2.4), the unsteady flow interaction studied by Sequeira and Miller [115] has been replicated. The results are shown in Figure 4.5, in terms of the normalised amplitude of the unsteady lift coefficient at design incidence. The lift coefficient has been normalised by the gust amplitude. The 2D VLM (blue circles) has a much closer correspondence to the URANS results (black stars), compared to the Sears function (red line). This shows that the absence of returning wake corrections for 2D unsteady transfer functions can have a significant detrimental effect on their accuracy. As gust distortion is neglected in both the 2D VLM and the Sears function, the increase in accuracy with the VLM is not due to this effect.

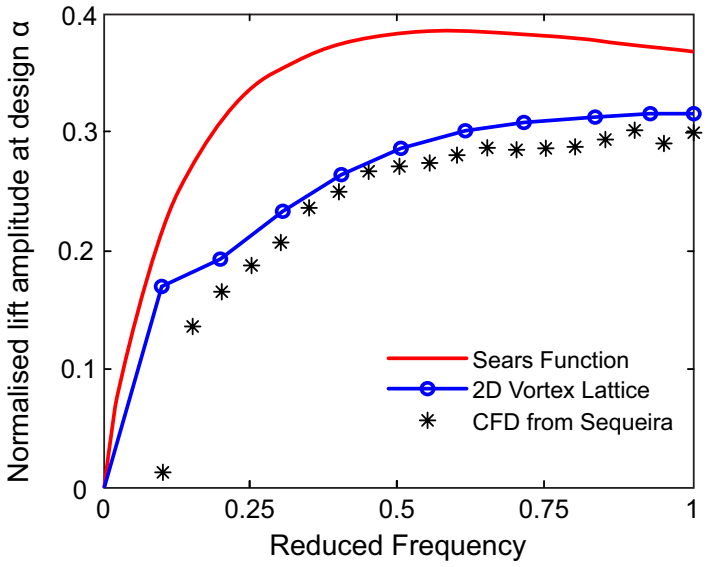

Fig. 4.5 The results from URANS simulations obtained by Sequeira and Miller [115] (reprinted with permission) for the response of a 2D tidal turbine aerofoil to a sinusoidal gust, compared to prediction by the Sears function and the 2D VLM. The latter includes returning wake effects.

While returning wake models have been included in some 2D transfer functions, their applicability to 3D geometries is unknown. The Loewy function was initially developed to predict the unsteady aerodynamic forces on helicopter blades. These have very high aspect ratios, which makes it likely that 2D assumptions hold along a majority of the span. It is not known whether a fully three-dimensional system responds differently to the returning wake, compared to a 2D system. As such, this chapter aims to assess whether the Loewy function is capable of predicting the wake resonance conditions for a 3D rotating system.

4.2.4 Chapter objectives

In light of the key differences between 2D and 3D geometries highlighted above, this chapter aims to:

1. Show how the presence of streamwise wake vorticity and the finite nature of the spanwise wake vorticity affect aerofoil response to unsteady gusts.

2. Investigate whether the local reduced frequency is an appropriate parameter for quantifying the response of a 3D aerofoil.

3. Assess whether the Loewy function is capable of capturing wake resonance in a rotating 3D system.

4. Find the geometric parameters governing the degree of deviation from 2D aerofoil theory.

These objectives will be met in the following sections by studying the response of a range of aerofoil and rotor geometries to unsteady gust forcing, using the 3D VLM introduced in Chapter 3 (Section 3.2.4). A prescribed wake model is used throughout, assuming that the wake leaves the trailing edge with the steady freestream velocity (the effects of wake distortion will be discussed in Chapter 5).

4.3 Test cases

4.3.1 Geometry

Figure 4.6 illustrates the geometries that will be used in the following sections. In all cases, the aerofoil section is a flat plate and the mean incidence is zero. The first case studied is a uniform finite wing, followed by tapered and swept wings. Finally, a single, rotating flat plate is considered. Between them, the cases show the influence of different geometry features on the wake, and therefore on the unsteady response.

Note that whenever reduced frequency is given (Equation 4.1), it is defined with respect to local conditions, using the local relative velocity and local chord length at the given spanwise position, unless otherwise specified. Exceptions will be made in some cases for the rotating geometries, where the reduced frequency at mid-span is sometimes used as reference, in which case this is clearly labelled as "mid-span reduced frequency". For the swept wing in Figure 4.6c, the local chord length is defined as the chord line parallel to the steady incident flow. This means that its spanwise reduced frequency distribution is the same as that of an unswept wing with the same aspect ratio, and is constant along the span for both swept and unswept geometries. For rotating geometries, the local chord length is defined to be the same as a non-rotating blade with the same planform.

4.3.2 Gusts

In order to isolate the effects of 3D geometry, none of the unsteady gusts applied to the aerofoils in this chapter have any spanwise variation, i.e. they are "spanwise uniform" throughout. If applied to an infinite and uniform wing, the response to these gusts would be fully predicted by 2D theory at any spanwise location. Two types of gusts are applied: uniform gusts and sinusoidal gusts. The former acts uniformly over the aerofoil chord, and

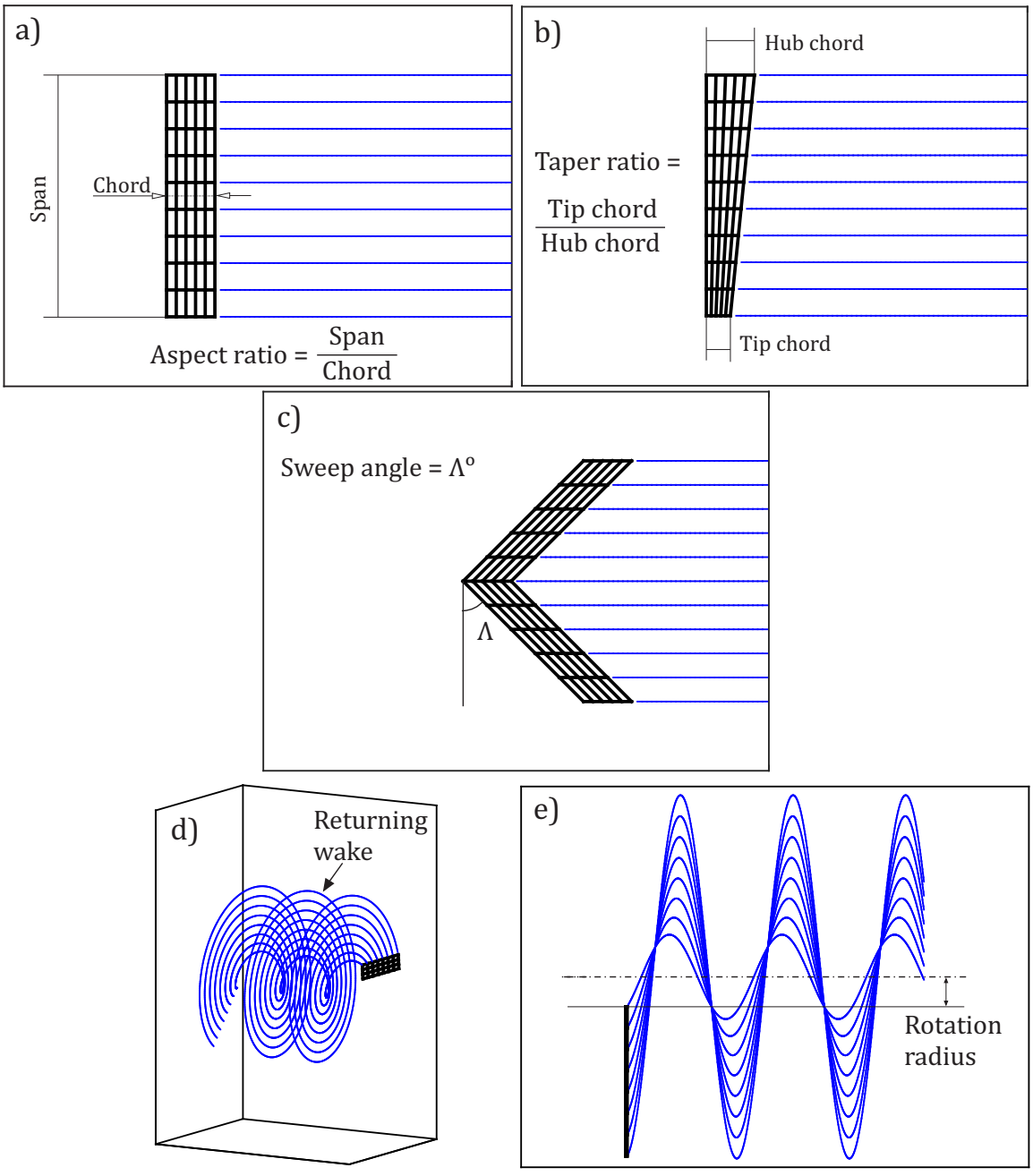

Fig. 4.6 The geometries used for the analysis of 3D unsteady load response in this chapter. (a) Finite wing, (b) tapered wing, (c) swept wing, (d & e) rotating flat plate.

the latter has a sinusoidal variation spatially. The velocity variation due to the uniform gust is given by:

$$v = \eta U_\infty e^{i\omega t} \tag{4.2}$$

Here η gives the amplitude of the oscillating gust velocity, as a fraction of the steady freestream velocity U_∞. The velocity variation due to the sinusoidal gust is given by:

$$v = \eta U_\infty e^{i\omega(t-x/U_\infty)} \tag{4.3}$$

Both gusts are always modelled as acting in the transverse direction relative to the aerofoil. For rotors this is achieved by making the gust oscillate in the same direction as U_∞, in the direction of the axial freestream. Relative to the rotational reference frame this results in a gust that is approximately transverse to the aerofoil (see Figure 4.7 for an illustration).

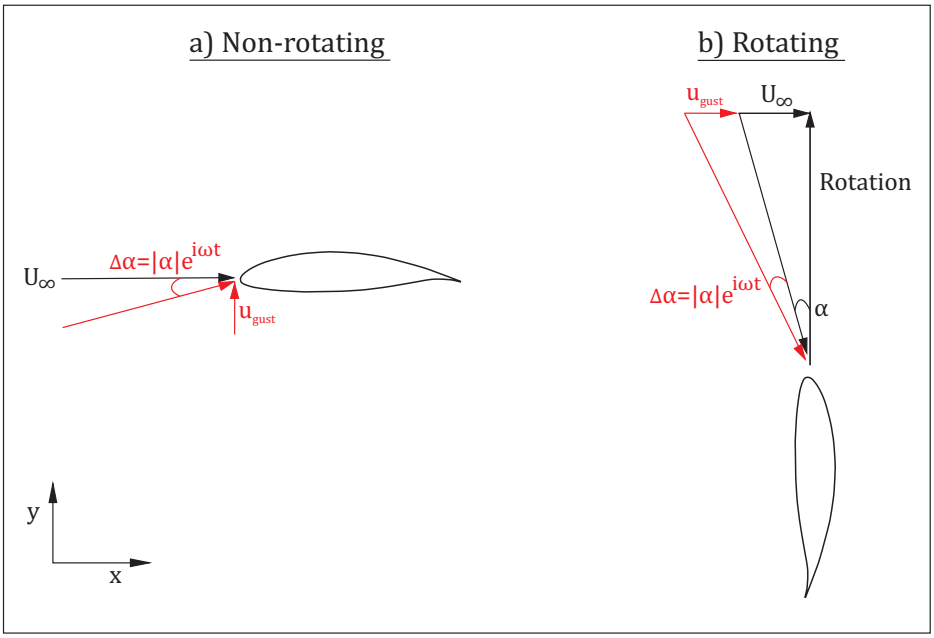

Fig. 4.7 (a) Aerofoil interacting with transverse gust. (b) Velocity triangle for a rotating blade section, interacting with an axial gust.

The results from the VLM will be compared with the predictions of 2D classical aerofoil theory. In a 2D system the lift generated by a uniform gust is given by the Theodorsen function. The unsteady lift coefficient is obtained as follows:

$$Cl = [2\pi C(k/2) + i\pi k/2] tan^{-1}(\hat{\alpha}) e^{i\omega t} \tag{4.4}$$

The Theodorsen function $C(k/2)$ is arguably the most common unsteady transfer function used in marine, wind and aerospace industries. For rotating systems a modifier for the returning wake is required, meaning that $C(k/2)$ in Equation 4.4 must be replaced by the Loewy function (Equation 2.10, see Chapter 2 Section 2.5.2 for further details).

For a sinusoidal 2D gust the unsteady lift is given by the Sears function, as follows:

$$Cl = 2\pi S'(k/2)tan^{-1}(\hat{\alpha})e^{i\omega t} \tag{4.5}$$

Note that $S'(k)$ refers to the phase-shifted Sears function, which is given in Chapter 2 (Equation 2.9). The original transfer function was derived assuming that the aerofoil mid-chord was located at the origin. Now it is more common to assume that the aerofoil leading edge is located at the origin, which requires a transformation of the original Sears function.

All the above transfer functions are based on the assumption of inviscid, incompressible flow in 2D, and are applicable to harmonic gusts, taking the reduced frequency k (Equation 4.1) as an input parameter. An overview of the details and development of these unsteady transfer functions was given in Chapter 2, Section 2.5. In this chapter they will be used to compare 2D theory to the results for 3D geometries. As such the limits of their applicability to 3D geometries will be established.

The results in the coming sections will be shown in terms of the normalised magnitude and phase of the unsteady lift. The normalised unsteady lift amplitude is given by:

$$|Cl'_N| = \frac{|L'|}{0.5\rho U^2 S[2\pi\hat{\alpha}]} \tag{4.6}$$

Here U is the relative local flow velocity at each spanwise position, and S is the surface area. The lift magnitude is normalised by the quasi-steady lift of a 2D flat plate, which is given by $2\pi\hat{\alpha}$. This means that at zero reduced frequency the 2D transfer functions will predict a normalised amplitude of 1. The 3D geometries will have a quasi-steady lift magnitude of less than 1, because of the steady-state downwash induced by the streamwise wake vorticity.

The phase of the unsteady lift is given by:

$$\angle Cl'_N = tan^{-1}\left(\frac{Im(L')}{Re(L')}\right) \tag{4.7}$$

This expression gives the phase difference between the quasi-steady response, which oscillates exactly in time with the gust oscillation, and the unsteady response. A positive phase means that the unsteady lift is leading the gust, while a negative phase means that the unsteady lift is lagging behind the gust.

Now that the methods for the chapter have been introduced, the unsteady response of each geometry in Figure 4.6 will be discussed in turn.

4.4 Finite wing

The most basic example of a 3D geometry undergoing unsteady gust forcing is a flat-plate wing with finite span, as illustrated in Figure 4.6a. It is a good starting point for the study of 3D geometry effects, because of its similarity to the 2D case, with the only difference being the finite span. It will be shown that this case, despite its simplicity, can be used to demonstrate most of the physical effects associated with unsteady load response in 3D.

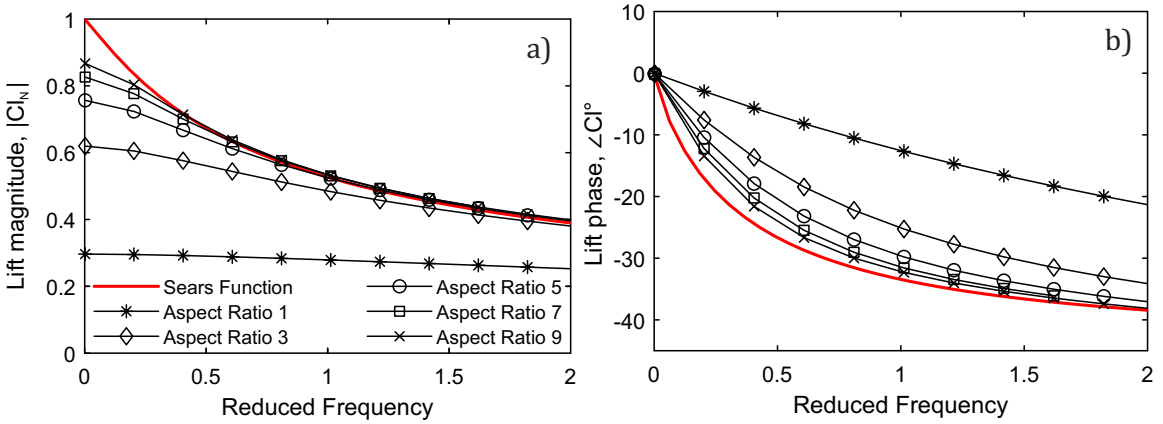

Fig. 4.8 Unsteady load response at mid-span of flat-plate aerofoils at different aspect ratios, undergoing forcing by a sinusoidal gust. (a) Magnitude, (b) phase.

4.4.1 Unsteady loading

Figures 4.8 and 4.9 show the lift response at mid-span of aerofoils with aspect ratios from 1 to 9. Figure 4.8 shows the response to a sinusoidal gust (Equation 4.3), compared to prediction by the 2D Sears function (equation 4.5), while Figure 4.9 shows the response to a uniform gust (Equation 4.2), compared to the 2D Theodorsen function (Equation 4.4). The results are shown in terms of normalised lift amplitude, as defined by Equation 4.6, and the phase of the

lift, as defined by Equation 4.7.

In both Figure 4.8a and Figure 4.9a, it can be seen that the lift amplitude at zero reduced frequency (quasi-steady response) changes with aspect ratio, such that the quasi-steady 3D results do not agree with the 2D function. This is due to the inherent reduction in steady lift in a finite wing, caused by the downwash of the streamwise wake vorticity mentioned in Section 4.2.1. However, as the reduced frequency increases, the mid-span load response of the finite wings can be seen to approach the 2D response in both the sinusoidal and uniform gust cases. The rate of this approach increases with the aspect ratio of the aerofoil, with the aspect ratio 1 aerofoil showing a substantially lower response amplitude than the 2D characteristic even at large reduced frequencies.

The phase of the response (Figures 4.8b and 4.9b) agrees with the 2D prediction at zero reduced frequency before diverging, and then approaching the 2D prediction again at high frequencies. The agreement at zero frequency is expected because the quasi-steady response must, by definition, be in phase with the gust forcing in both 2D and 3D. The phase does not approach the 2D prediction as rapidly as the amplitude, and only reaches the 2D characteristic for high aspect ratio geometries at large reduced frequencies.

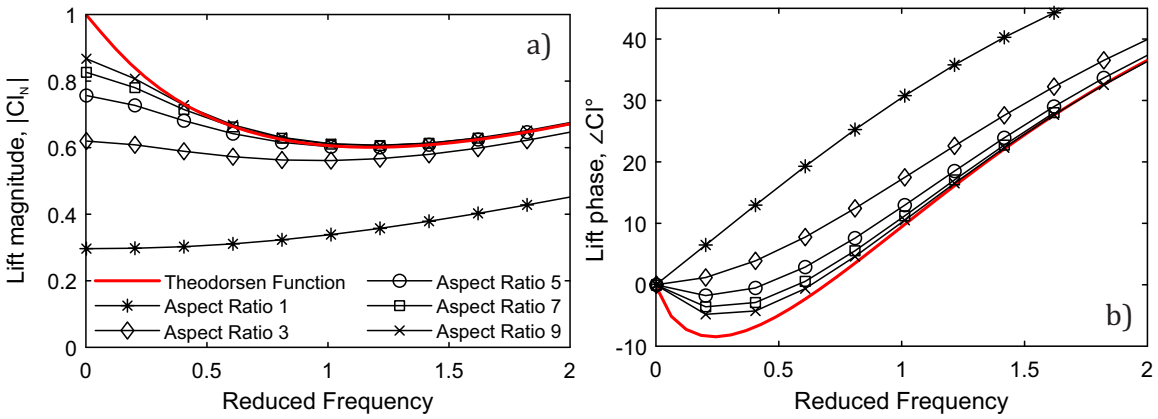

Fig. 4.9 Unsteady load response at mid-span of flat-plate aerofoils at different aspect ratios, undergoing forcing by a uniform gust. (a) Magnitude, (b) phase.

The unsteady loading on a finite wing will vary across the span, even in response to spanwise-uniform gusts. This is shown in Figure 4.10, which gives the spanwise distribution of lift response to a uniform gust (given by Equation 4.2), for the same range of aspect ratios as in Figures 4.8 and 4.9. The reduced frequency is kept fixed at 1.0.

Figure 4.10 shows that, for all aspect ratios, the amplitude of the unsteady load response is reduced as the wing tip is approached. As the aspect ratio increases, a larger proportion of the span exhibits 2D behaviour, although the lift magnitude (Figure 4.10a) approaches the 2D prediction faster than the phase (Figure 4.10b) – for an aspect ratio of 9, the lift magnitude is equal to the 2D case over the middle 60% of the span, whereas the phase approaches the 2D phase over the middle 30%. This discrepancy can be explained by the effect of the unsteady wake, which will be shown later.

The phase variation in Figure 4.10b also shows that the tip response leads the mid-span response, for all aspect ratios. This means that the wing tip and the mid-span do not respond in phase with each other, even when there is no spanwise gust variation. The results in Figure 4.10 are obtained for a uniform gust, but they are qualitatively similar for sinusoidal gust response, suggesting the same underlying causes.

It is important to note that the distribution of unsteady spanwise lift amplitude shown in Figure 4.10a is not proportional to the quasi-steady lift distribution. As such, it is not possible to obtain the unsteady response of the 3D wing by applying a correction to the Theodorsen function to account for the quasi-steady 3D wake downwash. This will be elaborated on as the chapter progresses.

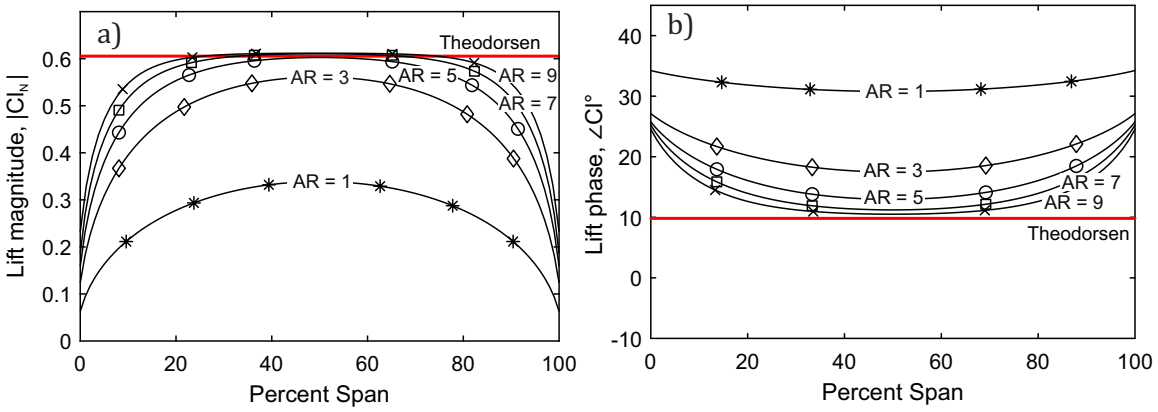

Fig. 4.10 Distribution of load response along the span for finite wings at different aspect ratios, undergoing uniform gust forcing with reduced frequency 1.0. (a) Magnitude, (b) phase.

As was noted above in Figures 4.8 and 4.9, the mid-span lift response of a finite wing approaches the 2D response with increasing reduced frequency. However, this trend does not persist over the full length of the span. We can show this by considering the lift magnitude

and phase relative to the 2D response, over a range of reduced frequencies. To do this, we define the relative lift amplitude as:

$$|Cl'_{REL}| = \frac{|Cl'_N(k)|}{|Cl'_{2D}(k)|} \tag{4.8}$$

Here the numerator is given by the 3D response, using Equation 4.6, and the denominator given by the 2D transfer function, defined in Equation 4.4 for uniform gusts. The 3D phase response relative to the 2D function can simply be given as:

$$\angle Cl'_{REL} = \angle Cl'_{2D}(k) - \angle Cl'_N(k) \tag{4.9}$$

Figure 4.11 shows the spanwise variation of relative lift amplitude and phase, as defined in Equations 4.8 and 4.9, for an aerofoil with aspect ratio 5. The gust forcing is uniform, and the response is shown for a selection of reduced frequencies in the range 0 to 1. The quasi-steady 3D response is given by $k = 0.0$.

Looking at load amplitude (Figure 4.11a), the mid-span response approaches the 2D amplitude with increasing reduced frequency, as could be seen in Figure 4.9. However, near the wing tips the change to the relative load amplitude is much smaller as the frequency increases. As a result, the difference in load response between the wing tip and mid-span increases with reduced frequency. This is seen more clearly in the phase of the response (Figure 4.11b), where the phase near the wing tips actually moves further away from the 2D prediction with increasing reduced frequency, while at mid-span the phase approaches the 2D response.

The spanwise variation in phase has significant implications for parameters such as root bending moment, where the integral of the load along the wing is important. Any significant phase difference between the responses at different locations will result in a lower amplitude than for a case where the loads act in phase along the whole span.

The findings in Figure 4.11 show that the difference between wing tip and mid-span response increases with reduced frequency, in terms of both magnitude and phase. As stated above, it is important to note that this difference, and the unsteady response characteristic of each spanwise position, is not proportional to the steady 3D lift distribution (shown by the $k = 0.0$ line in Figure 4.11a). This means that the lift response of different spanwise positions cannot be predicted by simply including the effect of the quasi-steady downwash from the

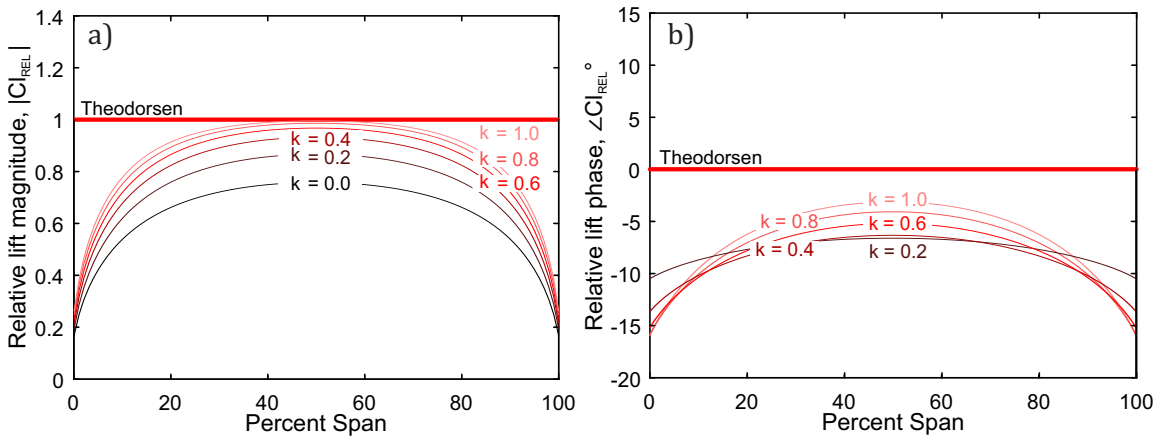

Fig. 4.11 Distribution of relative load response along the span for a finite wings with aspect ratio 5, undergoing uniform gust forcing for a range of reduced frequencies. (a) Magnitude, (b) phase.

streamwise wake vorticity, which is inherent to finite-wing geometries. The unsteady flow causes significant changes to the streamwise wake vortices, which must be accounted for to capture the 3D response accurately.

4.4.2 3D wake downwash

In Section 4.2.1, the 3D nature of the wake was shown to be a key difference between 2D and 3D aerofoil behaviour. We can explore the behaviour of the wake and its effect on the unsteady response by looking at the spanwise distribution of wake-induced downwash at the leading edge. The downwash reduces the variation in angle of attack seen by the aerofoil, and thus provides 'damping' of the unsteady response. Figure 4.12 shows the magnitude of the downwash velocity for a transverse gust of reduced frequency 1.0, normalised by the freestream velocity, for a wing with aspect ratio 5. Figure 4.13 shows the downwash for the same frequency, for a wing with aspect ratio 11. In both cases the wings are interacting with a sinusoidal gust that is uniform along the span.

The wake influence has been divided into two parts: the downwash created by the spanwise wake vorticity component, and that created by the streamwise wake vorticity component (as illustrated in Figure 4.3). The spanwise wake vorticity does not exist in a quasi-steady flow. In 2D unsteady analysis only the spanwise wake vorticity is present, and it extends uniformly to infinity.

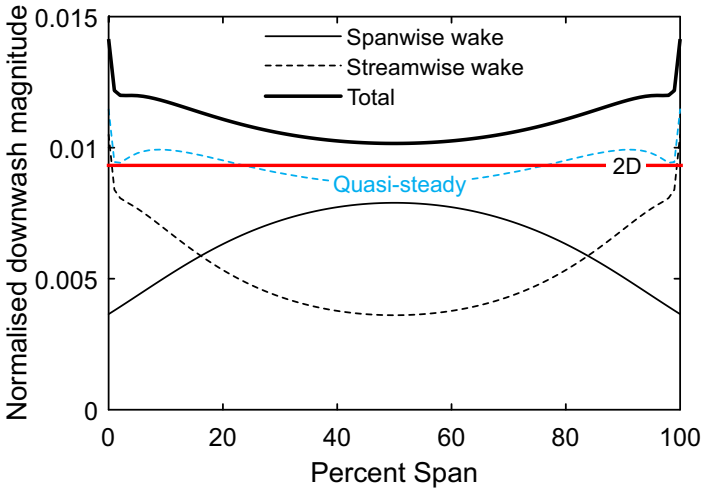

Fig. 4.12 Distribution of wake-induced downwash along the leading edge of a finite wing with aspect ratio 5, normalised by the freestream velocity, divided into contributions by the streamwise and spanwise wake vorticity. Unsteady downwash is for $k = 1.0$.

Considering first the downwash induced by the spanwise wake vorticity (thin, solid black lines in Figures 4.12 and 4.13), the downwash induced by this wake component decreases when approaching the wing tips; this is due to the wake being finite. This is a deviation from 2D analysis (solid red line), which assumes infinite spanwise wake vorticity, and is the first source of the deviation from 2D unsteady behaviour observed in the 3D cases.

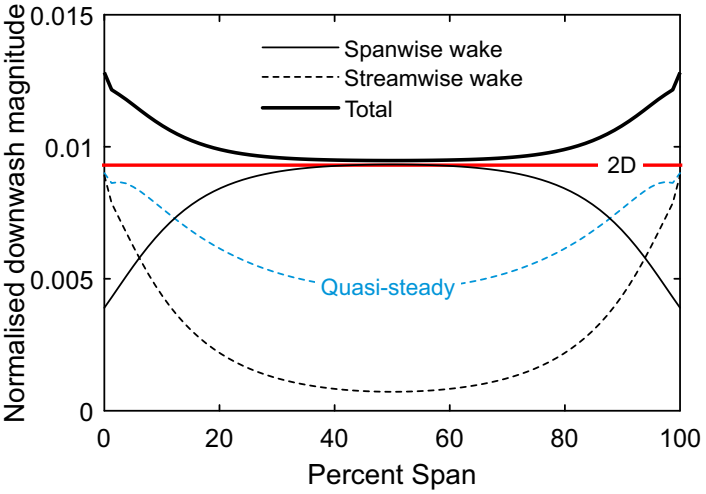

Fig. 4.13 Distribution of wake-induced downwash along the leading edge of a finite wing with aspect ratio 11, normalised by the freestream velocity, divided into contributions by the streamwise and spanwise wake vorticity. Unsteady downwash is for $k = 1.0$.

The second source of 3D unsteady behaviour is that of the downwash from the streamwise wake vorticity, which is not modelled at all in 2D. This is illustrated by the dashed lines in Figures 4.12 and 4.13. The quasi-steady downwash from the streamwise wake vorticity is shown in blue, while the unsteady downwash is shown in black. It can be seen that the magnitude of the downwash from the streamwise wake vorticity diminishes substantially around the mid-span when the reduced frequency is increased. As mentioned in Chapter 2 (Section 2.7.1), this behaviour has been explained by Namba [95], who showed that a vortex line in the streamwise direction, with harmonically varying circulation strength, will generate less downwash at the leading edge as the frequency of oscillation increases. Near the wing tips, however, the downwash induced by the streamwise wake vorticity remains large at $k = 1.0$.

The combination of the streamwise and spanwise vorticity downwash for $k = 1.0$ is shown by the thick black lines in Figures 4.12 and 4.13. In both cases, the total downwash is lower at mid-span than at the wing tips, meaning that there is less damping of the unsteady response at the mid-span than at the tips. This explains why the mid-span exhibits a larger response than the wing tips in Figures 4.10 and 4.11. The shape of the spanwise distribution of downwash does not match the load response exactly. This may be because the sections of aerofoil are not independent from one another, and so the loading on one section will affect the response of another. Thus, the translation from downwash to load is not linear.

It is also interesting to note that the total downwash (solid black lines) is similar at mid-span for both aspect ratios. This is in line with Figure 4.8a, which shows that the unsteady load amplitude at mid-span is virtually identical for the two aspect ratios. However, the balance of the streamwise and spanwise wake vorticity components making up the total downwash is different for the two aspect ratios: in Figure 4.12 (aspect ratio 5) the total downwash at mid-span is made up of a significant part of both streamwise and spanwise wake vorticity. In Figure 4.13 (aspect ratio 11) the downwash at mid-span is almost entirely generated by the spanwise wake vorticity. This means that while the load response of the wing with aspect ratio 5 appears to be tending towards the 2D result at $k = 1.0$, the final result is actually the result of a combination of spanwise and streamwise wake vorticity downwash effects, both of which have significant 3D features.

While the load amplitude at $k = 1.0$ is very close to the 2D value for both aspect ratio 5 and 11, Figure 4.8b shows that the two cases have slightly different phase response at mid-span. This can be explained by considering the phase of the two downwash components.

Figures 4.12 and 4.13 show the magnitude of the downwash, but the two wake components generally do not act in phase with one another. This can be illustrated more clearly by considering the mid-span downwash at a range of reduced frequencies.

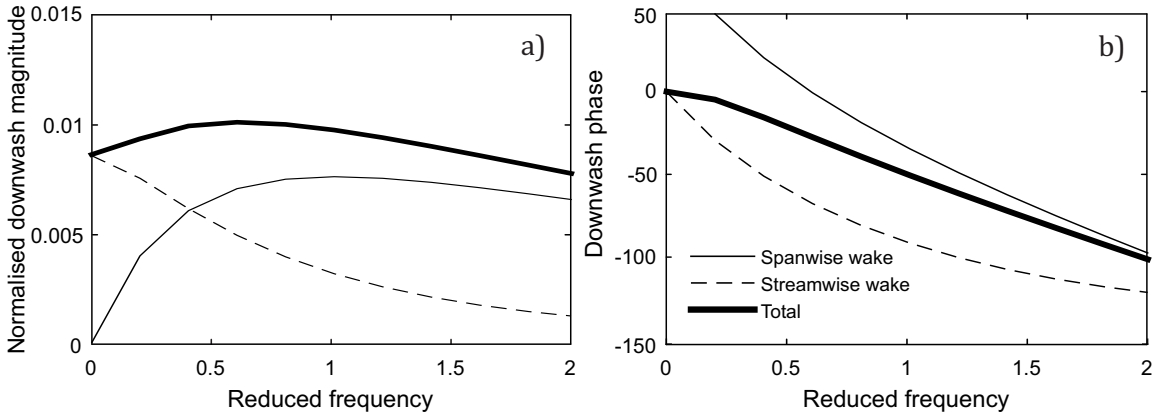

Fig. 4.14 (a) Magnitude and (b) phase of the wake-induced leading edge downwash, normalised by the freestream velocity, at mid-span of a finite wing with aspect ratio 5 undergoing sinusoidal gust forcing. The downwash is divided into streamwise and spanwise wake vorticity components.

Figure 4.14 shows the downwash at mid-span of the wing with aspect ratio 5, undergoing sinusoidal gust forcing. The magnitude (4.14a) and phase (4.14b) of the downwash is shown against reduced frequency. The behaviour of the streamwise and spanwise wake vorticity components can be seen to differ significantly: the downwash magnitude from the streamwise vorticity is at its peak at $k = 0.0$ (quasi-steady) and then diminishes. The downwash magnitude from the spanwise vorticity, on the other hand, peaks at $k = 1.0$ and then diminishes gradually. The total downwash can be seen to be increasingly made up of the spanwise component of vorticity as the reduced frequency increases.

Looking at the phase variation of the two wake components (Figure 4.14b), the total phase approaches the phase of the spanwise wake vorticity downwash with increasing reduced frequency. At $k = 1.0$ however, the total phase still has some contribution from the streamwise wake vorticity component. This is different to the wing with aspect ratio 11, for which the mid-span downwash amplitude and phase are shown in Figure 4.15. With a larger aspect ratio, the properties of the spanwise wake vorticity component dominate the total response throughout the majority of the frequency range. At $k = 1.0$ the total phase response (4.14b) is almost exclusively composed of downwash from the spanwise wake vorticity.

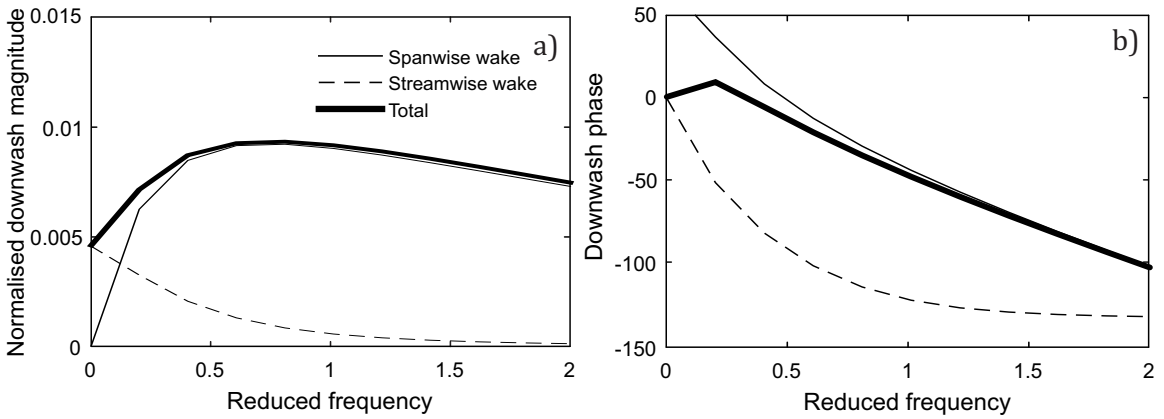

Fig. 4.15 (a) Magnitude and (b) phase of the wake-induced leading edge downwash, normalised by the freestream velocity, at mid-span of a finite wing with aspect ratio 11 undergoing sinusoidal gust forcing. The downwash is divided into streamwise and spanwise wake vorticity components.

The contribution of each of the wake components to the total downwash properties explain the behaviour seen in Figure 4.8: the magnitude of the response at mid-span is the same for aspect ratios 5 and 9 at $k = 1.0$, because the total magnitude of the downwash is approximately the same. However, for the lower aspect ratio the downwash is made up of a combination of the streamwise and spanwise vorticity downwash, which have differing phase properties. As a result, the mid-span phase response seen in Figure 4.8b for a wing with aspect ratio 5 is further from the 2D characteristic than that of the aspect ratio 11 wing, as is expected. The latter has a mid-span downwash that is almost entirely composed of the properties of the spanwise vorticity component at $k = 1.0$, which leads to a phase response that is virtually identical to the 2D response. This illustrates how the combined effects of the streamwise and spanwise wake vorticity components together drive the total unsteady response.

4.4.3 Finite wing study: conclusions

The results from the study of finite wing geometries show that the 3D nature of the wake has a significant effect on the unsteady load response of an aerofoil. The parameters determining the degree of 3D effects present in the response were found to be aspect ratio, reduced frequency and proximity to the wing tips. The unsteady response approached the 2D characteristic with increasing reduced frequency, and the rate of this approach increased with increasing aspect ratio. However, near the wing tips the response remained strongly 3D, even at high aspect ratios and frequencies.

The difference between the mid-span and tip response, in terms of both phase and amplitude of the load, was found to increase with aspect ratio and reduced frequency. This is of particular importance for the calculation of blade bending moments, and other analysis involving integration of the load along the span.

The findings in this section show the importance of modelling both the streamwise and the finite spanwise wake vorticity components for accurate estimates of the load response. Both must be modelled as unsteady, as the properties of each is a strong function of the reduced frequency. The relative contributions of the two wake components can be examined by considering the leading edge downwash induced by each component. Changes in the downwash from both streamwise and spanwise wake vorticity drive the overall magnitude and phase of the response.

Throughout this section the unsteady response to uniform gusts and to sinusoidal gusts has been used almost interchangeably. This is because the results are qualitatively similar for the two gusts, and the drivers of the load response are caused by the same changes to the wake. As such, no special distinction between the two gusts is necessary.

4.5 Tapered wing

Having determined the major effects of the downwash from both the spanwise and streamwise wake vorticity components on the loading of a finite aerofoil, we now study the effects of different geometry features, starting with blade taper. Figure 4.6b shows the tapered blade used in this analysis, and gives the definition of taper ratio. The leading edge is unswept, such that the incoming gust is in phase across the blade. Since the incident velocity is the same at all spanwise positions but the chord varies, the local reduced frequency (given by Equation 4.1) decreases linearly along the span as the chord length decreases. As an example we consider a wing with aspect ratio 5 (as referenced to the mid-span chord length), and with a taper ratio of 0.4.

Figure 4.16 shows the unsteady lift response of the tapered blade (blue line) at 20% span against the local reduced frequency, undergoing forcing by a sinusoidal gust. The lift characteristic for an untapered wing with the same aspect ratio and flow conditions is shown for comparison (black line). The difference between the two characteristics is marked, and can be seen to be approximately constant for all reduced frequencies. As such, the offset in lift distribution between the tapered and untapered blade is the same in quasi-steady

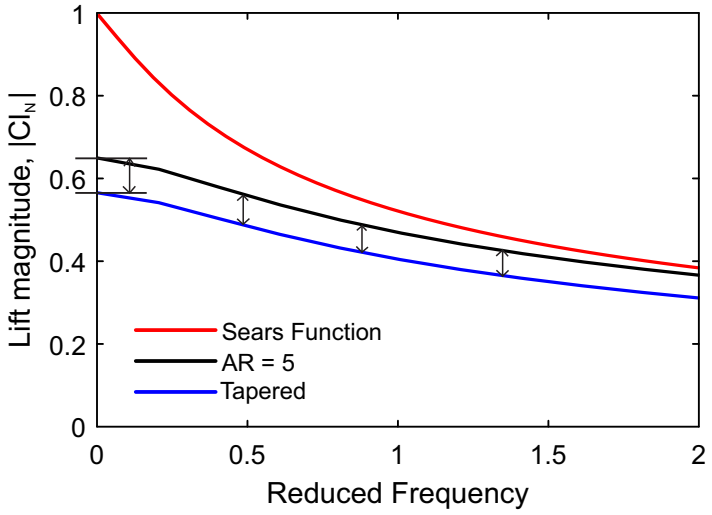

Fig. 4.16 The magnitude of unsteady lift response at 20% span, comparing an untapered wing with aspect ratio 5 to a tapered wing with the same aspect ratio, and taper ratio 0.4. The gust forcing is sinusoidal.

and unsteady flow. This allows us to make a correction to the tapered wing response by subtracting the quasi-steady difference between the tapered and untapered lift distributions from the unsteady response of the tapered blade:

$$Cl_{corrected} = Cl_{tapered} - \Delta Cl_{quasi-steady} \tag{4.10}$$

The effect on the spanwise lift distribution of this correction is shown in Figure 4.17. The spanwise distribution of lift magnitude for the tapered wing, undergoing gust forcing at mid-span reduced frequency 1.0, is shown with the solid blue line. The black line denotes the lift distribution for an untapered wing of the same aspect ratio. The unsteady lift response is asymmetrical about the mid-span in the case of the tapered blade, peaking near the wing tip with the shorter chord length. However, the corrected lift distribution (blue dashed lines) virtually removes the asymmetry, making the response equivalent to that of the untapered aerofoil.

These results suggest that a linearly tapered geometry affects the unsteady lift response in a quasi-steady manner. Furthermore, this means that the unsteady response of a tapered blade can be characterised by the mid-span reduced frequency. This was found to be the case for the range of taper ratios used in this study (λ = 0.2 to 1.0).

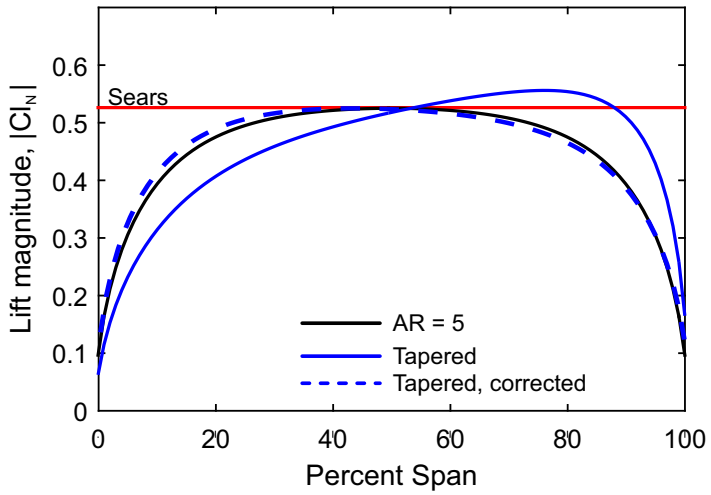

Fig. 4.17 Spanwise distribution of lift for a tapered wing with aspect ratio 5, taper ratio 0.4, undergoing uniform gust forcing at mid-span $k = 1.0$. The load distribution of an untapered wing with the same aspect ratio is shown for comparison. The Sears function is evaluated for the untapered wing.

As with the untapered finite wings considered in the previous section, the unsteady response of tapered blades is governed by the properties of the 3D wake downwash. Figure 4.18 shows the downwash distribution for the tapered blade, for gust forcing at mid-span reduced frequency 1.0. Again the wake influence is divided into the downwash caused by the spanwise and streamwise wake vorticity components. Both components of downwash on their own can be seen to vary significantly along the span, with strong asymmetry. However, by comparison the total downwash (thick black line) is almost symmetrical, and very similar to the total downwash of the equivalent untapered wing in the same flow conditions (red dashed line). This is due to the combined effect of the streamwise and spanwise wake vorticity components, both of which individually have significant variation along the span. However, they add up to create a near-symmetrical total downwash. This further emphasises the need to model both components of the wake unsteadily, as their combined effect is what drives the unsteady response in 3D.

Note that while the downwash of the tapered blade, as shown in Figure 4.18, is approximately symmetrical at $k = 1.0$, the spanwise load distribution in Figure 4.17 is not. The quasi-steady downwash, marked as the dashed blue line in Figure 4.18, is strongly asymmetrical, and results in an asymmetric load distribution in quasi-steady flow conditions. However, the load response retains its spanwise asymmetry even when the downwash becomes increasingly symmetrical. This suggests that the correction used in Figure 4.17 is not truly quasi steady, but rather that the effect of the unsteady wake is "cancelled out" by an

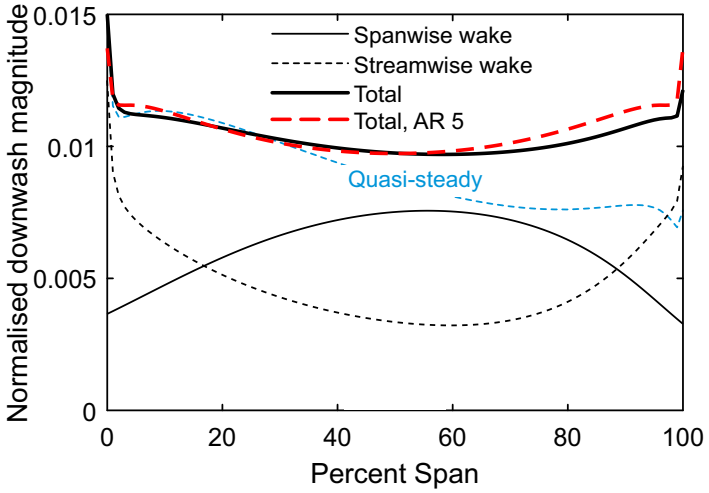

Fig. 4.18 Induced downwash velocity by the unsteady streamwise and spanwise wake vorticity components, normalised by the freestream velocity, for a tapered blade with aspect ratio 5, taper ratio 0.4. The gust is sinusoidal, with mid-span $k = 1.0$. The downwash of an untapered blade in the same flow conditions is shown for comparison.

unsteady effect that is asymmetric. This implies that the downwash is not the sole driver of the unsteady response. While the definite cause of the asymmetry could not be established in this study, it is likely that the effect is proportional to the linear variation of the chord length along the span, and is possibly related to the added mass force. On this topic, it is noteworthy that the type of "quasi-steady" correction used for the tapered blade was not found to be applicable to any other geometry evaluated in this chapter.

4.6 Sweep

Looking next at the effect of sweep, we consider uniform gusts interacting with backward- and forward-swept geometries. Figure 4.6c shows the swept geometry considered here, and gives the definition of sweep angle (which is positive for the backward-swept wing shown, where the wing tips are axially behind the mid-span). A uniform (Theodorsen-type) gust is used, as defined in Equation 4.2, because the resulting flow field changes everywhere simultaneously, meaning that there is no phase variation in the spanwise direction of the swept blade. The sinusoidal (Sears-type) gust, as defined in Equation 4.3, would cause a spanwise phase variation in the gust-aerofoil interaction. While this is also an important 3D effect, it is outside the scope of this chapter, as the focus here is on the effect of the geometry. The effect of spanwise variation in gust shape will be addressed in Chapter 6.

Figure 4.19 shows the unsteady lift response at mid-span for two swept wings with aspect ratio 5 (blue lines), compared to an unswept wing of the same aspect ratio (black line). The sweep angles are 45^o (backward-swept – solid line) and -45^o (forward-swept – dashed line). The main thing to be noted here is that the effect of sweep on the unsteady response varies with reduced frequency. It was shown in Section 4.5 that the unsteady response of a tapered wing had a constant offset from the untapered result, and the effect of taper could therefore be calculated by accounting for the quasi-steady load distribution (see Figure 4.17). As there is no constant offset in Figure 4.19, the effect of sweep cannot be accounted for by considering the quasi-steady loading distribution. It can also be seen that neither the amplitude nor the phase of the response approaches the 2D result at high reduced frequencies – in both the forward- and backward-swept cases, the agreement in load amplitude is closest at around $k = 1.0$, before the lines diverge as the reduced frequency is increased further. The phase lags further behind the 2D characteristic as the reduced frequency increases. This is also different from the unswept case (black line on Figure 4.19b), where the 3D response leads the 2D response for all frequencies.

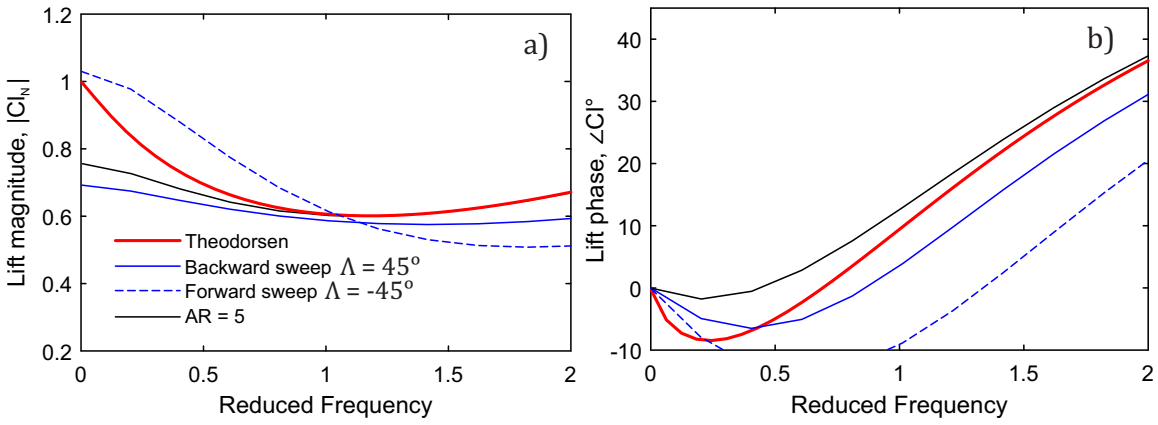

Fig. 4.19 Unsteady response characteristics at mid-span for a 45^o backward-swept wing and -45^o forward-swept wing, compared to an unswept wing with the same aspect ratio. (a) Magnitude and (b) phase of the unsteady response. The gust is uniform.

There is significant variation in the unsteady response along the span of the swept wings. This spanwise variation also changes substantially with reduced frequency. This is best illustrated by the unsteady response relative to the 2D response, as defined by Equations 4.8 and 4.9. The spanwise distribution of relative lift amplitude and phase is shown in Figure 4.20, for the 45^o backward-swept wing, over a range of reduced frequencies.

Looking first at the load amplitude (4.20a), the trend is quite different to that of an unswept wing (shown in Figure 4.11). As observed in Figure 4.19, the response initially approaches the 2D characteristic with increasing reduced frequency, but after $k = 0.8$ it recedes relative to the 2D line. The peak load amplitude also moves from the quarter-span point to the mid-span. Looking at the phase (4.20b), there is substantial variation in phase response between different spanwise locations. As discussed in Section 4.4.1, significant phase variation along the span will result in lower integrated loads (root bending moment, for example), as the loads at different spanwise locations do not act in phase with each other. Comparing Figure 4.20b with Figure 4.11b, the different behaviour is clear – the minimum at the mid-span and the increasing phase lag are both features of the swept case that are not observed for the unswept finite wing.

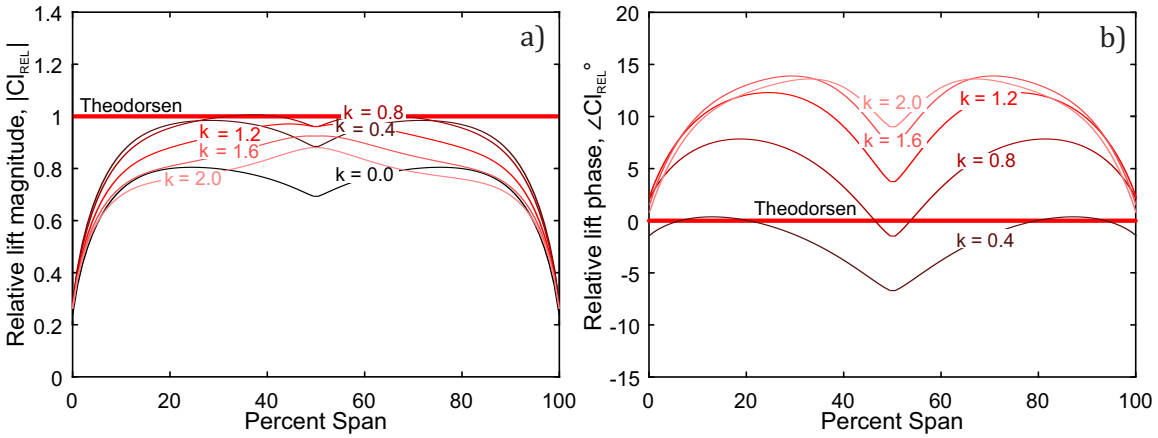

Fig. 4.20 Relative spanwise lift amplitude (a) and phase (b) of the unsteady response of a $\Lambda = +45^o$ backward-swept wing with aspect ratio 5 to a uniform gust.

Figure 4.21 shows the spanwise distribution of relative lift response for the -45^o forward-swept wing. Again, this wing configuration does not appear to approach the 2D characteristic, but is closest to the 2D response at $k = 1.0$. The load amplitude (4.21a) initially increases with increasing reduced frequency, peaking at mid-span. However, above $k = 0.4$ the trend is reversed. The amplitude gradually diminishes in the mid-span region, and the amplitude is approximately uniform across the majority of the span at high reduced frequencies ($k > 1.2$). The phase of the load response (4.21b) starts out leading the 2D response for the majority of the span at $k = 0.4$, but increasingly lags behind as the reduced frequency increases. As with the backward-swept wing, there is significant spanwise variation in the phase, even at high reduced frequencies, and this will affect the integrated loads.

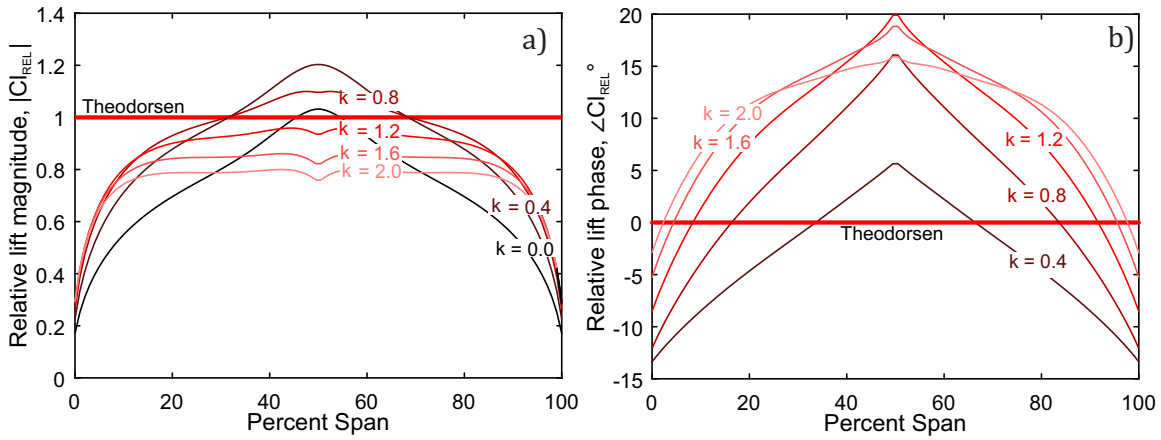

Fig. 4.21 Relative spanwise lift amplitude (a) and phase (b) of the unsteady response of a Λ = -45^o forward-swept wing with aspect ratio 5 to a uniform gust.

The previous sections showed that the 3D nature of the wake was a primary driver of the unsteady load response for 3D geometries. The spanwise distributions of wake downwash for both the backward-swept and forward-swept blades are shown in Figure 4.22, for a uniform gust with $k = 1.0$. As with the cases considered in Sections 4.4 and 4.5, the total induced downwash (thick black line) can be seen to be strongly dependent on both the streamwise and the spanwise components of the wake vorticity. This downwash profile stands out from the earlier examples: unlike the cases shown in Figures 4.12, 4.13 and 4.18, the two components of downwash in Figure 4.22 do not combine to produce approximately two-dimensional response around the mid-span. In the outboard sections of the backward-swept wing (Figure 4.22a) the spanwise wake vorticity contributes the most to the total downwash. Near the mid-span on the other hand, the streamwise wake vorticity effect is most strongly felt. This is the opposite trend to that of the unswept wings in Figures 4.12 and 4.13, and again leads to an unsteady response that cannot be captured by 2D models nor corrected for by the steady loading distribution.

Considering the forward-swept wing (Figure 4.22b), again the total downwash is influenced by both wake components throughout most of the span. The downwash is very large across the span, and in particular the mid-span downwash is much larger than any value seen in other cases (the y-axis has been extended to 4.5 times larger than other downwash plots to accommodate this value). In fact, the maximum downwash velocity is larger than the incoming gust amplitude. Note that, as was shown in Figures 4.14 and 4.15, the spanwise and streamwise wake vorticity do not act in-phase with each other. This means that the total downwash in Figure 4.22 is not a linear sum of the downwash induced by the streamwise

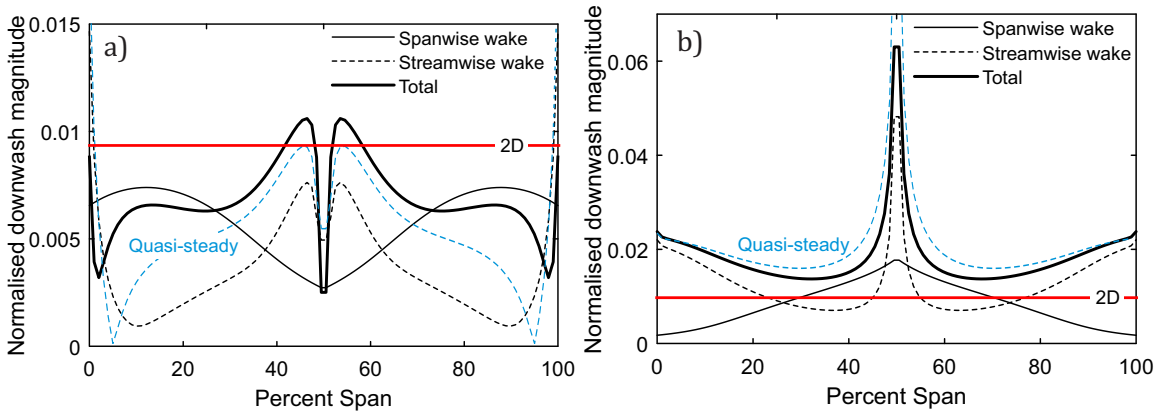

Fig. 4.22 Induced downwash velocity by the unsteady streamwise and spanwise wake vorticity components, normalised by the freestream velocity, for swept blades with aspect ratio 5, at (a) +45^o backward-sweep and (b) -45^o forward-sweep. Uniform gust, $k = 1.0$.

and spanwise wake vorticity components.

The complexity of the wake influence in these swept-wing cases shows the importance of modelling both streamwise and spanwise wake vorticity components in 3D. The two components are both strongly affected by the spanwise geometry variation, and deviate significantly from 2D predictions even though there is no spanwise variation in the gust. In contrast to the earlier cases, the response of a swept wing does not approach 2D behaviour as the reduced frequency increases.

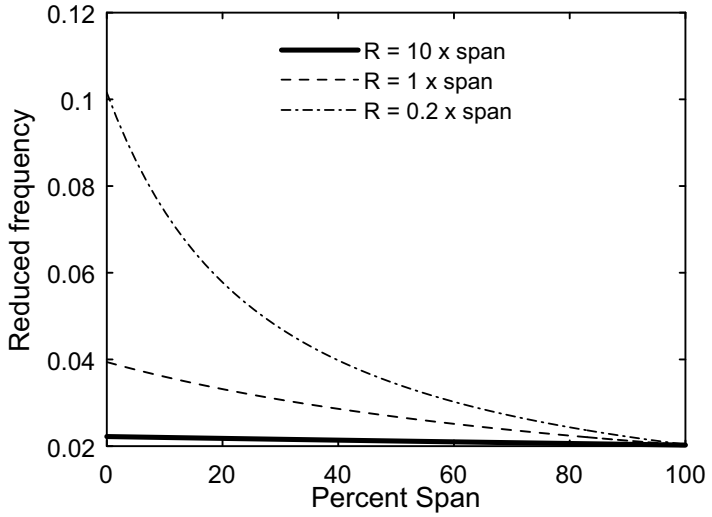

Fig. 4.23 Spanwise distribution of reduced frequency, with gust frequency $\omega = 1.0$, for rotating blades with different rotation radii.

4.7 Rotating blade

In order to investigate the effects of rotation on unsteady load response, a single-bladed rotor with a flat-plate aerofoil is studied, as shown in Figure 4.6d and 4.6e. The blade has an aspect ratio of 5, and is untapered and untwisted. The angle of attack at the blade tip is zero. Since the returning wake effect is an important aspect of the unsteady response of a rotor, the TSR has been set to 10. This relatively large value of TSR reduces the speed at which the wake convects away from the rotor relative to the rotational speed, and therefore increases the returning-wake interaction. The gust applied is uniform, given by Equation 4.2, acting in the axial flow direction. The results are compared to predictions from using the Loewy function (given in Equation 2.10), evaluated at mid-span.

One of the primary 3D effects of rotation is that the reduced frequency varies along the span, as was the case with the tapered aerofoil investigated in Section 4.5. In this case, however, the variation is not linear, since the relative blade velocity is a function of the rotational and the axial velocity. The closer an aerofoil section is to the hub, the larger proportion of the relative velocity will be due to the axial velocity. This causes a nonlinear decrease in velocity when moving from the tip to the hub. The smaller the radius of rotation – defined as the distance from the centre of rotation to the hub (see Figure 4.6e), and non-dimensionalised by the blade span – the more non-linear, and significant, the variation in reduced frequency will be. The local reduced frequency k at each spanwise position depends on the relative velocity, and will therefore vary with local radius, r:

$$k = \frac{\omega c}{[U_\infty^2 + (\Omega r)^2]^{1/2}} \tag{4.11}$$

Figure 4.23 shows the spanwise distribution of reduced frequency, for unit gust harmonic frequency ($\omega = 1.0$), for three rotation radii: $R = 10 \times span$, $R = 1 \times span$ and $R = 0.2 \times span$. By keeping ω, the freestream velocity and rotor rotational speed (Ω) constant, the spanwise variation in reduced frequency is only due to the change in local radius. The rotor TSR is kept constant at 10. The three cases will be used to demonstrate the effect of changing rotation radius on the unsteady aerofoil response.

Figure 4.24 shows the spanwise distribution of unsteady lift amplitude and phase for the three rotation radii, relative to the amplitude and phase predicted by the 2D Theodorsen function. The spanwise response of a non-rotating blade at the same aspect ratio and flow conditions is shown for comparison. The response is obtained for axially uniform gust forcing at mid-span reduced frequency 1.0 (note that there are no returning wake effects at

this frequency, as will be see in Figure 4.25). Equations 4.8 and 4.9 are used to obtain the response, as in Figures 4.11, 4.20 and 4.21. Note that Figure 4.24 shows the magnitude and phase relative to the 2D prediction, making the Theodorsen function a horizontal line, despite the fact that the 2D lift response varies along the span (as will be discussed in Figure 4.25). The blade hub is at 0% span, and the tip at 100% span.

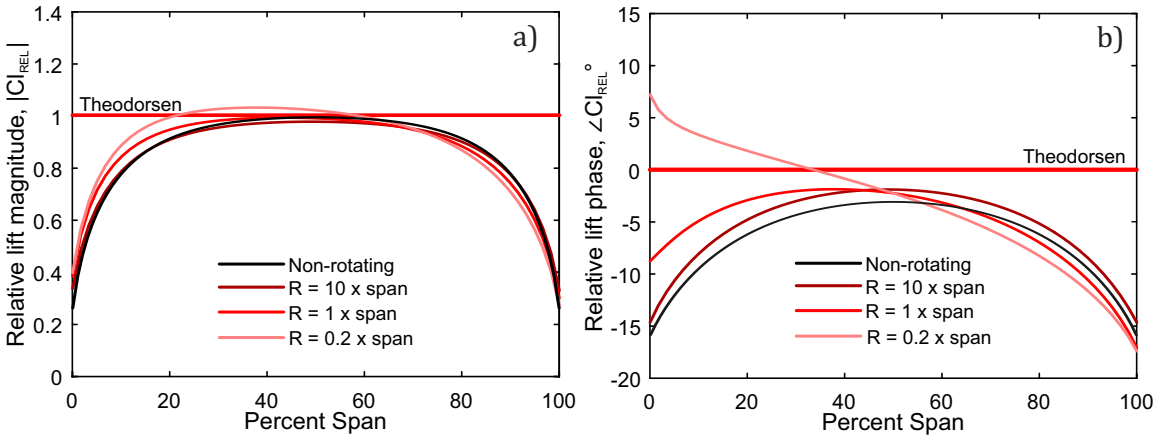

Fig. 4.24 Spanwise distribution of relative load response for rotating blades at different rotation radius, undergoing uniform gust forcing at mid-span $k = 1.0$. (a) Magnitude and (b) phase, relative to the Theodorsen function.

With high rotation radius, $R = 10 \times span$ (dark red), the radius is sufficiently large that the response is similar to that of a non-rotating flat plate with the same aspect ratio (black line). As the rotation radius decreases, however, the relative load amplitude increases slightly near the hub and decreases near the tip. In the case of the phase variation, at the two larger rotation radii the 3D response leads the 2D prediction at all spanwise points (a negative phase angle indicates a phase lead relative to the 2D function). With $R = 0.2 \times span$, on the other hand, the hub response instead lags behind the 2D prediction.

Figure 4.25 shows the absolute spanwise variation of lift amplitude and phase for the blade with $R = 0.2 \times span$ (i.e. not relative to the 2D prediction, which is shown in red). Here the variation of the 2D amplitude and phase along the span can be seen as well. Figure 4.25b shows that the 2D function predicts a strong variation in phase along the span, with the hub leading the tip response by 40-50^o. The 3D system, on the other hand, has a less extreme phase variation along the span. In fact, the phase response from the mid-span to the blade tip is approximately in-phase, only varying by about 5^o.

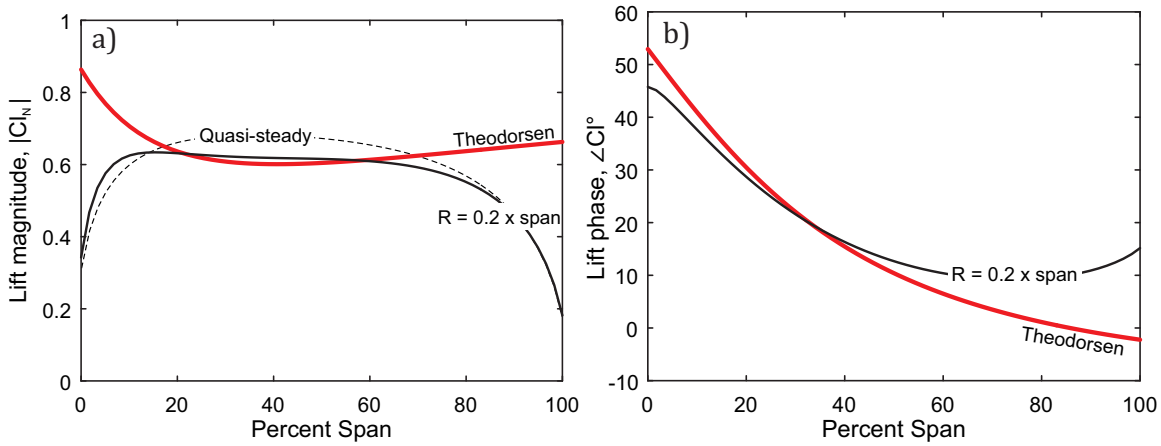

Fig. 4.25 Spanwise distribution of (a) load amplitude and (b) phase of a rotating blade at TSR 10, undergoing axially-uniform gust forcing, at mid-span $k = 1.0$. The results are compared to the 2D Theodorsen function.

Figures 4.24 and 4.25 suggest that the spanwise variation in the phase of the response (4.24b and 4.25b) is more strongly affected by the blade rotation than is the unsteady lift amplitude (4.24a and 4.25a). The 3D effects in the rotating system appear to "level out" the spanwise phase response, relative to the 2D prediction. This behaviour could be explained by the "equalising" aspect of the 3D aerodynamic system. In 3D modelling, spanwise interaction between blade sections is allowed. This means that the response of an individual blade section is determined not only by the local flow conditions, but is also affected by the blade sections and wakes in its immediate vicinity. This causes local sections to tend away from their isolated 2D response, and towards the global response of the whole blade. Namba [95], in his analysis of unsteady aerofoil response in 3D, also noted an "equalising" effect of spanwise flow variation on the unsteady response.

The tendency of 3D geometry to "even out" the phase response along the span is of potential consequence in applications where the integrated load is important, such as for tidal turbine bending moments. If the spanwise load response occurs in phase, especially in the outboard section of the blade, this results in a larger total bending moment than an out-of-phase load distribution. This is a potential danger of using 2D functions for preliminary design, as they may predict a more pronounced phase variation along the span. However, this effect is likely to be minor compared to the 3D effect of load reduction near the blade tip; in Figure 4.25, the total lift on the outer 50% of the blade is 20% lower in 3D, compared to the lift predicted by the 2D function, despite the loading acting in-phase. This is because of the lift reduction near the blade tip.

The results in Figure 4.25 also suggest that the local reduced frequency will not necessarily be a good indicator of the response of individual spanwise sections, as they often deviate strongly from the 2D response calculated using the local reduced frequency. Instead, the "evening-out" effect of the 3D system pushes the response of individual sections towards a global average. As a result, it may be sensible to look at the unsteady response in terms of a "global frequency", rather than the frequency of individual blade sections. The results of this chapter so far suggest that the mid-span reduced frequency may be a suitable choice for such a global frequency.

In order to study the returning wake in more detail, Figure 4.26 shows the load response of the blade rotating at $R = 0.2 \times span$. The amplitude and phase of the load response at three spanwise positions is plotted against the mid-span reduced frequency. An additional benefit of using a global frequency (in this case the mid-span reduced frequency) rather than the local frequency is that the response of the 3D system to a single gust event can be represented by a vertical line in Figure 4.26. This is more practical for the purpose of evaluating the response of a system to a given gust.

The 2D predictions by the Theodorsen (dashed red lines) and Loewy (solid red lines) functions at mid-span conditions are shown in Figure 4.26 for comparison. The peaks and troughs in the load response predicted by Loewy correspond to wake-resonance conditions. At the peaks, the wake downwash from the returning wake sheets cancel each other out, thus reducing the wake damping and increasing the load response. At the troughs, the opposite happens: the downwash from successive returning wakes act together to increase the aerodynamic damping of the wake.

Figure 4.26a shows that the mid-span response (black line) approaches 2D behaviour at reduced frequencies above about 0.5. The Loewy function predicts the location of the peaks and troughs of the returning wake interaction with reasonable accuracy, although the peaks and troughs of the Loewy function occur at slightly lower reduced frequency than the 3D model. The Loewy function also overpredicts the magnitude of the load peaks at mid-span, by about 20% in the case of the first peak (at $k = 0.2$). This is because the returning wake interaction occurs in a frequency range where the effect of the streamwise wake vorticity is substantial (as was shown in Section 4.4), and the 2D Loewy model captures the returning wake effects but neglects the streamwise wake vorticity altogether.

Another notable feature of Figure 4.26 is the behaviour of the hub (solid blue line) and tip (dashed blue line) sections. The tip loading is more or less constant at all reduced frequencies and is always lower than the mid-span load, as was the case in the non-rotating case (Figure 4.10). The hub, however, follows a totally different trend, meaning that there is an increasing asymmetry in the response across the blade span as the reduced frequency is increased. At high reduced frequencies, the hub response is larger than the mid-span response, and the phase lead becomes very large.

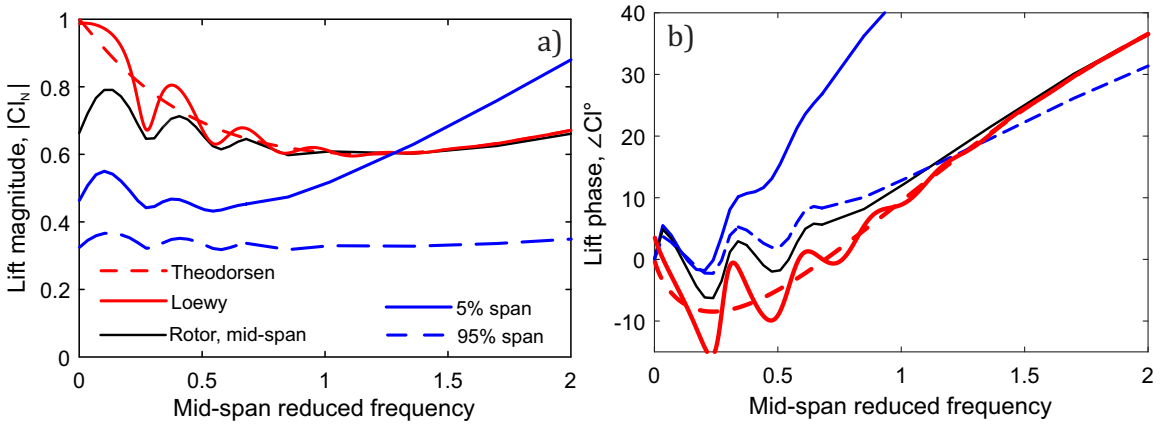

Fig. 4.26 The unsteady load (a) magnitude and (b) phase of a rotating flat plate at TSR 10, undergoing axially uniform gust forcing. $R = 0.2 \times span$.

The causes of the unsteady behaviour of the rotating blades can again be traced to the 3D wake downwash. Figure 4.27 shows the spanwise distribution of downwash for the rotating blade with $R = 0.2 \times span$, for mid-span reduced frequencies 0.7 (4.27a) and 1.7 (4.27b). The two cases demonstrate once more that it is vital to model the individual changes to both the spanwise and the streamwise wake vorticity in order to predict the total unsteady load response accurately.

In Figure 4.27a there is significant spanwise asymmetry in the downwash induced by both streamwise (solid grey) and spanwise (dotted grey) wake vorticity components. However, the peak of the spanwise wake vorticity downwash is located at almost exactly the same spanwise position as the lowest point of the streamwise wake vorticity downwash. As a result, the total downwash (solid black line) is almost level and near-symmetrical about the mid-span. At this frequency, the hub and tip showed relatively similar response magnitude.

Looking at Figure 4.27b, the increase in reduced frequency has caused some significant changes to both downwash components. The streamwise wake vorticity still induces

an asymmetric downwash, with the lowest point at approximately the same location as in Figure 4.27a (at about 35% of span). The spanwise wake vorticity, however, is now much closer to symmetrical about the mid-span. Furthermore, while the peak downwash induced by spanwise vorticity is approximately the same in both cases, the minimum value of the streamwise wake vorticity downwash decreases with reduced frequency (as was found in Section 4.4). As a result, Figure 4.27b shows a strong asymmetry in the total downwash with a minimum near 25% of span. This indicates that as the reduced frequency increases, there is significantly less aerodynamic damping near the hub than near the tip of the blade.

This reduction in damping near the hub is the cause of the behaviour seen at high frequencies ($k > 1$) in Figure 4.26, where the hub amplitude increases exponentially with mid-span reduced frequency, and the phase response leads that of the mid-span by over 30^o. These are both signs of low aerodynamic damping, which allows the added mass response to dominate the unsteady loading. Figure 4.27 shows that the unsteady behaviour of both the streamwise and the spanwise wake vorticity components in combination are instrumental in generating the response of a 3D system. Approximating the streamwise wake vorticity effects as quasi-steady is not appropriate, and would result in severe errors in the unsteady load predictions.

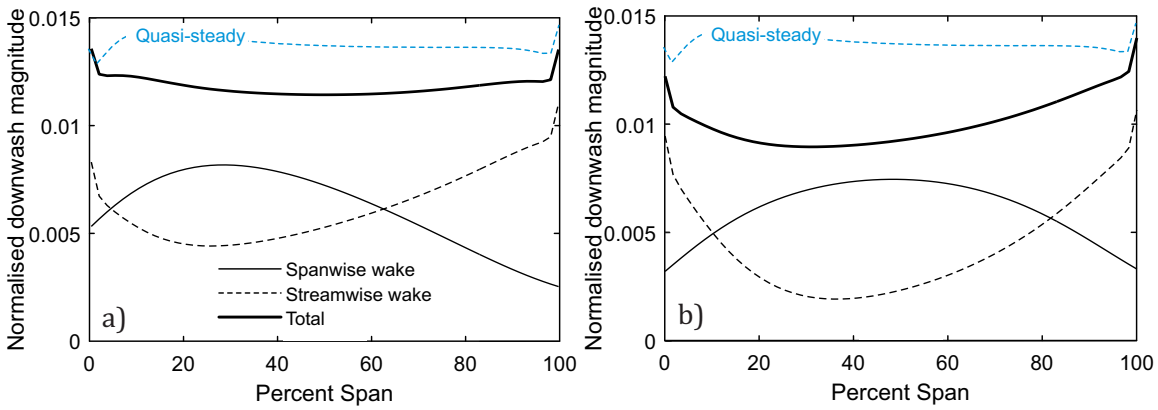

Fig. 4.27 Downwash distribution along the span, normalised by the freestream velocity, for the rotating blade with $R = 0.2 \times span$, undergoing axially uniform gust forcing. (a) $k = 0.7$, (b) $k = 1.7$.

4.8 Conclusions

This chapter has demonstrated that one of the primary drivers of the difference between 2D and 3D inviscid unsteady response is the 3D nature of the wake. The 3D response is affected by the spanwise wake vorticity being finite for a finite-span geometry, while it is assumed to extend infinitely in a 2D approximation. The 3D response is also affected by the presence of an unsteady streamwise component of wake vorticity, which is not modelled at all in a 2D system. The combined effect of these streamwise and spanwise wake vorticity components must be considered in order to predict the unsteady response correctly. It is not possible to assume that the streamwise wake vorticity behaves in a quasi-steady manner, as doing so would create significant errors in the prediction of unsteady response. This will be shown in more detail in Chapter 5.

Through studying the unsteady response of non-rotating finite wings of various aspect ratios undergoing spanwise-uniform gust forcing, the geometry factors determining the level of unsteady 3D effects on an aerofoil were determined to be the following:

1. Reduced frequency – 3D effects increase with decreasing reduced frequency.
2. Aspect ratio – 3D effects increase with decreasing aspect ratio.
3. Proximity to tip – 3D effects are always strong in the vicinity of aerofoil tips.

An exception to the reduced frequency factor was however observed in the case of swept wing geometry. For both forward-and backward-swept geometries, the unsteady response was not found to approach the 2D characteristic when the reduced frequency was increased. In this case, 3D effects remained dominant in the full range of tested frequencies.

The phase of the load response was observed to vary significantly along the span, leading to different spanwise sections responding out of phase with each other, even when there was no spanwise variation in gust shape or reduced frequency. This is of particular importance to any application where the load is integrated along the blade span, for example in the evaluation of blade bending moments. This finding therefore has implications for the prediction of the fatigue life of tidal turbines, since spanwise phase differences will reduce the total load fluctuation on the blade. However, this effect will likely be counteracted by the drop in loading due to tip effects.

In the case of a tapered wing, the change to the response characteristic compared to an untapered wing was shown to be the same as the change to the quasi-steady load distribution.

The unsteady response could effectively be characterised by the mid-span reduced frequency, rather than the local. However, this was the only geometry where such a quasi-steady correction could be applied; for all other geometries the spanwise variation in loading changed substantially with reduced frequency.

The effect of rotation was especially visible in the spanwise variation of the unsteady phase response. A rotating blade has a nonlinear spanwise variation in reduced frequency, and so even a 2D model will predict a variation in unsteady response. However, the spanwise variation in unsteady response was seen to be less extreme in the 3D system compared to the 2D predictions. The response was pushed towards a "global average" across the span. The frequency at which returning wake resonance occurred was found to be reasonably well predicted by the Loewy function, although the peaks and troughs of the resonant response occurred at slightly lower frequencies compared to that predicted by the 3D system. However, neither the load amplitude nor the absolute value of the phase were well predicted by the 2D Loewy function. As with the non-rotating cases, the changes in behaviour could be accounted for by considering the downwash induced by both the streamwise and spanwise components of wake vorticity.

Throughout this chapter the effects of wake distortion have been neglected, and the wake is assumed to leave the wing trailing edge with the steady freestream velocity. This assumption is used in all transfer functions obtained from 2D unsteady aerofoil theory (such as the Sears and Theodorsen functions). It is generally considered a good assumption for aerofoil sections and wings, as any wake deformation will occur far enough downstream as to have little effect on the loading. For rotating blades, on the other hand, wake deformation is potentially more significant due to the returning wake effects. As the wake stays in proximity to the rotating blades for longer, deformation of the wake may affect the blade loading. This has not been accounted for in this chapter, but will be considered in more detail in the next chapter (Sections 5.2.2 and 5.4.3).

Chapter 5

Unsteady load response of a tidal turbine geometry

5.1 Introduction

In the previous chapter, different aerofoil shapes were considered and the key 3D geometric parameters governing unsteady response determined. This chapter now focuses on the unsteady response of a specific, model-scale tidal turbine geometry. The turbine on which the geometry is based has been used extensively for experimental tests in other studies (see for example [141]). The load response of this turbine to unsteady inflow conditions will be investigated, and compared to predictions by 2D classical aerodynamic theory.

It was determined in Chapter 4 that the most important driver of unsteady response in 3D was the unsteady wake. In a 3D model, the unsteady wake consists of two perpendicular vortical components: spanwise and streamwise. The former is included in 2D models, but is assumed to extend infinitely and uniformly in the spanwise direction. The latter is inherent to any finite-span geometry, but is neglected in 2D models. Furthermore, Chapter 4 showed that it is not possible to account for the streamwise wake vorticity using the quasi-steady loading distribution. Finally, it was also shown that the 'returning wake' has a significant impact on the unsteady response of a rotating geometry.

Due to the importance of the unsteady wake in determining blade forcing, this chapter will investigate the consequence of assuming a prescribed wake shape. In the vortex lattice model (VLM) used in Chapter 4, it was assumed that the wake left the aerofoil trailing edge with the steady, relative freestream velocity. As a result, no wake rollup or distortion effects

were included. For propeller or turbine geometries, this may be an inadequate assumption.

The steady validation cases in Chapter 3 showed that the load distribution for a two-bladed rotor was predicted differently for a prescribed wake model and a free-vortex wake model. The free-vortex wake model is able to capture two effects that are neglected by the prescribed wake solver: the change in wake propagation speed (higher for a propeller, lower for a turbine), and the rollup of the wake which causes the vorticity to collect near the blade tips. In Chapter 3, the free-vortex model was confirmed to give a better fit to steady state experimental data (see Figure 3.8b) because it captures these two effects.

This chapter uses the time-domain VLM described in Chapter 3 in order to quantify the impact of these wake effects on the unsteady turbine response. In order to estimate the effect of the reduced wake propagation speed over a range of gust frequencies, a steady wake correction is obtained by using the time-stepping VLM to generate the steady-flow wake shape, and then prescribing this corrected shape in the frequency-domain VLM (see Section 3.2.5 for further details).

As well as the steady-state rollup effects, the wake could potentially be further distorted by interaction with the unsteady flow. This cannot be accounted for using a correction to the frequency domain VLM solver, but the effect will be investigated using the time-domain VLM.

In order to validate the inviscid VLM results, and to determine whether there are significant viscous effects for this geometry, the results of steady and unsteady RANS simulations will be discussed. The unsteady wake development will be studied in some detail, to determine how an unsteady wake might interfere with downstream turbines in an array.

In the first part of this chapter, the frequency-domain VLM with a prescribed-wake model will be used to analyse the inviscid turbine performance, in a similar manner to the analysis performed in Chapter 4. The time-stepping VLM will then be used to estimate the effect of wake distortion and propagation speed on the unsteady response. Having studied the inviscid turbine response, the URANS simulations will be used to show some of the qualitative features of the unsteady flow and to validate the VLM results. Finally, a parametric study of the unsteady turbine response will be shown, using the standard prescribed wake frequency-domain VLM and the corrected VLM, both of which will be compared to the

URANS results over a range of reduced frequencies. An illustration of the model turbine, and its representation in VLM and RANS, can be seen in Figure 5.1.

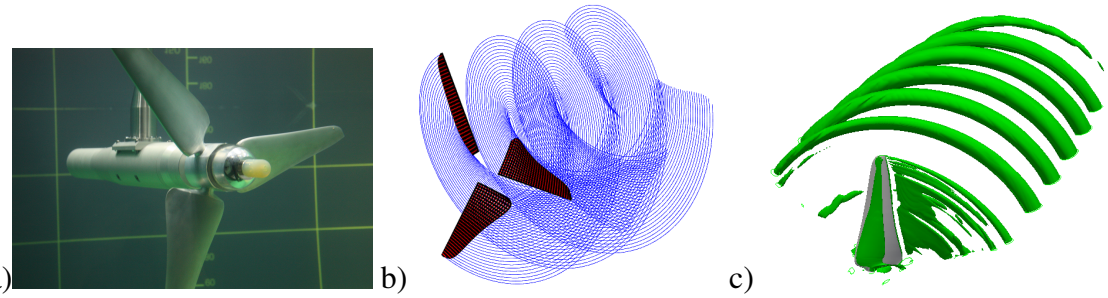

Fig. 5.1 The tidal turbine analysed in this chapter. (a) Experimental test [35], (b) VLM, (c) RANS.

5.1.1 Simulating unsteady gust interaction

In the simulations presented in this chapter, two classes of harmonic unsteady gusts were made to interact with the turbine: axially uniform gusts and annular-sinusoidal gusts. These two types of gust are illustrated in Figure 5.2, with Figure 5.2a representing an axially uniform gust, the velocity magnitude given by the following expression:

$$|\mathbf{u}_{gust}| = \eta U_\infty e^{i\omega t} \tag{5.1}$$

Figure 5.2b represents an annular-sinusoidal gust, given by the following expression:

$$|\mathbf{u}_{gust}| = \eta U_\infty e^{i\omega(t-\theta/\Omega)} \tag{5.2}$$

Here θ is the annular position, and Ω is the rotational speed of the turbine in raidans per second. The purpose of selecting these gusts was not to represent accurate ocean turbulence conditions, but to generate harmonic gusts that are easily parameterised based on amplitude and frequency, and are straightforward to generate in URANS simulation and in VLM. They also correspond in a simple way to gusts used in linear analytic theory (specifically to the Theodorsen function, which applies to chordwise-uniform gusts, and the Sears function which applies to sinusoidal gusts). As such, these gusts are ideal for the objective of determining the applicability of 2D aerodynamic models to a 3D aerofoil geometry, via a parametric study.

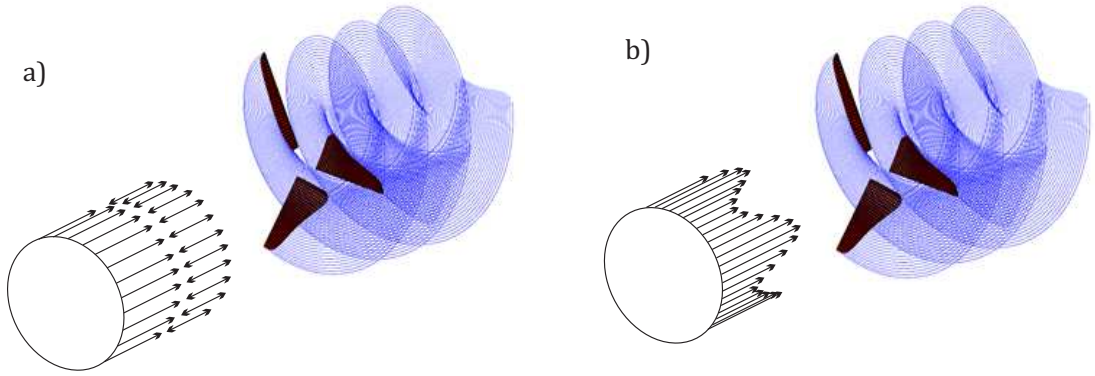

Fig. 5.2 The two types of harmonic gust simulated in this chapter. (a) Axially uniform, and (b) annular-sinusoidal.

5.2 Inviscid modelling of the turbine load response

In this section the inviscid response of the turbine as calculated by the VLM will be presented. A general study will first be performed using the frequency-domain VLM, with a prescribed wake assuming that the wake vortices leave the trailing edge with the freestream velocity. After this, the effect of wake distortion on the inviscid response will be shown using time-stepping VLM.

5.2.1 Frequency-domain VLM

The prescribed-wake frequency domain vortex lattice model used in Chapter 4 is used here to analyse the unsteady response of the model tidal turbine. A uniform gust (Figure 5.2a, Equation 5.1) is applied, acting in the axial direction. As in Chapter 4, the unsteady lift response is shown normalised by the 2D quasi-steady lift, such that the 2D lift amplitude is 1 at zero reduced frequency (using Equations 4.6 and 4.7, in Chapter 4).

Figure 5.3 shows the amplitude (5.3a) and phase (5.3b) of the unsteady load response of the turbine. The response is plotted at three spanwise positions; at 5% span (near the hub), at mid-span, and at 95% span (near the tip). The response is plotted against the mid-span reduced frequency, rather than the local reduced frequency. This was motivated in Chapter 4, where it was argued that a "global frequency" for the whole 3D system is more practical. This use of a global frequency means that the response to a single gust event can be represented by a single vertical line at constant frequency in Figure 5.3. The mid-span response (black line) is compared to the 2D Theodorsen (dashed red) and Loewy (solid red) functions.

The first thing to note in Figure 5.3 is that the Loewy function, which includes the returning wake effect, does not predict any large deviation from the Theodorsen function. Apart from small deviations at low reduced frequencies ($k < 0.4$) the two functions can be used interchangeably. This is likely to be due to the fact that the analysis is performed for the rated TSR of 4 (see Figure 3.17), which means that the wake propagates more quickly relative to the rotor rotation compared with the TSR 10 simulations in Chapter 4. This will reduce the returning wake effects.

The 3D VLM predicts a more significant wake resonance than the 2D function, and predicts it to occur at higher reduced frequency. A small shift in the occurrence of wake-resonant peaks in the unsteady characteristic was found for the rotor geometry in Chapter 4 Section 4.7, but the shift is more pronounced here. In the region where the returning wake interaction is the strongest, over the reduced frequency range 0.0 to 0.8, the 3D wake effects are also significant (see Chapter 4 Section 4.4). As such, the 2D Loewy function fails to predict both the magnitude and phase of the unsteady interaction, even at mid-span.

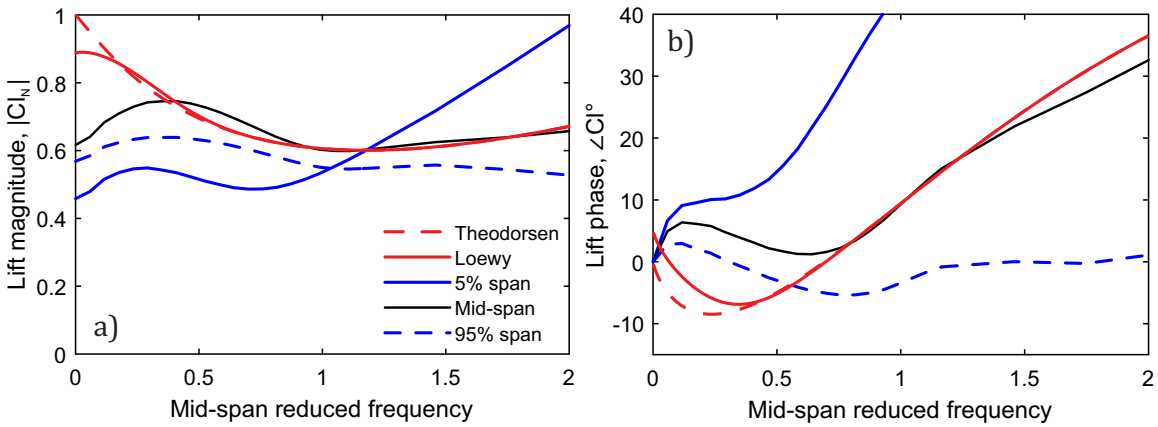

Fig. 5.3 The unsteady load (a) magnitude and (b) phase of the tidal turbine geometry, at TSR 4, undergoing axially uniform gust forcing.

As with the rotating flat plate in Chapter 4, there is a clear spanwise asymmetry in the unsteady load response. Figure 5.3 shows that the hub response (solid blue line, 5% span), experiences less aerodynamic damping than both the mid-span and the aerofoil tip region (dashed blue line, 95% span). This is visible through the rapid increase in amplitude and the strong phase lead at the hub, both of which signify a dominance of added mass effects in the unsteady response. The tip, on the other hand, has a more constant load amplitude throughout the frequency range, and generally has a small phase lag, suggesting greater wake

damping.

Figure 5.4 shows the spanwise load response of the turbine to an axially uniform gust with a mid-span frequency of 0.9. The results are compared to the Theodorsen function, which gives the same result as the Loewy function at this frequency. While there is a significant spanwise variation in load response, as with the rotating flat plate in Chapter 4 it is not as extreme as that predicted by the 2D theory. As observed for the rotating aerofoil in Chapter 4, the response is levelled out – pushed towards a global average – by spanwise interactions. This is especially relevant for the spanwise distribution of phase (Figure 5.4b): if there is significant phase variation of the unsteady load along the span, the total forces and bending moments acting on the blade roots will be reduced, as the load of the different blade sections will be acting out of phase with each other. If instead the unsteady load response is acting in phase along the span, this will amplify the total forces and moments.

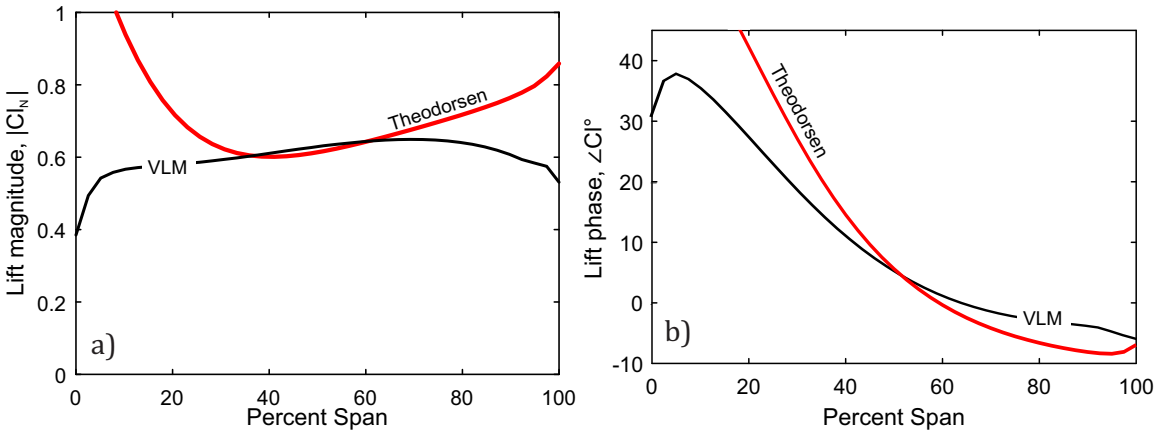

Fig. 5.4 Spanwise distribution of (a) load amplitude and (b) phase of the model turbine, at TSR 4, undergoing axially-uniform gust forcing. The mid-span reduced frequency is 0.9. The results are compared to the 2D Theodorsen function.

While Figure 5.4b shows that the spanwise variation in phase is smaller than that predicted by the 2D characteristic, it is still notable that the mid-span and tip sections are out of phase with each other by over 10^o. This in contrast to the rotating flat plate in Chapter 4 (Figure 4.25), for which the outer 50% of span responded approximately in phase, and will result in lower unsteady blade root bending moments for the turbine than for the flat plate geometry. However, it should be noted that the effect of spanwise phase difference is likely dwarfed by the 3D tip-loss, which significantly reduces the loads near the tip.

5.2.2 Time-domain VLM

The analysis in the previous section was carried out using frequency-domain VLM, with a prescribed wake assuming that the wake leaves the trailing edge with the steady freestream velocity. This section will explore the impact of this assumption, using a time-domain VLM.

In this section the model turbine is simulated undergoing unsteady gust forcing, first by an axially uniform gust and then by an annular-sinusoidal gust. The gust amplitude is set to 15% of the mean axial flow for both gust events. While the gust amplitude is not relevant to the non-dimensional lift response as calculated by the frequency-domain VLM, it is relevant for the wake distortion by the gust that is explored in this section. Each gust event is simulated at two different mid-span reduced frequencies: $k = 0.35$ and $k = 1.1$.

Each unsteady load analysis is repeated with different conditions for the wake generation. First a prescribed-wake case is performed, with the wake leaving the trailing edge with the freestream velocity. This is the same assumption as was used throughout Chapter 4, and is considered the "baseline" case. After this a free-vortex wake is used, in which the wake vortices can interact with each other. This causes rollup of the wake, as well as a reduction of the wake propagation speed in the turbine shadow. This wake condition has been shown to be generated using Equation 3.11b (see Chapter 3), and will be referred to as "wake rollup". In the third iteration of the analysis, the wakes are not allowed to interact (i.e. there is no rollup), but the wake can be distorted by the unsteady gust. This corresponds to wake generation through Equation 3.11c. Finally, in the fourth iteration, the wake vortices are both allowed to interact and to be affected by the unsteady gust. This corresponds to wake generation through Equation 3.11d.

Figure 5.5 is a bar chart of the mean power coefficient (Equation 3.19) and the amplitude of the fluctuating power coefficient due to an axially uniform gust, as predicted by the time-stepping VLM with each of the four methods of wake generation. Figure 5.5a shows the response for mid-span $k = 0.35$, while 5.5b shows the response for mid-span $k = 1.1$. The dark blue bars represent the "baseline" prescribed-wake case. Looking first at the effect of wake rollup, which is shown by the light blue bars, the results indicate that wake rollup has a significant impact on the mean power coefficient. This is in line with the steady-state validation study performed in chapter 3 (section 3.4, see Figure 3.17), which determined that the inclusion of wake rollup reduced the predicted power coefficient of the turbine. The effect on the unsteady amplitude is comparatively very small in the lower frequency case (5.5a), but more prominent at the higher frequency (5.5b), where it reduces the unsteady load

amplitude by about 7%.

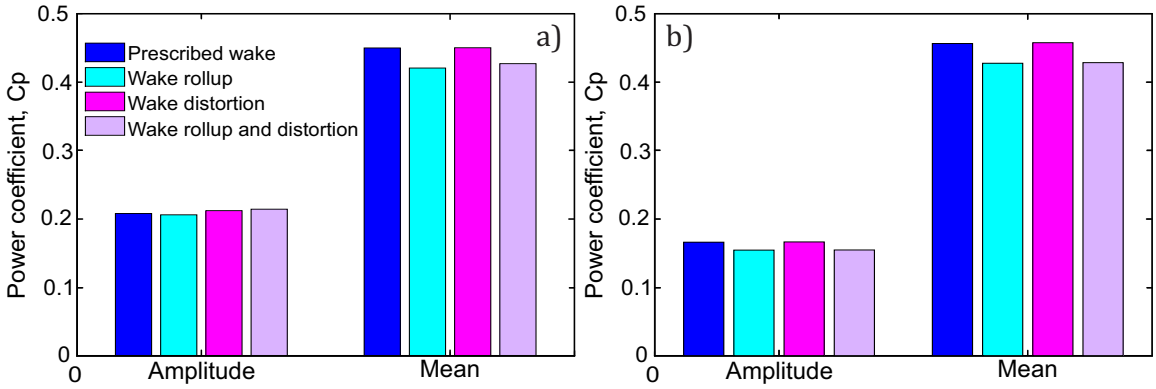

Fig. 5.5 The unsteady amplitude and mean power coefficient, as predicted by the different time-domain VLM simulations, for an axially uniform gust. Mid-span reduced frequency is (a) 0.35, and (b) 1.1.

Turning now to the case including wake distortion by the unsteady gust (bright pink bars), and comparing it to the baseline case, the effect on the mean power coefficient is minimal. At the lower frequency, the amplitude of the unsteady response increases slightly, but only by about 2%. At the higher frequency there is no change to the wake distortion case compared to the baseline. Thus, the wake changes due to gust distortion have a marginal impact on the unsteady response, despite the relatively large gust amplitude (15% of the mean axial flow). The case including both wake rollup and distortion (light pink bars) shows a reduction in mean power due to the wake rollup, and a slight increase in unsteady response amplitude due to the wake distortion, at the lower frequency. At the higher frequency, this case is virtually identical to the case with only wake rollup included (light blue bars). Overall, with an axially-uniform gust, changing the wake model has a minimal impact on the unsteady response of the turbine, though the wake rollup has a bigger impact than that of the distortion, and rollup also reduces the mean power by 10%.

Figure 5.6 shows results for the same four wake models but with the turbine undergoing sinusoidal gust forcing, as illustrated in Figure 5.2b. The unsteady flow amplitude is again 15% of the mean freestream velocity, and the mid-span reduced frequency is 0.35 in Figure 5.6a and 1.1 in 5.6b. As with the uniform gust case, the mean value of the loading is reduced by the wake rollup (light blue), and in this case it also impacts the unsteady load amplitude at both frequencies.

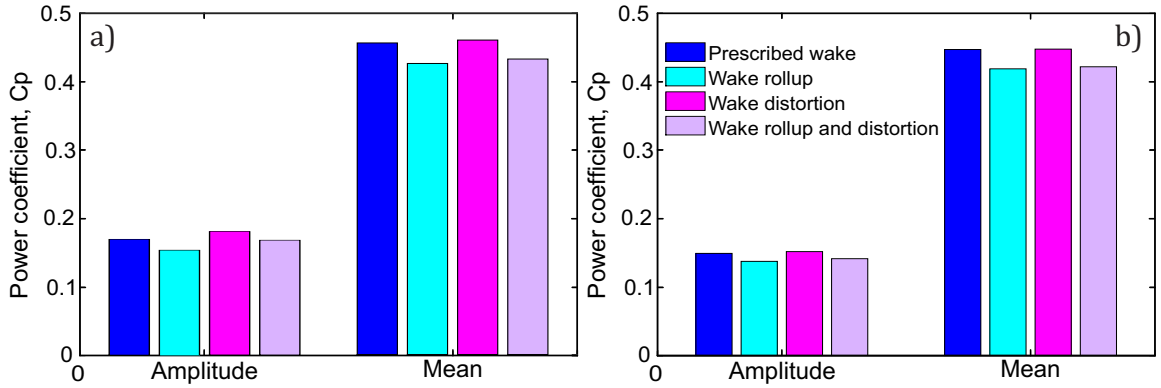

Fig. 5.6 The unsteady amplitude and mean power coefficient, as predicted by the different time-domain VLM simulations, for an axially uniform gust. Mid-span reduced frequency is (a) 0.35, and (b) 1.1.

The results in Figure 5.6 differ from the uniform gust case in Figure 5.5 in that wake rollup effects (light blue) have a more significant impact on the unsteady load amplitude compared to the baseline prescribed wake case (dark blue). The unsteady amplitude is reduced by 10% for the low frequency case (5.6a) and by 8% for the high frequency case (5.6b). The gust distortion effects (bright pink case) have an impact on the unsteady load amplitude at the lower reduced frequency, increasing it by 7%, but are relatively modest at the higher frequency.

A few observations can be made about the results shown in Figures 5.5 and 5.6. The effect of wake distortion by the gust appears to be most strongly felt at low reduced frequencies, but is negligible at high frequencies. The effect of wake rollup reduces the mean load throughout, and also reduces the unsteady load amplitude in the case of a sinusoidal gust (Figure 5.6). For the uniform gust (Figure 5.5), wake rollup only affected the unsteady load amplitude at the higher frequency.

There are a few possible reasons as to why the characteristics of the load response differ between the low-frequency and high-frequency result in Figure 5.5, and why they do not in Figure 5.6. The two physical effects responsible for inviscid unsteady loading are the downwash caused by the unsteady wake and the added mass. If, for a particular unsteady flow case, the wake is the dominant factor of the two, changes to the wake should have a relatively larger effect on the load response. This may be the case for the case for the sinusoidal gust loading in Figure 5.6, and for the high-frequency uniform gust in Figure 5.5b.

In both Figure 5.5 and 5.6 the wake rollup and gust distortion effects superpose in an approximately linear way, and so the two phenomena appear to be independent of one another. Not shown here is the effect on the phase of the unsteady response. This was found to change slightly with different wake models, but only in the order of 3-5^o.

Having determined that the wake rollup effect can have an impact on both steady and unsteady load, and that the effect of wake distortion is relatively minimal at least at high frequencies, we can use the corrected frequency-domain VLM introduced in Section 3.2.5 of Chapter 3 to investigate the effect of wake rollup over a range of reduced frequencies. While this wake correction will not give answers exactly equivalent to the time-domain VLM using the full free-vortex wake model (Equation 3.11d), it does enable the effects of wake rollup on the unsteady response to be quantified in a parametric study. This can be done quickly and at a high blade and wake lattice resolution, which is prohibitively time-consuming using the time-domain VLM (see Section 3.2.2). This parametric study will be shown later in this chapter, in Section 5.4.3. First, the URANS simulations will be introduced and the effect of viscosity and non-linearity on the wake and unsteady loads will be discussed.

5.3 Viscous modelling: URANS

The details of the turbine geometry and the RANS simulation details can be found in Chapter 3, Section 3.3. The turbine is a 3-bladed model (see Figure 5.1), and a single blade in a third of an annulus was modelled in the RANS simulations, with periodic boundaries to account for the remaining blades. The results are extrapolated to full-annulus, which will be shown below in Sections 5.4.1 and 5.4.2. The turbine nacelle and support structure are not modelled.

To generate the axially uniform gust (Figure 5.2a) in the URANS simulations, a uniform harmonic oscillation (Equation 5.1) was applied to the axial velocity across the whole inlet. Since the OpenFOAM incompressible solver is pressure-driven, this creates an instantaneous change in pressure across the whole computational domain at every time step. The annular-sinusoidal gust (Figure 5.2b, from Equation 5.2) was generated through spatial variation of the inlet velocity: the axial inlet velocity was set to vary sinusoidally with the annulus angle, with no variation in time. This meant that the turbine blades rotated through a series of steady jets, the magnitude of which varied sinusoidally around the annulus.

Unlike the uniform gusts, the annular-sinusoidal gusts did not propagate instantaneously through the domain, but travelled with the flow. As such, the sinusoidal gusts required more simulation time, and the gust amplitude diminished gradually due to dissipation (see Figure 5.7). All sinusoidal gusts were tested in empty inlet domains prior to simulation, so that the amplitude of the gust at the blade location could be found for a given inlet gust amplitude. For the final simulations, both the gusts and the unsteady turbine wakes were allowed to propagate fully through the domain before the final data was recorded.

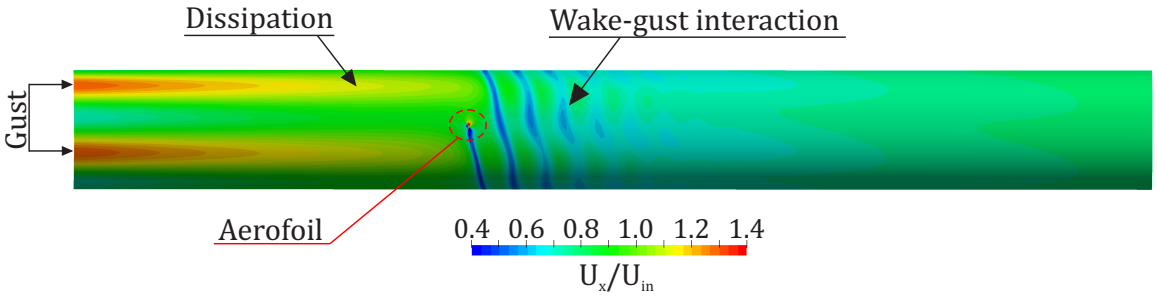

Fig. 5.7 Contours of axial velocity from a URANS simulation of an annular-sinusoidal gust interacting with the turbine. Circumferential cut at 90% blade span.

Simulating only a third of the turbine annulus places no restriction on the axially uniform gust, as each blade is affected equally and at the same time by the uniform gust. The annular-sinusoidal gusts, however, must have an integer number of sinusoidal wavelengths present in the domain to avoid a discontinuity at the periodic boundary. When simulating a third of an annulus the spatial gust distribution must be given by $sin(3\theta n)$, where n is an integer. The maximum value of n considered in this study was 2, as gusts with higher frequencies were found to dissipate excessively by the time they reached the rotor plane. The reduced frequencies of gusts with $n > 2$ were also much higher than the range considered in this project.

In order to study the effects of gust amplitude on the viscous unsteady response, two different unsteady velocity amplitudes were considered for the axially uniform gusts: 7.5% and 15% of the steady axial freestream velocity. These gust amplitudes correspond to a mid-span angle of attack variation of $\pm 1.5^o$ and $\pm 3.0^o$, respectively. The incidence variation at the hub will be larger, while it will be smaller at the tip.

As mentioned in Chapter 3 (Section 3.3.1), the PIMPLE algorithm used by OpenFOAM's pimpleDyMFoam solver allows for stable transient simulations at Courant numbers much larger than 1. For the axially uniform gust simulations the Courant number was set to 1,000

Table 5.1 Summary of the unsteady gusts interacting with the turbine in the URANS simulation.

No.	Type	Amplitude u_{gust}/U_x	Mid-span reduced frequency, k
1.	Annular-sinusoidal	0.09	1.10
2.	Annular-sinusoidal	0.08	2.15
3.	Axially uniform	0.15	0.15
4.	Axially uniform	0.075	0.35
5.	Axially uniform	0.15	0.75
6.	Axially uniform	0.075	1.15

while the unsteady turbine wake was propagating through the domain. When the unsteady wake reached the domain outlet the Courant number was reduced first to 100 for at least one load cycle, and then to 10 until a sufficient amount of data had been collected. For the annular-sinusoidal gusts, the Courant number was kept at 100 while the gust was propagating through the domain, as raising it to 1,000 caused the gust to dissipate completely. A Courant number of 10 resulted in a time step that could capture frequencies up to 17,000 Hz, according to the Nyquist criterion. As a comparison, the turbine rotational frequency was 1.8 Hz and the highest gust frequency tested was 10.9 Hz. As such, a Courant number of 10 was sufficient to capture the relevant oscillations in the flow. This assumption was justified by the results, as reducing the Courant number from 100 to 10 did not alter the unsteady load response.

5.4 URANS simulation results

This section presents the results from the unsteady RANS simulations. A summary of the different unsteady gusts tested, parameterised in terms of their mid-span reduced frequencies and amplitudes, is given in Table 5.1. Axially uniform gusts refer to the gust depicted in Figure 5.2a, while annular-sinusoidal gusts are depicted in Figure 5.2b.

First some qualitative features of the unsteady flow field will be examined, primarily focusing on wake development. After this, the unsteady loads predicted by the URANS illustrations will be compared to VLM results, and the importance of viscous effects for the unsteady loads of this turbine geometry will be determined.

5.4.1 The wake

In this section we look at the changes to the turbine wake as a result of the turbine interacting with the unsteady gusts. Two different gust events are chosen to illustrate the wake effects: an annular-sinusoidal gust with mid-span reduced frequency 1.1 (gust No. 1 in Table 5.1), and an axially uniform gust with mid-span reduced frequency of 0.75 (gust No. 5 in Table 5.1). There is an important difference between these two gusts, related to the wake-resonance condition associated with returning wake effects. The unsteadiness in a particular returning wake segment can act either in phase or out of phase with that of the segments one revolution up- and down-stream of it. The annular-sinusoidal gust is creating a wake where all returning wake segments are acting approximately in-phase; this causes resonance. The axially uniform gust shown in this section (gust No. 5 in Table 5.1), however, is not at a resonant condition, so the different returning wake segments are not acting in phase.

Figure 5.8 shows the velocity flow fields for the turbine under steady flow conditions and responding the two different gusts. In each case, the top plot is a circumferential cut showing the aerofoil section at 90% span, while the bottom plot gives the meridional view. These views show the differences in the returning wake features of each individual case. In the steady flow case (Figure 5.8a), the wake (visible as a dark blue stripe) decreases in strength as it propagates away from the turbine.

Comparing the flow field caused by the sinusoidal gust (5.8b) with the steady flow field (5.8a), the 2D aerofoil view shows the variation in wake strength caused by the unsteady gust interaction. The peaks of the wake strength in each returning wake segment are marked with a dashed line on Figure 5.8b. The line is nearly horizontal , indicating that the returning wake segments act approximately in phase (it is not exactly horizontal; this is likely to be because of wake swirl) . The wake is also propagating further downstream in the unsteady case than the steady simulation; the steady wake is mostly dissipated at 1.5 turbine diameters downstream, according to Figure 5.8, while the peaks of the unsteady wake are visible well past 2 turbine diameters downstream.

Looking now at the flow field caused by the uniform gust (Figure 5.8c), at the 2D aerofoil view at 90% span, there is significant variation in the strength of the returning wake segments. The peaks of each returning wake segment are marked with dashed lines, and they can be seen to occur at different positions around the annulus. There is a stark difference between a wake which is "in-phase" with the gust (as for the sinusoidal gust case in 5.8b), and a wake which is "out-of-phase" with the gust (as for the uniform gust in 5.8c). Again, the gust

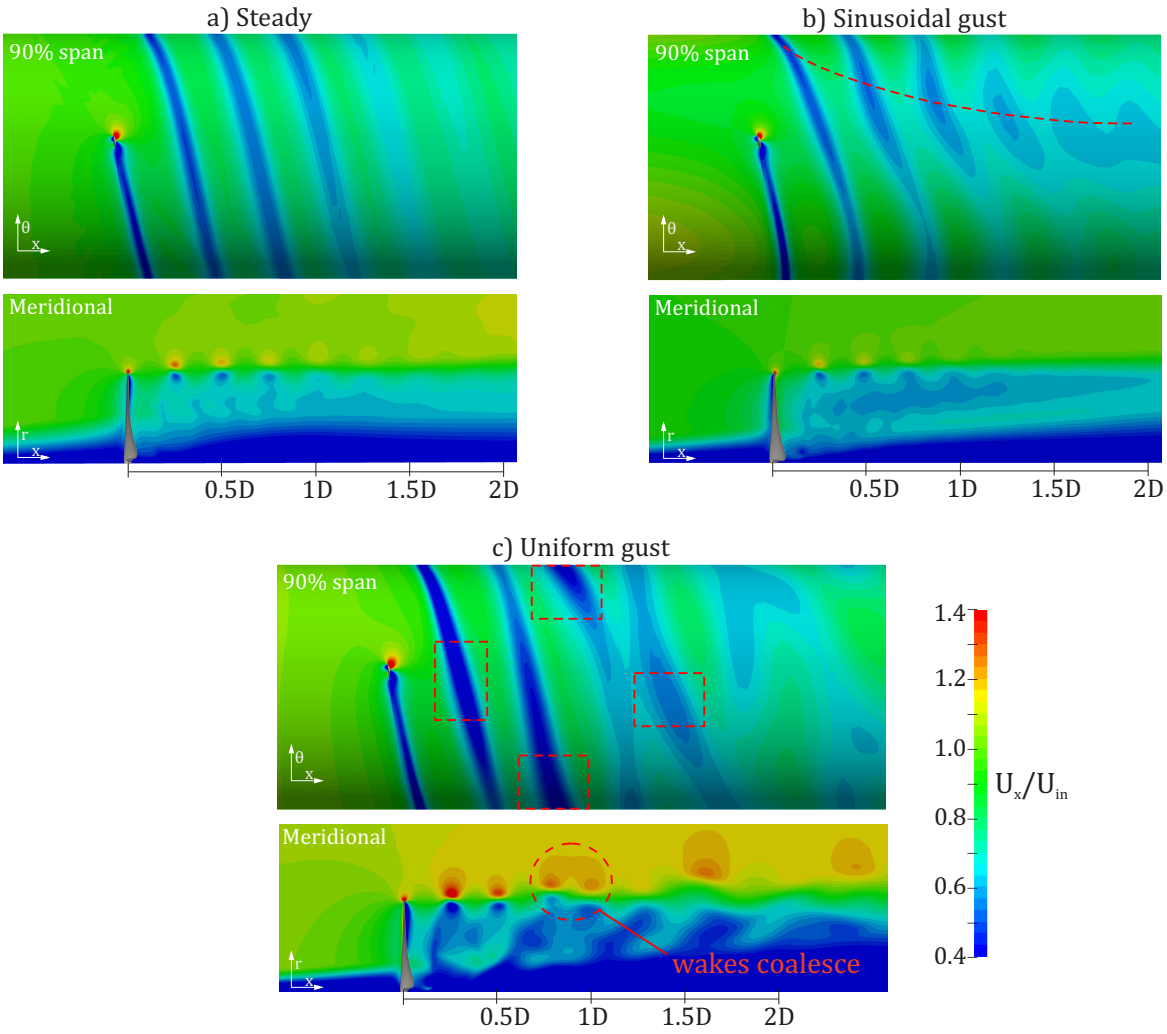

Fig. 5.8 Flow fields of normalised axial flow, shown as circumferential cuts at 90% span, and as meridional cuts at mid-plane. (a) Steady flow, (b) sinusoidal gust (No.1 in Table 5.1, $k = 1.1$), (c) uniform gust (No. 5 in Table 5.1, $k = 0.75$).

propagates further downstream without dissipating compared to the steady wake.

An additional interesting feature of the wake intermittency of the uniform gust can be seen in the meridional view in Figure 5.8c. The intermittent strengths of the returning wake sheets are causing the wake to become unstable. As a result, the tip vortices interact strongly with each other and appear to coalesce as they move downstream (marked in the meridional view in Figure 5.8c). This can be seen more clearly by considering the vorticity contours of the flow field. Figure 5.9 shows the vorticity contours in the meridional view, for the steady flow case (5.9a), for the sinusoidal gust (5.9b), and for the uniform gust (5.9c). Both the steady flow and the sinusoidal gust flow result in stable tip vortex formation, and the tip

vortices dissipate as they move downstream. The uniform gust conditions, on the other hand, result in an unstable wake formation, which breaks down as the wake convects downstream. The tip vortices appear to coalesce into groups of 2 or 3, effectively reducing the spatial frequency of the wake to a third of the blade passing frequency.

There are two important things to note about this wake behaviour as a result of the uniform gust. First, the returning wake segments were not observed to coalesce for all the uniform gust cases. They were found to do so most strongly at mid-span reduced frequency 0.75, which is the condition shown in Figures 5.8 and 5.9. As such, the instability of the wake is a function of the gust frequency relative to the turbine rotational frequency, rather than the gust type or amplitude. This is because the instability is driven by adjacent returning wake vortex segments having different strengths (see figure 5.8c). Second, this behaviour is strongly three-dimensional, as it is the radial movement of flow that allows the returning wake segments to coalesce.

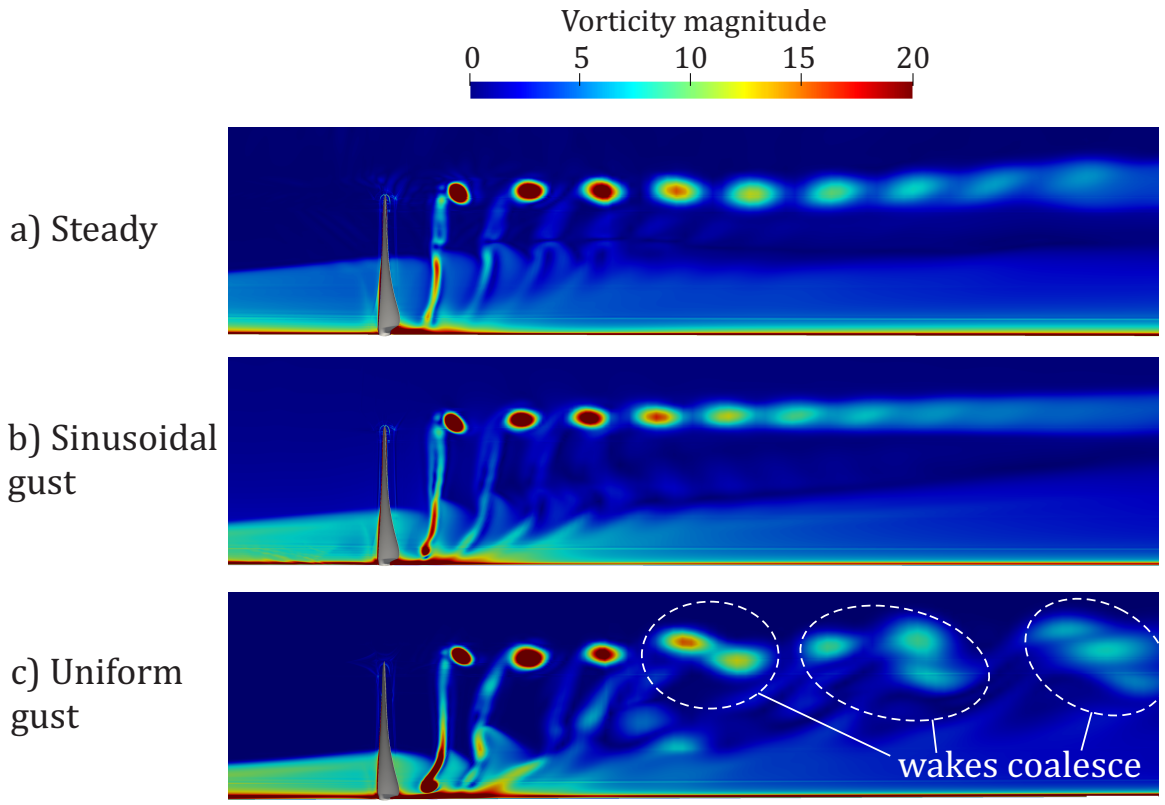

Fig. 5.9 Meridional view showing contours of vorticity magnitude for the steady flow and two unsteady flow states. (a) Steady flow, (b) sinusoidal gust (No.1 in Table 5.1, $k = 1.1$), (c) uniform gust (No. 5 in Table 5.1, $k = 0.75$).

5.4.2 Viscous effects

One of the objectives of the URANS study was to quantify the impact of viscous effects and stall on the unsteady response of this particular tidal turbine geometry. As was mentioned in Chapter 3 (section 3.3.2) the turbine geometry causes very large angles of attack around the hub section of the blade. As such, the gusts applied are likely to cause significant unsteady stall events in this region.

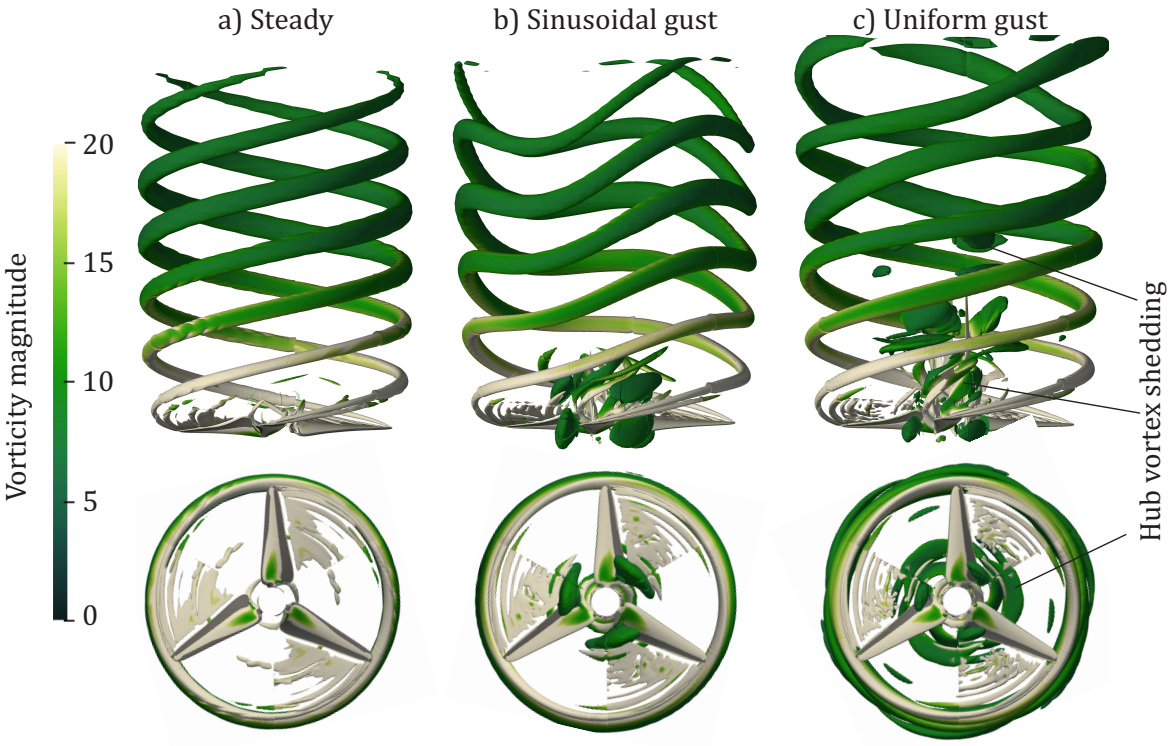

Fig. 5.10 3D vortex contours, identified using the q-criterion, for the steady flow and two unsteady flow states. The sinusoidal gust is No. 1 in Table 5.1 ($k = 1.1$), and the uniform gust is No. 5 in Table 5.1 ($k = 0.75$). The simulations were performed on a third of an annulus, and have been extrapolated to show the full-annulus flow field.

A qualitative view of the viscous stall effects in the 3D system can be seen by using the q-criterion to plot 3D contours of vorticity. The q-criterion is a method of vortex identification, which defines vortices as areas where the magnitude of the vorticity is greater than that of the rate-of-strain [58]. Figure 5.10 shows the vortices in the flow as identified by the q-criterion, for the steady flow (5.10a), the sinusoidal gust flow (5.10b), and the uniform gust flow (5.10c). The 3D contours represent the boundaries of the vortices, and are coloured by the local strength of the vorticity. Note that the simulations were performed on a third of the turbine annulus, and the data in Figure 5.10 has been extrapolated to show the full-annulus

flow field.

As observed above, the wakes of steady flow and the sinusoidal gust flow in Figure 5.10 are more stable than the wake of the uniform gust flow. Looking at the plan view (top row of Figure 5.10), the shape of the wake resulting from the sinusoidal gust (5.10b) oscillates in a sinusoidal manner; this oscillation is due to deformation by the gust. Despite these oscillations, the wake remains stable, as can be seen most clearly in the axial view (bottom row of Figure 5.10b). There is virtually no radial movement of the wake segments in the case of the sinusoidal gust. The uniform gust (5.10c), on the other hand, can be seen to have significant wake instability. The axial view shows radial movement in the returning wake segments, which is an indicator of the instability that results in wake coalescing, as was observed in Figure 5.9c.

Figure 5.10 also shows some of the hub separation events that we expect in the unsteady flow cases, as a result of the large angle of attack around the hub section. The steady flow case does not show any large-scale hub separation, though a small separation is visible on the blades. By contrast, both the sinusoidal gust and the uniform gust cause large-scale separation events around the hub, resulting in significant vortex shedding from the turbine hub. The shed hub vortices are marked on the uniform gust case in Figure 5.10c. They can also be seen in the sinusoidal case (5.10b), but are more prevalent and visible further downstream for the uniform gust case.

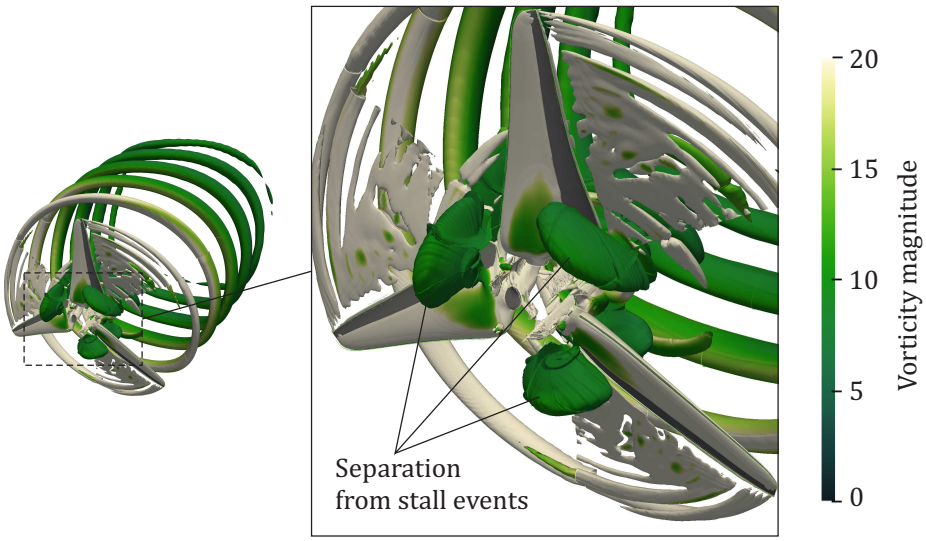

Fig. 5.11 Turbine hub stall in unsteady gust forcing, illustrated using 3D vortex contours identified using the q-criterion. The gust is sinusoidal (No. 1 in Table 5.1, $k = 1.1$).

The hub stall events are shown in more detail in Figures 5.11 and 5.12, which show the 3D vortex contours of the sinusoidal and uniform gust cases, respectively, identified with the q-criterion. Again, the results have been extrapolated from the simulation of a third of an annulus, to show the full-annulus flow field. In both cases, large-scale separation events are clearly visible around the turbine hub, and it can be seen that the hub stall is the cause of the additional vorticity observed in Figure 5.10. Again, the sinusoidal gust case exhibits a larger degree of unsteady hub separation than the uniform case. The influence of these stall events on the unsteady loading experienced by the turbine will be discussed below.

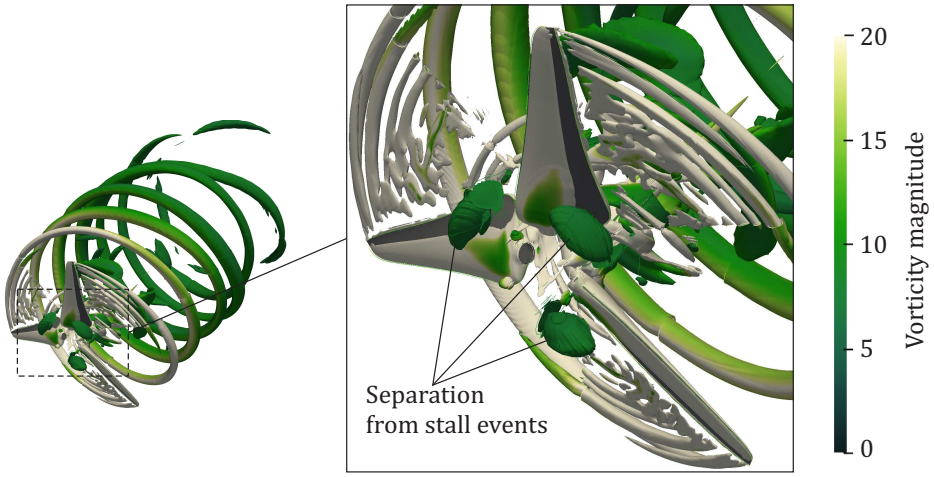

Fig. 5.12 Turbine hub stall in unsteady gust forcing, illustrated using 3D vortex contours identified using the q-criterion. The gust is uniform (No. 5 in Table 5.1, $k = 0.75$).

Having looked at some qualitative features of the flow field and wakes, we now look at the blade loading resulting from the unsteady gust interaction. As mentioned above in Section 5.3, the gusts and the unsteady wakes were allowed to propagate fully through the domain before the final measurements of load amplitude and phase were taken. The oscillating load showed some transient behaviours during this period, and in some cases the load history had evidence of significant nonlinear stall events. Figure 5.13 shows an example of the measured power coefficient during this start-up period, for a sinusoidal gust with mid-span reduced frequency 1.1 (gust No. 1 in Table 5.1). When the unsteady wake has propagated through the domain and reached the exit plane, the unsteady loading settles to its fully-developed oscillating behaviour. All the data shown in this chapter is taken from the fully developed stage.

It can be seen that that the average power coefficient during this fully-developed unsteady stage is higher than that predicted in the steady simulations. It is not clear whether this is

due to an inherent difference between the steady and unsteady solvers, or whether this is a feature of the unsteady flow interaction. It is interesting to note, however, that Holst et al [61] also conducted a large-scale CFD study of a tidal turbine interacting with unsteady flow, and they also found their transient simulations to have a gradually increasing mean load over the course of the simulation. This happened while their unsteady wake was propagating through the domain, but they do not mention whether the mean value settled at a later point in the simulation, after the unsteady wake had reached the exit plane.

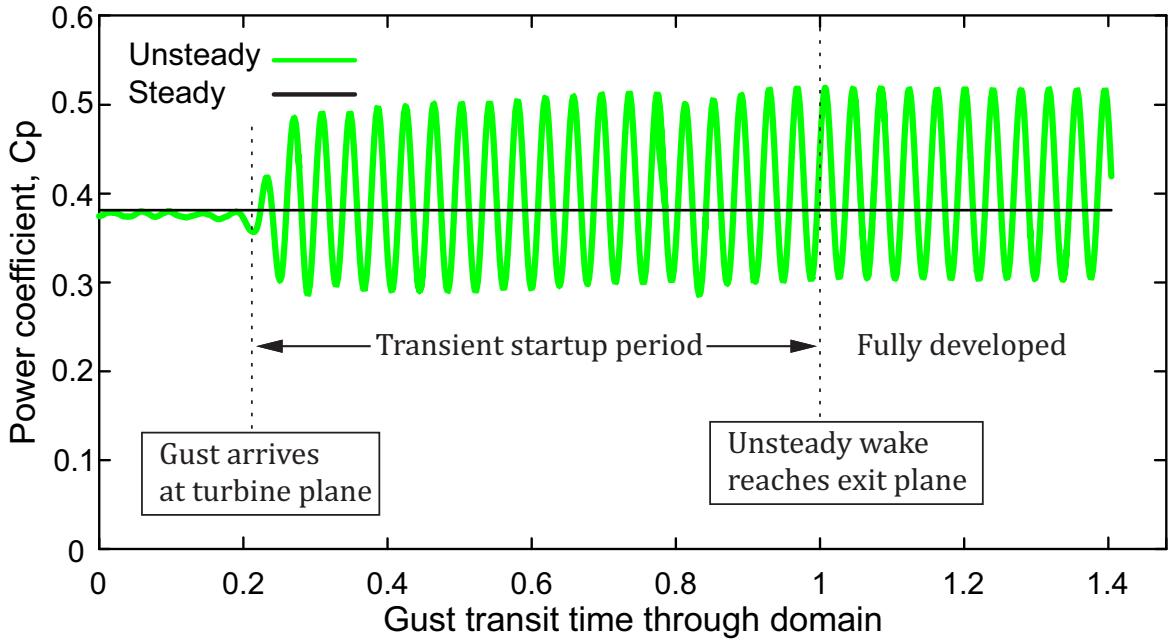

Fig. 5.13 Start-up sequence for the unsteady torque response to an annular-sinusoidal gust, at mid-span reduced frequency 1.1 (No 1 in Table 5.1).

Figure 5.14 shows a single load cycle of thrust coefficient (5.14a) and power coefficient (5.14b), taken from a point in the simulation after the fully-developed oscillating behaviour has been reached. The load cycles for two gusts are shown; that of a sinusoidal gust with mid-span reduced frequency 1.1 (No. 1 in Table 5.1) and a uniform gust with mid-span reduced frequency 0.15 (No. 4 in Table 5.1). The mean value over each cycle has been marked (dashed lines), as well as the thrust and torque predicted by the steady RANS simulations (black line).

As noted above, the URANS simulations settle to a higher mean thrust and torque than that predicted by the steady RANS solver. The response cycles to the two gusts also show different behaviours. These specific gust cases are shown here to illustrate the difference

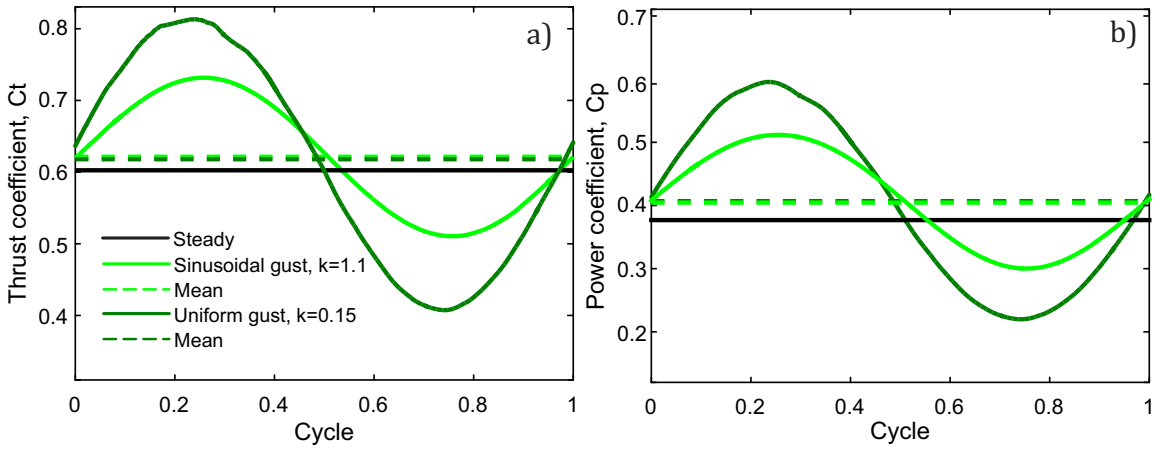

Fig. 5.14 A single unsteady turbine load cycle, as predicted by URANS simulation of a sinusoidal gust (No. 1 in Table 5.1) and a uniform gust (No. 4 in Table 5.1).

between a case with little visible viscous effects, and one with more substantial viscous effects. The unsteady load response to the sinusoidal gust (light green lines) varies smoothly, and is close to a perfect sinusoid. The load response to the uniform gust (dark green lines), on the other hand, does not vary smoothly. This is especially true in the region of peak load, where neither the thrust nor torque changes smoothly. They both deviate from the sinusoidal shape that would be predicted by an inviscid solver. This nonlinear response therefore signifies the presence of unsteady separation events.

The nonlinear behaviour shown in Figure 5.14 was more pronounced for the gusts with lower reduced frequencies. The gusts marked No. 3-5 in Table 5.1 showed some signs of nonlinear viscous effects during the fully-developed oscillations, while gusts No. 1, 2 and 6 did not. Notably, then, the gust frequency seemed to be more significant for the unsteady viscous stall to occur than the gust amplitude, for this geometry and this particular set of gust parameters.

5.4.3 Validation of VLM, and the applicability of 2D inviscid modelling to 3D viscous systems

In this section the URANS results are compared to the inviscid 3D VLM and to predictions by 2D classical unsteady aerofoil theory. The frequency-domain VLM is used, in both the original prescribed-wake form, and with the steady correction for wake rollup described in Chapter 3, Section 3.2.5. Earlier in this chapter, in Section 5.2.2, wake rollup was shown to impact both the mean turbine load and the amplitude of unsteady load response to gusts.

Table 5.2 Non-dimensional parameters used in this section to represent the unsteady flow response.

Name	Nomenclature	Equation
Torque (Nm)	Q	
Thrust (N)	T	
Turbine rotation (rad/s)	Ω	
Power coefficient	C_p	$Q\Omega/(0.5\rho U_\infty^3 A)$ (Equation 3.19)
Thrust coefficient	C_t	$T/(0.5\rho U_\infty^2 A)$ (Equation 3.20)
Gust amplitude	η	$\Delta u_{gust}/(2U_\infty)$
Unsteady power coefficient	C_p/η	$(Q-\bar{Q})\Omega/(0.5\rho U_\infty^3 A\eta)$
Unsteady thrust coefficient	C_t/η	$(T-\bar{T})/(0.5\rho U_\infty^2 A\eta)$

The steady wake correction to the VLM allows for further evaluation of wake rollup effects, across a range of reduced frequencies. In this section, the ability of 2D and 3D inviscid modelling to predict the unsteady loading of a tidal turbine geometry is thus evaluated, and the importance of wake rollup effects is quantified.

The results in this section are shown in terms of unsteady normalised power and thrust coefficients, the former of which is a measure of the unsteady torque and the latter of the unsteady thrust. These were found by Sequeira [114] to be an appropriate way of normalising the unsteady response of turbine aerofoils to gusts of different amplitudes. The definition (given in Table 5.2) is the unsteady variation in power or thrust coefficient, normalised by the unsteady flow amplitude η (which is expressed as a fraction of the mean axial flow). Note that the power and thrust coefficients are normalised with respect to the mean flow conditions.

Figure 5.15 shows the unsteady power coefficient over a single load cycle for two different axially uniform gusts and an annular-sinusoidal gust. In each plot, the URANS (green lines) and the two 3D VLM versions (black and blue lines) are compared to predictions by 2D aerofoil theory (red lines), using the Theodorsen function for the load response to uniform gusts and the Sears function for the response to sinusoidal gusts.

Figure 5.15a shows the response to uniform axial oscillation with mid-span reduced frequency 0.15. It shows that the Theodorsen function over-predicts the load amplitude for this relatively low-frequency gust, while the two VLM cases give similar answers that correspond more closely to the URANS. As observed above, the URANS is not a perfect sinusoid and displays some nonlinear viscous effects, but the 3D VLM gives a good approximation to the response. Figure 5.15b shows the response to another axially uniform gust, but this time with

mid-span reduced frequency 0.75. In this case, the 2D and 3D models give similar results, and again have good agreement with the URANS. A slight improvement of the agreement is given by the VLM with wake correction (blue line).

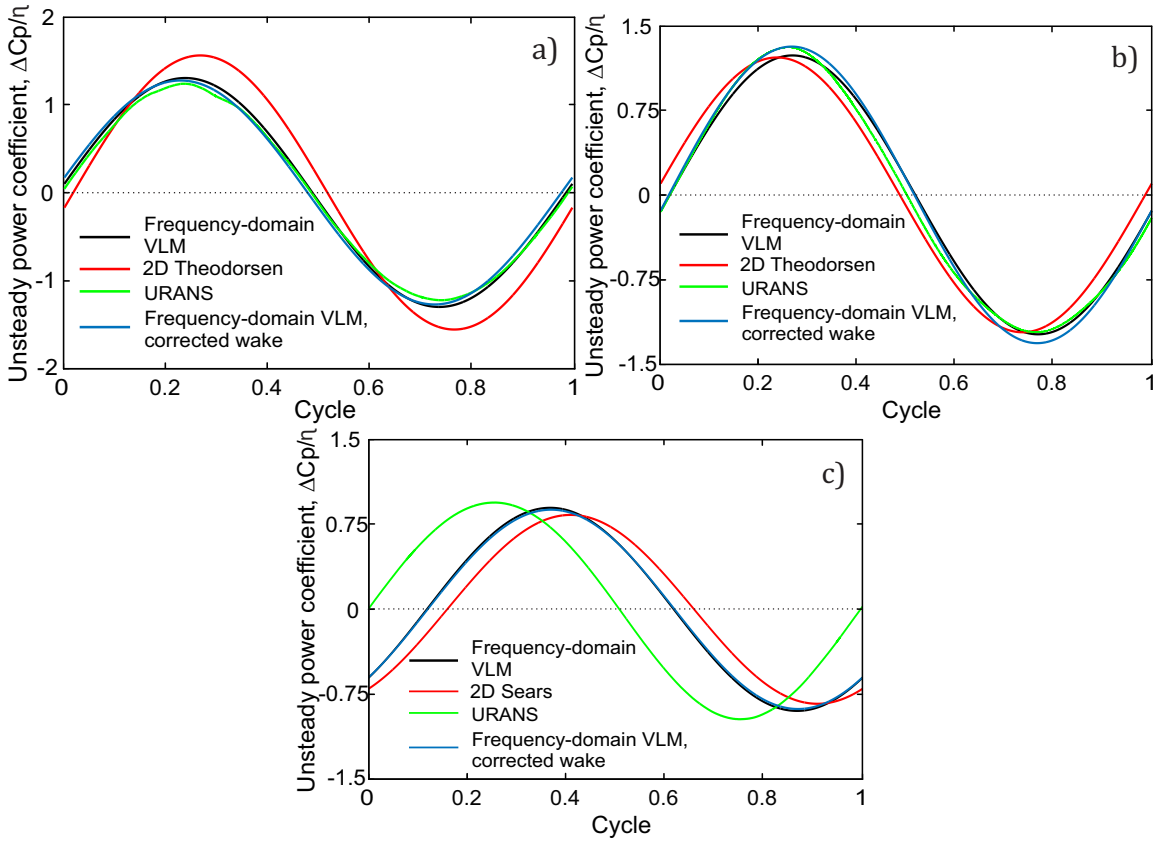

Fig. 5.15 A single load cycle of the turbine, in terms of the unsteady power coefficient (definition in Table 5.2). (a) Axially uniform gust at mid-span $k = 0.15$, (b) axially uniform gust at mid-span $k = 0.75$, (c) annular-sinusoidal gust at mid-span $k = 1.1$.

Figure 5.15c shows the response to an annular-sinusoidal gust with mid-span reduced frequency 1.1. Here, a different trend is observed in the results: both the 2D and 3D inviscid models severely over-predict the phase lag caused by the unsteady flow interaction. The amplitude is most under-predicted by the 2D model, while the two 3D VLM predictions are almost identical and agree more closely with the amplitude predicted by the URANS simulation.

To illustrate the results more clearly, and in order to see the trends predicted across a range of unsteady flow frequencies, Figures 5.16 to 5.19 show the unsteady response in terms of the amplitude and phase of the sinusoidal response. This is plotted against the mid-span

reduced frequency. The amplitude is defined as the peak-to-peak normalised power or thrust coefficient. In the URANS results the phase varies slightly over the load cycle. The phases associated with the URANS results shown in the figures are therefore averaged over one load cycle.

Figures 5.16 and 5.17 show the unsteady amplitude and phase of the turbine load response to axially uniform oscillating inflow; Figure 5.16 shows the power coefficient while Figure 5.17 shows the thrust coefficient. Predictions from the URANS, original VLM and corrected VLM are shown. The 2D result is obtained using the Theodorsen function. Considering first the amplitude of the normalised power coefficient (Figure 5.16a), the original VLM (black line) prediction corresponds well to the URANS results (green line), and the original VLM is within 4% of the URANS at all the data points.

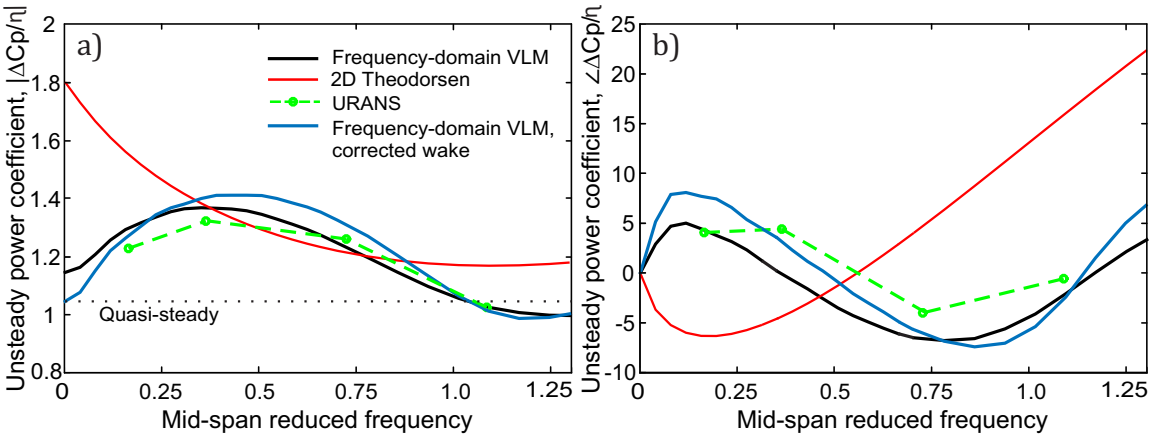

Fig. 5.16 (a) Amplitude and (b) phase of unsteady turbine response to axially uniform gusts of different frequencies, in terms of the normalised power coefficient.

The 2D model, by contrast, starts out by over-predicting the amplitude at low frequencies, and then under-predicts it in the intermediate frequency range, before returning to over-predicting at high frequencies – the trend is totally different from any of the 3D models. The wake correction to the VLM (blue line) has a fairly significant impact on the characteristic, but does not necessarily improve the correspondence to the URANS results. Figure 5.16b shows a similar trend in the phase. The deviation between 2D and 3D response prediction is significant, with the phase responses following completely different trends and the 3D model offering better agreement with the URANS results.

Figure 5.17 shows the turbine load response in terms of the normalised thrust coefficient. While there is still fairly good agreement between the URANS and the 3D VLM predictions,

the inviscid models under-predict the amplitude compared to URANS results at the lower gust frequencies. The 2D prediction also tends to under-predict the response other than at low frequencies. As with the power coefficient, the trend given by the 2D model is a different shape from the 3D models. Unlike the results for power coefficient in Figure 5.16, in this case the addition of the steady wake correction to the VLM improves the agreement with the URANS. As in Figure 5.16, the phase (Figure 5.17b) of the 3D model is in closer agreement than the 2D model with the URANS. Again, it should be noted that it was difficult to define the phase from the URANS results.

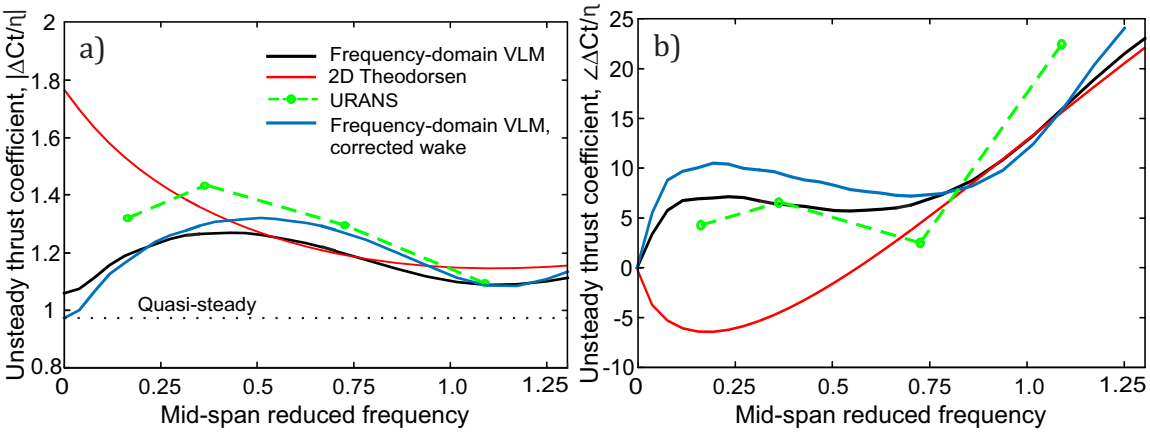

Fig. 5.17 (a) Amplitude and (b) phase of unsteady turbine response to axially uniform gusts of different frequencies, in terms of the normalised thrust coefficient.

As mentioned in the previous section, the likelihood of flow separation and other non-linear effects was primarily determined by the gust frequency for this set of gusts, with the lowest gust frequencies showing more nonlinear behaviour. It was also noted that the stall occurrences were confined to the vicinity of the hub, meaning that the load effects due to stall are unlikely to affect the unsteady torque to any significant degree. They may, however, have an effect on the thrust, and so a possible explanation for the deviation from inviscid prediction for the thrust at low frequencies in Figure 5.17 may be the unsteady separation events. This is of potential importance for unsteady load calculations, as viscous effects in this range result in both 2D and 3D inviscid models under-predicting the load amplitude. This will have a detrimental effect on the accuracy of fatigue life calculations carried out using an inviscid model.

Figure 5.17 shows that the thrust coefficient approaches the 2D characteristic with increasing reduced frequency. Figure 5.16, however, shows the power coefficient deviating significantly from the 2D function throughout the frequency range. This can be explained

by considering the characteristics of unsteady flow in 3D. In the previous chapter, the local unsteady lift was found to approach the 2D characteristic at high frequencies. This finding held everywhere except near the blade tips, where 3D effects dominated throughout the reduced frequency range. This suggested that for tidal turbines 3D effects would have the most significant consequences for unsteady torque and bending moment, since these are mainly generated near the blade tips. Thrust, on the other hand, would approach 2D behaviour at high reduced frequencies. This corresponds to what we see in Figure 5.16 and Figure 5.17.

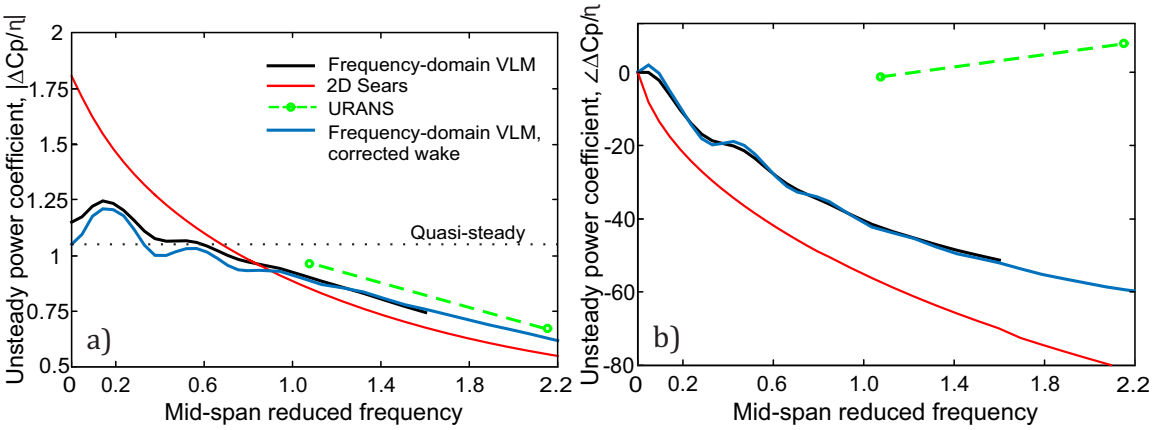

Fig. 5.18 (a) Amplitude and (b) phase of unsteady turbine response, in terms of the normalised power coefficient. The response is to annular-sinusoidal gusts.

Figures 5.18 and 5.19 show the response to inflow varying sinusoidally around the turbine annulus. As above, the URANS and 3D VLM results are compared to the 2D prediction, this time from the Sears function. In this case, due to the limitations on the simulation of sinusoidal inflow mentioned in Section 5.3, only two inflow frequencies were simulated in URANS. Figure 5.18 shows the unsteady response in terms of the normalised power coefficient. The amplitude is quite well predicted by the 3D VLM compared to the URANS results. The phase, however, is not well predicted at all (as also noted in relation to Figure 5.15). The two VLM solvers give almost identical results, so the wake correction does not make a big difference to the response characteristic, in contrast to the case of the axially uniform gusts in Figures 5.16 and 5.17.

Figure 5.19 shows the unsteady normalised thrust coefficient. Again, the amplitude compares well between the URANS and VLM results. The steady wake VLM correction does not significantly affect the results, other than slightly amplifying the returning wake effects. As mentioned in the discussion of Figures 5.16 and 5.17, we expect the thrust to approach the 2D characteristic at high reduced frequencies, but not the torque. This is

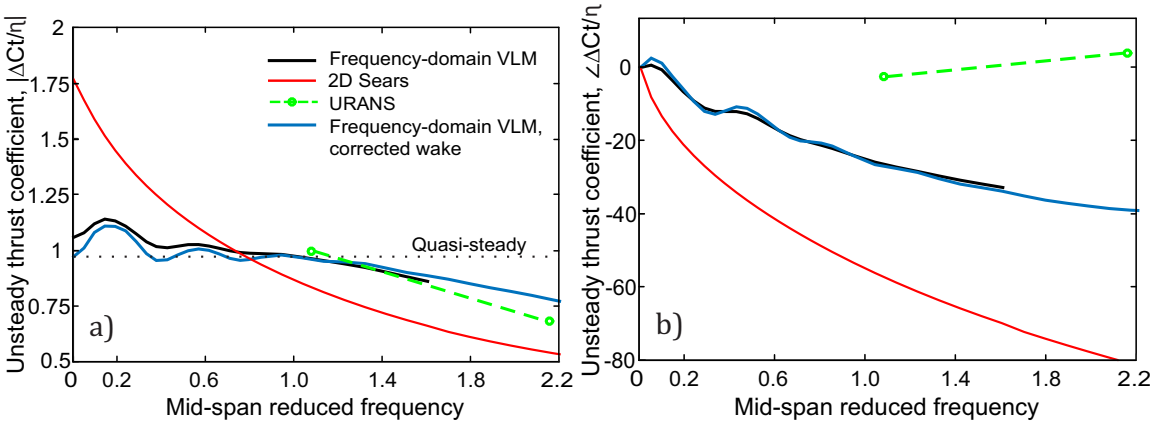

Fig. 5.19 (a) Amplitude and (b) phase of unsteady turbine response, in terms of the normalised thrust coefficient. The response is to annular-sinusoidal gusts.

because 3D effects are confined to the tip region at high frequencies (see Chapter 4 for more details on this). Notably, however, in Figures 5.18 and 5.19 the trend is the opposite. The unsteady power coefficient (Figure 5.18) appears to approach the 2D characteristic, while the thrust coefficient (Figure 5.19) does not.

A possible explanation for the break from the expected trend in Figure 5.18 and Figure 5.19 could be that the effect of the unsteady wake is substantially smaller for the annular-sinusoidal gust, compared to the axially uniform gust. Recall that inviscid unsteady response consists of added mass forces and aerodynamic damping by the unsteady wake. For a sinusoidal gust the added mass will be relatively small, and if the wake damping is also small the response will be approximately quasi-steady. This is in fact what we see for the thrust coefficient, in Figure 5.19a. For reduced frequencies below 1.0 the characteristic oscillates around approximately the quasi-steady value (dashed line) – the oscillations are due to returning wake effects. Also at high frequencies the lack of wake damping causes the unsteady thrust to deviate from the 2D prediction.

The unsteady power coefficient (Figure 5.18) is more affected by 3D wake damping than the thrust, because it is primarily dependent on the load near the blade tips. As such, the unsteady amplitude of the power coefficient is less than the quasi-steady value throughout the majority of the frequency range, resulting from the aerodynamic damping by the 3D wake. However, its apparent similarity to the 2D characteristic at high frequencies is likely to be a coincidence, as the physical origin of the wake damping is different for the 2D and 3D models (see Chapter 4).

The relatively small influence of the unsteady wake is also a possible explanation for the small phase response of the URANS results, seen in Figures 5.18b and 5.19b. The URANS predicts substantially smaller phase response compared to predictions by both the Sears function and 3D VLM, both of which predicts a gradually increasing phase lag throughout the frequency range. Diminished wake damping is a possible reason for the small phase response, but does not explain why the 3D VLM does not predict the same trend as the URANS. It is possible that the discrepancy stems from the difficulty in defining phase for the URANS case. The gust is generated through sinusoidally varying the axial flow around the turbine annulus (see Figure 5.2b), and the phase is obtained assuming that the gust front reaches the leading edge of the blade uniformly, with no spanwise variation. However, this is a simplifying assumption; because the leading edge of the blade does not extend in a straight line radially, the blade hub will meet the gust front "ahead" of the blade tip. The effect of this spanwise variation in gust arrival is hard to predict, but may be the cause of the discrepancy in phase between the URANS and VLM results.

5.4.4 Discussion

From the results presented in this section we can conclude that the 3D inviscid VLM provides good predictions of the unsteady load response. The steady wake correction provides a slight improvement to the accuracy of the model in some cases, but by far the most significant is the improvement by using a 3D model instead of 2D functions. The 2D characteristic has been proven to be unable to predict the unsteady load response. The inadequacy of the 2D model is particularly stark in the case of blade torque. This is because 3D effects are concentrated at the tips of the blade, which contribute more strongly than the inboard sections to torque.

Comparing the 2D and 3D predictions of load amplitude in Figures 5.16 to 5.19, some important differences can be seen. The 3D models show that the peak load amplitude is not the quasi-steady value (which is what the 2D models predict), but occurs in the reduced frequency range 0.4-0.6 for axially uniform gusts, and in the range 0.1-0.3 for annular-sinusoidal gusts. In the case of the axially uniform gusts, the load amplitude is also under-predicted by the 2D function in this range. As such, neither the quasi-steady response nor the 2D functions can be assumed to give conservative estimates of unsteady loading.

The 3D unsteady wake was shown in Chapter 4 to drive the unsteady load response. It is important to note the implication of this finding for the validity of load estimates based on 2D models. In BEMT modelling the performance of a turbine is evaluated at individual

2D blade sections, and corrections are applied to the 2D lift coefficient to account for the steady-flow downwash by the 3D wake (for example, using Prandtl's tip loss correction). If these quasi-steady corrections are applied to an unsteady 2D lift characteristic, rather than accounting for an unsteady 3D wake, the load amplitude will be severely under-predicted. Many past studies on 3D unsteady aerofoil response have utilised the assumption of a quasi-steady streamwise wake vorticity. A recent example is the lifting line model developed by Boutet and Dimitriadis [14].

To illustrate the hazard of assuming that 3D wake downwash can be corrected using the quasi-steady result, Figure 5.20 shows the unsteady load amplitude of the turbine for axially uniform gusts, in terms of the amplitude of the unsteady power coefficient. The figure shows the prediction by the 3D frequency-domain VLM (black line), and the prediction by the 2D Theodorsen function (solid red line). Shown for comparison is the result predicted by the Theodorsen function when corrected to account for quasi-steady 3D wake downwash (dashed red line). This effectively means that the load alleviation resulting from downwash induced by the streamwise wake vorticity in quasi-steady flow is used to correct the load in 2D unsteady flow. At reduced frequency 0.5, this results in the corrected Theodorsen function under-predicting the unsteady load amplitude by over 60% compared to the 3D response.

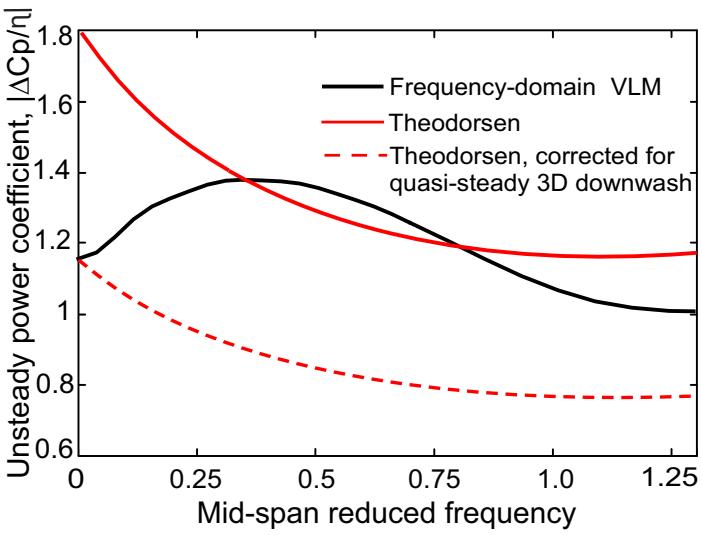

Fig. 5.20 Unsteady amplitude of the unsteady turbine response, in terms of normalised power coefficient. The response is to axially uniform gusts.

5.5 Conclusions

The objective of this chapter has been to estimate the 3D effects of wake rollup and gust distortion of the wake when calculating the unsteady load response of a tidal turbine to gusts, and to quantify viscous effects. One of the end goals of this study is to illustrate the differences between 2D and 3D unsteady flow response, and to show how 3D unsteady effects can impact turbine lifetime predictions.

The URANS study presented in this chapter revealed some effects of unsteady flow interaction on the turbine wake propagation and stability. The unsteady wake propagated further downstream in the domain before dissipating in the unsteady flow cases, compared to the steady flow benchmark case. In one gust case the unsteady wake became unstable, with different returning wake segments coalescing due to the intermittent strength of the wake vorticity. This did not occur in other simulations, as the instability emerged as a function of the gust frequency relative to the turbine rotational frequency. The effect was found to be strongly 3D, as it occurred through radial movement of the wake.

The results of this chapter show that while viscous effects can be important to unsteady load calculations, especially unsteady thrust, inviscid modelling in 3D is an appropriate tool for first-order calculations of turbine unsteady load response. Switching from 2D to 3D modelling results in significant gains in accuracy, as the physics of the 3D unsteady flow field are fundamentally different from 2D flow.

Considering the differences between 2D and 3D unsteady flow shown in Chapter 4, it is important to note what the consequences are for the applicability of 3D quasi-steady corrections (such as Prandtl's tip-loss correction) to 2D aerofoil sections when evaluating unsteady load response. Figure 5.20 showed that applying quasi-steady 3D load corrections to 2D unsteady transfer functions results in the unsteady load amplitude being strongly under-predicted. As such, it is potentially hazardous to apply steady 3D wake corrections to unsteady load predictions.

The trends predicted by the 3D frequency-domain VLM corresponded well with the URANS simulations. The time-domain VLM showed that including wake rollup affected the mean turbine loading and the unsteady load amplitude, and that distortion of the wake by the gust had minimal effect on the unsteady load at high frequencies. The prescribed wake used in the frequency-domain VLM can be corrected to account for wake rollup, but wake distortion cannot be corrected for. Including wake rollup effects in the frequency-domain

VLM increased the returning-wake effects, and gave marginally improved agreement with the URANS results. The speed of the frequency domain tool compared to the time-domain VLM more than compensates for the small loss of accuracy due to missing the distortion term. As such, this study shows that the inviscid vortex lattice model in 3D is accurate for first order prediction of unsteady turbine loads, and is a suitable tool for tidal turbine design.

Chapter 6

The effect of 3D gusts on unsteady response

6.1 Introduction

The previous two chapters focused on the effect of 3D geometry on unsteady gust response, and showed that the deviations from 2D predictions are largely due to the 3D wake. In these previous chapters, the gusts were designed to act uniformly along the span. This was in order to isolate the effects of 3D geometry on gust response that would otherwise be entirely 2D. Building on the knowledge of the past two chapters, this chapter deals with the unsteady response of 3D blades to gusts that are also 3D, varying in the spanwise direction relative to the blade.

In Chapter 2 an outline of the features of turbulent channel flow was given, and it was shown that tidal sites are highly turbulent with strongly three-dimensional flow fields. At the intermediate and large turbulent eddy scales, which are the most relevant for turbine load calculations, the turbulence is also strongly anisotropic. It was clear from a review of previous works that the relationship between the length scale of turbulent flow features and the unsteady load response of tidal turbines is not well established. While the streamwise turbulence intensity is widely acknowledged to be directly related to unsteady loading, the importance of the spatial shape of the turbulence has not been established.

It is therefore a challenge for designers to account for the intermittent, anisotropic turbulence present at tidal sites, and to determine what scales of turbulence have the most potential to do damage. It is intuitive to think that very small turbulent length scales are likely to

have negligible effects on the unsteady loads, but what is the limit beyond which this is true? It is necessary to know this information when choosing potential sites for development, so that initial site surveys can collect site data that is relevant for unsteady load response. From a turbine design perspective, it is also relevant to know what type of turbulence has the potential to do most damage to the turbine.

There is an additional problem facing designers looking to model realistic turbulence-blade interaction. The unsteady load models used in industry-standard BEMT codes use analytical 2D transfer functions from classical theory to obtain the load response at each blade section. However, all linear analytic functions are gust-specific, such that each function will only predict accurate load response to the gusts for which it was developed. For designers predicting unsteady response from the realistic ocean environment with highly turbulent 3D flow, choosing the correct gust transfer function is a challenging task. Often a realistic gust will not correspond well to any of the gust definitions available, and the high level of spatial anisotropy in the channel only compounds this issue. There is, therefore, a need for a more generalised approach for modelling the interaction of tidal turbine blades with unsteady flow.

In Chapter 4 the effects of 3D geometry on unsteady load response was determined by performing several test cases with different geometries. Adopting the same approach to finding the effect of spatial length scale on unsteady load response would require a large number of simulations, testing a range of gusts with different spatial shapes on several different geometries. In this chapter, we instead perform analysis allowing us to find the gusts to which a certain blade geometry is sensitive. In essence, the question we want to answer, and that is relevant to turbine designers, is this: *given a certain blade geometry, what kind of gusts does the designer need to look for in the flow field*?

To answer this question, this chapter uses eigenmode decomposition of the unsteady aerodynamic system. Eigenmode analysis has the benefit of giving fundamental information on how the aerodynamic system responds to forcing by a gust of any shape. This gives an improved understanding of unsteady gust interaction in both 2D and 3D, and it will be shown here that this understanding in turn enables a descriptive view of how blades interact with different turbulent length scales in the flow. This will be used to inform designers and site surveyors of the range of length scales that have the potential to damage the blade. The analysis will also show the existence of a cut-off spatial length scale beyond which turbulence no longer affects the unsteady loads on the turbine blades.

The eigenmode framework also provides generality to the gust-aerofoil interaction problem, since it allows the unsteady response of an blade geometry to be analysed independently of the gust. The gust-specific response will be shown to be reduced to the interaction between the gust and the eigenmodes of the system. This provides a step towards a generalised treatment of unsteady gust response, allowing gusts of any shape to be analysed in the same framework. This prevents designers from being restricted to the pre-defined gusts used in classical aerofoil theory.

In this chapter, the eigenmode decomposition method will first be introduced. Initial example cases will then be carried out in 2D to show the working principles of eigenmode decomposition. After that, the analysis will be extended to 3D systems and used to find the spatial cut-off length scale for unsteady load interference for a given blade geometry.

6.2 Eigenmode decomposition

Eigenmode decomposition of aerodynamic systems is described in a number of works by Hall and Florea [56] [38], whose methods are the basis of the work carried out in this chapter. They performed eigenmode decomposition of 2D and 3D aerodynamic systems, using both inviscid panel methods and Euler solvers as a base, for the purpose of investigating aerofoil interaction with unsteady gusts. Their objective was to develop a low-order model for calculating aerofoil response to transient gust flow, by using only a small number of the system eigenmodes. They successfully replicated the unsteady response using a small number of eigenmodes, if an additional quasi-steady correction term was also included. The method used in this chapter is based on the same principles and methodology as the method used by Hall and Florea, and has been adapted to work with the frequency-domain vortex lattice model (VLM) described in Chapter 3.

In Chapter 3 the vortex lattice model was shown to solve a matrix equation of the following form:

$$\mathbf{A\Gamma} = \mathbf{u} \tag{6.1}$$

The right hand side represents the unsteady freestream velocity normal to the blade surface. The vector $\mathbf{\Gamma}$ represents the unknown circulation strengths associated with each vortex panel, and is what gives the blade its lifting properties. The matrix $\mathbf{A}$ contains all the information about the blade geometry. In constructing the matrix $\mathbf{A}$, the Biot-Savart law (Equation 3.8) is used to obtain the induced velocity on every lattice collocation point by every vortex present in the lattice, given the vector of unknown panel circulations $\mathbf{\Gamma}$. In the case of the

frequency-domain model, $\mathbf{A}$ also contains the prescribed shape of the wake.

In previous chapters, the matrix $\mathbf{A}$ has been inverted to obtain the vector of unknown circulations $\boldsymbol{\Gamma}$. Instead, $\mathbf{A}$ can be decomposed into its eigenmodes. The process of eigenmode decomposition is similar to normal mode decomposition of an oscillating system (which is used, for example, to find the resonant frequency of beams). In the case of an oscillating system, the matrix is often real and symmetric, meaning that the resulting modes are orthonormal. This simplifies the analysis and means that the resonant frequencies of the system are represented by the individual modes. Because the modes of symmetric matrices are orthonormal, they will be independent of each other, in a manner analogous to x-and y-axes in a 2D system: magnifying the x-component of a vector has no effect on the y-component. The properties of the eigenmodes mean that the general motion of the system can be reconstructed as a linear superposition of the modes. For a 2D vortex lattice model divided into N panels, eigenmode decomposition will yield $N+1$ individual modes. For 3D VLM, eigenmode decomposition will yield N modes. The difference between 2D and 3D VLM is discussed in Chapter 3, Section 3.2.4.

The vortex lattice influence matrix $\mathbf{A}$, given in 2D by Equation 3.14 and in 3D by Equation 3.14, is complex and non-symmetric, meaning that none of the associated simplifications of symmetric matrices can be made. The eigenmodes will not be orthonormal, and so the modes will not necessarily be independent of each other, and the excitation of one mode will influence the others. The modes will, however, be linearly independent, meaning that no one eigenvector can be represented as a sum of the other eigenvectors. Because of the linear independence of the modes, they can still be used to recreate the response of the system to an arbitrary input, using superposition.

Representing $\mathbf{A}$ in the form of an eigenvalue equation is equivalent to finding all the possible cases where the induced surface normal velocity is a linear function of the blade circulation (i.e., $\mathbf{A}\boldsymbol{\gamma} = \mu\boldsymbol{\gamma}$). Writing the results in matrix form, the right eigenvector equation is given by:

$$\mathbf{A}\mathbf{V}_R = \mathbf{V}_R\boldsymbol{\Lambda} \tag{6.2}$$

where $\mathbf{V}_R$ is the matrix of right eigenvectors and $\boldsymbol{\Lambda}$ the diagonal matrix of eigenvalues. Similarly, the left eigenvector equation is given by:

$$\mathbf{V}_L\mathbf{A} = \mathbf{V}_L^H\boldsymbol{\Lambda} \tag{6.3}$$

Where $\mathbf{V}_L$ is the matrix of left eigenvectors and the superscript H indicates the Hermitian, the complex conjugate transpose of the matrix. If the eigenvectors are scaled correctly, the orthogonal properties of the left and right eigenvectors give the following relations:

$$\mathbf{V}_L^H \mathbf{V}_R = I \tag{6.4}$$

$$\mathbf{V}_L^H \mathbf{A} \mathbf{V}_R = \mathbf{\Lambda} \tag{6.5}$$

where I is the identity matrix. The purpose of the eigenmode decomposition of the aerodynamic system is to find an expression for the lattice circulation vector $\mathbf{\Gamma}$ in the following form:

$$\mathbf{\Gamma} = \sum^{k} \mathbf{V}_{Rk} c_k \tag{6.6}$$

Here the circulation vector associated with the blade is expressed as a sum of the right eigenvectors $\mathbf{V}_R$, each multiplied by a weight function $\mathbf{c}$. To solve Equation 6.1 we now have to find the eigenvectors of $\mathbf{A}$ and their associated weights. The weight parameters determine how much of each eigenmode contributes to the total circulation. This representation is possible because of the linear independence of the eigenvectors. The form of Equation 6.6 is chosen as such because it allows the weight vector $\mathbf{c}$ to be found, using the eigenmode properties as follows:

Substituting for $\mathbf{\Gamma}$ in Equation 6.1, using Equation 6.6:

$$\mathbf{A} \mathbf{V}_R \mathbf{c} = \mathbf{u} \tag{6.7}$$

Using the second orthogonality property (Equation 6.5):

$$\mathbf{V}_L^H \mathbf{A} \mathbf{V}_R \mathbf{c} = \mathbf{V}_L^H \mathbf{u} = \mathbf{\Lambda} \mathbf{c} \tag{6.8}$$

Finally, inverting $\mathbf{\Lambda}$, an equation for $\mathbf{c}$ is found:

$$\mathbf{c} = \mathbf{\Lambda}^{-1} \mathbf{V}_L^H \mathbf{u} \tag{6.9}$$

This equation shows that the properties of the weight vector $\mathbf{c}$ are determined by the inverse of the eigenvalues ($\mathbf{\Lambda}^{-1}$), the left eigenvectors ($\mathbf{V}_L^H$), and the vector representing the unsteady flow distribution on the blade ($\mathbf{u}$). In fact, it is the relationship between the left eigenvectors and the gust velocity vector that determines the properties of $\mathbf{c}$: the magnitude of each component of the $\mathbf{c}$-vector is a result of taking the dot product of the corresponding mode

eigenvector with the gust velocity vector. This implies that if the gust is similar in shape to the left eigenvector, the weight associated with that eigenmode will be large. The largest weight that a certain eigenmode could theoretically have would be in the case when the gust is identical to the mode. This interaction between the flow velocity and the eigenvectors will be referred to in this thesis as "*mode resonance*".

The benefit of this decomposition of $\mathbf{\Gamma}$ into two components, $\mathbf{V}_R$ and $\mathbf{c}$, is that the unsteady response can now be studied by looking at the properties of these two components. The eigenvectors $\mathbf{V}_R$ are determined entirely by the blade geometry, prescribed wake shape, and reduced frequency, as described in the influence matrix $\mathbf{A}$, which is independent of the spatial variation of gust velocity. The eigenvectors also represent a measure of what the aerodynamic system is "capable" of doing: the blade can only respond to forcing with a linear sum of its eigenmodes. This means that the eigenvectors show the fundamental properties of the aerodynamic system and its capability to respond to *any given input*.

The decomposition of $\mathbf{\Gamma}$ into the eigenvectors and weight functions means, as a result, that the only effect the gust shape has on the unsteady blade response is to determine the magnitude of the weight function. The way in which the blade can respond is already determined by the eigenvectors; the gust shape then determines how much each eigenmode will contribute to the total unsteady blade circulation. The more similar a gust is to an eigenmode, the more that mode will contribute to the total unsteady circulation.

The decomposition method described above can form the basis of a general view of unsteady response. By studying the eigenmodes in isolation, the general capability of an aerodynamic system to respond to arbitrary unsteady forcing can be determined. The mode resonance, through the weight vector $\mathbf{c}$, can then show how gusts interact with the modes to determine how a mode contributes to the overall response. This also gives us the ability to answer the question raised in this chapter: what kind of gust does the designer need to know about when considering a potential tidal site? In analysing the eigenmodes of the system, some modes will be found to have a larger capability than others to generate torque or thrust on a given turbine geometry. Given the principle of mode resonance, these modes will correspond to the gust shapes that would be the most damaging to the blade geometry. This information can be used to identify potential threats to the turbine at a given site.

This chapter applies the above analysis to a range of geometries, 2D and 3D, to achieve a deeper understanding of gust-aerofoil interaction, and to demonstrate how spatial variation in

gust shapes affect the unsteady load response. The analysis is performed using the frequency-domain vortex lattice code with prescribed wake, as outlined in Chapter 3 Section 3.2.4. The FORTRAN package "lapack" (Linear Algebra Package) was used to find the eigenmodes of the influence matrix.

6.3 Eigenmodes of a 2D flat plate

The purpose of this section is to illustrate the eigenmode analysis described above, to show some of the properties of the eigenmodes of an aerodynamic system, and to demonstrate the principle of mode resonance. This will be done by confining the analysis to a 2D flat plate at zero mean angle of attack. This is the same simplified model as the one used to derive the transfer functions in classical aerodynamic theories, such as the Sears function and the Theodorsen function. The 2D vortex lattice model for a flat plate aerofoil was illustrated in Chapter 3 Section 3.2.4, in Figure 3.1.

6.3.1 Properties of the eigenmodes

To obtain the response of the unsteady aerodynamic system to an unsteady gust, a matrix equation in the form of Equation 6.1 must be solved. In accordance with the description in the previous section, we will do this by finding the eigenmodes of the influence matrix $\mathbf{A}$ (the form of which is given by Equation 3.14). Equations 6.2 and 6.3 are solved to obtain the eigenvalues and eigenvectors of the flat plate. Recall that the right eigenvectors are used to construct the aerofoil circulation using Equation 6.6, and as such each individual right eigenvector is analogous to an aerofoil circulation vector. Similarly, the left eigenvectors are each analogous to a surface-normal velocity vector, since they represent a resonance condition with the unsteady flow velocity in Equation 6.9.

Figure 6.1 shows the six first eigenvectors, right (black) and left (red), found through decomposition of the 2D flat plate aerofoil. They are obtained for reduced frequency $k = 0.4$. It is necessary to specify the reduced frequency of the harmonic system, since the model is solved in the frequency-domain. The influence matrix is dependent on the harmonic frequency ω (related to the reduced frequency as $k = \omega c/U$, Equation 2.2) when determining the influence of the unsteady wake (see Equation 3.14). It is however independent of the spatial shape of the gust, meaning that the desired generality of the method is preserved. Note also that the eigenvectors are normalised such that their maximum absolute value is 1. Solid lines represent the real components of each eigenvector, while dashed lines represent

the imaginary components.

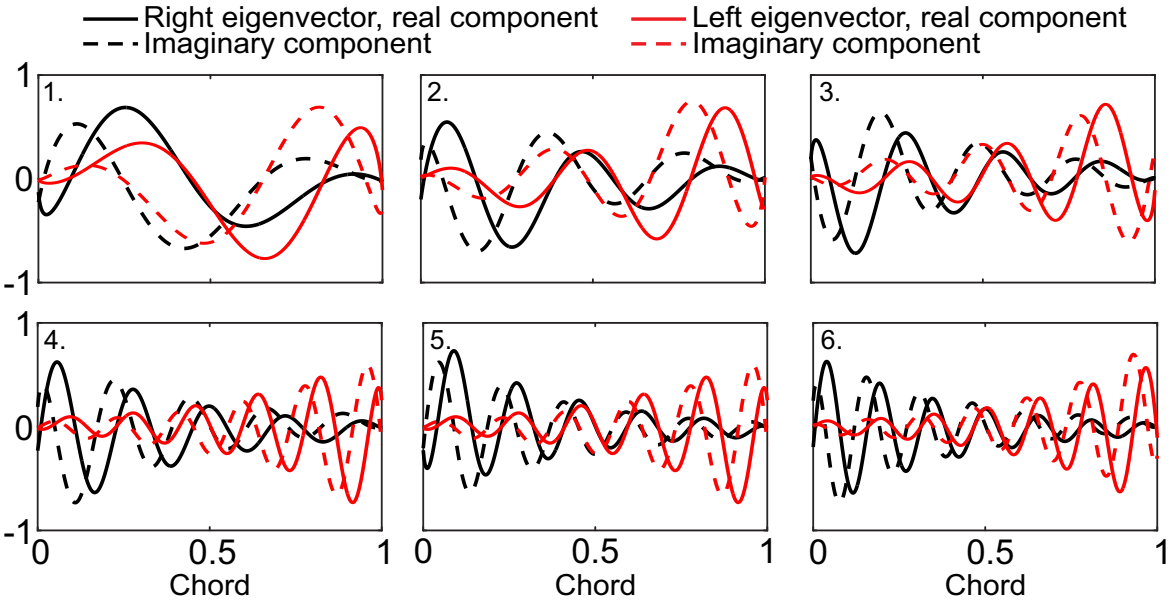

Fig. 6.1 A set of right and left eigenvectors associated with a 2D flat plate aerofoil. The reduced frequency is $k = 0.4$.

There is an observable structure to the eigenvectors in Figure 6.1. The vectors take the form of sinusoids with decreasing wavelengths, the number of oscillations over the chord length getting increasingly higher as the mode number is increased. The sinusoids also have a clear peak, located near the leading edge for the right eigenvectors (black lines), and near the trailing edge for the left eigenvectors (red lines). At this point, recall that the left eigenvectors represent how the aerofoil interacts with the flow field, while the right eigenvectors show how the aerofoil can respond to the flow field. This means that the results in Figure 6.1 agree with a commonly known fact about aerofoils in attached flow conditions; that interaction with or modifications to the trailing edge region impacts the aerofoil lifting properties more than a corresponding action near the leading edge (hence the use of trailing edge flaps for aerodynamic control). The eigenvectors in Figure 6.1 agree with this because the left eigenvectors, responsible for flow interaction effects through Equation 6.9, have their peak amplitudes near the trailing edge. This means that interaction in this region will result in a larger mode weight compared to interaction near the leading edge, which in turn will result in larger load response.

Figure 6.2 shows the eigenvalues of the flat plate aerofoil geometry, plotted in the complex plane. The reduced frequency is 0.4. The eigenvalues have been normalised by the number of lattice points used in the 2D VLM. The eigenvalues are distributed along a semicircle of unit

diameter. A selection of right eigenvectors associated with the modes are also included, and they indicate that the wavelength of the eigenvector associated with an eigenvalue gradually decreases as the eigenvalues approach the real axis.

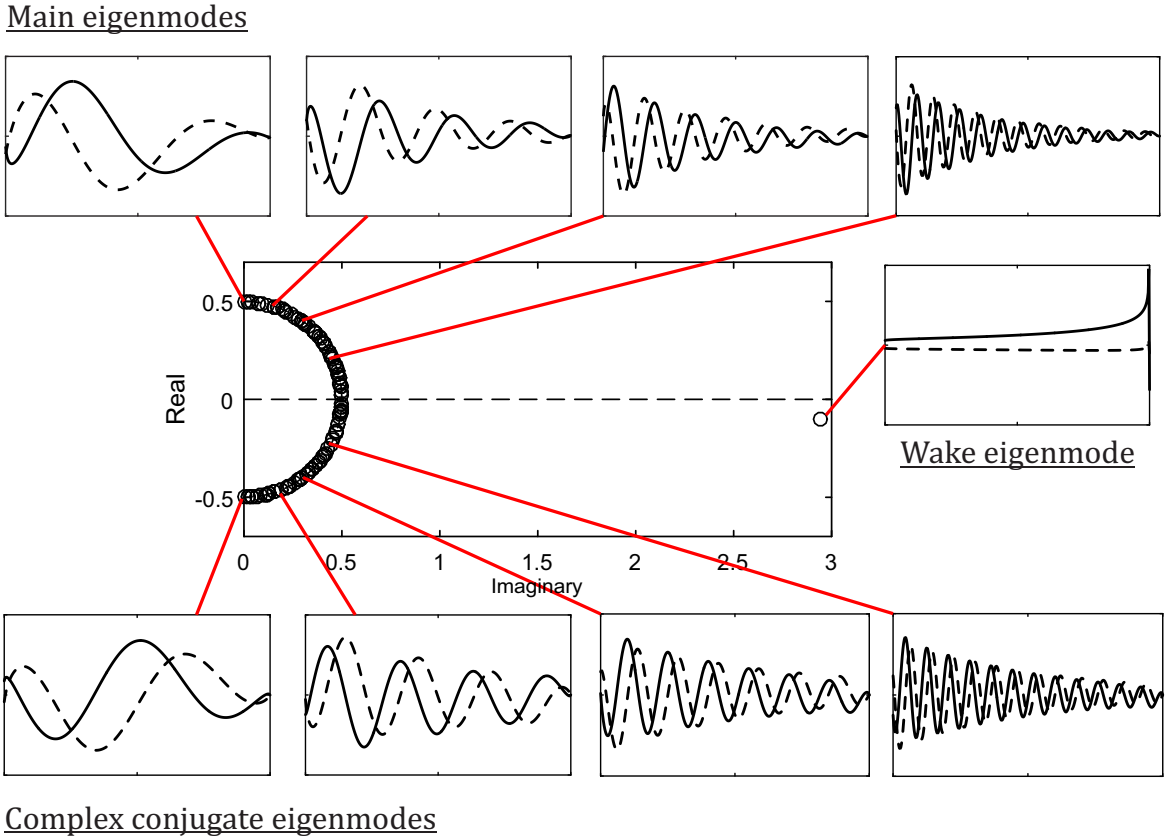

Fig. 6.2 Eigenvalues of the 2D flat plate aerofoil, normalised by the number of lattice points (Λ/n), plotted in the complex plane. A selection of associated right eigenvectors are also shown, with real (solid black line) and imaginary (dashed line) components. The reduced frequency is $k = 0.4$.

The distribution of the eigenvalues in Figure 6.2, in a semicircle symmetric about the real axis, suggest that they occur as a set of complex conjugate pairs. In fact, in the quasi-steady case, the eigenvalues are distributed such that they occur in pairs of exact complex conjugates, the upper half of the complex plane being mirrored in the lower half. The eigenvectors associated with the eigenmode pairs are also complex conjugates of each other. So in the quasi-steady case, the system consists of a set of exact complex conjugate modes. This pairing means that when Equation 6.6 is used to obtain the aerofoil circulation, the complex components of each mode cancel out exactly on summation with their own complex conjugates. This leads to the quasi-steady response of the system having no complex com-

ponent of response, i.e. it acts in phase with the gust forcing, as expected. The exception to this paired-conjugate behaviour is the "wake eigenmode", marked in Figure 6.2, which is a different shape, has an eigenvalue with much larger magnitude, and has no complex conjugate partner. This mode will be discussed in more detail below.

As the reduced frequency increases, the eigenvalues and vectors begin to shift in their positions and shapes, such that they are no longer perfect complex conjugates. This leads to a net imaginary component on summation when using Equation 6.6, which results in the phase lag associated with unsteady response. This shift in the eigenmodes appear to come about in order to preserve the Kutta condition at the trailing edge. Figure 6.3 shows a right eigenvectors of the flat plate (marked as mode no. 2 in Figure 6.1) at different frequencies. As before, the solid line represents the real component, and the dashed line the imaginary component. This vector represents aerofoil circulation, and it can be seen that the effect of increasing k is to shift the peak circulation from the leading edge to the trailing edge. This shift in the eigenmodes appears to come about in order to preserve the Kutta condition, to counteract the intensity of the unsteady wake which is increasingly concentrated near the aerofoil trailing edge as the frequency increases.

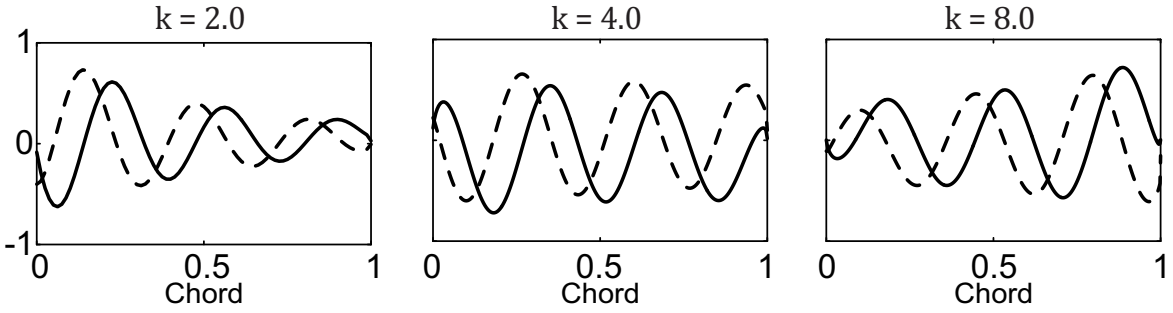

Fig. 6.3 An example of a right eigenvector (mode no. 2 in Figure 6.1) of a flat plate undergoing harmonic forcing. The figures show the progressive changes to the mode as the reduced frequency k increases.

In Figure 6.3, and later on in this section, very high frequencies ($k > 2.0$) are used for the purpose of illustrating the shifting mode properties. It is worth noting that the Kutta condition has not been verified for such high frequency oscillations; experimental studies have historically given conflicting reports on the applicability of the Kutta condition at higher frequencies [65]. As such, any studies relying on the Kutta condition at harmonic frequencies of 2.0 or higher are only as accurate as the Kutta condition allows them to be, which at this point is not known. The use of the vortex lattice model and eigenmode decomposition at high reduced frequencies is only used for illustration in this section. Later in this chapter,

when the eigenmode decomposition of 3D geometries is analysed, the frequency ranges will be restricted to within feasible bounds (and within the range of unsteady flow experienced by a tidal turbine). For now, the shifting properties of the eigenmodes with increasing k can be further illustrated by looking at the change to the wake eigenmode.

The wake-associated mode is marked in Figure 6.2, and is distinctly different from the other modes in the system. It does not follow the sinusoidal vector shape, and the eigenvalue lies separate from the semicircle in the complex plane. In quasi-steady conditions, the wake eigenvalue lies on the real axis, with no imaginary component. As the harmonic system frequency increases the eigenvalue moves into the complex plane. For example, in Figure 6.2, $k = 0.4$, the wake eigenvalue is located slightly below the real axis, denoting a phase lag between the wake and the gust.

It should be noted at this point that the existence of this wake mode is necessary because in the 2D VLM the wake circulation needs to be stated explicitly and separately from the circulation of the remaining aerofoil panels in the model. This requires an extra row in the influence matrix, representing Kelvin's theorem, in order to close the set of equations (for further details on this aspect of the model, see Chapter 3 Section 3.2.4). In the 3D VLM this additional matrix row is no longer necessary, and as such no specific wake-associated mode appears, as will be seen in the later sections of this chapter. In the 2D model used in this section, however, the wake-associated mode can be examined to give further information of the behaviour of the unsteady system as the harmonic frequency increases.

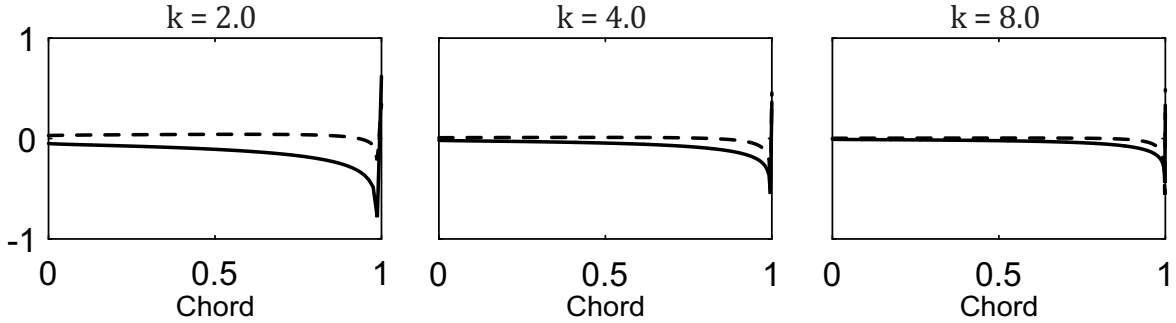

Fig. 6.4 The wake-associated mode (marked in Figure 6.2) of the flat plate, for increasing reduced frequency k.

Figure 6.4 shows the wake-associated mode for the flat plate, which was marked in Figure 6.2, showing how it gradually changes as the reduced frequency increases. The effect of the wake becomes increasingly concentrated near the trailing edge of the aerofoil. This

is consistent with the observation made in Chapter 4 that the unsteady wake has a more localised influence on the flow at higher harmonic frequencies, and is because the aerofoil chord becomes longer relative to the harmonic wavelength of the wake.

6.3.2 Mode resonance

Having looked at some of the properties of the 2D eigenmodes, the principle of mode resonance will now be demonstrated. This is done by applying a sinusoidal gust forcing to the flat plate aerofoil, setting the velocity vector **u** in Equation 6.1 to be:

$$u = \eta U_\infty e^{i\omega(t-x/U_\infty)} \tag{6.10}$$

The response of a flat plate aerofoil to this gust is normally obtained by using the Sears function, and the 2D vortex lattice model is able to replicate this response (see Chapter 3 Section 3.2.7 for validation). This is also the same gust as was used in Chapter 4 during the investigation of 3D blade response (Equation 4.3). In Figure 6.1, it was shown that the eigenvectors associated with a flat plate aerofoil have a sinusoidal structure. As such, the principle of mode resonance suggests that the associated weight c of each mode should peak when the sinusoidal gust wavelength is the same as the wavelength of the mode. To illustrate this, the weights associated with the modes marked 1-5 shown in Figure 6.1 are calculated for sinusoidal gust forcing using Equation 6.10, and plotted against reduced frequency. Figure 6.5a shows the results.

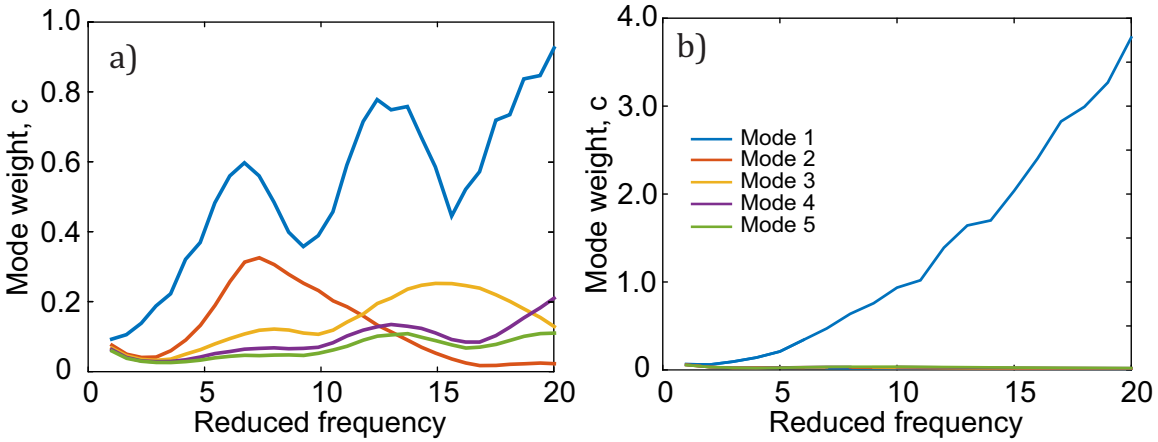

Fig. 6.5 Magnitude of the weight function for the first five eigenmodes shown in Figure 6.1. (a) Sinusoidal gust forcing, (b) uniform gust forcing.

As in the previous section, the maximum harmonic frequency used in Figure 6.5 is very large ($k = 20$); the results at such high frequencies will not necessarily be realistic due to the potential breakdown of the Kutta condition. It is however easier to demonstrate mode resonance in the inviscid system by showing the results over a large range of frequencies. As the reduced frequency increases, so does the gust frequency according to Equation 6.10. Looking at Figure 6.1, the wavelength of mode 2 is shorter than that of mode 1, and mode 3 has shorter wavelength than mode 2, and so on. As such, we expect the weight of each mode to peak when the gust wavelength is similar to the mode wavelength, and then recede again as the frequency increases further. This is in fact what we see in Figure 6.5a, and it is especially visible for modes 2 and 3. The weight of mode 2 peaks at $k = 7$ and then recedes. It is then followed by mode 3 peaking at $k = 16$ and then receding, as the harmonic frequency increases further.

Figure 6.5a shows further that the weight of mode 1 has a different trend compared to the other modes: overall, the weight increases from left to right, but there are two distinct troughs at $k = 10$ and $k = 15$. This difference in the weight of mode 1 is due to a unique behaviour of the associated eigenvector which is not observed in the other modes. Figure 6.6 shows the right eigenvector of mode 1, for a selection of harmonic frequencies. As the frequency increases, the eigenvector undergoes more radical change than the other modes (compared to mode 2 over a similar frequency range in Figure 6.3), with the circulation being more level along the chord and concentrating at a peak near the trailing edge. This is believed to be related to the change to the unsteady wake, which is also increasingly concentrated near the trailing edge (as was shown by the wake-associated mode in Figure 6.4). The shift of mode 1 as seen in Figure 6.6 appears to be in response to the increased trailing edge wake intensity, cancelling out the effect of the wake to preserve the Kutta condition.

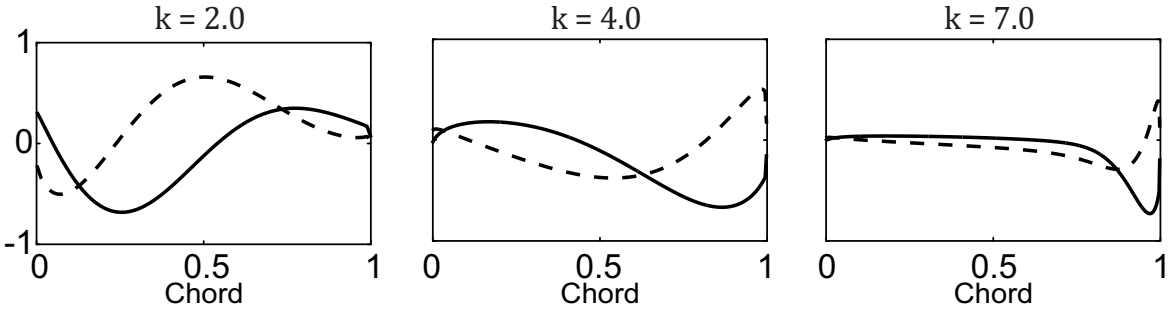

Fig. 6.6 The right eigenvector of mode 1 (as marked in Figure 6.1 and Figure 6.5). The figures show the progressive changes to the mode as the reduced frequency k increases.

As a contrast to the weight resonance to the sinusoidal gust shown in Figure 6.5a, Figure 6.5b shows the weights of the same modes as they interact with a uniform gust, given by (Equation 4.2):

$$u = \eta U_\infty e^{i\omega t} \tag{6.11}$$

The resonant peaks and troughs found in Figure 6.5a are absent in Figure 6.5b. Instead, the weight of mode 1 dominates the response. This is because the gust is always uniform and so never 'matches' the shape of any of the higher order modes. As the frequency increases, however, the first mode becomes uniform across most of the aerofoil (as seen in Figure 6.6) and therefore it is the closest to the gust in shape. This finding suggests that, for uniform gusts, mode 1 contributes by far the most to the unsteady circulation, especially at high frequencies.

6.3.3 Modal reconstruction

To conclude the 2D results section, and to illustrate the capability of the eigenmode decomposition method to obtain the correct aerofoil response, Figure 6.7 shows the chordwise distribution of aerofoil circulation amplitude, normalised by the gust amplitude, for the flat plate aerofoil undergoing sinusoidal gust forcing. The solution given by the 2D VLM is compared to the solution by modal reconstruction (using Equation 6.6). The VLM result and the reconstructed eigenmode results can be seen to be equivalent.

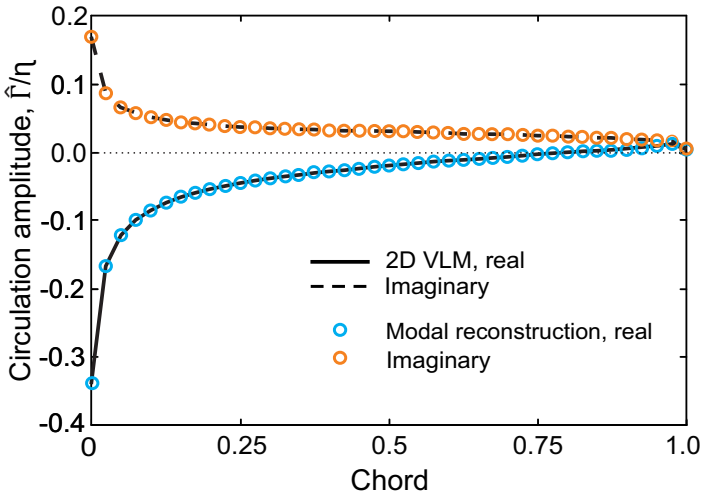

Fig. 6.7 Chordwise circulation distribution of a flat plate undergoing sinusoidal gust forcing. Black lines represent the VLM solution, while the red and blue dots represent the solution constructed by summing the eigenmodes.

6.4 Aerodynamic eigenmodes of 3D blades

Having determined some properties of 2D aerofoil eigenmodes, and explained the principle of mode resonance, we can now expand the study to 3D blades. The analysis is identical to that used for 2D aerofoils, using the methods outlined above in Section 6.2. The difference is only in the influence matrix used to describe the blade. In this section the 3D influence matrix **A** is the one given in Equation 3.16 (see Chapter 3 Section 3.2.4), for frequency-domain VLM with a prescribed wake assuming the wake vortices to leave the trailing edge with the freestream velocity.

The most important difference between the 2D and 3D influence matrices (Equations 3.14 and 3.16, respectively) is due to the need to explicitly include an expression for wake circulation in the 2D model. This requires an extra row in the influence matrix, representing Kelvin's theorem, in order to close the set of equations. This is not necessary to include in the 3D model, as Kelvin's theorem is inherently satisfied in the 3D model. This change in the influence matrix introduces some changes to the eigenmodes, as will be seen below.

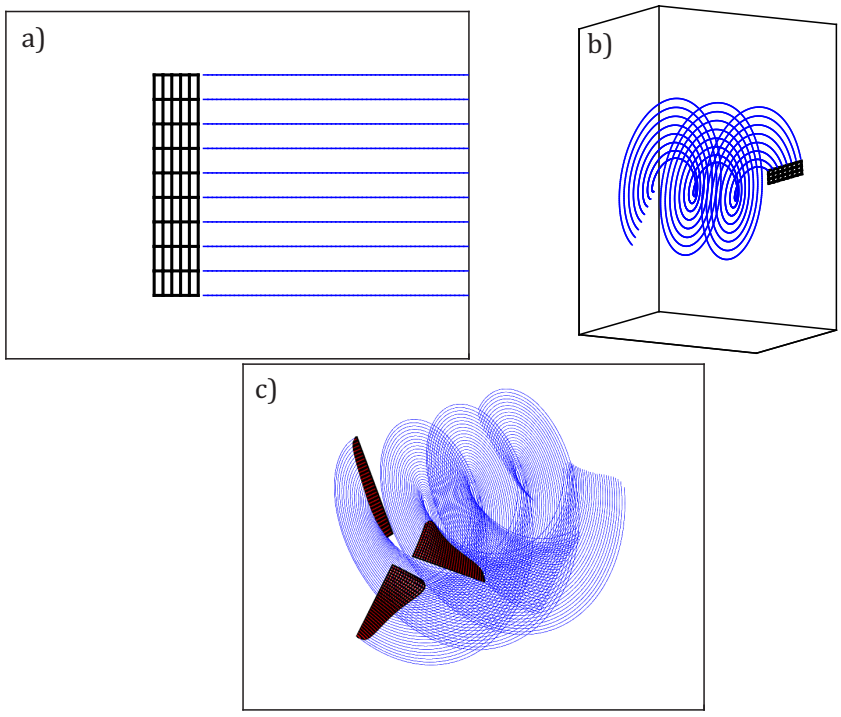

Fig. 6.8 The 3D geometries used for eigenmode analysis in this section.

Figure 6.8 shows the 3D geometries that will be used for the eigenmode analysis in this section. First a flat plate wing with finite span (6.8a) is tested. This simple case illustrates

some of the fundamental differences between 2D and 3D flow. Next, the same flat-plate geometry is tested, but now with rotation (6.8b), rotating at TSR 10. Finally, the eigenmodes of the tidal turbine geometry analysed in chapter 5 are found (6.8c).

While the previous section was intended to demonstrate some of the principles of eigenmode analysis in 2D, this section will show how these principles can be applied practically to analyse how a blade will interact with 3D gusts in the flow field. The results presented below illustrate how the spatial distribution of turbulence affects the unsteady response of a blade.

6.4.1 Finite wing

Figure 6.9 shows a selection of right and left eigenvectors ($\mathbf{V}_R$ and $\mathbf{V}_L$ from equations 6.2 and 6.3), resulting from eigenmode decomposition of the finite wing in Figure 6.8a. The wing has an aspect ratio of 5, and only the real components of the eigenvectors are shown. It was shown in Section 6.3.1 that the right eigenvectors (top row of Figure 6.9) represent blade circulation, while the left eigenvectors (bottom row of Figure 6.9) represent surface normal velocity. Again, the eigenvectors in Figure 6.9 display a clear pattern of behaviour. Like the 2D modes (Figure 6.1), there is a chordwise sinusoidal variation with gradually decreasing wavelength. However, in the 3D model there is also a spanwise sinusoidal variation in the mode (this pattern persists for wings of different aspect ratios). Note that the eigenvectors plotted in Figure 6.9, and in the remainder of this chapter, are obtained for quasi-steady reduced frequency ($k = 0.01$). The eigenvectors obtained at higher reduced frequencies were qualitatively similar to the quasi-steady vectors; the patterns of spanwise and chordwise variation in mode strength occured in the same way at all reduced frequencies tested. Because of this, the reduced frequency does not substantially impact the results shown in this section.

Looking at Figure 6.9, already we can identify a feature of 3D gust response based on the principle of mode resonance: the response of a blade to a gust that varies in the spanwise direction will be substantially different compared to the response of a gust that is uniform in the spanwise direction. This is because a gust with spanwise variation will resonate more with eigenmodes that also vary along the span, if their wavelengths are similar to that of the gust. A spanwise uniform gust, on the other hand, will resonate with the eigenmodes that are closer to constant along the span.

Looking now at the eigenvalues of the finite wing, plotted in the complex plane, Figure 6.10 would suggest substantial differences between the 3D system and the 2D counterpart in Figure 6.2; the eigenvalues do not occur on a semicircle in the 3D system, as they did in

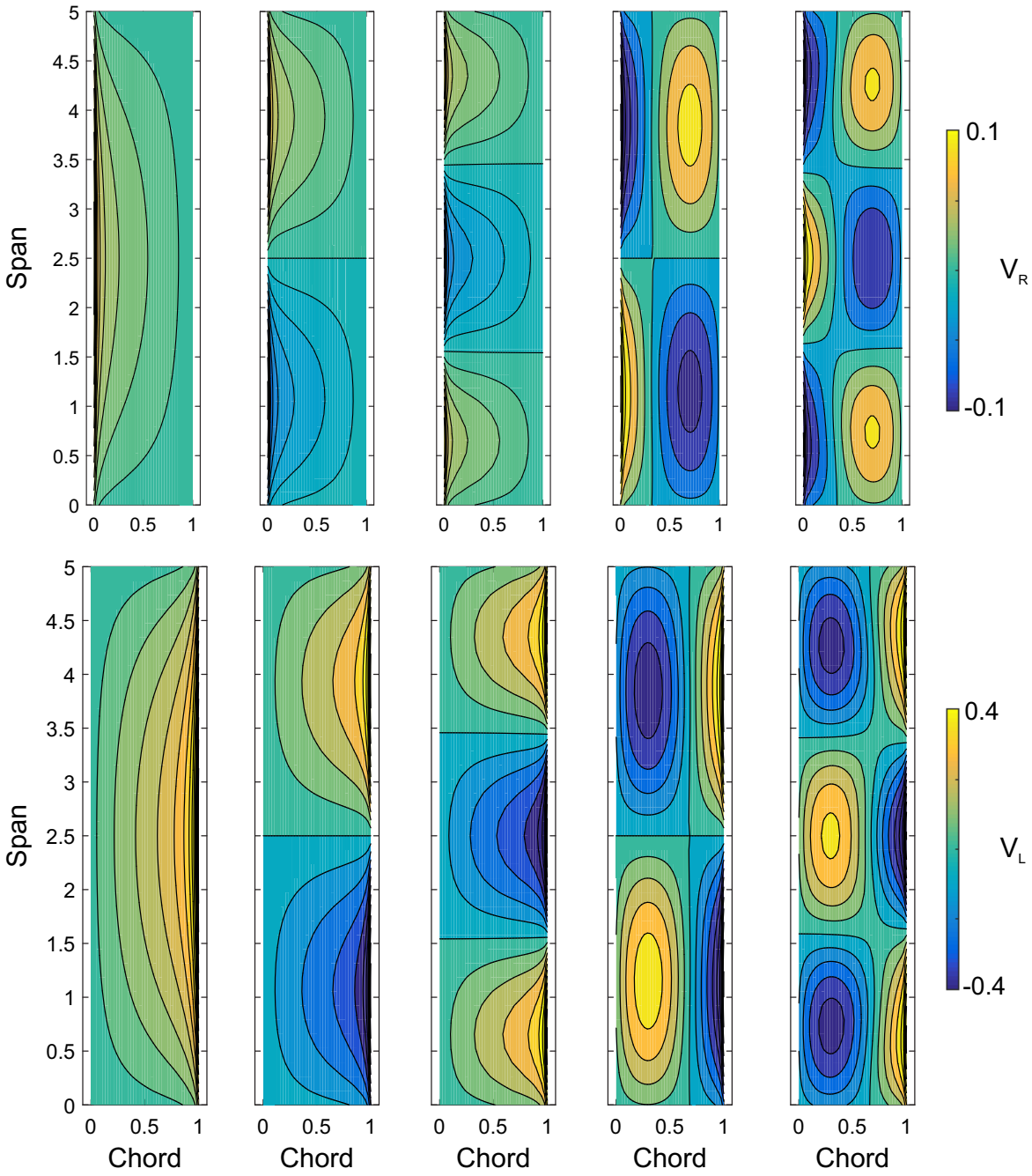

Fig. 6.9 A selection of right (top row) and left (bottom row) eigenvectors from the finite wing geometry in Figure 6.8a ($k = 0.01$). Only the real component of each vector is shown. For the right eigenvectors, the contours represent the surface distribution of blade circulation associated with each mode. For the left eigenvectors, the contours represent surface normal velocity.

2D. This difference is, however, largely superficial. In the 2D system the eigenvalues (and corresponding eigenvectors) occurred in complex-conjugate pairs, which in quasi-steady conditions cancelled out the imaginary component of the response. In the 3D system, in quasi-steady conditions (marked with reduced frequency $k = 0.01$ in Figure 6.10) the eigenvalues all occur on the real axis in the complex plane; none of them have any imaginary component. As the reduced frequency increases ($k = 0.5$ and $k = 1.0$ in Figure 6.10) the complex component of each eigenvalue increases in magnitude, resulting in an overall positive imaginary component which represents phase lag of the unsteady load response. The corresponding eigenvectors also obtain a complex component that increases in magnitude with the harmonic frequency.

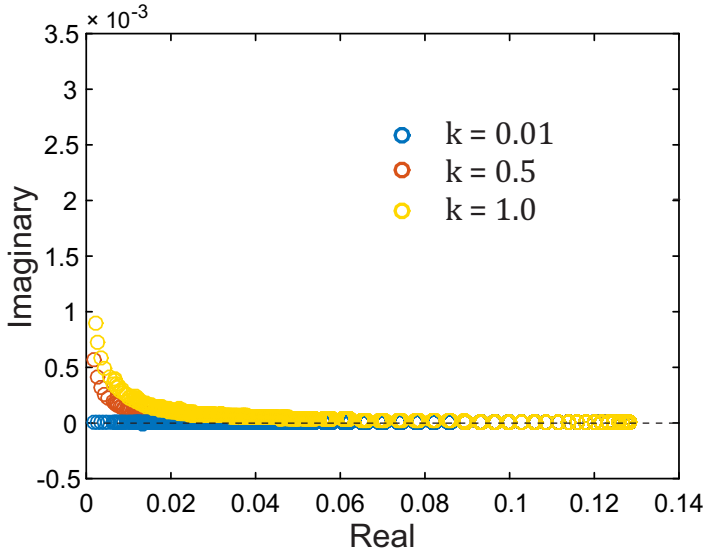

Fig. 6.10 The eigenvalues associated with the flat-plate wing in Figure 6.8a, at different harmonic system frequencies.

The reason why the eigenmodes do not appear as complex conjugate pairs in the 3D system might be because Kelvin's condition is inherently satisfied (see chapter 3 section 3.2.1 for more details on this aspect of the 3D model). The 2D eigenvalues showed behaviour consistent with preserving Kelvin's condition by generating pairs of counter-rotating vortices. As this is no longer necessary in the 3D model, the unsteady response appears simply as a deviation of the modes from the real axis.

At the start of this chapter, in Section 6.2, the "capability" of eigenmodes to generate unsteady lift was introduced as a means of analysing blade response to gusts in a generalised manner. We will now perform this analysis on the finite wing geometry, and demonstrate

how this can be used to identify potentially damaging gusts in the flow. This is done by finding the lifting properties of each eigenmode, by setting $\mathbf{\Gamma} = \mathbf{V}_R$ for each mode and using the Kutta-Joukowski theorem (equation 3.5) to calculate the lift generated by the eigenvector.

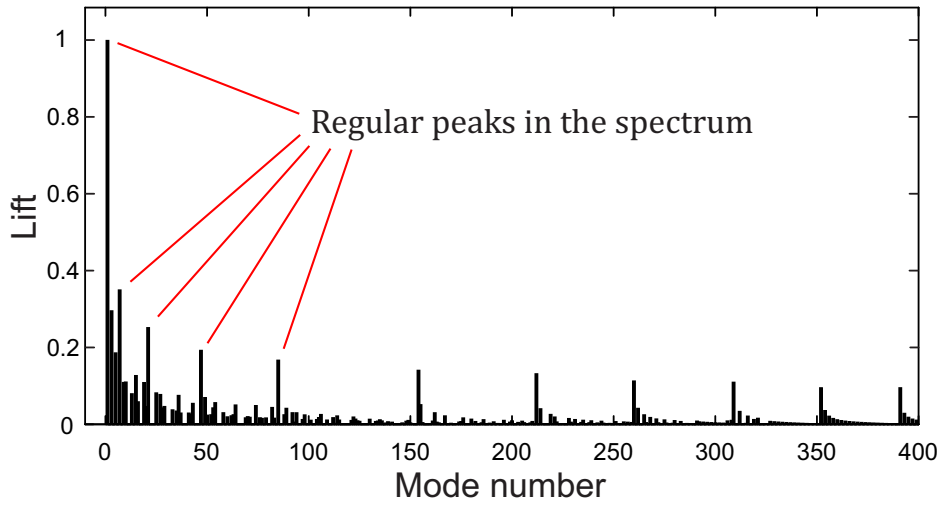

Fig. 6.11 The lift generated by each of the eigenmodes derived from the finite wing geometry in Figure 6.8a, normalised by the lift magnitude of the largest mode. The reduced frequency is quasi-steady.

The lift generated by each eigenmode of the finite wing shown in Figure 6.8a is plotted in Figure 6.11, as a bar chart of lift magnitudes against mode number. In this analysis the absolute value of lift is not important, but rather the relative lift magnitude of each eigenmode compared to the others. Therefore, the lift magnitude of each mode has been normalised by the magnitude of the largest mode. The results are obtained for a quasi-steady harmonic system frequency, but the trends were found to be similar at higher frequencies. There is a clear trend in the results; there are regular peaks in the load spectrum which contribute disproportionally large loads compared to the surrounding modes. These modes have something in common, which is illustrated in Figure 6.12, which shows the left (velocity) eigenvectors corresponding to the first five peaks marked in the load spectrum in Figure 6.11. Above each eigenvector is the lift it generates, as a percentage of the largest mode lift. It can be seen that these modes all correspond to blade response acting in an approximately uniform way across the span. From the principle of mode resonance – an eigenmode will contribute more to the total load response if it is similar to the forcing gust – the results in Figure 6.11 and Figure 6.12 indicate that the gusts with the potential to cause the largest loads on this geometry are spanwise-uniform gusts. This makes intuitive sense: a gust affecting the whole span at once is likely to cause a larger response than one that varies along the span. The

important question to answer is how a gust that is intermittent along the span will affect the unsteady load response.

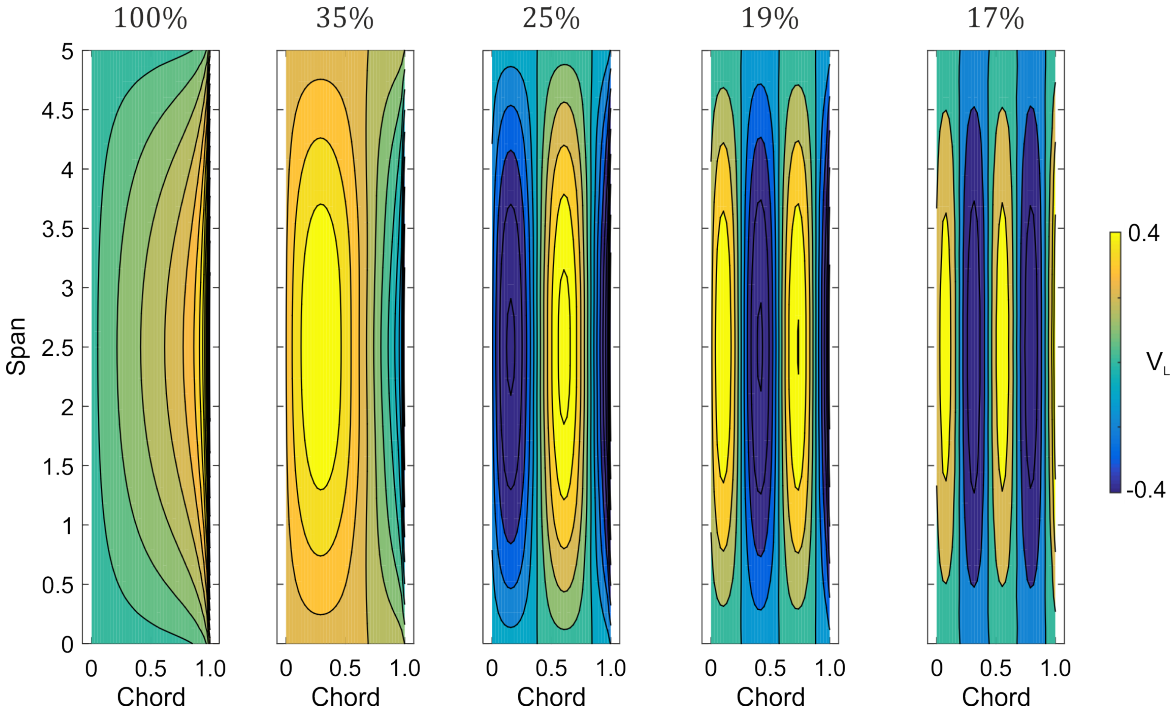

Fig. 6.12 The left eigenvectors associated with the first five peaks marked in Figure 6.11. Above each mode is the lift it generates, shown as a percentage of the largest mode lift.

We can answer this question by sorting the eigenmodes by the magnitude of their generated lift. This has been done as a bar chart in Figure 6.13. The capability to generate lift can be seen to diminish rapidly along the load spectrum, with the first few modes contributing almost all of the loading. At this point we can define a "cut-off" value for lift, beyond which we define the lift contribution by a mode to be negligible. This cut-off is in a sense arbitrary, and can be chosen by anyone carrying out the analysis as they please, depending on the desired fidelity in the calculations. The cut-off value chosen throughout this chapter is 5% of the maximum load, which is marked in Figure 6.13 by a vertical line. The modes to the left of this line represent the modes with the largest potential contribution to lift, while the modes to the right are negligible.

The eigenmodes to the left of the cut-off line in Figure 6.13 will correspond to the gusts most likely to cause damage in the turbulent flow field, by the principle of mode resonance. By studying the spatial shapes of the modes that occur before the cut-off line, it is possible to determine what level of spatial intermittency a gust can have while still generating non-

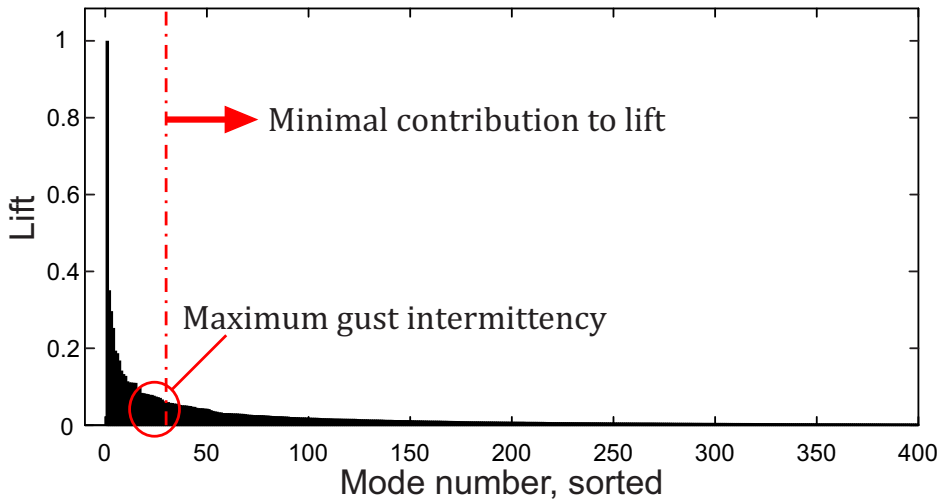

Fig. 6.13 The lift generated by each of the eigenmodes derived from the finite wing geometry in Figure 6.8a, normalised by the lift magnitude of the largest mode, sorted by the load magnitude. The harmonic frequency is quasi-steady.

negligible loads. Figure 6.14 shows the left eigenvector found through this process, which corresponds to the maximum spanwise intermittency a gust can have before the unsteady lift generated can be considered negligible on this blade geometry (to see the modes from which the selection was made, see Appendix A). Figure 6.14 suggest that a gust with spanwise wavelength less than about 20% of the wing span will have virtually no effect on the unsteady lift, compared to gusts with longer spanwise wavelengths.

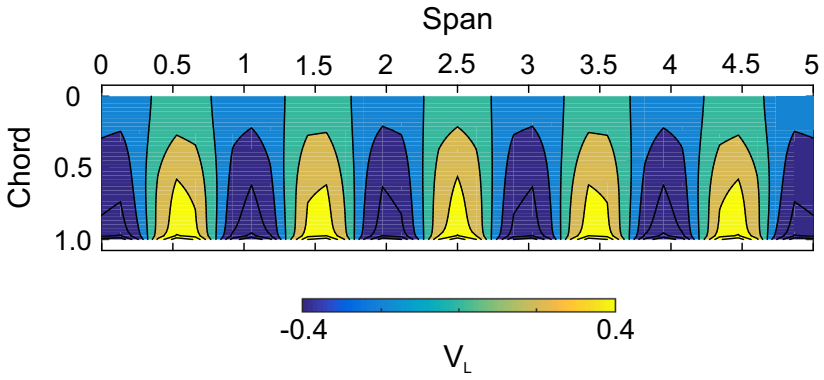

Fig. 6.14 The shortest spanwise wavelength that occurred before the cut-off value for potential lift contribution, as defined in Figure 6.13.

6.4.2 Rotating flat plate

The same analysis will now be applied to a single rotating flat plate (geometry illustrated in Figure 6.8b). The blade is untwisted and has aspect ratio 5, making it the same geometry as was used in the previous section, only this time rotating at TSR 10. The rotation radius is equal to the blade chord. Figure 6.15 shows the eigenvalues for the rotating blade with three different reduced frequencies. The main difference between the rotating and non-rotating eigenvalues (shown in Figure 6.10) is that the rotating blade gives eigenvalues that are more dispersed in the complex plane. Even at very low reduced frequency ($k = 0.01$, blue dots), the eigenvalues do not all lie on the real axis. The small number of eigenvalues with imaginary components do, however, exist as complex conjugate pairs such that the total imaginary component is zero and there is no phase lag. As the reduced frequency increases, the eigenvalues no longer lie on a single line, but spread through gradually increasing imaginary components.

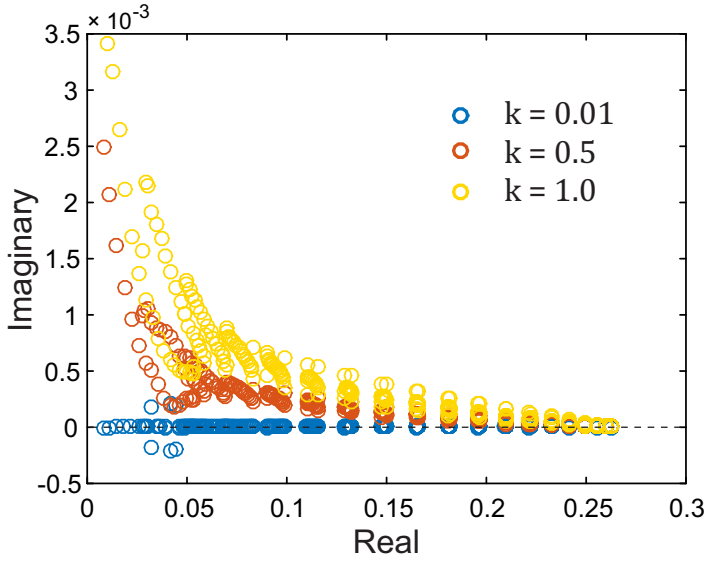

Fig. 6.15 Eigenvalues for the rotating blade geometry in Figure 6.8b, plotted in the complex plane.

As in the previous section, we can now calculate the load characteristics of each eigenmode, by setting $\mathbf{\Gamma} = \mathbf{V}_R$ and using the Kutta-Joukowski theorem to calculate the induced lift. We can also decompose the resulting force vector into thrust and out-of-plane bending moment acting on the rotor blade. Again, the analysis was performed for quasi-steady reduced frequency. The resulting thrust properties of each mode are shown in Figure 6.16, as a bar chart. As in the case of the non-rotating flat plate (Figure 6.11), there are regular peaks in the load spectrum. Figure 6.17 shows the five eigenvectors that generate the largest thrust on

the rotor blade. Again, because the important quantity is the relative magnitudes of the thrust generated by each mode compared to the others, the thrust generated by each mode is shown as a percentage of the largest mode thrust. The modes are all close to spanwise-uniform in shape, which is the same as was found previously for the non-rotating plate.

Figure 6.17 also shows that a shift has taken place in the shape of the eigenvectors as a result of the blade rotation. The right eigenvectors (top row) have shifted such that the peak blade circulation occurs closer to the hub of the blade. The left eigenvectors (bottom row), on the other hand, have shifted such that their peaks occur closer to the blade tip. This shift indicates that the blade tip is more sensitive to gust events than the hub in a rotating system, since the left eigenvectors represent the interaction between the blade and the unsteady gusts.

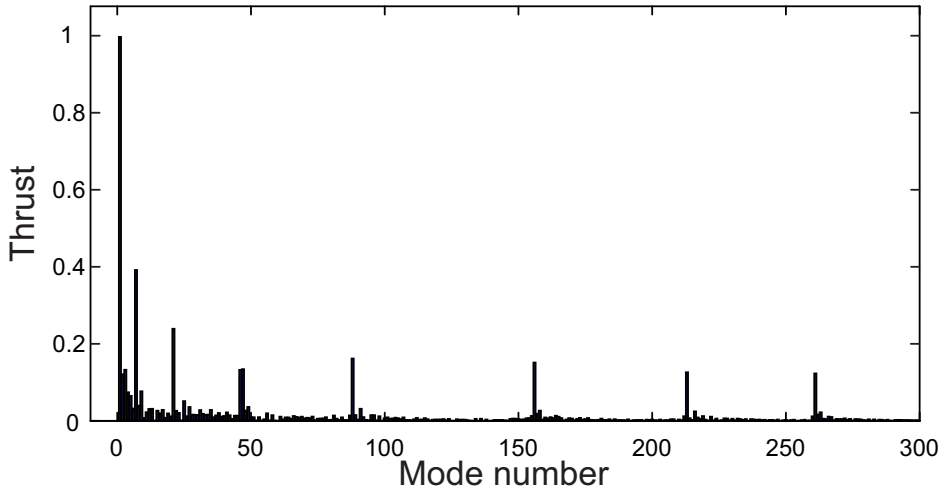

Fig. 6.16 The thrust generated by each eigenmode of the rotating blade in Figure 6.8b, normalised by the thrust magnitude of the largest mode. The harmonic frequency is quasi-steady.

In addition to the thrust, the bending moment of each mode can also be calculated as a mode property, and the eigenvectors corresponding to the largest bending moments can be found. In general, the modes that generated large thrust also resulted in large out-of-plane bending moments, such that spanwise-uniform gusts were found to be the most damaging. Figure 6.18 shows the five modes responsible for generating the maximum amount of bending moment, and it does reveal some differences compared to the maximum thrust modes in Figure 6.17. The 3rd and 5th modes are intermittent along the span, rather than uniform, showing that gusts with shorter spanwise length scales are still capable of generating large bending moments. This also shows that the blade bending moment is more sensitive than the

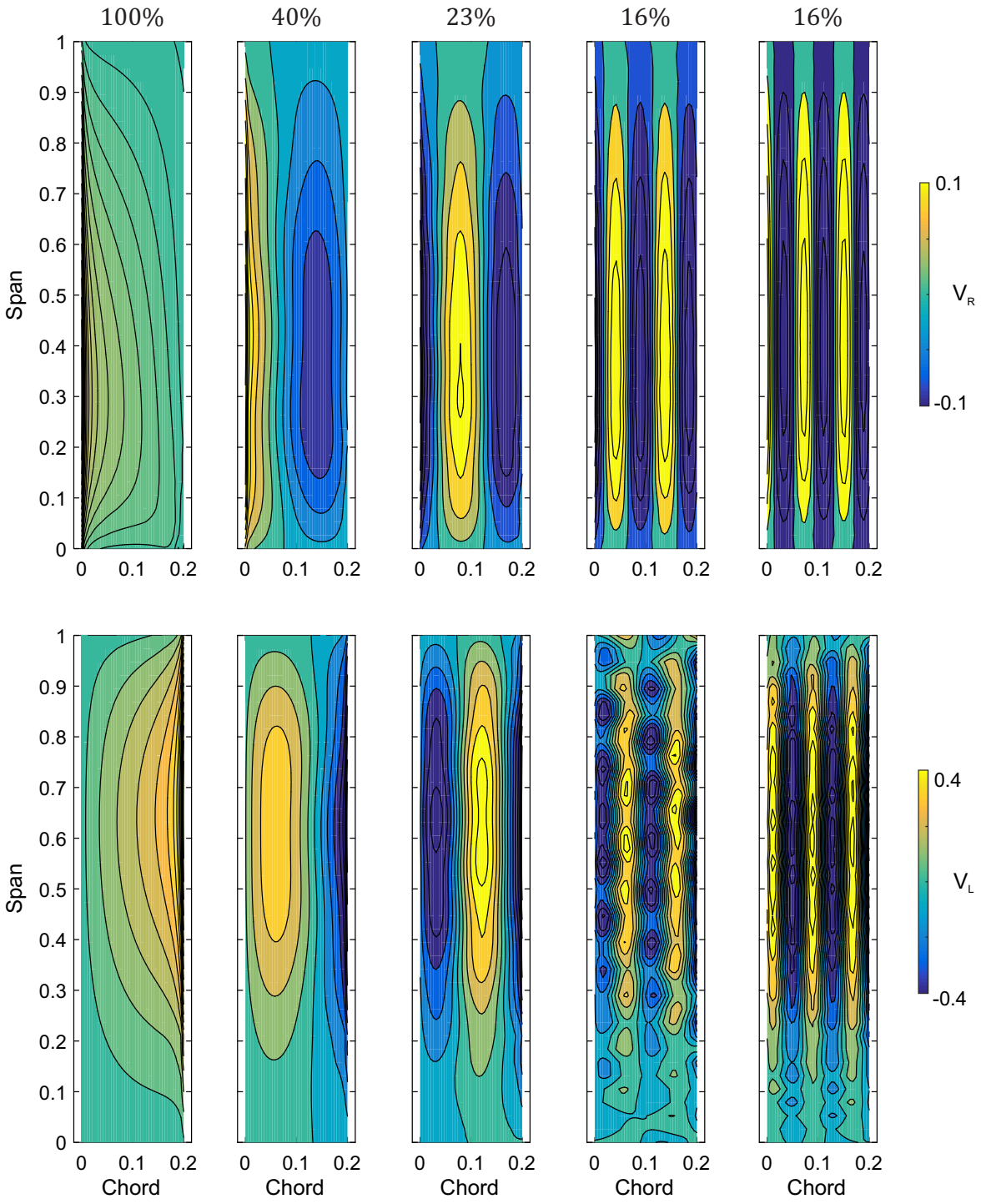

Fig. 6.17 Top five modes ($k = 0.01$) associated with maximum generated thrust on the rotating flat plate geometry shown in Figure 6.8b. Top row shows the right eigenvectors ($\mathbf{V}_R$), while the bottom row shows the corresponding left eigenvectors ($\mathbf{V}_L$). Above each mode is the thrust it generates, shown as a percentage of the largest mode thrust.

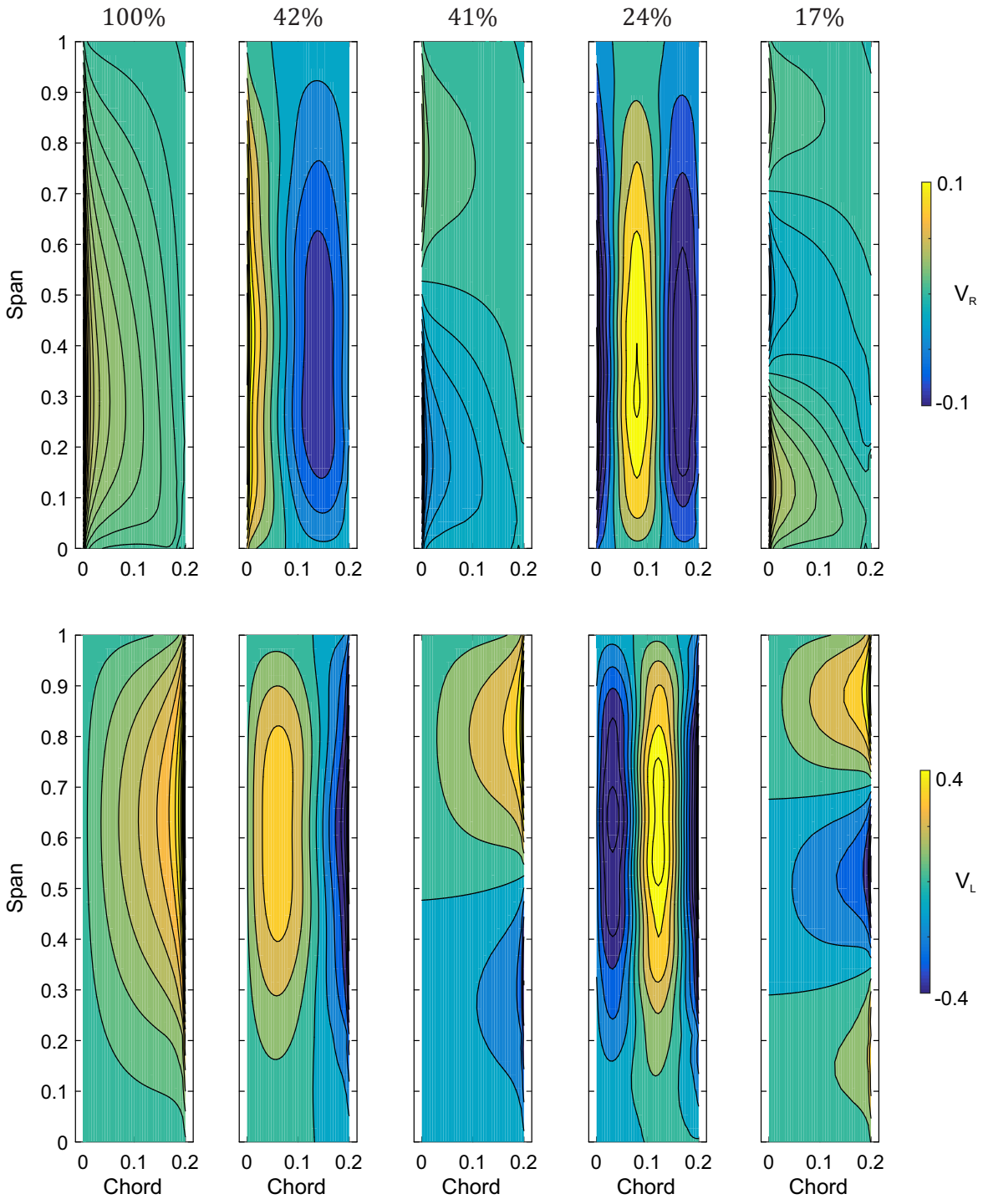

Fig. 6.18 Top five modes ($k = 0.01$) associated with maximum generated out-of-plane bending moment on the rotating flat plate geometry shown in Figure 6.8b. Top row shows the right eigenvectors ($\mathbf{V}_R$), while the bottom row shows the corresponding left eigenvectors ($\mathbf{V}_L$). Above each mode is the bending moment it generates, shown as a percentage of the largest mode bending moment.

thrust to gusts with spanwise variation in wavelength.

Through the same process used in the previous section, a cut-off value can be defined and used to find the minimum spanwise wavelength a gust can have while still producing non-negligible loads. Like before, the cut-off value is defined here as 5% of the maximum thrust or bending moment generated by the largest mode. Figure 6.19 shows the left eigenvectors found through this selection, the top vector representing the cut-off for thrust, and the bottom vector representing the cut-off for bending moment (the selection of modes considered can be found in Appendix A). The thrust can be seen to be negligible when the spanwise gust wavelength is shorter than 50% of the blade span, while the torque remains non-negligible for spanwise wavelengths down to 30% of the blade span. This result makes intuitive sense; the blade bending moment is strongly affected by forces acting on the outer section of the blade, near the tip, due to the dependence of moment on radius. As such, gusts acting on the outboard blade section will affect the torque, even if the gust is highly intermittent along the rest of the span.

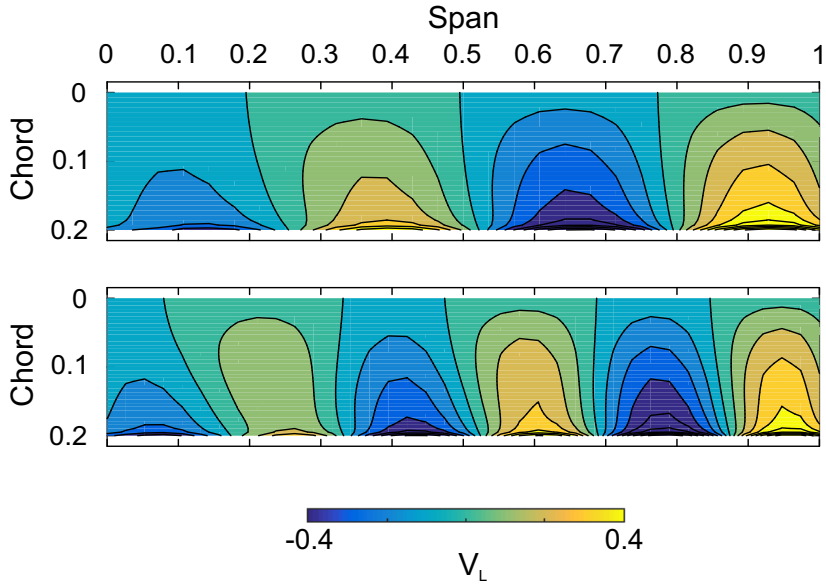

Fig. 6.19 The left eigenvectors associated with the cut-off point for thrust (top) and torque (bottom). Eigenvectors with smaller spanwise wavelength than these will make negligible contributions to the loading.

6.4.3 Model tidal turbine

To complete this chapter, the methodology of eigenmode analysis will be applied to a tidal turbine geometry. The geometry used in this section is a single blade from the turbine shown

in Figure 6.8c, which was also simulated in Chapter 5. The eigenmode analysis method demonstrated in the previous sections of this chapter will be used to identify gusts that are potentially damaging to the turbine. The turbine rotates at TSR 4, and has a twist and taper distribution to match the model turbine against which the vortex lattice model was validated in Chapter 3. Figure 6.20 shows the eigenvalues for the tidal turbine blade, at three reduced frequencies. Similar to the rotating plate in the previous section, the eigenvalues are more strongly dispersed in the complex plane compared to the non-rotating flat plate (Figure 6.10). In the quasi-steady case, the eigenvalues mainly lie on the real axis, with a small number of complex-conjugate pairs, as was the case with the rotating flat plate. At higher reduced frequencies (red and yellow circles), however, the eigenvalues occur over a smaller imaginary range than was observed for the rotating flat plate.

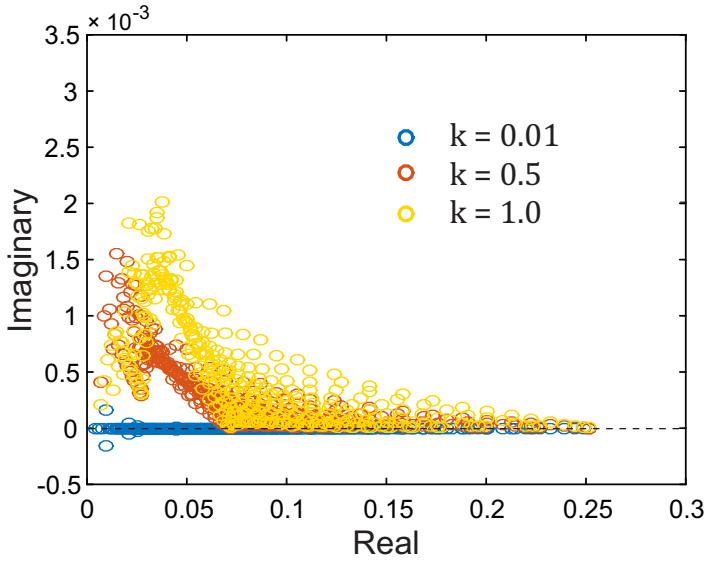

Fig. 6.20 Eigenvalues of the tidal turbine geometry shown in Figure 6.8c, plotted in the complex plane.

As before, the properties of each eigenmode are found in terms of the capability of each mode to generate thrust and out-of-plane bending moment. The analysis is again performed at quasi-steady reduced frequency. Figure 6.21 shows the results of this process in terms of the thrust of each mode, in the form of a bar chart. An important difference can now be seen, comparing the turbine geometry to the rotating and non-rotating flat plates. Looking at Figures 6.11 and 6.16, and comparing it to the result for the turbine geometry in Figure 6.21, the maximum thrust no longer occurs in regular peaks in the load spectrum. The reason for this can be found by looking at the five modes associated with the largest thrust response, shown in Figure 6.22. Again, the thrust generated by each mode is shown as a percentage of

the largest mode thrust. The mode capable of generating the largest thrust (leftmost column of Figure 6.22) is still the spanwise-uniform mode. However, the following modes all have some degree of spanwise intermittency. The turbine blade design has caused the relative response of the spanwise-uniform and the intermittent modes to become more similar. This means that a gust that is intermittent in the spanwise direction may still cause thrust loading comparable to that generated by a spanwise-uniform gust, for a realistic turbine design.

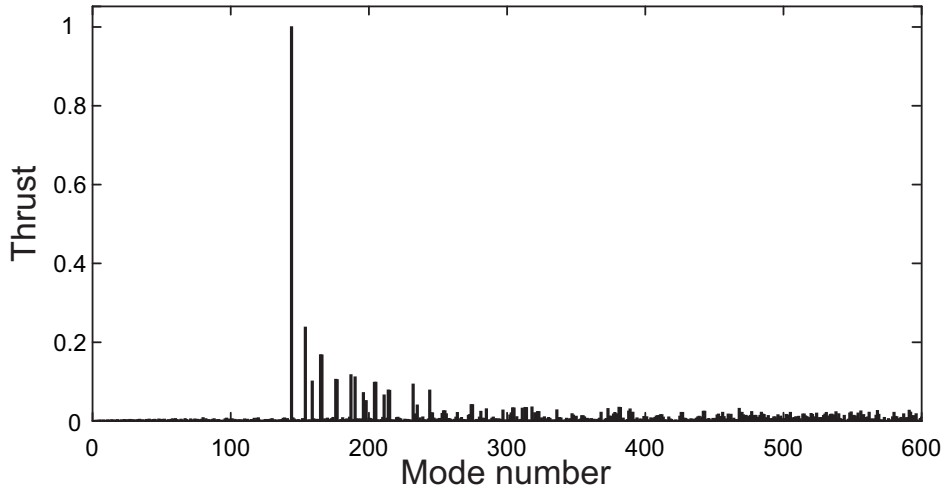

Fig. 6.21 The thrust generated by each eigenmode of the turbine blade shown in Figure 6.8c, normalised by the thrust magnitude of the largest mode. The harmonic frequency is quasi-steady ($k = 0.01$).

The behaviour observed for the thrust in Figures 6.21 and 6.22 is also observed for the out-of-plane bending moment, where again the regular peaks in the load spectrum were not found for the turbine geometry, as they were for the flat plate geometries studied above. Another interesting result seen in Figure 6.22 is that some of the left eigenvectors (bottom row) have their peak magnitudes near the hub of the blade, rather than the tip (i.e. the opposite of what was seen with the rotating flat plate). Since the left eigenvectors govern the blade interaction with gusts through mode resonance (see Equation 6.9), this indicates that gust interaction can cause large load response even if the gust is localised near the hub of the turbine.

As before, a cut-off can be defined below which the thrust or bending moment generated by a mode is less than 5% of that generated by the mode with the maximum response. The left eigenvectors associated with the cut-off modes found for the turbine geometry are shown in Figure 6.23 (the set of modes used for selection can be found in Appendix A). The cut-off mode for thrust (top vector in Figure 6.23) indicates that gusts with spanwise wavelength shorter than about 25% of the blade span will have negligible impact on the thrust. The

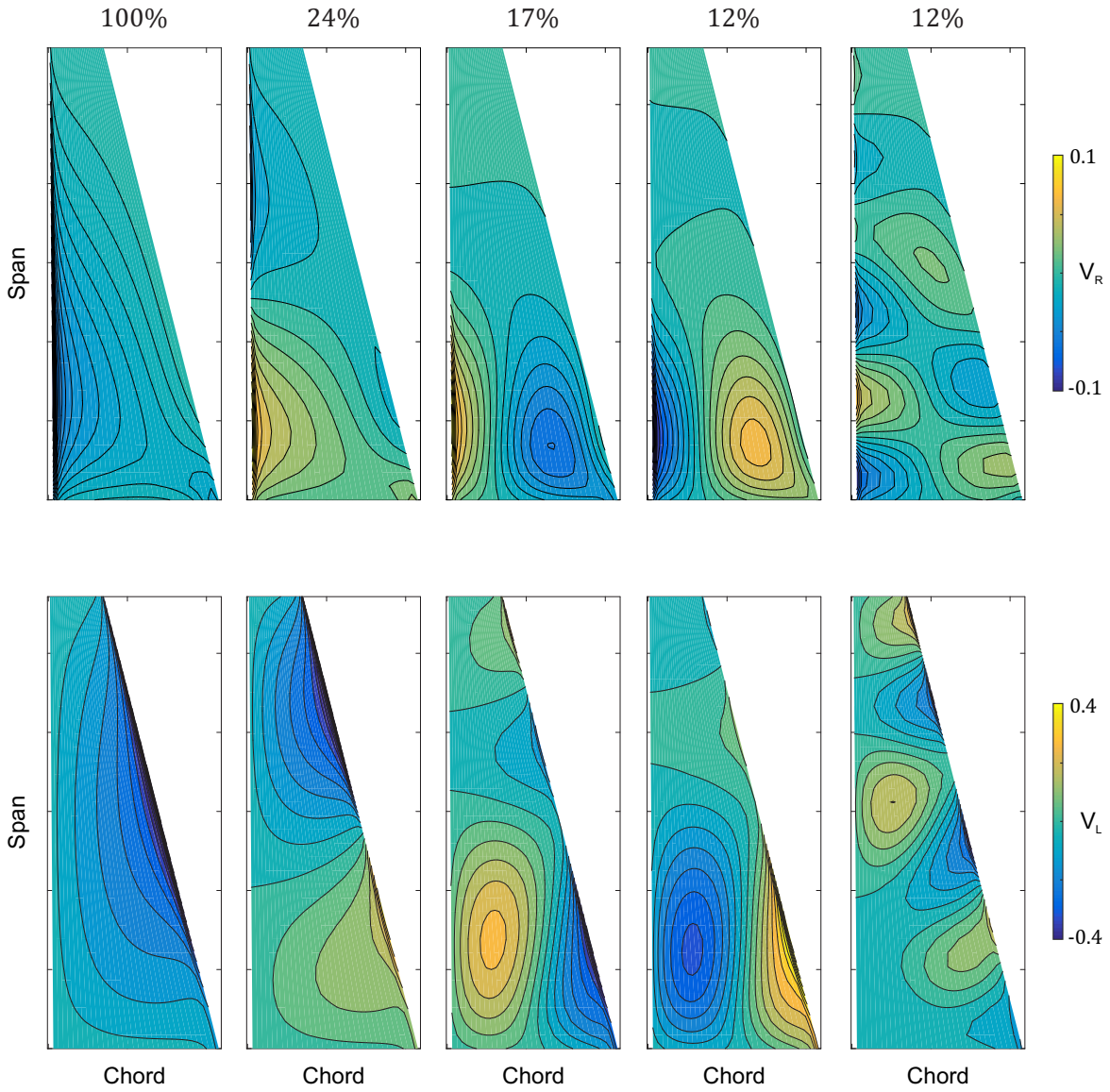

Fig. 6.22 The five sets of right and left eigenvectors (top and bottom rows, respectively) associated with the largest generated thrust in Figure 6.21 (at $k = 0.01$). Above each mode is the thrust it generates, shown as a percentage of the largest mode thrust.

bending moment (bottom vector in Figure 6.23), on the other hand, is affected by gusts with spanwise wavelength down to about 20% of the span. Note that this is a substantially shorter wavelength than the equivalent cut-off values for the rotating plate in the previous section. At the same time, the turbine eigenvectors do not conform as closely to sinusoidal harmonics as the flat plate geometries, and so is only approximately similar to a harmonic gust. This means that a sinusoidal gust aligned with the turbine trailing edge would be only partly correlated with the eigenmodes, which would reduced the total load response.

The results of this section indicate that a realistic turbine geometry is affected by a wider range of gusts than a simple flat plate rotor geometry, as gusts with a significant degree of spatial intermittency along the blade span are still capable of producing non-negligible response in the realistic turbine geometry.

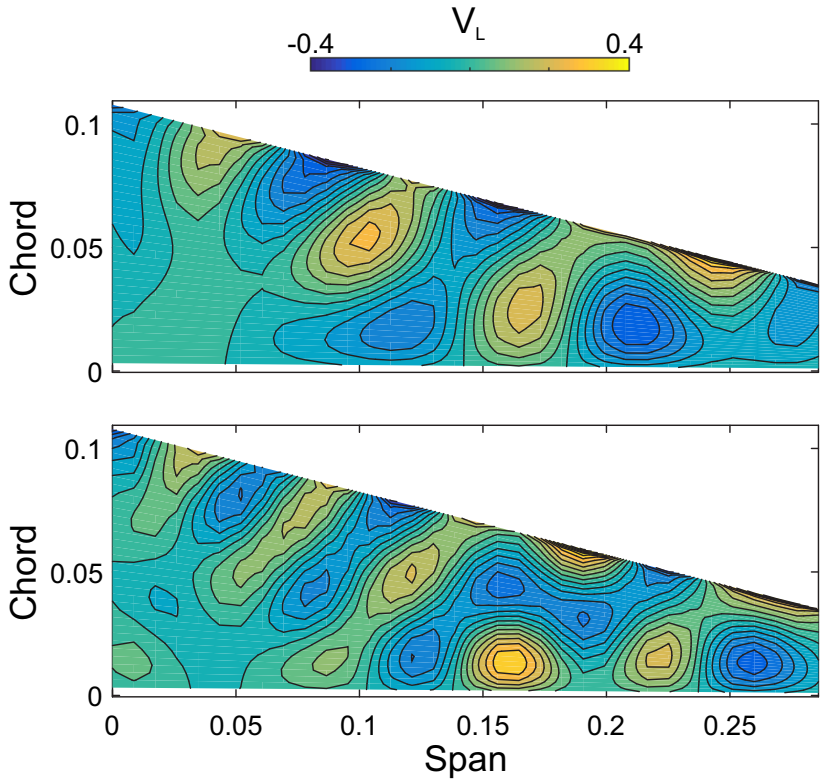

Fig. 6.23 The left eigenvectors associated with the cut-off point for thrust (top) and torque (bottom). Eigenvectors with smaller spanwise wavelength than these will make negligible contributions to the loading.

6.5 Conclusions

The purpose of this chapter has been to demonstrate a method of assessing the importance of gusts with different length scales, in terms of the unsteady load response of a tidal turbine. The principle of mode resonance, by which the load response of a blade to a gust is determined by the similarity of the gust to the blade eigenvectors, has been introduced. By this principle, it is possible to determine what types of gusts have the largest potential impact on a blade geometry.

The spatial extent of unsteady flow effects was shown to have a substantial effect on the ability of the gust to generate loads on the turbine. The spanwise wavelength was shown to be the strongest indicator of whether a gust will cause large unsteady loads. Spanwise-uniform gusts had by far the largest effect on the flat plate geometries tested, although this was not the case for a realistic turbine geometry. This finding further emphasises the importance of undertaking 3D modelling when estimating unsteady turbine loading, as previously highlighted in Chapters 4 and 5.

An important consequence of this methodology is its ability to inform tidal site surveyors about the spatial resolution necessary to capture the relevant turbulent length scales in the flow. While point-measurements of turbulence intensities and length scales are common, the results in this chapter highlight the need to measure the extent of turbulent features in the turbine plane.

The analysis presented in this chapter has enabled a definition of the maximum spatial resolution required to identify potentially damaging turbulence. This represents a first step towards providing the connective bridge between turbulent measurements and turbine load response. The framework of eigenmode decomposition also provides a more intuitive way of describing the response of a turbine to turbulence via the concept of mode resonance: the turbine load response depends on the spatial similarity of the turbulent eddies to the turbine eigenmodes.

This chapter has also demonstrated that there will be a 'cut-off' in the modes of a given geometry beyond which the contribution of the modes to the total unsteady response is small. This cut-off value in turn represents the minimum spanwise wavelength a gust can have, beyond which its effect on the turbine is negligible. For the tidal turbine geometry assessed in this chapter, the cut-off wavelengths were found to be 25% of span for thrust and 20% of span for torque. Gusts with a shorter spanwise wavelength than these cut-off values will

generate negligible unsteady loading, and thus may not need to be captured by site surveys or design models.

The results found in this chapter will provide a basis for the next chapter, where common unsteady phenomena found in tidal channels are classified in terms of their potential contribution to unsteady loads. This represents an important step in relating turbulent length scales to the unsteady load response of a tidal turbine in a realistic tidal power site.

Chapter 7

3D flow characterisation

7.1 Introduction

In the previous chapter a method based on eigenmode decomposition was demonstrated, and used to determine the importance of spatial variation of the unsteady gust when calculating the unsteady load response of an aerofoil. It was shown that as the spanwise wavelength of a gust decreased, the load response of the aerofoil decreased substantially, until a cut-off point of spanwise gust wavelength below which the gust had negligible effect. This cut-off wavelength was found to be shorter for unsteady bending moments than for thrust, meaning that unsteady blade bending moments are more sensitive to turbulence than unsteady thrust forces. In addition to this, spanwise-uniform gusts were found to have a disproportionally large contribution to unsteady turbine loading. With these considerations in mind, this chapter gives an assessment of the most common sources of unsteadiness in the tidal environment, and of their potential influence on turbine loads.

7.1.1 3D unsteady flow characterisation

The unsteady flow features analysed in this section will be divided into the following three categories: surface waves, turbulence (including ocean turbulence and larger-scale turbulent eddies caused by headland or bathymetry), and rotation through otherwise steady features (such as the channel shear layer). This categorisation is based on Sequeira and Miller's [115] work on the unsteady flow experienced by tidal turbines from the perspective of 2D blade sections. The majority of the analysis in this chapter will be devoted to surface waves and turbulence, after which rotation through steady flow features will be discussed briefly.

Furthermore, it has been verified that, from the perspective of a 2D aerofoil section, flow changes in the transverse direction have larger effects on the unsteady load than fluctuations aligned with the mean flow velocity [114]. From the perspective of a rotating turbine blade, shown in Figure 7.1, flow oscillations in the streamwise direction produce gusts in the relative frame that are approximately transverse to the mean flow direction (over the majority of the blade span). Fluctuations in the other two directions, however, will not contribute to large changes in angle of attack in the relative frame. A number of studies on turbines, both computational and experimental, have shown that perturbations in the streamwise flow direction have the greatest impact on turbine load response [114] [92] [6]. The other components of flow perturbation are comparatively negligible. For these reasons, only streamwise velocity fluctuations (as defined in Figure 7.1) are considered in this chapter.

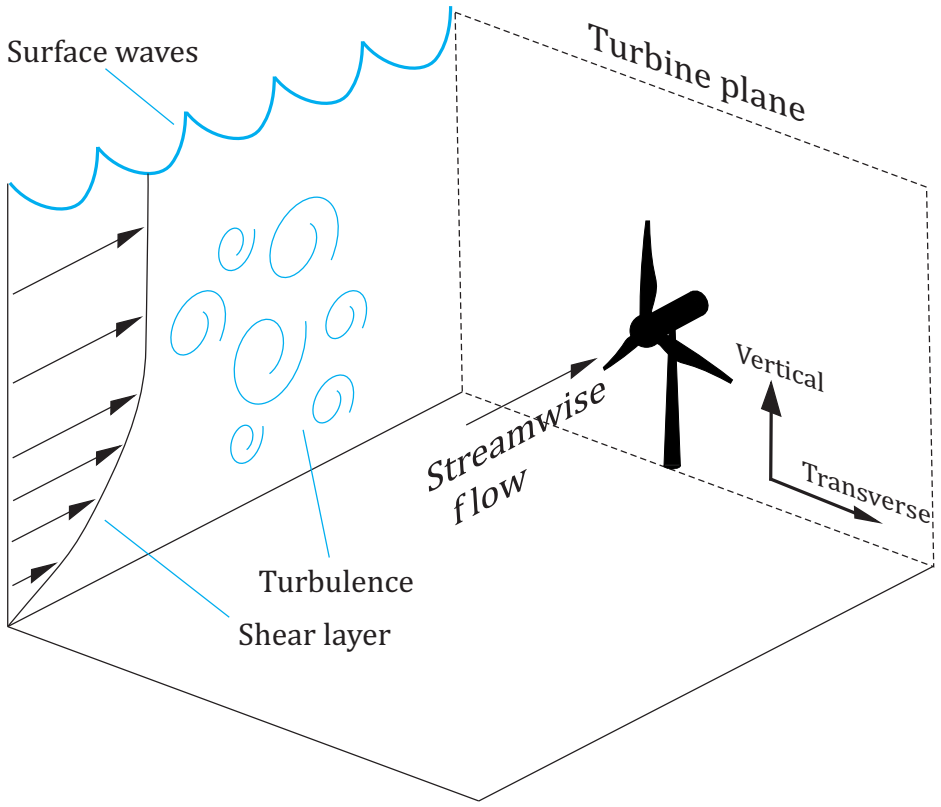

Fig. 7.1 Illustration of the unsteady flow in a tidal channel.

The different sources of unsteady flow will now be described in terms of their attributes when occurring in tidal flows, and their significance in fatigue load calculations will be assessed, accounting for 3D gust effects. Note that in realistic flow conditions, the presence of the turbine in the flow may distort the incoming unsteady flow. This effect is out of the

scope of the current study, and the unsteady flow is assumed to convect undisturbed past the tidal turbine.

7.2 Waves

The unsteady flow velocity induced by surface waves is greatest at the channel surface, and the amplitude then decreases with channel depth. Measurements suggest that regular waves at typical tidal sites can permeate to approximately 15 m below the surface [99]. Linear wave theory is most commonly used to estimate the wave-induced flow velocity, which uses measured wave heights and periodicity to estimate the induced velocity at various depths. However, nonlinear effects do occur in real flows and cause experimental measurements to deviate from predictions made by linear theory (see for example [6] or [72]). Studies have shown that waves moving perpendicular to the rotor plane result in the largest loads on tidal turbines, but there is currently no definition of the relationship between wave alignment and turbine loading.

According to linear wave theory the streamwise velocity perturbation induced by waves is given by [93]:

$$u = \frac{\pi H_{wave}}{T_i} . \frac{cosh(\frac{2\pi}{\lambda_{wave}} y) cos(\frac{2\pi}{T_0} t)}{sinh(\frac{2\pi}{\lambda_{wave}} h)} \tag{7.1}$$

Here H_{wave} is the significant wave height, defined as the mean amplitude (trough-to-crest) of the highest third of the recorded waves. T_i is the measured wave period, T_0 is the observed wave period (which differs from the measured wave period due to the Doppler effect), λ_{wave} is the wavelength, and y is the depth co-ordinate. In industry-standard design systems, such as Tidal Bladed [13], the effect of waves on the local blade velocity is obtained by linear superposition of the wave-induced velocities and the tidal current. This is not always strictly correct, as nonlinear effects can cause significant changes to the unsteady flow [6]. However, it is sufficient for a first-order approximation of wave-induced unsteady effects.

Using measured site data, Sequeira and Miller [115] estimated the gust amplitudes and reduced frequencies that were likely to affect a tidal turbine due to surface waves. The turbine used as an example was an 18 m diameter Alstom Tidal three-bladed design. At mid-span they found that the gust amplitudes experienced could range from 2 to 170% of the mean streamwise flow, the limit for static stall being 130% of the mean streamwise flow. The reduced frequency at mid-span was found to range from 0.05 to 0.21. They also determined that gusts caused by surface waves could be approximated as acting uniformly across the

aerofoil chord for modelling purposes, since the wavelengths are long relative to the blade thickness. As such, they determined that the Loewy function was the appropriate unsteady transfer function to use for finding the unsteady aerofoil loads (see Chapter 2 Section 2.5.2). We will now extend Sequeira and Miller's analysis for a 3D rotor geometry and consider waves moving at different angles relative to the freestream flow.

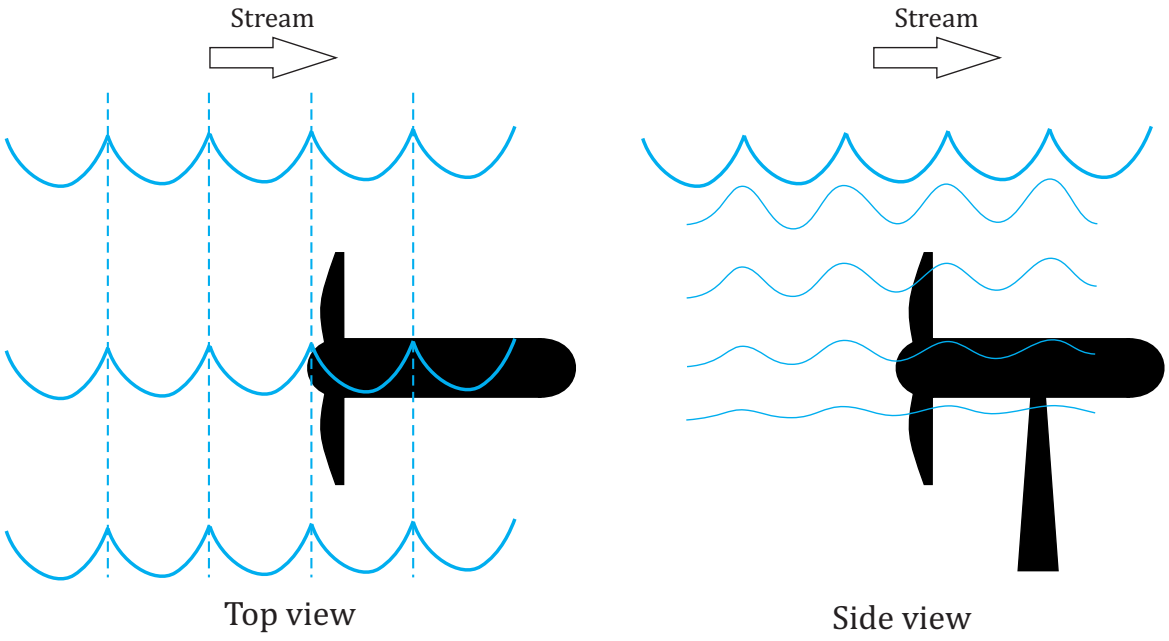

Fig. 7.2 Illustration of waves moving perpendicular to the rotor plane.

7.2.1 Waves moving in the direction of the tidal stream

Looking first at the case of waves moving perpendicular to the rotor plane, from a 3D perspective the unsteady flow induced by the waves can be considered to act in a spanwise-uniform manner. The flow state is illustrated in Figure 7.2. If the turbine blade is in a horizontal position the wave-induced gust will act uniformly across the whole span. If the turbine blade is in the vertical position, there will be variation in the gust amplitude based on water depth. However, the unsteady flow still acts "in-phase" along the span, the gust acting in the same direction at the same instant along the whole span. Because of the variation of gust amplitude with depth, there will also be a once-per-revolution component to the unsteady turbine response as a result of the wave interaction, which will be visible in the power and load spectra of the turbine in addition to the wave frequency itself. This unsteadiness can also be considered spanwise-uniform.

In the previous chapter it was determined that spanwise-uniform gusts have the potential to do by far the most damage to a tidal turbine, compared to gusts with some spanwise intermittency. This means that waves propagating perpendicular to the turbine plane can be classified as one of the most damaging unsteady gusts, from a 3D load perspective. This agrees with previous studies on wave effects, as mentioned above.

7.2.2 Oblique waves

It is generally assumed for the purpose of modelling that waves travel in-line with the tidal currents at a given site, with waves either following or opposing the current. This would give rise to the wave interaction shown in Figure 7.2. However, recent measurements indicate that significant wave-current misalignment does occur, with one study observing oblique wave conditions (defined as $> 20^o$ from the mean line) to occur more frequently than in-line wave conditions [79]. A theory for why this occurred was stated to be the channel bathymetry; tidal currents tend to follow the shapes of the channel floor, moving along bathymetric features. Waves, on the other hand, reflect off these same features, which tends to result in oblique radiation of the waves relative to the tidal current. This is likely to have important implications for the estimation of unsteady loads from wave-induced gusts.

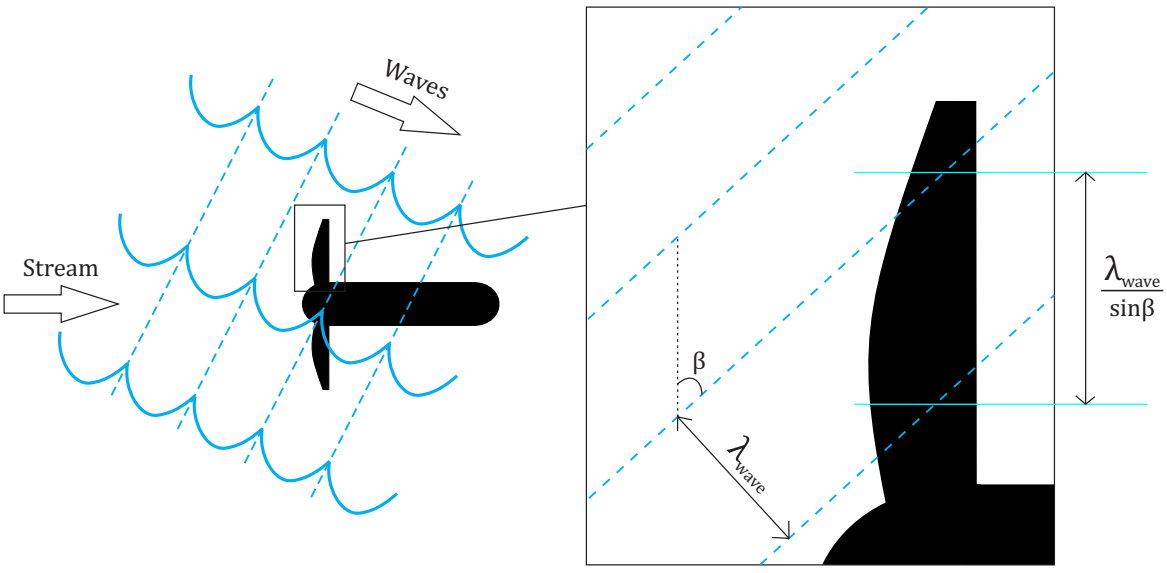

Fig. 7.3 Illustration of oblique wave interacting with a tidal turbine. The right hand view is for a blade in the horizontal position.

From the perspective of the spanwise gust wavelength, an oblique wave will produce radically different unsteady interference compared to a wave moving parallel to the stream. The unsteady gust may no longer be acting "in-phase" along the span, but have a spanwise variation that can be described by a gust wavelength λ_{gust}. The effect is most obvious when considering a turbine blade in a horizontal position, which is shown in Figure 7.3. The figure shows how a wave front approaching the turbine at an angle will generate a spanwise variation in the unsteady gust, the wavelength of which is dependent on the wave period λ_{wave} and approach angle β as follows:

$$\lambda_{gust} = \frac{\lambda_{wave}}{sin(\beta)} \tag{7.2}$$

Considering the definition of the cut-off spatial gust wavelength defined in the previous chapter, which is expressed as a fraction of the turbine blade span, the spanwise gust wavelength λ_{span} can be defined as:

$$\lambda_{span} = \frac{\lambda_{gust}}{D_{turbine}} = \frac{\lambda_{wave}}{sin(\beta)D_{turbine}} \tag{7.3}$$

As the approach angle β reduces, i.e. the wave approaches the direction of the tidal stream, the spanwise gust wavelength λ_{span} approaches infinity. If $\lambda_{span} > 1$ the gust can be considered as acting uniformly across the blade span. Furthermore, if λ_{span} is less than the cut-off value defined using the methodology outlined in the previous chapter, then the wave-induced turbine loads will be negligible when the blade is at its horizontal position.

Equation 7.3 is defined considering a turbine blade in the horizontal position. To account for turbine rotation when determining spatial gust wavelength along the span, the "effective" horizontal span can be used instead (see Figure 7.4). In such a case, Equation 7.3 can be modified to give:

$$\lambda_{span} = \frac{\lambda_{gust}}{|cos(\theta)|D_{turbine}} = \frac{\lambda_{wave}}{|cos(\theta)|sin(\beta)D_{turbine}} \tag{7.4}$$

Equation 7.4 indicates that twice per blade revolution (when the blade is vertical) the spanwise gust wavelength λ_{span} will go to infinity, so that at least twice per blade revolution the wave-induced gust can be considered as acting uniformly across the blade span. This suggests that even if a gust induced by an oblique wave causes spanwise variation below the cut-off wavelength, it will still produce a twice-per-rev unsteady interference on each blade. The proportion of the revolution over which the gust wavelength is above the cut-off

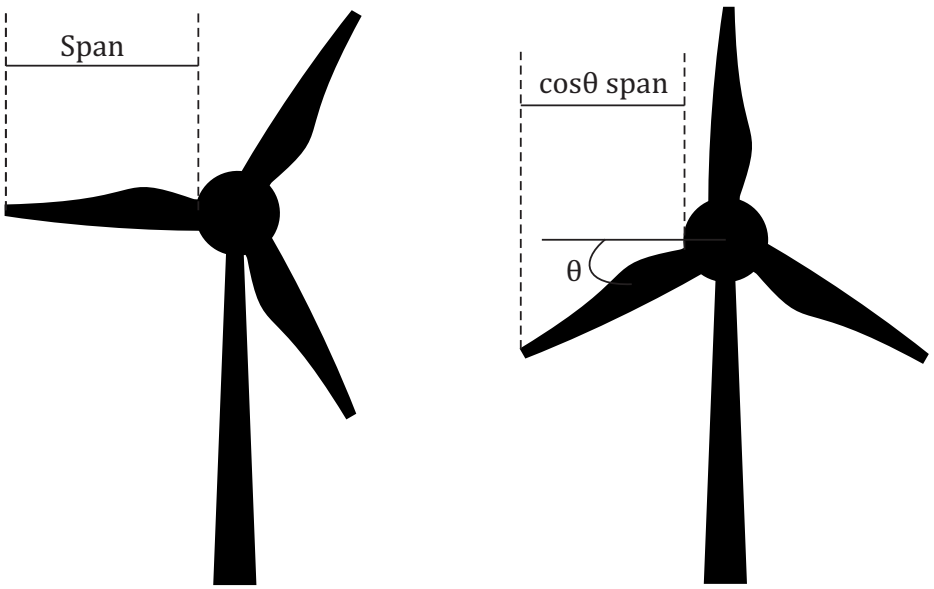

Fig. 7.4 Illustration of the effect of turbine rotation on the horizontal extent of the blade span.

wavelength will increase with the wavelength of the wave and will decrease with approach angle.

The form of Equation 7.3 shows a number of factors that will affect unsteady load response, as a result of spatial gust intermittency along the blade span. First of all, it is beneficial to have a large turbine diameter, $D_{turbine}$ – i.e. increasing the span of a blade will decrease the ratio of a given gust wavelength to span. Looking next at the wavelength of the surface waves, λ_{wave}, it can be obtained by:

$$\lambda_{wave} = TU_{wave} \tag{7.5}$$

Equation 7.5 implies that the spanwise gust wavelength λ_{span} resulting from the surface waves will be a function of wave period T and the wave propagation speed U_{wave}. Waves with shorter periods will result in smaller λ_{span} for oblique waves, potentially reducing the resulting unsteady load. Waves with slower propagation speeds will equally reduce λ_{span}, and as a result the unsteady load, for oblique waves.

We can conclude from this analysis that the dominating factors determining the effect of surface wave interaction on unsteady turbine loads are: the turbine diameter ($D_{turbine}$), the approach angle of the wave (β), the period of the wave (T) and the wave propagation speed (U_{wave}).

7.2.3 Finding the rate of occurrence of spanwise-uniform gusts from site data of wave conditions

At this point it is possible to make an estimate of the proportion of wave encounters that will result in spanwise-uniform interference, as well as the fraction which will be below the cut-off wavelengths defined in Chapter 6. This will be done by considering representative measurements from potential tidal sites. Lewis et al [79] measured the wave approach angle relative to the tidal stream at the Crown Estate tidal-stream demonstration zone in Anglesey, UK, for the purpose of determining the rate of occurrence of oblique waves relative to waves moving in the tidal stream direction. In a different study, Lewis et al [78] showed simulated wave data based on bathymetric conditions of three additional tidal sites: Pentland Firth, Orkney, and Pembroke (all in the UK). The measured and simulated data obtained by Lewis et al will form the basis of the estimates made in this chapter.

In their study of the flow at Anglesey, Lewis et al used ADCP measurements taken over a two-month period and divided the data into 36 bins, each of 10^o, where the angle denotes the wave direction relative to the East-West line. Notably, during this time only 8% of the recorded waves were "in line" with the tidal stream (defined as $< 20^o$ from the mean line of the tidal stream). The simulated data for the remaining three sites was divided into twelve bins, each of 30^o.

In the present study, the angle of approach of the waves relative to the turbine is defined as the difference between the mean angle of each bin and the mean tidal stream conditions of the respective sites, assuming the turbine plane to be aligned perpendicular to the mean tidal stream direction. While there was some slight asymmetry recorded in the directions of the flood and ebb tides, the deviations were small and for simplicity only the flood tide angle was used for the mean directional indicator for the analysis in this section.

In the case of the measurements from Anglesey, Lewis et al found that nearly 80% of the waves recorded occurred in the South-West directional quartile. Very few waves were recorded over the remaining 270^o. As such, the present study only uses data from the south-west directional quartile in the analysis of the Anglesey data.

For the three simulated sites, the periodicity of the waves was recorded and is shown in [78] and [79] as proportions of the total percentage of wave encounters present in each wave direction. The majority of the wave periods observed fell in the range $T = 0-3$ s or $T = 3-5$ s, while a small fraction (less than 5% of each bin) fell in the range $T = 5-9$ s.

For the purpose of simplification, the present study neglects the wave periodicities larger than $T = 5$ s. For the proportion of waves with periodicity in the range $T = 0-3$ s, an average value of $T = 2$ s was used to calculate the wavelengths, while for the waves in the range $T = 3-5$ s the value $T = 4$ s was used. In reality there will be a range of wave periods present in each of the directional bins, and each wave period needs to be individually recorded in order to make accurate calculations. However, this simplified estimate is sufficient to demonstrate the principles outlined in this chapter.

The data recoded at Anglesey, as presented in [79], did not include wave periodicity measurements. In order to obtain an estimate of the gust conditions for this study, a distribution of wave periods was chosen and applied to the wave occurrences in each directional bin. This distribution was based on the values found for the three simulated sites.

The wave propagation speed was not recorded for any of the sites in [78] and [79], but only the period of the waves T. However, the propagation velocity of a surface wave can be approximated using linear wave theory, assuming that the water depth is large (which is appropriate for typical tidal sites). The dispersion of a surface wave is given by [71]:

$$\omega^2 = g\kappa tanh(\kappa h) \tag{7.6}$$

where ω is the wave angular frequency, g is the gravity acceleration constant, κ is the wavenumber and h is the water depth. Given that the phase velocity is given by $U_{wave} = \omega/\kappa$, and that $tanh(\kappa h)$ is 1 for large h, the wave speed can be obtained as:

$$U_{wave} = \sqrt{g/\kappa} \tag{7.7}$$

Rewriting in terms of the wavelength, this is:

$$U_{wave} = \sqrt{g\lambda_{wave}/2\pi} \tag{7.8}$$

Inserting this expression into Equation 7.5, the following relation between the wavelength and the wave period is obtained:

$$\lambda_{wave} = \frac{g}{2\pi}T^2 \tag{7.9}$$

For the shortest wave period considered in this study, $T = 1$ s, this results in a wavelength of 1.56 m. The longest wave period, $T = 5$ s, resulted in wavelengths of 39.1 m. Note that Equation 7.1 shows that the wave-induced fluid particle velocity (which gives the amplitude of the unsteady gust) diminishes rapidly with increasing depth, at a rate proportional to

$cosh(2\pi h/\lambda_{wave}y)/sinh(2\pi h/\lambda_{wave})$, where y indicates depth. This means that for a specific wave height of 2 m (representative of the average height at the sites considered), the wave with the shortest wavelength would generate an unsteady gust amplitude of about 0.01 ms^{-1} at 1.5 m depth. This amplitude would likely produce negligible blade loads, although this also depends on the turbine geometry and mean flow conditions. Considering most turbines will be located deeper than 1.5 m, the impact of these waves can often be ignored. However, this study will only focus on the type of wave encountered, not the amplitude of the gusts. For a complete analysis of unsteady flow conditions, the amplitude would also have to be considered.

For the purpose of estimating the spanwise gust wavelength of surface waves at the four sites, we consider an 18 m diameter turbine. This is a large-scale device which, as noted earlier, will be beneficial in terms of its unsteady response to smaller scale gusts. For the purpose of estimation, we will use the cut-off wavelengths for unsteady torque and thrust that were found for the flat-plate rotor geometry in the previous chapter (see Chapter 6 Section 6.4.2). For the unsteady thrust, the cut-off wavelength was found to be half the length of the blade span, giving $\lambda_{span} = 0.25$. For the unsteady torque the cut-off wavelength was approximately a quarter of the span, i.e. $\lambda_{span} = 0.125$. Simplifying further by considering only the horizontal blade position, Equation 7.3 can be used along with the measurements of wave periods and approach angles, as outlined above, to estimate the rate of arrival of spanwise-uniform gusts.

Figure 7.5 shows the results of the analysis described in this section. The bar charts show how many of the wave encounters can be classified as either spanwise-uniform, intermediate or cut-off, as a percentage of the total number of wave encounters measured at each site. The uniform gusts will cause by far the largest unsteady loads on the turbines, while the waves beyond the cut-off values will not substantially affect the turbine loading. The waves in the "intermediate" range do result in some spanwise gust intermittency, but will still affect the turbine loading. The number of waves beyond the cut-off point for unsteady torque is shown as a fraction of the gusts beyond the unsteady thrust limit, as the torque cut-off imposes a more stringent limit on wavelength.

The results in Figure 7.5 show some differences in the wave conditions of the four sites, with substantial differences between the measured data at Anglesey and the three sets of simulated data. At Orkney almost 60% of wave events cause spanwise-uniform gusts, and about 20% are in the cut-off category. There were no waves causing spanwise intermittence

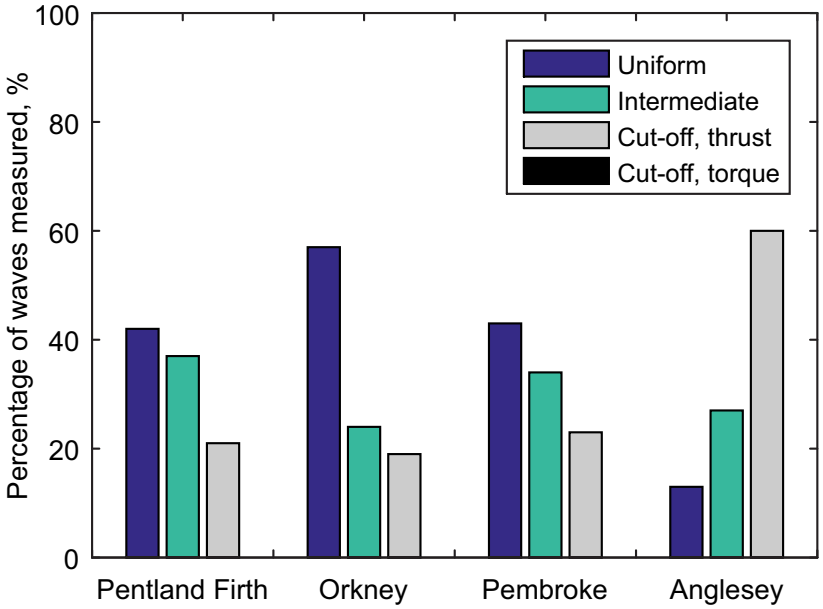

Fig. 7.5 Bar chart of gust encounter types, based on data recorded or simulated at four tidal sites and classified according to their spanwise gust wavelength. The analysis is performed on an 18 m diameter turbine. Note that no waves reached the cut-off condition for torque in this case.

that brought them beyond the cut-off wavelength for unsteady torque. As such, the wave environment at Orkney could be considered relatively harsh for tidal turbine development.

The data from Pentland Firth and Pembroke also shows that spanwise-uniform gusts are generated by approximately 40-45% of the measured waves, with slightly fewer at Pentland Firth. The two sites have relatively similar wave conditions. Pembroke has a slightly higher overall percentage of wave events falling in the "cut-off" category, compared to Pentland Firth. As such, Pembroke has a slight advantage. Anglesey shows radically different results compared to the other three sites, with the majority of waves in the "cut-off" category for thrust and only about 15% spanwise-uniform events. This is because, as mentioned earlier, only 8% of the wave encounters measured by Lewis et al were non-oblique [79].

As mentioned before, the 18 m diameter used in the example above is a large-scale device, which may not be available or appropriate for use at a given site. In order to illustrate how the wave conditions at the different sites would affect a smaller turbine diameter, Figure 7.6 shows the same analysis for a turbine with 10 m diameter. The effect of the diameter change on unsteady wave interaction is clearly detrimental; all sites apart from Anglesey now have substantially larger proportions of spanwise-uniform gusts as a result of the wave environ-

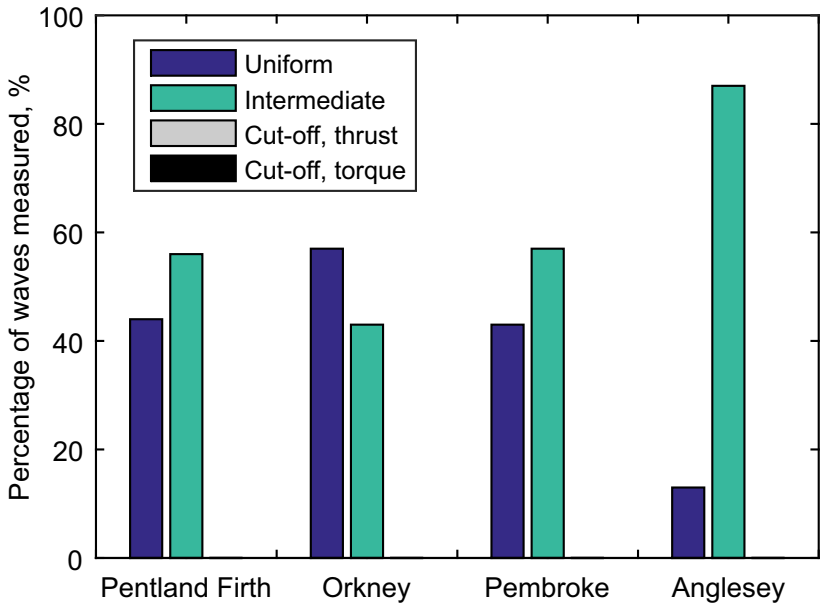

Fig. 7.6 Bar chart of gust encounter types, based on data recorded or simulated at four tidal sites and classified according to their spanwise gust wavelength. The analysis is performed on a 10 m diameter turbine. In this case, no wave conditions reached the cut-off wavelengths for either thrust or torque.

ment, and no waves fall beyond the cut-off wavelength for either unsteady torque or thrust. Anglesey remains the most beneficial wave environment out of the set. Reducing the turbine diameter to 3 m results in all sites producing 100% spanwise-uniform gusts.

It should be noted that the results are strongly dependent on the variation in wave periodicity. Given that the analysis in this section used some simplifications to generate the results presented in Figures 7.5 and7.6, the data should not be viewed as representative of the respective sites. In order to illustrate the effect of changing propagation speed and periodicity, Figure 7.7 shows estimates from the same data as was used to generate Figure 7.5, but this time analysed using the extremes of the available information on the two parameters. Figure 7.7a shows the results when using the upper range of wave periodicities ($T = 3$ s and $T = 5$ s). Figure 7.7b on the other hand shows the result when using the lower range of wave periodicities ($T = 1$ s and $T = 3$ s). There are similar trends in the results compared to Figure 7.5. Anglesey still seems to have the most favourable conditions, with no more than 10% uniform gust occurrences in any flow conditions. Orkney still has the harshest conditions, while Pembroke and Pentland Firth have similar conditions.

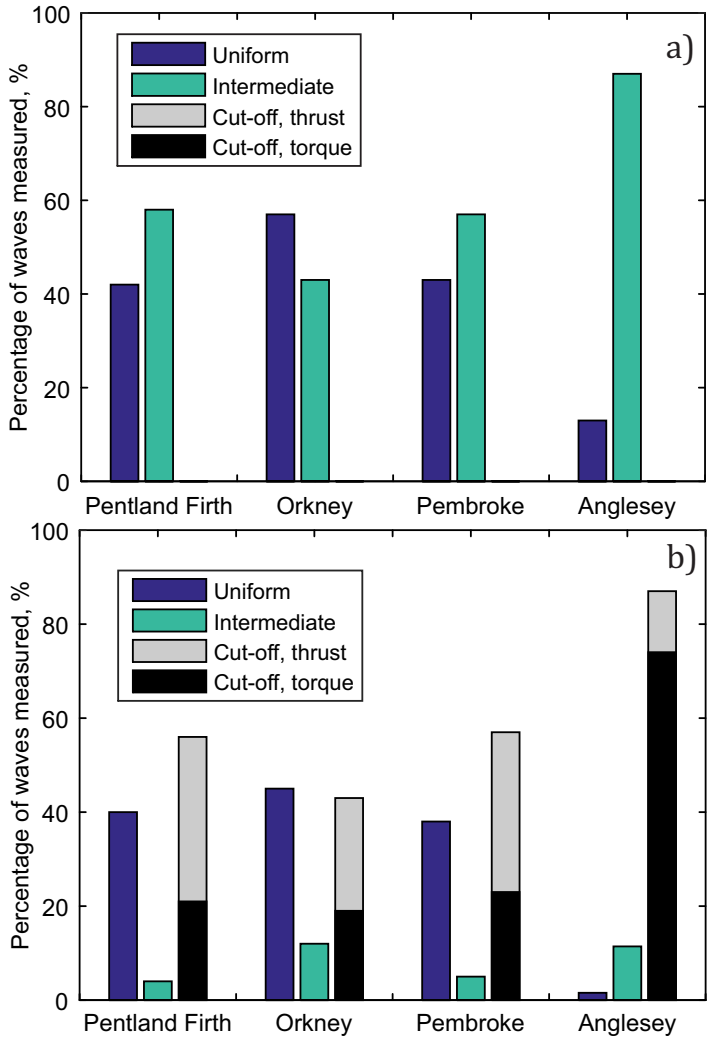

Fig. 7.7 Bar charts of gust encounter types, based on data recorded or simulated at four tidal sites. The analysis is performed on an 18 m diameter turbine. (a) Results obtained using higher bound of wave periods ($T = 3$ and $T = 5$). (b) Results obtained using lower bound of wave periods ($T = 1$ and $T = 3$).

The differences between Figure 7.5 and Figure 7.7 show the sensitivity of the analysis to measurement errors and assumptions. Nevertheless, the results illustrate how differences in wave conditions may be of vital importance when determining the suitability of certain sites for turbine deployment. They also show the profound impact on unsteady load predictions that results from consideration of 3D flow interaction. For a complete analysis of unsteady loads, the magnitudes of the gusts must also be accounted for; this study focused only on the occurrence of different gust types, while in reality some wave-induced gusts may be of negligible magnitude. While the method of analysis is highly dependent on the quality of measured site data, it represents a significant step forward in the consideration of oblique wave effects and site conditions in the calculation of unsteady turbine loads.

7.3 Turbulence

In this section the effect of tidal channel turbulence on the unsteady loads experienced by the turbine is assessed, taking into consideration spatial variation of the turbulent gusts along the turbine blade span.

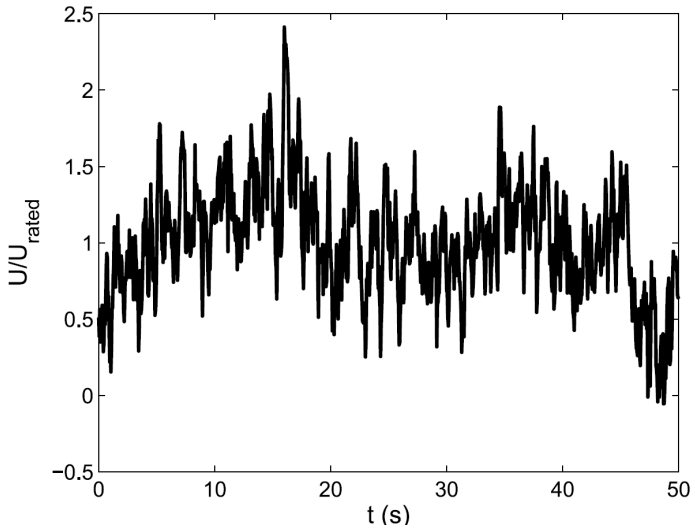

Fig. 7.8 Example of streamwise flow velocity at a typical tidal site, generated in Tidal Bladed [13]. Reprinted from [114] with permission.

An example of streamwise turbulence at a typical site, in terms of velocity fluctuations normalised by the mean flow, can be seen in Figure 7.8, simulated in the tidal turbine design software Tidal Bladed [13]. The fluctuation peaks can be seen to be very large, often over 80% of the mean flow velocity. This has the potential to cause extreme unsteady loading on

the turbines. Measured turbulence intensities (Equation 2.1) at tidal sites tend to fall in the range 10-20% [91]. Accounting also for the effects of eddies from upstream bathymetry features or headlands, Sequeira and Miller [115] found that this range of turbulence intensities resulted in gust amplitudes 10-60% of the mean axial flow. The question addressed in this chapter is whether some gust events can be assumed to have negligible effects on the turbine load, based on their length scales.

According to turbulent flow theory, turbulence can be visualised as a "cascade" of eddies, in which large eddies containing most of the kinetic energy gradually break down into smaller eddies, until they reach a scale where they can be broken down by viscous dissipation [125]. This is normally characterised as a spectrum of turbulence. The process of eddy breakdown is illustrated in Figure 7.9. While real turbulence consists of a continuum of different length scales, it is helpful to think of the flow as being made up of eddies gradually breaking apart into smaller scales.

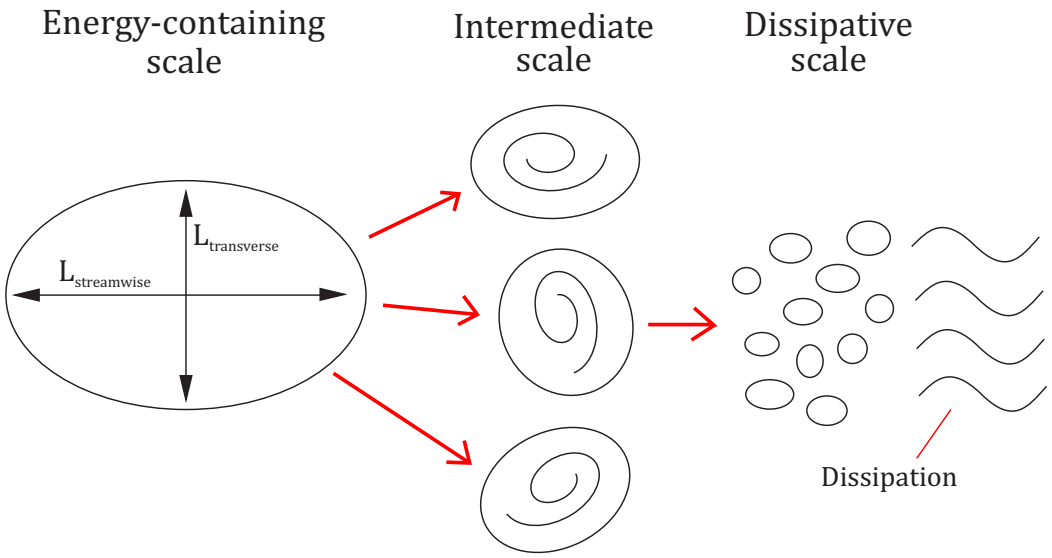

Fig. 7.9 Illustration of the turbulence cascade. Large energy-containing eddies break into successively smaller eddies, until they are dissipated by viscosity.

The largest eddies in turbulent flow are called the "energy-containing" or "inertial" eddies, and the characteristic length scales of these eddies have repeatedly been shown to influence the unsteady loads experienced by wind and tidal turbines (e.g. [12] [2]). However, as discussed in Chapter 2, there is significant uncertainty about the precise role of different turbulent length scales in determining the unsteady loads experienced by tidal turbines.

To estimate the range of reduced frequencies experienced by 2D tidal blade sections, based on measured turbulence conditions at tidal sites, Sequeira and Miller [115] used the characteristic integral and mixing length scales of the channel turbulence (L_{eddy}), as well as the eddy convection speed (U_{eddy}). The latter is generally assumed to be equal to the mean flow speed. The mixing length scale is determined by the mean shear gradient in the flow, while the integral length scale is defined as the spatial integral of the autocorrelation function of velocity [125]. The integral length scale is generally measured to be larger than the mixing length, but measurements show the two scales to follow the same pattern of occurrence in the flow [119].

The relationship between the turbulent length scales and the reduced frequency at each 2D blade section was found by Sequeira and Miller by using the following relation (from [97]):

$$k = \frac{2\pi c\left(\frac{U_\infty}{L_{streamwise}}\right)}{U_{rel}} \tag{7.10}$$

Here c represents the local aerofoil chord, and U_{rel} is the mean relative flow velocity at the blade section. The resulting reduced frequencies, based on measured site data, occurred in the range 0.02 to 0.65 at the mid-span of the 18 m diameter example turbine [115].

According to the findings in Chapter 6, the spatial extent of the turbulent eddies in the turbine plane will have a significant impact on the loading that they generate. A cut-off spanwise wavelength was identified, beyond which unsteady gusts had a negligible influence on the turbine. This cut-off wavelength will be used in this section in order to estimate the impact of 3D turbulent features on unsteady turbine load response. The analysis will be based on measured conditions at two representative tidal sites.

7.3.1 Turbulent length scales in channel flows

Industry-standard simulation software for tidal turbines will often use the von Karman atmospheric turbulence spectrum to simulate conditions in the sea [13], which measurements suggest is an appropriate approximation [94]. To estimate how the distribution of mixing length scales vary across a turbulent open channel flow, a parabolic function can be used [119]:

$$l_m = \kappa \frac{y}{H}\left(1 - \frac{y}{H}\right)H \tag{7.11}$$

In this notation H represents the depth of the channel, and the parameter κ is the Von Karman constant. The theoretical maximum length scale achievable in the channel is $kH/4$, at

mid-depth. Stacey et al [119] showed using measurements from Acoustic Doppler Current Profilers (ADCPs) that in an unstratified tidal channel the spatial distribution of mixing length scales is quite well represented by the parabolic function given in Equation 7.11. The exception is near the free surface of the channel, where the length scales do not go to zero. Stacey et al also showed the occurrence of several irregular peaks of much larger length scales than predicted by the parabolic function.

Equation 7.11 gives the theoretical mixing length scale, and it has been shown that the integral length scale follows a similar pattern [119]. If isotropic turbulence can be assumed, these length scales could also be used to estimate the extent of turbulent eddies in the turbine plane. Channel turbulence is, however, strongly anisotropic, especially over the low-frequency range. While streamwise length scales can be very large, hundreds of meters at some sites, the transverse scales will be limited by channel width and depth. Milne et al [94], measuring the turbulence at a site at the Sound of Islay, UK, recorded streamwise integral length scales of 17 m, while the vertical and transverse scales were both measured to be 4 m.

7.3.2 The effect of 3D turbulent eddies on turbine unsteady load response

For the purpose of determining the approximate effect of 3D turbulence on unsteady turbine load response, the vertical and transverse length scales must be included in the analysis, because they determine the spanwise extent of the gusts. For simplicity, the vertical and transverse scales will be assumed to be approximately equal. Denoting both length scales in the turbine plane as the "transverse" length scale (L_t), the spanwise gust wavelength (analogous to Equation 7.3) can be obtained from:

$$\lambda_{span} = \frac{L_t}{D_{turbine}} \tag{7.12}$$

This definition is based on the turbulent eddies interacting with the turbine in the manner illustrated in Figure 7.10. The "basic" gust shape of a certain wavelength, shown to the right in Figure 7.10, is based on the definition used by Tennekes and Lumley [125]. As in the previous section on wave interaction, $\lambda_{span} > 1$ means that the gust is spanwise-uniform. If λ_{span} is less than the cut-off value calculated through the eigenmode method shown in Chapter 6, the gust will have a negligible effect on the turbine load. For this section the cut-off values found for the flat plate rotor geometry in Section 6.4.2 will again be used

for analysis. This gives the cut-off for unsteady thrust as $\lambda_{span} = 0.25$ and the cut-off for unsteady torque as $\lambda_{span} = 0.125$. Again, the form of Equation 7.12 suggests that increasing the turbine diameter has beneficial consequences for the turbine load response to turbulence, as it will work to reduce λ_{span}.

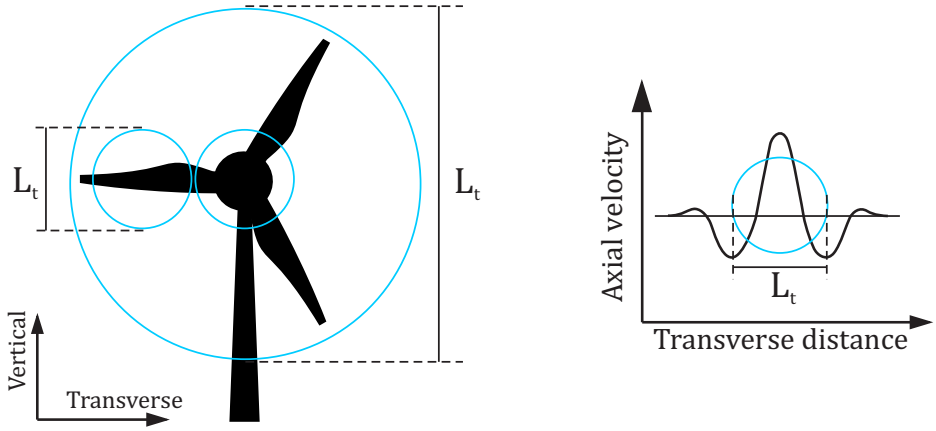

Fig. 7.10 Illustration of how the streamwise turbulent eddies are assumed to interact with the turbine in the model used in this chapter.

The eddy-turbine interaction in Figure 7.10 assumes that the eddy centre and the turbine axis are concentric. In a real channel flow this will of course not always be the case. In reality, if $\lambda_{span} > 1$ then the spatial wavelength of the gust along the blade span will be determined by the relative positions of the turbine and the turbulent eddies in the flow, as Figure 7.11 illustrates. Two turbines are considered interacting with eddies with $\lambda_{span} > 1$, but differently aligned. The turbine on the right is at the centre of an eddy, and so the gust acts uniformly along the span. For the turbine on the left, however, the edges of the turbulent eddy intersect with the turbine, and so there will be spatial intermittency in the gust effects.

While the placement of turbines relative to the turbulent gust events is relevant for an exact evaluation of when a gust can be approximated as acting uniformly across the blade span, this is outside the scope of the current study. It would require accounting for the probability of gust occurrence across the channel, producing an estimate of how often large-scale gusts are fully centred or partially-centred on the turbine. For a simplified analysis, this study assumes that the gust events are always centred on the turbine axis (as for the turbine to the right in Figure 7.11). This means that all gusts with $\lambda_{span} > 1$ are considered to act uniformly across the turbine.

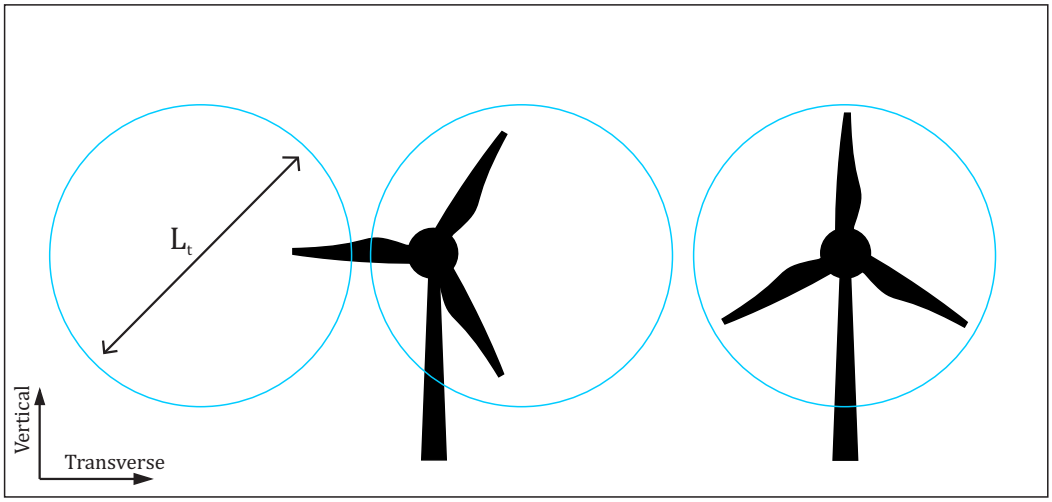

Fig. 7.11 Illustration of turbine interaction with large-scale turbulent flow features. The turbulent eddies represent streamwise flow oscillations with a finite spatial extent in the turbine plane.

7.3.3 Estimating 3D turbulent flow effects from site data

Using the measured power spectrum at a site, and assuming that Taylor's frozen gust hypothesis applies, it is possible to relate the eddy length scale to a point in the power spectrum as follows:

$$f = \frac{U}{L_{eddy}} \tag{7.13}$$

The propagation speed U of the turbulent eddies is commonly assumed to be equal to the mean flow speed, and this simplification has been adopted here. For isotropic turbulence, it is trivial to use this relation in combination with Equation 7.12 to find the turbulent spectral frequency below which the unsteady gusts will be spanwise-uniform. The spanwise cut-off frequency for unsteady torque and thrust can be similarly found, by setting $L_t = L_{eddy}$ in Equation 7.12:

$$f_c = \frac{U}{\lambda_{span} D_{turbine}} \tag{7.14}$$

If $\lambda_{span} = 1$, f_c will denote the highest frequency that causes spanwise-uniform gusts. If $\lambda_{span} = 0.25$ or $\lambda_{span} = 0.125$ the resulting frequency will denote the frequency limit beyond which turbulent energy will not affect the unsteady thrust and torque, respectively.

Figure 7.12 shows this analysis as applied to data measured at a potential tidal power site at Puget Sound (WA), in the United States. The measured turbulence power spectra was isotropic for a large section of the measured range, possibly due to the large width of the

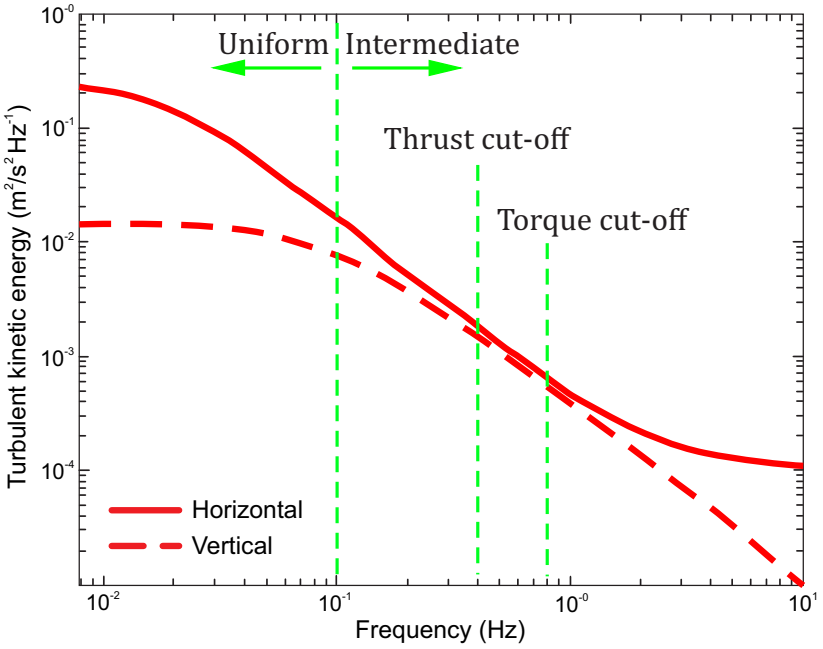

Fig. 7.12 Streamwise and vertical power spectra measured by Thomson et al [128] at Puget Sound, WA (USA), with limits for uniform, intermediate and cut-off eddy sizes shown in green (assuming isotropic turbulence).

channel. As such, Equation 7.14 can be used assuming isotropic turbulence. Thomson et al obtained the measurements through the use of Acoustic Doppler Velocimeters (ADVs), in order to sample high resolution velocity data at a point (the ADVs could resolve scales down to about 1 cm). ADCPs were used to obtain coarser measurements of larger volumes (the ADCPs could resolve scales down to about 1 m). Measurements were taken over a period of 7 days, at a point 4.7 m above the sea bed. The total channel depth was approximately 22 m.

The analysis performed to find the cut-off frequencies in Figure 7.12 was done given a 10 m diameter turbine. This results in all cut-off frequencies being located in the isotropic turbulence range, which simplifies the analysis. A large proportion of the turbulent energy spectrum can be seen to result in spanwise-uniform gusts. All of the large-scale energy-containing eddies will cause spanwise-uniform gust interaction, which will be detrimental to the fatigue life of turbines deployed in this location. The cut-off frequencies for torque and thrust occur at relatively high frequencies in the measured range. As such, the majority of the turbulent eddies present at the site will in fact have an impact on the unsteady load response of the turbine.

Milne et al [94] measured the properties of the turbulent flow conditions at a tidal site at the Sound of Islay in the UK, which is a narrower channel with higher degree of anisotropy. The impact of anisotropic turbulence on the turbine response can be illustrated by repeating the same analysis on the data of Milne et al, as was performed in Figure 7.12. The measurements were taken by Milne et al using an ADV, at a point 5 m above the sea floor. The mean depth in the channel was 55 m. Milne et al states that beyond turbulent reduced frequency $f_r = 0.5$, the turbulence appeared to be isentropic. The turbulent reduced frequency was defined as:

$$f_r = \frac{fz}{U} \tag{7.15}$$

The notation is the same as in Equation 7.13, with z denoting distance from channel floor. Milne et al used the measured flow data to obtain a best-fit line through the power spectra, using the von Karman spectral model. With this method, they identified the integral length scales in the flow to be $L_u = 17$ m in the streamwise direction, and $L_v = L_w = 4$ m in the vertical and transverse directions respectively.

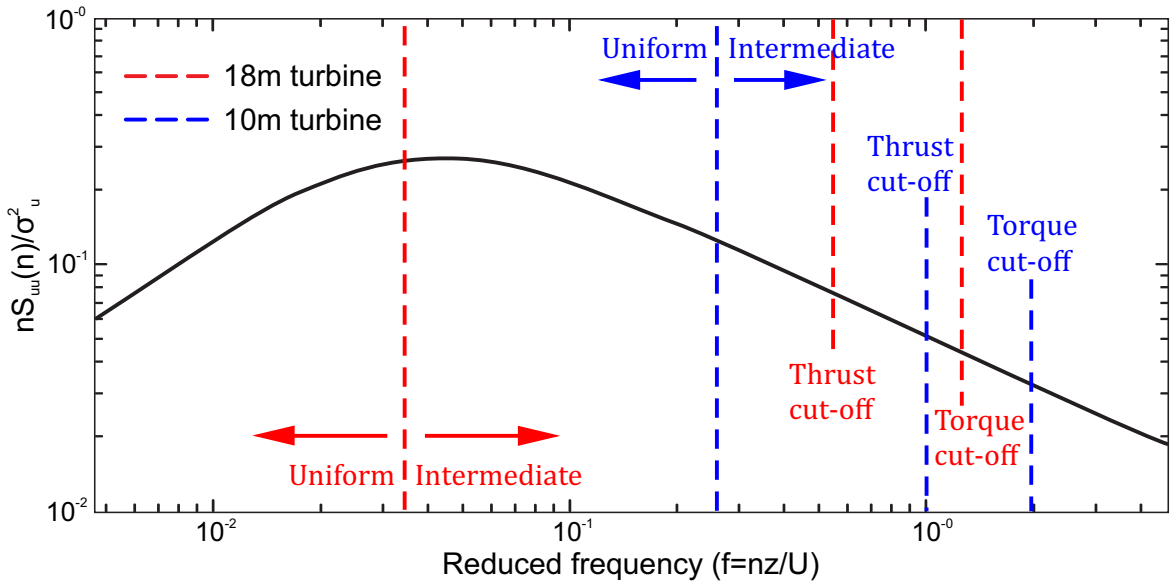

Fig. 7.13 Streamwise power spectra measured by Milne et al [94] at the Sound of Islay, UK.

Equation 7.14 can now be used to obtain an estimate for the cut-off frequencies associated with the streamwise power spectrum measured by Milne et al, by assuming that the spatial extent of the streamwise turbulent fluctuations is proportional to the ratio between the streamwise and transverse turbulent length scales (L_w/L_u), for the low-frequency turbulence. The analysis is performed for an 18 m diameter turbine and for a 10 m diameter turbine, to

illustrate the effect of turbine size on the results.

Figure 7.13 shows the cut-off frequencies calculated using Equation 7.14, plotted on top of the streamwise power spectrum for the turbulent site data measured by Milne et al. There is a substantial difference between the 18 m diameter turbine (red lines) and the 10 m diameter turbine (blue lines), which can be largely attributed to the anisotropy of the turbulence at the large scales. For the 18 m turbine a relatively small proportion of the turbulence results in spanwise-uniform gust events. Some of the large energy-containing eddies even appear to fall in the "intermediate" region. As isotropic conditions were found by Milne et al to occur at $f_r = 0.5$, the anisotropy does not affect the cut-off frequencies for thrust and torque. As such, a large proportion of the measured turbulent power spectra will have some effect on the turbine, but many of the large, energy-containing eddies will have a relatively limited effect. For the 10 m turbine on the other hand, the frequency limit for spanwise-uniform gusts occurs in the part of the spectrum where the turbulence is approximately isotropic. As such, all of the large energy-containing eddies will cause spanwise-uniform gusts. This illustrates the profound effects both channel anisotropy and turbine diameter can have on the turbine load response to turbulent inflow.

7.3.4 Discussion on the effects of turbulence

The method of analysis illustrated in this section is speculative at this point, and needs to be verified by experimental testing of turbines in turbulent conditions. As such, the results should not be considered representative of the respective sites. However, a recent experimental studies by Chamorro et al [18] on the impact of the turbulent flow spectrum on the power spectrum of a tidal turbines is notable in this regard. In their work, Chamorro et al identified a high-frequency region in the measured turbulence spectrum, starting at a "cut-off frequency" beyond which the turbine power was decoupled from the turbulence, apart from at multiples of the turbine rotational frequency. This result is qualitatively similar to the conclusions drawn in the present section (and in Chapter 6), on the effect that the spatial extent of gusts in the turbine plane has on the unsteady load, and the resulting existence of a cut-off frequency for turbulent loads beyond which turbulence will not interact with the turbine.

The results of Chamorro et al do not prove the validity of the theory presented here, but the qualitative agreement suggests that the theory may provide a physical basis for the experimental results. This could potentially result in a step-change in the understanding of

how measured turbulent spectra are coupled to the power and load response of tidal and wind turbines.

The results presented in Figure 7.13 suggested that turbulent anisotropy in a channel could significantly affect how a turbine responds to the turbulence. An assumption made in the analysis was that the spatial variation of the streamwise velocity in the turbine plane could be represented by the transverse turbulent length scales. This is not necessarily the case. A more rigorous analysis would require that the spatial extent of the streamwise velocity oscillations was measured. This could be done by finding the cospectrum of turbulence, obtained from the streamwise velocity fluctuations at two points in the flow, spatially separated in the turbine plane [97]. The process of finding the cospectrum of two points is illustrated in Figure 7.14. For harmonic flow acting uniformly over the whole turbine, the magnitude of the cospectrum at that frequency would go to infinity. The less the similarity between the two points, the lower the amplitude of the cospectrum would be.

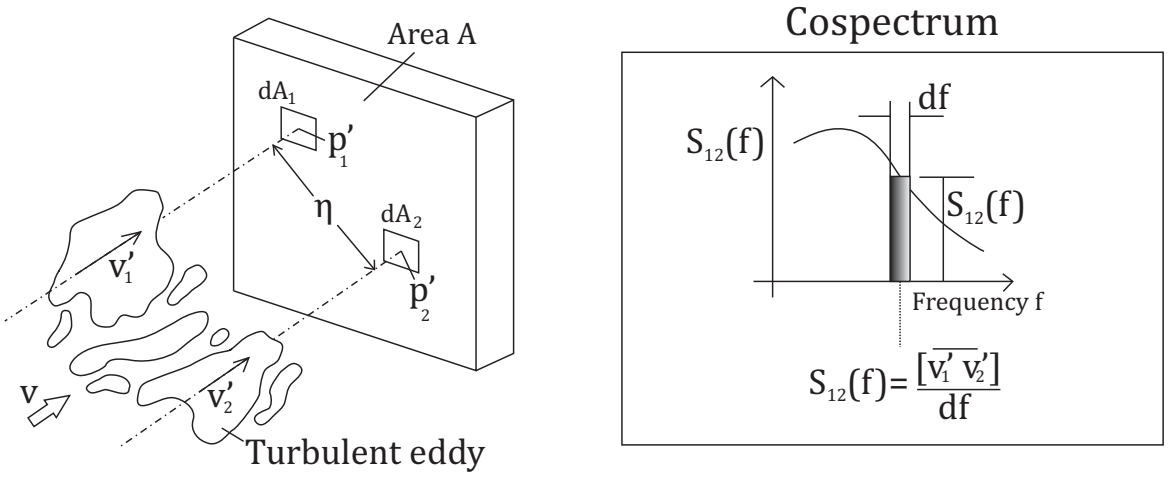

Fig. 7.14 Illustration of how the cospectrum of streamwise velocity fluctuation at two points is obtained. Reproduction of figure in [97].

The benefit of the eigenmode analysis presented in Chapter 6, in relation to this method, is that it provides an estimate of the spatial distance between two points of measurement that is required to capture all the relevant length scales in the flow. For example, using the cut-off limit found for the turbine in Chapter 6 (Section 6.4.3), measurements of the unsteady streamwise velocity should be undertaken at a transverse/vertical offset of 12.5% of the turbine diameter in order to capture all the scales of turbulence that will impact the unsteady thrust of the turbine. Unsteady gusts that are found to occur simultaneously at the

two measurement points will have an impact on the unsteady thrust.

To the author's knowledge, multi-point measurements of the resolution described here are generally considered as cost ineffective for turbine device developers. As such, the approximation based on the transverse length scale used in this section may be sufficient. However, the transverse and vertical extent of streamwise turbulent eddies in open channel flows is clearly a relevant parameter when determining the effect of turbulence on tidal devices. As such, it may be a relevant research topic for future study.

7.4 Rotation through steady flow features

If there are steady flow features in the tidal channel that vary spatially in the turbine plane, the turbine blades will experience periodic loading as they rotate through these flow features. The two main sources of this type of unsteady interaction is the channel shear profile and the potential field of the turbine support strut.

Sequeira and Miller [115] estimated the effects of these two unsteady features in terms of the local gust amplitude and reduced frequency at each 2D blade section. To estimate the effect of rotation through the shear layer they considered two different shear profiles: the standard 1/7 power law [13] and a shear profile measured by Soulsby [118]. The gust amplitude was determined by the axial flow velocity at the maximum and minimum vertical blade positions, and the reduced frequency by the rotational frequency. The two profiles gave virtually the same results: The mid-span reduced frequency was 0.21 for the blade used by Sequeira and Miller, and the gust amplitude was found to be about 5% of the steady axial flow velocity. This is at the very low end of the range of amplitudes induced by turbulence or waves (2 to 170% of the mean axial flow).

From a 3D perspective, rotation through the channel shear layer can be considered as a spanwise-uniform gust. The amplitude of the gust will change locally, with a maximum at the blade tip and a minimum at the hub, but the gust will act in the same direction at the same time along the whole span. The gust will be spanwise "in-phase". As was shown in Chapter 6, this type of unsteady interaction has the potential to do the most damage to the turbine. However, considering the very small amplitudes of the unsteadiness, the blade loading from rotation through the shear layer may still be negligible compared to the effect of turbulence and waves.

Similarly, the gust generated by the blade rotating through the potential field of the strut is spanwise-uniform. In this case the resulting gust amplitude is the same at all positions on the blade span. Sequeira and Miller estimated the effect of the strut by considering the first three Fourier harmonics of the relative velocity "seen" by the blade, and concluded that the unsteadiness had a relatively high reduced frequency (0.21 to 0.63 at mid-span). The amplitude, however, was even lower than that induced by rotation through the channel shear layer, at approximately 2% of the mean axial velocity. This is of course dependent on the proximity of the blades to the support strut. However, as tidal turbines are generally designed such that there is a fair distance between the support strut and the blades, this unsteady interference is likely to be negligible.

7.5 Conclusions

This chapter has built upon the conclusions about the effects of spanwise variation in the unsteady flow made in Chapter 6, and has considered the sources of unsteady flow that are typically found in tidal channels and analysed them based on their spanwise wavelength. The analysis is partially an extension of the work done by Sequeira and Miller [115], who analysed data from a number of different studies of flow conditions at tidal sites with the objective of finding the range of unsteady flow amplitudes and reduced frequencies likely to affect a tidal turbine. Their analysis was carried out from the perspective of 2D blade sections. The conclusions have now been expanded to also account for spanwise flow variation and new understanding of the unsteady response of 3D geometries.

The categories of unsteady flow examined were surface waves, turbulent eddies from the ocean and bathymetry, and rotation through otherwise steady flow features such as the shear layer. Sequeira and Miller found that rotation through nominally steady features usually occurred at very small unsteady amplitudes, which means they are likely to be negligible compared to turbulence and waves even though their 3D nature can be classified as spanwise-uniform.

In this chapter, surface waves and turbulence were studied in more depth, accounting for spanwise flow variation. Surface waves approaching along the normal of the rotor plane were shown to result in spanwise-uniform unsteady forcing. This is potentially hazardous, as the results presented in Chapter 6 showed that this is the most damaging type of gust (see Chapter 6 Section 6.4). As the approach angle becomes increasingly oblique, the gust interac-

tion becomes more intermittent along the span. The resulting intermittency is determined by the approach angle, the wave period and the wave propagation speed. The wave conditions at four different sites, as measured by Lewis et al [78] [79], were evaluated taking these 3D effects into account. The results of this analysis showed significant differences in the wave-induced gust encounters between the sites as a result of the obliqueness of the waves, indicating that 3D effects have a substantial role in determining the suitability of potential sites for development.

The occurrence of spanwise-uniform gusts resulting from flow turbulence in a channel was approximated using the streamwise turbulent power spectra from two tidal sites, measured by Thomson et al [128] and Milne et al [94]. Based on the results from Chapter 6, it was theorised that three regions of turbine response would occur as a result of a turbulent power spectrum: low-frequency eddies causing spanwise-uniform gusts, intermediate-frequency eddies resulting in spanwise intermittency in the unsteady gust, and high-frequency eddies which do not generate load on the turbine due to the spanwise gust wavelength being shorter than the specified cut-off value. The latter region was found for the two sites by assuming that the cut-off values for the spanwise gust wavelength identified for the flat plate rotor in Chapter 6 (Section 6.4.2) were applicable. The anisotropy of the channel turbulence was shown to significantly influence the extent to which turbulence interfered with the turbine. Increasing the turbine diameter also decreased the number of spanwise-uniform gust interactions, for both surface waves and turbulence effects.

While the above turbulence analysis is conceptual at present, it is notable that the presence of a distinct cut-off frequency in a turbulent spectra has been identified in experiments by Chamorro et al [18], beyond which turbulence and turbine power were decoupled. This is promising, showing that the 3D aspects of turbulence as described in this chapter may provide a flow-physical basis for the connection between measured turbulent spectra and resulting turbine response.

Chapter 8

Conclusions

8.1 Introduction

Tidal power stands out from other renewable energy sources in its predictability, and so tidal turbines have the potential to provide a source of baseload renewable energy in the UK. This would be a significant step towards a majority-renewables energy mix, and a crucial part of reaching the CO_2 emission targets set in international agreements. Several pre-commercial projects in the UK have already demonstrated the capability of the technology. However, unsteady hydrodynamic forces caused by ocean turbulence and waves have been identified as a primary challenge for further tidal turbine development. Unsteady forces affect the lifetime and reliability of the turbines, and therefore raise costs substantially. The models currently used to estimate unsteady forces on turbine blades have been shown to be unable to provide accurate predictions. This dissertation has addressed the importance of 3D effects when calculating unsteady gust loading on tidal turbine blades, as the assumption of locally 2D flow is one of the primary shortcomings of the unsteady models used at present.

At the start of this dissertation, three research questions were defined. These were:

1. What is the effect of 3D aerofoil geometry on the unsteady load response?
2. What are the limits of applicability of classical 2D unsteady aerofoil theories to 3D geometries?
3. How does spatial three-dimensionality of the unsteady flow field affect the resulting unsteady load response of a tidal turbine?

These questions were answered using a combination of low-order and high-order numerical simulation: a frequency-domain inviscid vortex lattice model was used to assess the effect of

3D aerofoil geometry on the unsteady gust response, while viscous simulations of a model turbine geometry were carried out using URANS CFD. The latter formed part of a study examining second-order effects on the unsteady response, such as wake deformation effects and viscous stall. It also provided a validation case for the vortex lattice model, showing that it was capable of first-order predictions of unsteady load response.

3D effects were divided into two categories: 3D geometry effects, and 3D gusts effects. Outlines of the conclusions drawn within each of these topics are given below.

8.2 3D geometry effects

8.2.1 Inviscid effects

The frequency-domain vortex lattice model was used to assess the impact of unsteady gusts on a range of 3D aerofoil geometries. None of the gusts had any variation in the spanwise direction, such that the gusts could be considered as two-dimensional, and the effect of 3D geometry features could be isolated. At first the effect of changing aspect ratio was evaluated, using a finite-span flat plate aerofoil interacting with sinusoidal and uniform transverse gusts. This relatively simple example nevertheless contained most of the significant features of 3D unsteady flow. At this stage, the importance of research question 1 was highlighted, as 3D geometry features were shown to significantly alter the unsteady loads compared to 2D predictions.

In order to answer research question 1 in more depth, a number of geometry parameters were identified as governing the degree of three-dimensionality of the unsteady load. These geometry factors were the following:

- Reduced frequency – 3D effects increase with decreasing reduced frequency.
- Aspect ratio – 3D effects increase with decreasing aspect ratio.
- Influence of tip flows – 3D effects are always strong in the vicinity of aerofoil tips.

Here "3D effects" are defined as deviation from the 2D prediction, in terms of either load amplitude or phase. At low aspect ratios, in proximity to the wing tips, and at low reduced frequencies the load amplitude was observed to be lower than that predicted by 2D theory. The phase of the load response was also observed to vary significantly along the span, leading to different spanwise sections responding out of phase with each other, even with no

spanwise variation in gust shape or reduced frequency. This is of particular importance to any application where the load is integrated along the blade span, for example in the evaluation of blade root bending moments.

A primary driver for the changes in unsteady load described above was found to be the 3D nature of the wake and the associated changes to the downwash. The 3D response is affected by the spanwise wake vorticity being finite for a finite-span geometry, while it is assumed to extend infinitely in a 2D approximation. The response is also affected by the presence of the unsteady streamwise component of wake vorticity, which is not modelled at all in a 2D system. While quasi-steady corrections exist for the downwash induced by the streamwise wake vorticity, this dissertation showed the streamwise wake vorticity to be strongly unsteady. This is in agreement with previous observations, such as those of Namba [96][95]. The combined effect of the downwash from the streamwise and spanwise wake vorticity components was shown to be the driver of unsteady response. As such, it is not possible to assume that the streamwise wake vorticity behaves in a quasi-steady manner. Doing so would significantly under-predict the amplitude of unsteady load response to gusts (see Figure 5.20).

Comparing a tapered finite wing to an untapered wing of the same aspect ratio (referenced to the mid-span chord), the difference in unsteady load response between the two was shown to be proportional to the quasi-steady lift distribution of each wing. As such, even though the reduced frequency varied along the span of the tapered wing, the mid-span reduced frequency was sufficient to describe the unsteady response of the wing. The effect of the tapering was effectively quasi-steady. However, taper was the only geometry feature where this was shown to be the case. For the case of a rotating blade, which causes a nonlinear spanwise variation in reduced frequency, the change to the unsteady characteristic as a result of rotation was not quasi-steady. Nevertheless, the mid-span reduced frequency was proposed as the most practical choice of governing frequency for the unsteady 3D system. This was partially justified by the "equalising" effect of the 3D geometry: the 3D response showed less extreme behaviour across the span than the 2D prediction, such that the response of an individual blade section was pushed towards a global average.

The importance of both the streamwise and spanwise wake vorticity components in combination for driving the unsteady load response was demonstrated several times. This was especially true in the case of a swept blade, which had no spanwise variation in reduced frequency or gust shape, but the nature of the 3D unsteady wake created a complex pattern of

response that did not approach the 2D response characteristic under any conditions.

Relating to research question 2, the inviscid parametric study showed that 2D unsteady aerofoil theory is only applicable to 3D geometries with high aspect ratios, and even then only in the mid-span region of the aerofoil. As rotation was added to the aerofoil, the response deviated more strongly from the 2D prediction, and the 2D Loewy function was shown to be unable to capture the returning wake effects accurately even at mid-span in the case of the model turbine geometry.

8.2.2 2nd order effects

Using the vortex lattice model in both time-and frequency-domain forms, as well as URANS CFD of a model turbine geometry, the impacts of wake deformation and of viscous separation on the unsteady load response were assessed. Again, spanwise-uniform gusts were used, such that the effects of 3D geometry could be isolated. The results showed that while viscous effects can be important to unsteady load calculations, especially in calculating the unsteady thrust, inviscid modelling in 3D is an appropriate tool for first-order calculations of turbine unsteady load response. Switching from 2D to 3D modelling resulted in significant gains in accuracy, as the flow physics of the 3D unsteady flow field are fundamentally different from 2D flow. Switching from inviscid to viscous modelling, however, gave more modest improvements in accuracy.

The effect of viscous separation/stall could be seen in the URANS results, and this was most prominent at lower gust frequencies, regardless of the gust amplitude. While distortion of the wake was found to have a relatively minor effect on the load response of the turbine, the downstream development of the wake may be relevant for turbine array configurations. Depending on the ratio of gust frequency to turbine rotational frequency, the structure of the unsteady wake could be seen to be either stable or unstable as it propagated downstream. Unstable wakes had returning wake sheets with alternating circulation strengths, leading to different wake segments interacting and eventually coalescing as they moved downstream. This was a strongly three-dimensional effect, and there was significant radial movement of the wake segments as they convected downstream.

A correction to the prescribed wake used in the vortex lattice model was developed, by using the time-domain model to find the steady-state wake shape, and then using this as an input to the frequency-domain model. This correction resulted in some accuracy gains in the load response, compared to the URANS results. However, the improvement was small in

comparison to the accuracy gained by using a 3D model instead of a 2D model. The speed of the frequency-domain tool compared to the time-domain VLM more than compensated for the small loss of accuracy that may occur due to missing a wake distortion term. Further to this, the changes in unsteady response due to the deformation of the wake by the incoming gust were found to be small.

8.3 3D gust effects

As well as studying the implications of 3D geometry on the unsteady response of a turbine, the effect of 3D gusts was examined (research question 3), with the aim of determining which unsteady flow properties can be correlated to turbine performance. While the intensity of the turbulent flow and the amplitude of surface waves has been shown to correlate strongly with increased turbine loads, the effects of realistic, 3D flow features have not been firmly established. While a number of studies have dealt with a 3D gust interacting with a 2D aerofoil with infinite span, there were few studies that dealt with 3D gusts interacting with 3D aerofoils or turbines.

In this dissertation, these queries were answered by performing eigenmode decomposition of solutions from the vortex lattice model used previously to assess the impact of 3D aerofoil geometry. Eigenmode analysis has the benefit of being able to give fundamental information on how the aerodynamic system is capable of responding to generic gust forcing. This provides an increased understanding of unsteady gust interaction, which in turn enables a descriptive view of how aerofoils interact with different turbulent length scales in the flow.

The eigenmode framework also provides generality to the gust-aerofoil interaction problem, since the model allows the unsteady response of an aerofoil geometry to be analysed independent of the gust shape. The response to any particular gust was then shown to be reduced to the interaction between the gust and the eigenmodes of the aerodynamic system, through the principle of "mode resonance". By this principle, gusts that were similar in shape to a given eigenmode "resonated" with the mode, and increased its contribution to the total lift response of the aerofoil. This made it possible to determine what types of gusts had the largest potential impact on an aerofoil geometry as follows: different eigenmodes were shown to have different capability of generating load response. As such, if a gust resonates with an eigenmode capable of generating large loads, that gust will result in a large load response in the aerofoil. By studying the eigenmodes with the largest capability to generate

loads, the gusts capable of doing the most damage to the turbine were therefore identified.

Through eigenmode decomposition, the spatial extent of unsteady flow features was shown to have a substantial effect on the ability of a given gust to generate loads on the turbine. The spanwise intermittency was shown to be the strongest indicator of whether a gust will cause large unsteady loads. Spanwise-uniform gusts had by far the largest impact on the flat plate geometries tested. On a realistic turbine geometry, however, the spanwise-uniform gusts were less dominant in generating load response, and gusts with more significant intermittency were also shown to be capable of generating large loads. This suggests that turbine design could potentially be used to modulate the turbine's response to unsteady flow features by 'tuning' the eigenmodes away from lengthscales that are expected to be prevalent in the inflow.

8.3.1 Practical implications

The eigenmode analysis enabled the identification of "cut-off" spanwise wavelengths below which unsteady gusts had negligible effects on the unsteady load response. In Chapter 7, applying this finding to experimental measurements from different tidal sites showed potentially profound implications in terms of the impact of site conditions on turbine fatigue life.

The concept of a cut-off frequency was applied first to surface wave interaction. The direction of travel of the waves relative to the turbine plane was shown to have a substantial impact on the intermittency of the resulting unsteady gusts along the turbine blade span. Using representative data from four prospective tidal sites, the percentage proportion of "spanwise-uniform" wave-induced gusts were shown to vary significantly between the sites. The larger the percentage of uniform gusts, the more damage the wave interaction is likely to cause to a turbine at the site. However, it was also shown that gusts in any flow direction would cause a twice-per-rev unsteady interaction with the turbine, as any wave-induced gust will be spanwise-uniform when the blade is in a vertical position.

Similarly, the impact of spatial intermittency was analysed in the context of flow turbulence. Measured inertial and mixing length scales were used to define a cut-off point in the turbulent spectrum above which turbulence would induce spanwise-uniform gusts. Anisotropy of the turbulence was shown to have a significant impact on the proportion of the turbulent spectrum that would cause spanwise-uniform gusts. The relative length of the turbine diameter was also shown to be a significant factor, with larger diameters likely to

perform more favourably in turbulent conditions.

While the practical implications of the effect of spanwise-intermittency on aerofoil gust response are largely conceptual at present, a number of studies have shown that turbine power is directly correlated to the measured turbulent energy spectrum below a certain cut-off turbulent frequency. This is promising, showing that the 3D aspects of turbulence as described in Chapter 7 of this dissertation may provide a flow-physical basis for the connection between measured turbulent spectra and resulting turbine response.

8.4 Future work

This project has identified several research areas deserving of further investigation. The primary need for the tidal industry relates to the development of an unsteady hydrodynamic model that includes both the effect of the spanwise wake vorticity being finite and the existence of an unsteady streamwise wake vorticity. A vortex lattice model such as the one used in this project is capable of capturing both of these effects, and would be suitable for use in industrial design with some further development. However, it is also worth investigating the option of developing unsteady correction factors to account for the 3D wake, rather than quasi-steady corrections, which can be used within existing BEMT models.

A potentially significant aspect of unsteady gust interaction is the distortion of gusts by the turbine potential field. This issue has not been addressed at all in this dissertation, where the "frozen gust" assumption has been used throughout. It is known that in a 2D system the gust and aerofoil potential fields are coupled in certain situations, but much less is known about the coupling between a 3D gust field and 3D aerofoils. When estimating the effects of turbulence on a turbine the frozen gust assumption is almost universally used, but if the presence of the turbine distorts the upstream flow field this assumption is invalid and a source of error. As such, further study is required on the impact of the turbine potential field on the upstream turbulence.

While the majority of this dissertation dealt with inviscid loads, Chapter 5 included a study using viscous URANS simulations which revealed additional unsteady flow features related to stall behaviour and wake propagation. The scope of this project did not allow for further investigation into these phenomena, and as such there is a need for future work on the topic. One of the notable viscous effects was the presence of significant hub stall in the unsteady simulations. It is not known how hub stall as a result of unsteady flow is affected

by 3D geometry and rotation, and how well stall occurrence is predicted by 2D strip-theory. This is especially relevant to the phenomenon of dynamic stall, which is predicted to occur in this region of the turbine. For tidal turbines, it is also of importance to further understand how dynamic stall occurs on thick aerofoils that fail via trailing-edge (as opposed to leading-edge) stall.

In Chapter 6 of this dissertation, it was demonstrated that the eigenmodes of an aerofoil determine how the aerofoil responds to unsteady gust interaction. Furthermore, the results indicated that the aerofoil design modulates how the aerofoil responds to unsteady gusts, and what types of gusts the aerofoil is most sensitive to. This is significant, but a detailed study of turbine design is outside the scope of this project. An important step in taking the eigenmode decomposition method further is to carry out such a design study, and use it to demonstrate whether a turbine can be designed to be resistant to the turbulent conditions measured at a particular site.

Finally, there is a need to examine further the impact of spatial non-uniformity and 3D gusts on turbine loads, primarily through carefully controlled experimental studies. Chapters 6 and 7 of this dissertation suggest that gusts that are intermittent along the span of an aerofoil are generally less harmful than gusts that are uniform along the span. This needs to be investigated experimentally, and the importance of the spatial extent of turbulent gusts in the turbine plane must be determined in terms of its impact on unsteady blade loading. Similarly, the impact of oblique waves relative to waves moving in line with the tidal stream must be further investigated, in light of the findings presented in chapter 7. Doing this will greatly enhance our understanding of the flow physics underlying unsteady hydrodynamic load response of tidal turbines.

Appendix A

Eigenmodes

In Chapter 6 of this thesis, a method is introduced in which eigenmode decomposition is used to identify what types of gusts are most damaging to a given aerofoil geometry. The method is carried out on three aerofoil geometries in 3D (see Figure 6.8); a flat-plate aerofoil with aspect ratio 5, a rotating flat plate at the same aspect ratio rotating at TSR 10, and a model turbine geometry (also used in Chapter 5). For each of these, the aerodynamic eigenmodes were found and sorted after their capability to produce either lift, thrust or out-of-plane bending moment on the aerofoils. Due to the principle of "mode resonance" introduced in Chapter 6, the modes capable of generating the largest loads correspond in spatial shape to the gusts capable of doing the most damage to the aerofoils.

For each of the three geometries, a "cut-off" mode was identified, beyond which modes have negligible contribution to the aerofoil load response. The cut-off limit was defined as 5% of the load generated by the largest mode. This allowed the identification of the minimum spanwise wavelength, below which a gust will not generate significant unsteady load response. In Chapter 6 only the final modes selected through this process were shown. In this Appendix, the sets of eigenmodes from which the selection was made are shown.

Figure A.1 shows the first 20 modes of the flat-plate aerofoil with aspect ratio 5, sorted by generated lift magnitude. The majority of the modes are approximately uniform along the span (some of the higher-order spanwise-uniform modes are highly intermittent along the chord, making them difficult to plot clearly). The cut-off mode identified is marked with a dashed red line. Any mode which was more intermittent along the span than this marked mode generated lift magnitude less than 5% of that of the largest mode (top left in Figure A.1).

Figure A.2 shows the first 20 modes of the rotating flat plate with aspect ratio 5, rotating at TSR 10. The modes are sorted by generated axial thrust. Again, many of the modes are approximately uniform in the spanwise direction. The cut-off mode has been marked with a red dashed line. Note that the mode immediately to the right of the marked cut-off mode has a shorter spanwise wavelength, but it was not chosen as the cut-off mdoe as it generated less than 5% of the thrust of the largest mode (top left in Figure A.2). Note also that there are two modes that appear to be highly intermittent in the second row of Figure A.2. These have been neglected from the selection process, as they result from numerical errors in the thrust calculations for high-order modes. These high-order modes show behaviour similar to aliasing, which can result in localised load spikes on the aerofoils when calculating thrust and bending moment. This is not physical, and as such these modes were not included in the selection process.

Figure A.3 shows the first 20 modes for the same rotating flat-plate aerofoil, but now sorted by contribution to the out-of-plane bending moment. The cut-off mode has been marked with a dashed red line. Again, in the third row there are two highly intermittent modes. These are also a result of numerical errors in the bending moment calculation, and have as such been neglected from the selection.

Figure A.4 shows the first 20 modes of the model tidal turbine geometry, which rotates at TSR 4, sorted by contribution to axial thrust. The cut-off mode has again been marked with a dashed red line. The modes with higher spanwise intermittency than this marked mode were fond to generate less than 5% of the thrust generated by the largest mode (top left in FIgure A.4). Figure A.5 shows the first 20 modes of the same geometry, sorted now by the contribution to the out-of-plane bending moment. The cut-off mode has been marked with a red dashed line. The mode immediately to the right of the cut-off mode has been neglected from selection, as it results from numerical error in the bending moment calculations.

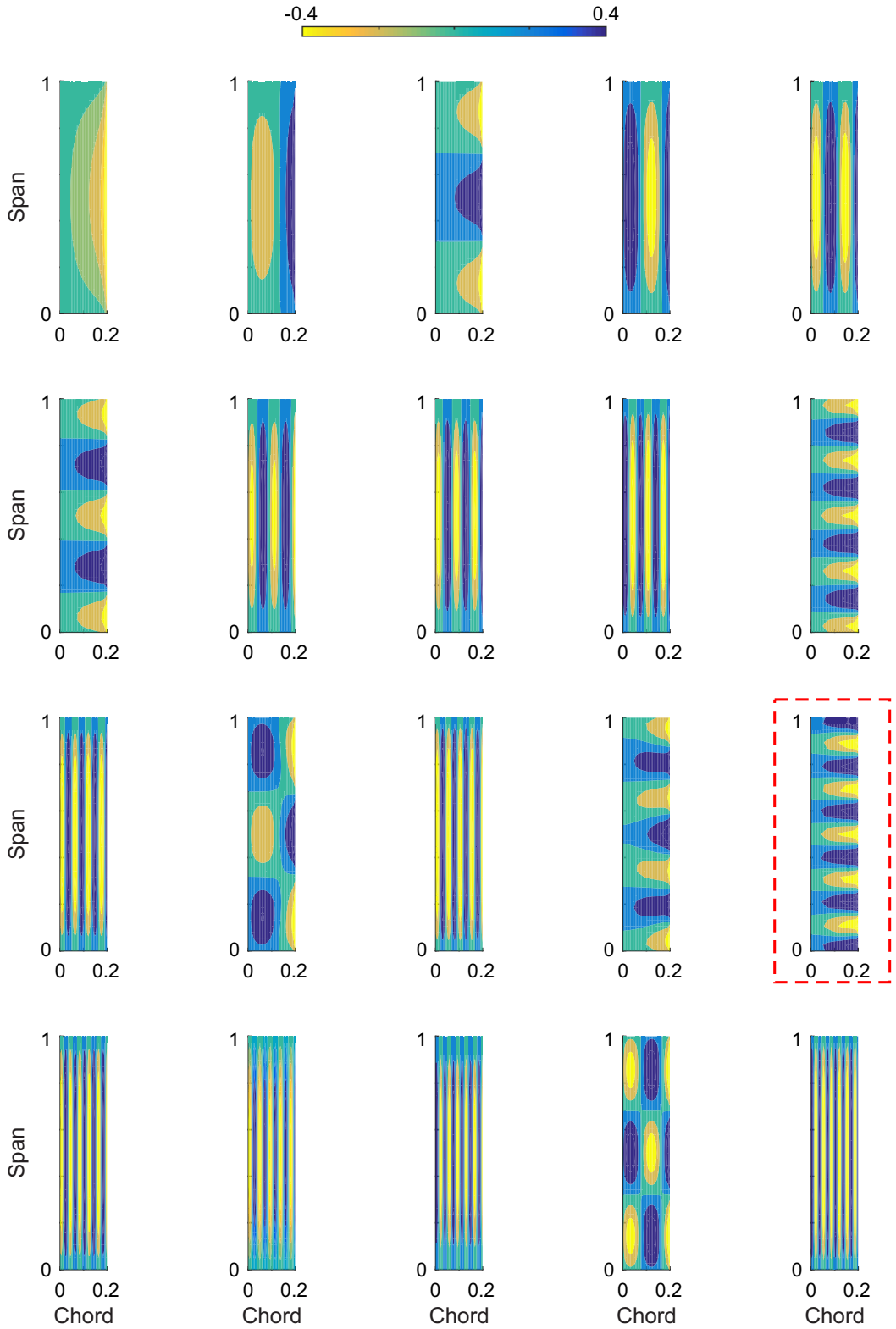

Fig. A.1: The 20 modes generating the maximum amount of lift on a flat-plate aerofoil with finite span, aspect ratio 5. The cut-off mode, as selected in the process described in Chapter 6, is marked in red.

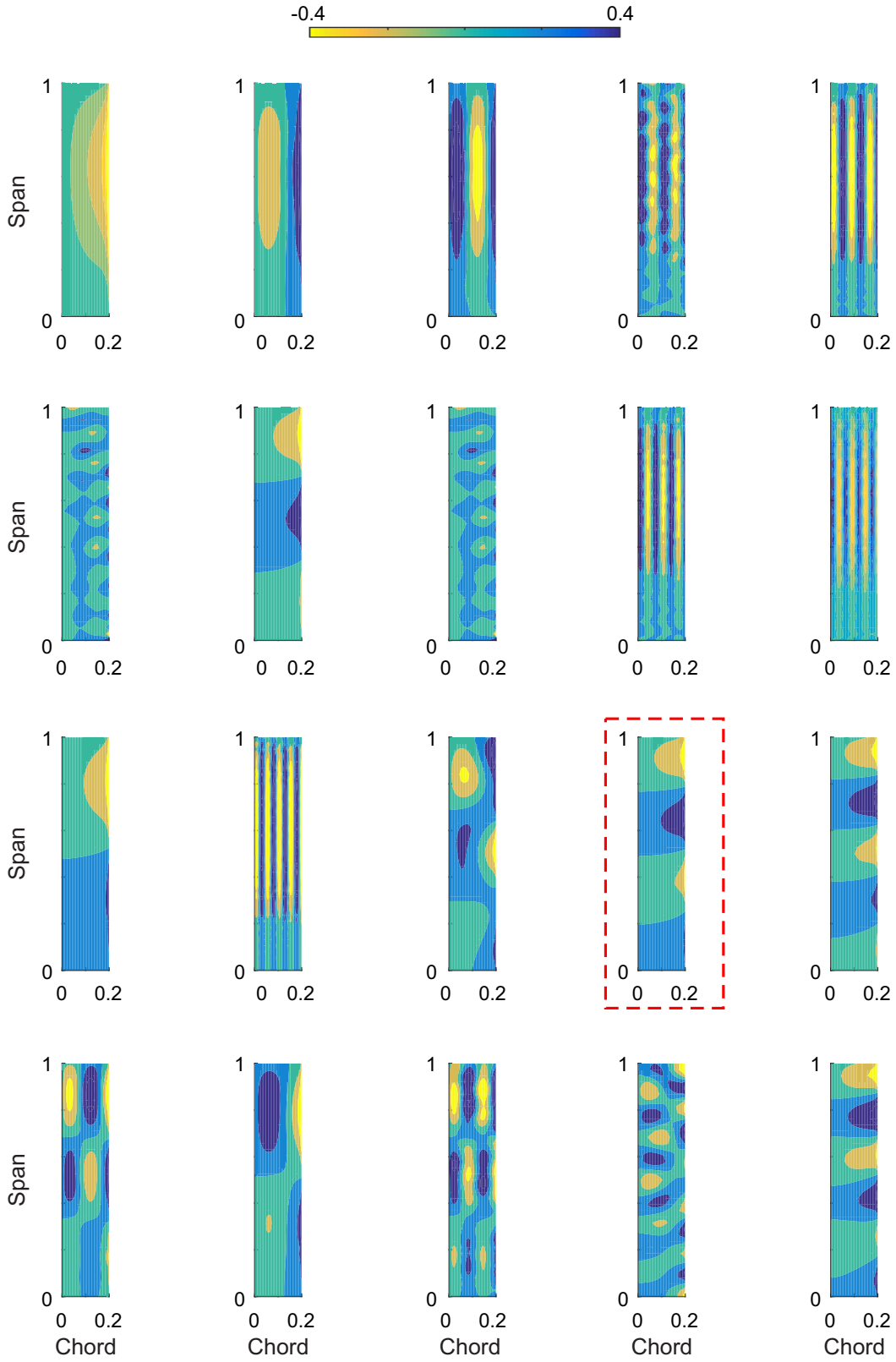

Fig. A.2: The 20 modes generating the maximum amount of thrust on a flat-plate rotating aerofoil with aspect ratio 5, rotating at TSR 10. The cut-off mode, as selected in the process described in Chapter 6, is marked in red.

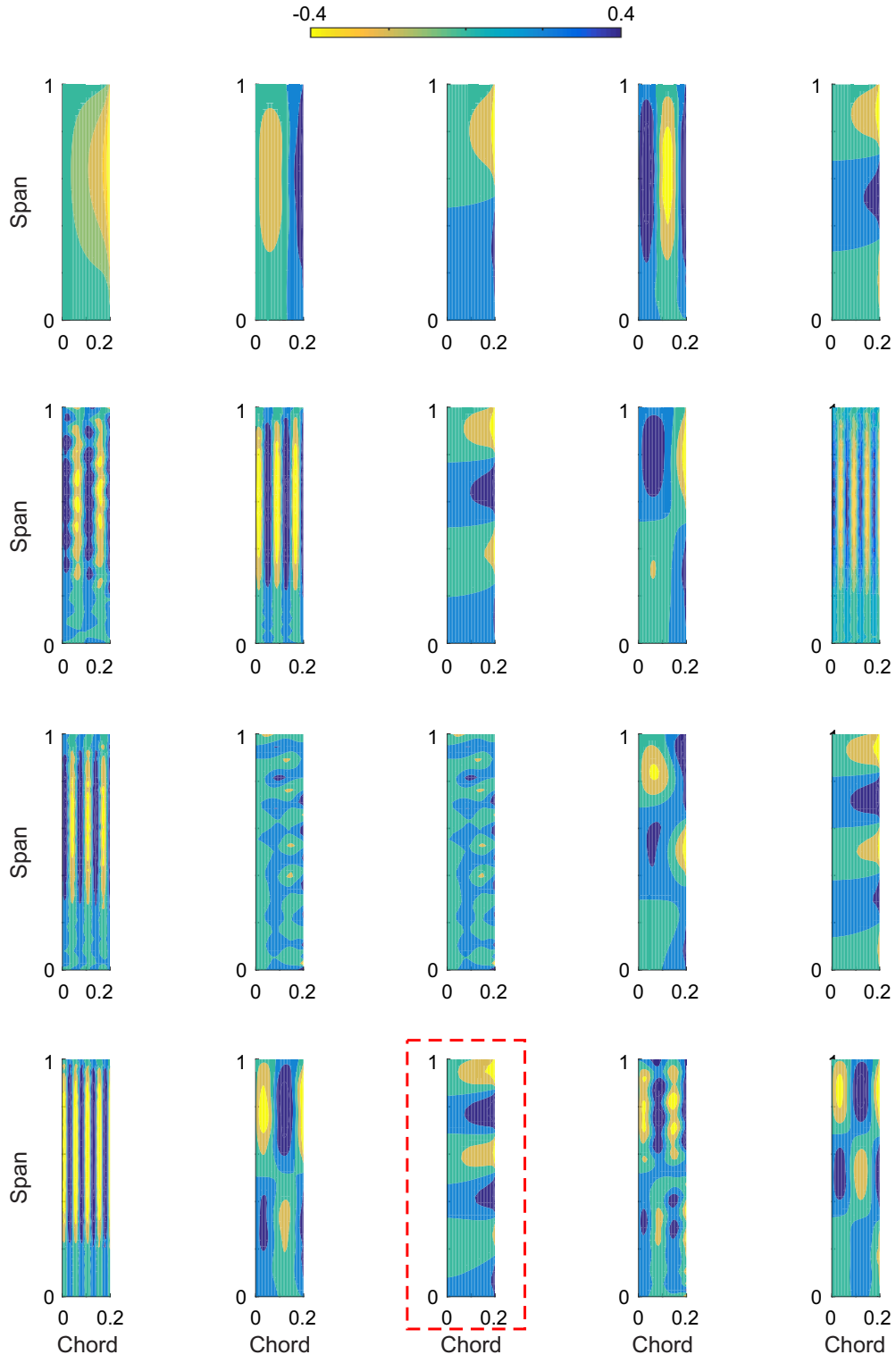

Fig. A.3: The 20 modes generating the maximum amount of out-of-plane bending moment on a flat-plate rotating aerofoil with aspect ratio 5, rotating at TSR 10. The cut-off mode, as selected in the process described in Chapter 6, is marked in red.

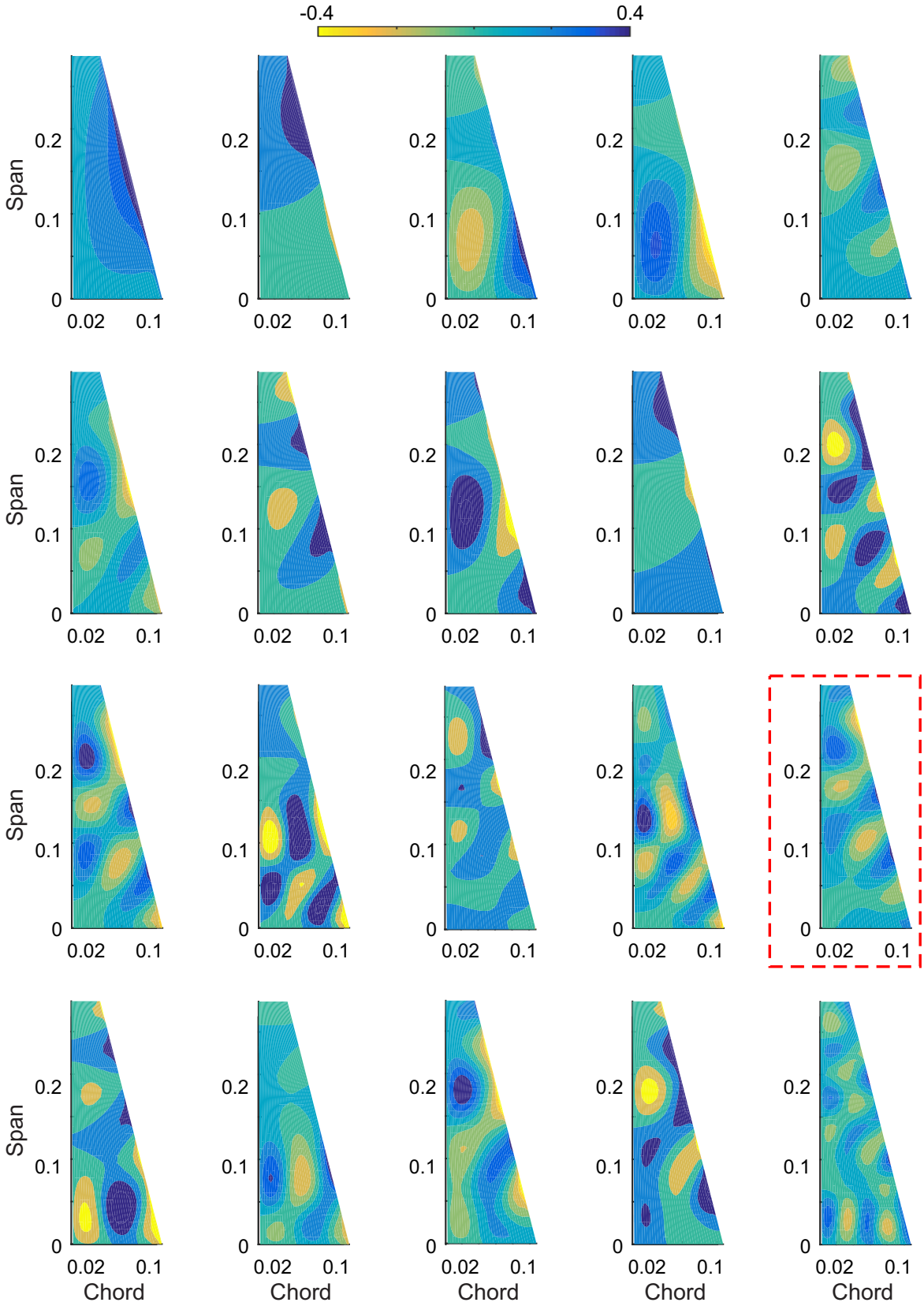

Fig. A.4: The 20 modes generating the maximum amount of thrust on a model tidal turbine blade, rotating at TSR 4. The cut-off mode, as selected in the process described in Chapter 6, is marked in red.

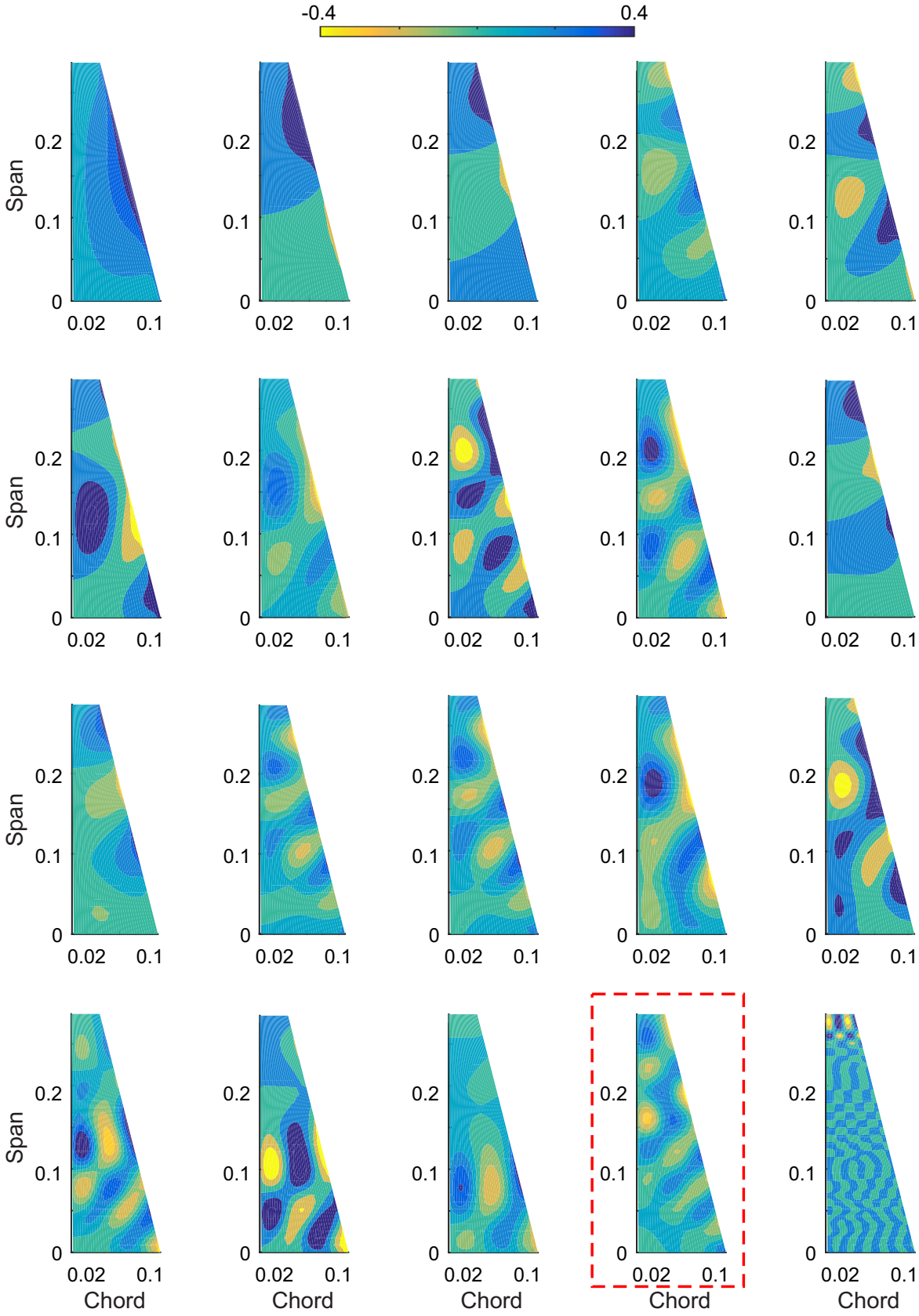

Fig. A.5: The 20 modes generating the maximum amount of out-of-plane bending moment on a model tidal turbine blade, rotating at TSR 4. The cut-off mode, as selected in the process described in Chapter 6, is marked in red.

References

[1] Acum, W. E. A. (1963). The Comparison of Theory and Experiment for Oscillating Wings. *Current Papers No. 681, Ministry of Aviation Aeronautical Research Council*.

[2] Afgan, I., McNaughton, J., Rolfo, S., Apsley, D., Stallard, T., and Stansby, P. (2013). Turbulent flow and loading on a tidal stream turbine by LES and RANS. *International Journal of Heat and Fluid Flow*, 43:96–108.

[3] Ahmadi, A. R. and Widnall, S. E. (1985). Unsteady lifting-line theory as a singular perturbation problem. *J. Fluid Mech.*, 153:59–81.

[4] Apsley, D. D., Stallard, T., and Stansby, P. K. (2018). Actuator-line cfd modelling of tidal-stream turbines in arrays. *Journal of Ocean Engineering and Marine Energy*, 4:259–271.

[5] Atassi, H. (1984). The Sears problem for a lifting airfoil revisited – new results. *J. Fluid Mech.*, 141:109–122.

[6] Barltrop, N., Varyani, K. S., Grant, A. D., Clelland, D., and Pham, X. P. (2006). Wave-current interactions in marine current turbines. *Proceedings of the Institution of Mechanical Engineers, Part M: Journal of Engineering for the Maritime Environment*, 220:195–203.

[7] Barmby, J. G., Cunningham, H. J., and Garrick, I. E. (1951). Study of Effects of Sweep on The Flutter of Cantilever Wings. *NACA Report 1014*.

[8] Barnes, C. J. and Visbal, M. R. (2019). Computational Investigation of the Effect of Sweep on Parallel Vortical-Gust/Wing Interactions. *AIAA SciTech Forum*.

[9] Bird, H. and Ramesh, K. (2018). Theoretical and Computational Studies of a Rectangular Finite Wing Oscillating in Pitch and Heave. *6th European Conference on Computational Mechanics (ECCM 6), 7th European Conference on Computational Fluid Dynamics (ECFD 7)*.

[10] Black and Veatch (2001). The commercial prospects for tidal stream power. *Technical report, DTI*.

[11] Black and Veatch (2011). UK Tidal current resource and economics. *Technical report No 121393, Carbon Trust*.

[12] Blackmore, T., Myers, L., and Bahaj, A. (2016). Effects of turbulence on tidal turbines: Implications to performance, blade loads, and condition monitoring. *International Journal of Marine Energy*, 14:1–26.

[13] Bossanyi, E. (2007). GH Tidal Bladed Theory Manual.

[14] Boutet, J. and Dimitriadis, G. (2018). Unsteady Lifting Line Theory Using the Wagner Function for the Aerodynamic and Aeroelastic Modeling of 3D Wings. *Aerospace*, 5(3).

[15] Burton, T., Sharpe, D., Jenkins, N., and Bossanyi, E. (2001). *Wind Energy Handbook*. John Wiley & Sons Ltd.

[16] Caradonna, F. X. and Tung, C. (1981). Experimental and Analytical Studies of a Model Helicopter Rotor in Hover. *NASA Technical Memorandum 81232*.

[17] Carlier, C., Pinon, G., Germain, G., Rivoalen, E., and Gaurier, B. (2015). A Synthetic-Eddy-Method to Represent the Ambient Turbulence in Numerical Simulation of Marine Current Turbine. *European Wave and Tidal Energy Conference (EWTEC) Proceedings*.

[18] Chamorro, L. P., Hill, C., Morton, S., Ellis, C., Arndt, R. E. A., and Sotiropoulos, F. (2013). On the interaction between a turbulent open channel flow and an axial-flow turbine. *J. Fluid Mech.*, 716:658–670.

[19] Chamorro, L. P., Hill, C., Neary, V. S., Gunawan, B., Arndt, R. E. A., and Sotiropoulos, F. (2015). Effects of energetic coherent motions on the power and wake of an axial- flow turbine. *Physics of Fluids*, 27.

[20] Cheng, H. K. (1975). Unsteady lifting-line theory as a singular perturbation problem. *Unsteady Aerodynamics, Proc. Symp. at Univ. Arizona*, pages 719–739.

[21] Cho, S. H., Kim, T., Song, S. J., and Shin, S. J. (2007). Seabed drag coefficient under tidal currents in the eastern Irish Sea. *AIAA Journal*, 45(5):1000–1006.

[22] Chopra, M. (1974). Hydromechanics of lunate-tail swimming propulsion. *J. Fluid Mech.*, 64(2):375–392.

[23] Chopra, M. and Kambe, T. (1977). Hydromechanics of lunate-tail swimming propulsion. Part 2. *J. Fluid Mech.*, 79(1):49–69.

[24] Clark, T. H. E. (2015). Turbulence in Marine Environments (TiME): A framework for understanding turbulence and its effects on tidal devices. *Proc. 11th Eur. Wave Tidal Energy Conf.*

[25] Cordes, U., Kampers, G., Meiner, T., Tropea, C., Peinke, J., and Hölling, M. (2017). Note on the limitations of the Theodorsen and Sears functions. *J. Fluid Mech.*, 811(R1).

[26] Corkery, S. J., Babinsky, H., and Harvey, J. (2018). On the development and early observations from a towing tank-based transverse wing-gust encounter test rig. *Experiments in Fluids*, 59(9).

[27] Culpo, M. (2012). Current Bottlenecks in the Scalability of OpenFOAM on Massively Parallel Clusters. *Partnership for Advanced Computing in Europe*.

[28] Delorm, T. M., Zappala, D., and Tavner, P. J. (2011). Tidal stream device reliability comparison models. *Proceedings of the Institution of Mechanical Engineers, Part O: Journal of Risk and Reliability*.

[29] Dominguez, F., Achard, J., Zanette, J., and Corre, C. (2015). A BEM-RANS approach for the fast power output prediction of ducted vertical-axis water turbines. *Proc. 11th Eur. Wave Tidal Energy Conf.*

[30] Drela, M. (2007). A users guide to MSES 3.05.

[31] Du, Z. and Selig, M. (1998a). A 3-D stall-delay model for horizontal axis wind turbine performance prediction. *ASME Wind Energy Symposium*.

[32] Du, Z. and Selig, M. (1998b). The effect of rotation on the boundary layer of a wind turbine blade. *Renewable Energy*, 20(2):167–181.

[33] Durbin, P. A. and Hunt, J. C. R. (1980). On surface pressure fluctuations beneath turbulent flow round bluff bodies. *J. Fluid Mech.*, 100:161.

[34] Edmunds, M., Williams, A. J., Masters, I., and Croft, T. N. (2015). BEM-CFD: A Revised Model for Accurate Prediction. *Proc. 11th Eur. Wave Tidal Energy Conf.*

[35] Farman, J. R. (2016). Wireless RF Telemetry for Rotating Frame Data Acquisition and Control. *XXIII Biannual Symposium on Measuring Techniques in Turbomachinery*.

[36] Fernandez-Rodriguez, E., Stallard, T., and Stansby, P. (2014). Experimental study of extreme thrust on a tidal stream rotor due to turbulent flow and with opposing waves. *Journal of Fluids and Structures*, 51:354–361.

[37] Filotas, L., T. (2002). Theory of airfoil response in a gusty atmosphere Part I - Aerodynamic Transfer Function. *UTIAS Report No. 139*.

[38] Florea, R. and Hall, K. C. (1998). Eigenmode Analysis of Unsteady Flows about Airfoils. *Journal of Computational Physics*, 147:568–593.

[39] Gant, S. and Stallard, T. (2008). Modelling a tidal turbine in unsteady flow. *Proc. Eighteenth Int. Offshore Polar Eng. Conf.*, 8(2007):473–480.

[40] Gaonkar, G. H. and Peters, D. A. (1988). Review of dynamic inflow modelling for rotorcraft flight dynamics. *Vertica*, 12:213–242.

[41] Garrett, C. and Cummins, P. (2007). The efficiency of a turbine in a tidal channel. *Journal of Fluid Mechanics*, 588:243–251.

[42] Gaurier, B., Davies, P., Deuff, A., and Germain, G. (2013). Flume tank characterization of marine current turbine blade behaviour under current and wave loading. *Renewable Energy*, 59.

[43] Gerolymos, G. and Vallet, I. (1994). Validation of 3-D Euler Methods for Vibrating Cascade Aerodynamics. *Proceedings of ASME International Gas Turbine and Aeroengine Congress and Exposition*.

[44] Glauert, H. (1929). The Force and Moment on an Oscillating Airfoil. *ARC R and M 1242*.

[45] Glauert, H. (1935). Airplane Propellers. *Aerodynamic Theory – A General Review of Progress, Volume IV*.

[46] Goldstein, M. and Atassi, H. (1976). A complete second-order theory for the unsteady flow about an airfoil due to a periodic gust. *J. Fluid Mech.*, 74(4):741–765.

[47] Golubev, V., Atassi, H., and Lipatov, A. (1997). 3-D unsteady effects in annular cascades with swirl and comparison with 2-D strip theory. *3rd AIAA/CEAS Aeroacoustics Conference*.

[48] Golubev, V. V., Brodnick, J., Nguyen, L., Dudley, J. G., and Visbal, M. R. (2012). High-Fidelity Simulations of Airfoil Interaction with Upstream Turbulence. *AIAA Fluid Dynamics Conference and Exhibit*.

[49] Golubev, V. V. and Dreyer, B. D. (2009). High-Accuracy Viscous Simulations of Gust Interaction with Stationary and Pitching Wing Sections. *47th AIAA Aerospace Sciences Meeting*.

[50] Golubev, V. V. and Nguyen, L. (2010). High-Accuracy Low-Re Simulations of Airfoil-Gust and Airfoil-Vortex Interactions. *AIAA< 40th Fluid Dynamics Conference and Exhibit*.

[51] Graham, J. M. H. (May 1970). Lifting Surface Theory for the Problem of an Arbitrarily Yawed Sinusoidal Gust Incident on a Thin Aerofoil in Incompressible Flow. *Aerodynamics Quarterly*.

[52] Green, M. O. and McCave, I. N. (1995). Seabed drag coefficient under tidal currents in the eastern Irish Sea. *J. Geophys. Res. Ocean.*, 100(C8):16057–16069.

[53] Greenshields, C. J. (2018). OpenFOAM User Guide, version 6.

[54] Guermond, J. and Sellier, A. (1976). A unified unsteady lifting-line theory. *J. Fluid Mech.*, 229:427–451.

[55] Gupta, S. and Leishman, J. G. (1989). Dynamic stall modelling of the S809 aerofoil and comparison with experiments. *Wind Energy*, 9(6):521–547.

[56] Hall, K. C. (1994). Eigenanalysis of Unsteady Flows About Airfoils, Cascades, and Wings. *AIAA Journal*, 32(12).

[57] Hall, K. C. and Lorence, C. B. (1992). Calculation of Three-Dimensional Unsteady Flows in Turbomachinery Using the Linearized Harmonic Euler Equations. *ASME*.

[58] Haller, G. (2005). An objective definition of a vortex. *J. Fluid Mech.*, 525.

[59] Hansen, M. O. L. and Madsen, H. A. (2011). Review Paper on Wind Turbine Aerodynamics. *J. Fluids Eng.*, 133(11).

[60] Hobbs, N. P. (1957). The transient Downwash Resulting From the Encounter of an Airfoil With a Moving Gust Field. *Journal of the Aeronautical sciences*.

[61] Holst, M. A., Dahlhaug, O. G., and Faudot, C. (2014). CFD Analysis of Wave-Induced Loads on Tidal Turbine Blades. *IEEE Journal of Oceanic Engineering*, 40(3).

[62] Howard, K. B., Hu, J. S., Chamorro, L. P., and Guala, M. (2015). Characterizing the response of a wind turbine model under complex inflow conditions. *Wind Energy*, 18:729–743.

[63] Jackson, R., Graham, J. M. R., and Maull, D. J. (1973). The lift on a wing in turbulent flow. *Aeronautical Quarterly*, 24.

[64] Katz, J. and Plotkin, A. (2001). *Low-Speed Aerodynamics*. Cambridge University Press.

[65] Katz, J. and Weihs, D. (1981). Wake Rollup and the Kutta Condition for Airfoils Oscillating at High Frequency. *AIAA Journal*.

[66] Kazarina, M., Kazarin, P., Nguyen, L., Golubev, V. V., Borener, S., Hufty, D., Pasiliao, C. L., and Visbal, M. R. (2016). Effects of Time-Harmonic Gust and Turbulence on Unsteady Aerodynamic Responses of Loaded Low-Speed Airfoils. *AIAA SciTech*.

[67] Keddington, M. (2015). Computational fluid dynamics simulations of oscillating wings and comparison to lifting-line theory. Master's thesis, Utah State University.

[68] Kinnas, S. A. and Hsin, C. (1992). Boundary Element Method for the Analysis of the Unsteady Flow Around Extreme Propeller Geometries. *AIAA Journal*.

[69] Kotsovinos, N. E. (1988). Secondary currents in straight wide channels. *Appl. Math. Model.*, 12(1):22–24.

[70] Kussner, H. G. (1935). Zusammenfassender Bericht uber den instationaren Auftrieb von Flugeln. *Luftfahrtforschung*, 13(12):410–424.

[71] Lamb, H. (1945). *Hydrodynamics*. Dover Publications, New York.

[72] Lawrence, J., Kofoed-Hansen, H., and Chevalier, C. (2009). High-resolution metocean modelling at EMEC's (UK) marine energy test sites. *8th European Wave and Tidal Energy Conference (EWTEC)*.

[73] Lee, T. and Gerontakos, P. (2004). Investigation of flow over an oscillating airfoil. *J. Fluid Mech.*, 512:313–341.

[74] Leishman, J. G. (2002). Challenges in Modeling the Unsteady Aerodynamics of Wind Turbines. *Wind Energy*, 5:85–132.

[75] Leishman, J. G. (2006). *Principles of Helicopter Aerodynamics*. Cambridge University Press.

[76] Leishman, J. G. and Beddoes, T. (1989). A Semi-Empirical Model for Dynamic Stall. *Journal of the American Helicopter Society*, 34(3).

[77] Leung, J. M., Wong, G. G., Weymouth, G. D., and Rival, D. E. (2018). Modelling Transverse Gusts Using Pitching, Plunging and Surging Airfoil Motions. *AIAA Journal*.

[78] Lewis, M., Neill, S., and Hashemi, M. R. (2014). Realistic Wave Conditions and their Influence on Quantifying the Tidal Stream Energy Resource. *Applied Energy*, 136:495–508.

[79] Lewis, M., Neill, S., Robins, P., Goward-Brown, A., and Stallard, T. (2018). Misalignment of Currents and Waves at Tidal Energy Sites. 6th Oxford Tidal Energy Workshop, 26-27 March.

[80] Lloyd, T., Turnock, S., and Humphrey, V. (2011). Unsteady CFD of a Marine Current Turbine using OpenFOAM with Generalised Grid Interface. *Proceedings of the 14th Numerical Towing Tank Symposium, UK*.

[81] Loewy, R. G. (1957). A Two-Dimensional Approximation to the Unsteady Aerodynamics of Rotary Wings. *J. of the American Helicopter Soc.*, 24(2):81–92.

[82] Lysak, P. D., Capone, D. E., and Jonson, M. L. (2016). Measurement of the unsteady lift of thick airfoils in incompressible turbulent flow. *Journal of Fluids and Structures*, 66:315–330.

[83] Masquelier, M. L. (1982). Application of the vortex-lattice method to propeller performance analysis. Master's thesis, Air Force Institute of Technology.

[84] Massaro, M. and Graham, J. (2015). The effect of three-dimensionality on the aerodynamic admittance of thin sections in free stream turbulence. *Journal of Fluids and Structures*, 57:81–90.

[85] McCann, G., Hitchcock, S., and Lane, S. (2008). Implications of Site-Specific Conditions on the Prediction of Loading and Power Performance of a Tidal Stream Device. *2nd International Conference of Ocean Energy (ICOE 2008)*.

[86] McCroskey, W. J. (1981). The Phenomenon of Dynamic Stall. *NASA Technical Memorandum 81264*.

[87] McCroskey, W. J. (1982). Unsteady Airfoils. *Ann. Rev. Fluid Mech.*, 14:285–311.

[88] McNae, D. (2013). *Unsteady Hydrodynamics of Tidal Stream Turbines*. PhD thesis, Imperial College London.

[89] Medina, A., Rockwood, M., Garmann, D., Visbal, M., and Ahmed, A. (2019). On the Characteristics of Three-Dimensional Dynamic Tip Stall on a Swept Wing. *AIAA SciTech Forum*.

[90] Milne, I. A. and Day, A. H. (2012). Horizontal-axis tidal turbine blade loading for multi-frequency oscillatory motion. *18th Australasian Fluid Mechanics Conference*.

[91] Milne, I. A., Day, A. H., Sharma, R. N., and Flay, R. G. J. (2013a). Blade loads on tidal turbines in planar oscillatory flow. *Ocean Eng.*, 60:163–174.

[92] Milne, I. A., Sharma, R., Flay, R., and Bickerton, S. (2010a). A Preliminary Analysis of the Effect of the Onset Flow Structure on Tidal Turbine Blade Loads. *OCEANS IEEE - Sydney*.

[93] Milne, I. A., Sharma, R. N., Flay, R. G. J., and Bickerton, S. (2010b). The Role of Waves on Tidal Turbine Unsteady Blade Loading. *Proceedings of the 3rd International conference on Ocean Energy (ICOE), Bilbao*.

[94] Milne, I. A., Sharma, R. N., Flay, R. G. J., and Bickerton, S. (2013b). Characteristics of the turbulence in the flow at a tidal stream power site. *Philosophical Transactions of the Royal Society A*, 371.

[95] Namba, M. (1987). Chapter 4: Three-dimensional flow. *AGARD Manual on Aeroelasticity in Axial-FLow Turbomachines Volume 1: Unsteady Turbomachinery Aerodynamics*.

[96] Namba, M. and Toshimitsu, K. (1997). Double Linearisation Theory of Three-Dimensional Cascades With Vibrating Blades Under Spanwise-Nonuniform Mean Loading, I: Subsonic Flow. *Journal of Sound and Vibration*, 148:41–68.

[97] Naudascher, E. and Rockwell, D. (1994). *Flow-Induced Vibrations*. A. A. Balkema, Rotterdam/Brookfield.

[98] Neill, S., Vögler, A., Goward-Brown, A., Baston, S., Lewis, M., Gillibrand, P., Waldman, S., and Woolf, D. (2017). The wave and tidal resource of Scotland. *Renewable Energy*, 114:3–17.

[99] Norris, J. V. and Droniou, E. (2007). Update on EMEC activities, resource description, and characterisation of wave-induced velocities in a tidal flow. *Proceedings of the 7th European Wave and Tidal Energy Conference (EWTEC), Porto, Portugal.*

[100] Olczak, A., Lande-Sudall, D., Stallard, T., and Stansby, P. K. (2015). Evaluation of rans bem and self-similar wake superposition for tidal stream turbine arrays. *In Proceedings of the 11th European Wave and Tidal Energy Conference (EWTEC)*.

[101] Ouro, P., Stoesser, T., Ramirez, L., and Harrold, M. (2018). Validation of an les-alm to simulate arrays of tidal turbines. 6th Oxford Tidal Energy Workshop, 26-27 March.

[102] Pereira, R., Schepers, G., and Pavel, M. (2011). Validation of the Beddoes – Leishman Dynamic Stall Model for Horizontal Axis Wind Turbines Using MEXICO data. *49th AIAA Aerospace Sciences Meeting*, pages 207–2019.

[103] Peters, D., Boyd, D., and He, C. (1989). Finite-state induced flow model for rotors in hover and forward flight. *Journal of the American Helicopter Society*, 34(4):5–17.

[104] Peters, D. and He, C. (1995). Finite state induced flow models Part 2: Three dimensional rotor disk. *Journal of Aircraft*, 32(2):323–333.

[105] Prasad, D. and Verdon, J. M. (2002). A Three-Dimensional Linearized Euler Analysis for Classical Wake/Stator Interactions: validation and unsteady response predictions. *Aeroacoustics*, 1(2).

[106] Rockwell Geyer, W. (1993). Three-Dimensional Tidal Flow Around Headlands. *Journal of Geophysical Research*, 98(C1):955–966.

[107] Sankaran, R. and Jancauskas, E. D. (1992). Direct measurement of the aerodynamic admittance of two-dimensional rectangular cylinders in smooth and turbulent flows. *Journal of Wind Engineering and Industrial Aerodynamics*, 41-44:601–611.

[108] Scarlett, G. T., Sellar, B., van den Bremer, T., and Viola, I. M. (2018). Unsteady Hydrodynamics of a Full-Scale Tidal Turbine. *7th European Conference on Computational Fluid Dynamics (ECFD 7)*, pages 313–341.

[109] Scarlett, G. T., Sellar, B., van den Bremer, T., and Viola, I. M. (2019). Unsteady hydrodynamics of a full-scale tidal turbine operating in large wave conditions. *Renewable Energy*, 143:199–213.

[110] Schepers, J. G., Heijdra, J., Foussekis, D., Oye, S., Rawlinson-Smith, R., Belessis, M., Thomsen, K., Larsen, T., Kraan, I., Visser, B., Carlen, I., Ganander, H., and Drost, L. (2002). Verification of European wind turbine design codes (ECN-C-01-055). *Technical report, European Commission - EU JOULE Project*.

[111] Schulten, J. B. H. M. (1982). Sound Generated by Rotor Wakes Interacting with a Leaned Vane Stator. *AIAA Journal*, 20(10).

[112] Sclavounos (1987). An unsteady lifting-line theory. *Journal of Engineering Mathematics*, 21(3):201–226.

[113] Sedky, G., Jones, A., and Lagor, F. (2019). Lift modeling and regulation for a finite wing during transverse gust encounters. *AIAA SciTech Forum*.

[114] Sequeira, C. L. (2014). *Hydrodynamics of Tidal Stream Turbines*. PhD thesis, Cambridge University.

[115] Sequeira, C. L. and Miller, R. J. (2014). Unsteady Gust Response of Tidal Stream Turbines. *Proceedings of the IEEE/MTS OCEANS*.

[116] Snel, H. (2004). Application of a modified Theodorsen model to the estimation of aerodynamic forces and aeroelastic stability. *European Wind Energy Conference, London, 22-25 November*.

[117] Snel, H. and Schepers, J. G. (1993). Investigation and modelling of dynamic inflow effects. *Proceedings of the European Community Wind Energy Conference (ECWEC), Travemunde, Germany*.

[118] Stacey, M., Monismith, G., and Burau, J. (1990). Chapter 15: Tidal current boundary layers. John Wiley & Sons Ltd. *The Sea: Ocean Engineering Science*, pages 523–566.

[119] Stacey, M., Monismith, G., and Burau, J. (1999). Measurement of Reynolds stress profiles in unstratified tidal flow. *Journal of Geophysical Research*, 104(C5):10,933–10,949.

[120] Stevens, P. R. R. J., Babinsky, H., Manar, F., Mancini, P., Jones, A. R., Nakata, T., Phillips, N., Bomphrey, R. J., Gozukara, A. C., Granlund, K. O., and Ol, M. V. (2017). Experiments and Computations on the Lift of Accelerating Flat Plates at Incidence. *AIAA Journal*, 55(10).

[121] Strbac, G. and Chaudhuri, B. (2014). Sustainable electrical systems. Lecture Notes, Imperial College London, Department of Electrical and Electronic Engineering.

[122] Sugar-Gabor, O. (2018). A general numerical unsteady non-linear lifting line model for engineering aerodynamics studies. *Aeronautical Journal*, 122(1254):1199–1228.

[123] Suzuki, A. and Hansen, A. C. (1999). Generalised Dynamic Wake Model for YawDyn. *AIAA Journal*.

[124] Tangler, J. L. (2002). The Nebulous Art of Using Wind Tunnel Aerofoil Data for Predicting Rotor Performance. *Wind Energy*.

[125] Tennekes, H. and Lumley, J. L. (1972). *A first course in turbulence*. M.I.T. Press.

[126] Theodorsen, T. (1935). General theory of aerodynamic instability and the mechanism of flutter. *NACA Techical Report no. 496*.

[127] Thinh, N., Sylvain, G., Thiebot, J., and Santa Cruz, A. (2015). On the use of turbulence models for simulating the flow behind a tidal turbine represented by a porous media. *In Proceedings of the 11th European Wave and Tidal Energy Conference (EWTEC)*.

[128] Thomson, J., Polagye, B., Durgesh, V., and Richmond, M. C. (2012). Measurements of turbulence at two tidal energy sites in puget sound, WA. *IEEE J. Ocean. Eng.*, 37(3):363–374.

[129] Verdon, J. M. (2001). Linearized Unsteady Aerodynamic Analysis of the Acoustic Response to Wake / Blade-Row Interaction. *NASA Contractor Report 2001-210713*.

[130] Verley, R. L. P. and Moe, G. (1978). The effect of cylinder vibration on the drag force and the resultant hydrodynamic damping. *Technical Report STF60 A79061, Norwegian Institute of Technology*.

[131] von Karman, T. and Sears, W. R. (1938). Airfoil Theory for Non-Uniform Motion. *J. of the Aeronautical Sciences*, 5(10):379–390.

[132] Von Mises, R. (1959). *The Theory of Flight*. Addison-Wesley.

[133] Wagner, H. (1925). Uber die Entstehung des Dynamischen Auftriebes von Tragflugeln. *Zeitschrift fur Angewandte Mathematik und Mechanik*, 5(1):17–35.

[134] Wang, T. and Coton, F. N. (2005). Prediction of the unsteady aerodynamic characteristics of horizontal axis wind turbines including three-dimensional effects. *Proceedings of the Institution of Mechanical Engineers, Part A: Journal of Power and Energy*, 214:385–400.

[135] Wei, N. J., Kissing, J., Wester, T. T. B., Wegt, S., Schiffman, K., Jakirlic, S., Hölling, M., Peinke, J., and Tropea, C. (2018). Insights into the Periodic Gust Response of Airfoils. (Under review).

[136] Whelan, J., Graham, J., and Peiró, J. (2009). Inertia Effects on Horizontal Axis Tidal-Stream Turbines. *Proceedings of the 8th European Wave and Tidal Energy Conference (EWTEC)*, pages 586–591.

[137] Whelan, J. I. (1987). *A fluid dynamic study of free-surface proximity and inertia effects on tidal turbines*. PhD thesis, Imperial College London.

[138] Wimhurst, A. and Willden, R. H. J. (2018). Computational observations of the tip loss mechanism experienced by horizontal axis rotors. *Wind Energy*, 21(7):544–557.

[139] Winter, A. I. (2011). Differences in fundamental design drivers for wind and tidal turbines. *Proceedings of IEEE OCEANS*.

[140] Yates Jr., E. C. (1966). Modified-strip-analysis method for predicting wing flutter at subsonic to hypersonic speeds. *J. Aircraft*, 3(1).

[141] Young, A. M., Farman, J. R., and Miller, R. J. (2016). Load alleviation technology for extending life in tidal turbines. *Progress in Renewable Energies Offshore-Proceedings of 2nd International Conference on Renewable Energies Offshore, RENEW*.

[142] Young, Y. L., Motley, M. R., and Yeung, R. W. (2010). Three-Dimensional Numerical Modeling of the Transient Fluid-Structural Interaction Response of Tidal Turbines. *Journal of Offshore Mechanics and Arctic Engineering*, 132(1).